CRC PRESS · TAYLOR & FRANCIS

A curated FreeBook for IGARSS 2019

Natural Hazards Monitoring with Remote Sensing

CRC Press
Taylor & Francis Group

www.crcpress.com/environmental-science

Contents

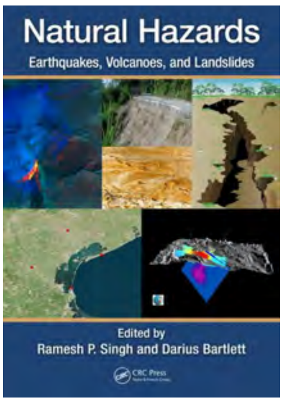
Natural Hazards
Earthquakes, Volcanoes, and Landslides
Edited by
Ramesh P. Singh and Darius Bartlett

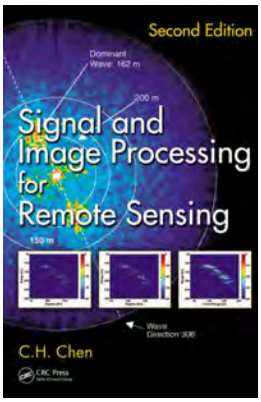
Second Edition
Signal and Image Processing for Remote Sensing
C.H. Chen


Satellite Altimetry Over Oceans and Land Surfaces
Edited by
Detlef Stammer
Anny Cazenave

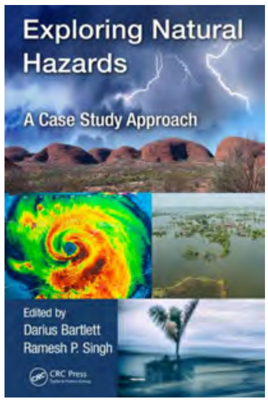
Exploring Natural Hazards
A Case Study Approach
Edited by
Darius Bartlett
Ramesh P. Singh

5 Satellite Radar Imaging and Its Application to Natural Hazards

Matt E. Pritchard and Sang-Ho Yun

CONTENTS

5.1 INTRODUCTION

Satellites provide critical global views for natural hazard characterization in advance of a crisis, as well as immediate damage assessment during or after a natural disaster (Voigt et al. 2007). While ground- and aircraft-based observations are also essential tools for hazard assessment and disaster response, satellites provide advantages to observe an area spanning hundreds of kilometres that may have had significant damage to infrastructure.

Radar images can be compared in multiple ways to measure ground changes before and during natural hazard events, like earthquakes, volcanic eruptions, floods, wildfires and landslides. Radar has unique capabilities compared with other remote sensing techniques; radar can 'see' through clouds and at night. More than a dozen civilian radar satellites are now available; the use of radar images has increased. New satellites with multisensors are required to monitor all potential hazards associated with land, ocean and atmosphere. We review five different change measurements that can be made by radar:

1. Amplitude
2. Phase (interferometry)
3. Along-track displacements and subpixel movements
4. Topography
5. Coherence

We discuss how each type of change detected can be applied to natural hazards or responding to natural disasters. A combination of different measurements is often necessary to avoid ambiguities in measurements (e.g. using both amplitude and coherence change to find the outline of flood zones under windy conditions, or using phase change and topography change for volcanic unrest).

We focus here on civilian satellite imaging radar systems that send electromagnetic pulses to the ground, record the reflections and then transmit the data back to Earth, where it can be formed into images. A commonly used method of combining many pulses together to make detailed images is called Synthetic Aperture Radar (SAR) (Figure 5.1). SAR is complementary to other types of remote sensing imagery, and in some cases it is superior because

- The satellite sends the electromagnetic signal, and images can be made day or night
- The radar signal penetrates through clouds
- Images taken at different times can be compared to forecast impending hazards or provide detailed maps of areas affected by disaster

In this chapter, we provide an overview of the natural hazard applications of imaging radar that complements recent technical reviews (Simons and Rosen 2015) and updates summaries of the hazard applications of SAR (Tralli et al. 2005; Lu et al. 2010a,b). We first briefly review five types of measurements made by radar that can be applied to the study of natural hazards (earthquake, volcano, flood, wildfire, cryosphere, landslide and coastal hazards) (Table 5.1), explain how the data can be used in rapid damage assessment during and in the immediate hours after a disaster, and then provide practical advice about the different types of radar data characteristics from the current and future satellites. We concentrate on applications on land or near land.

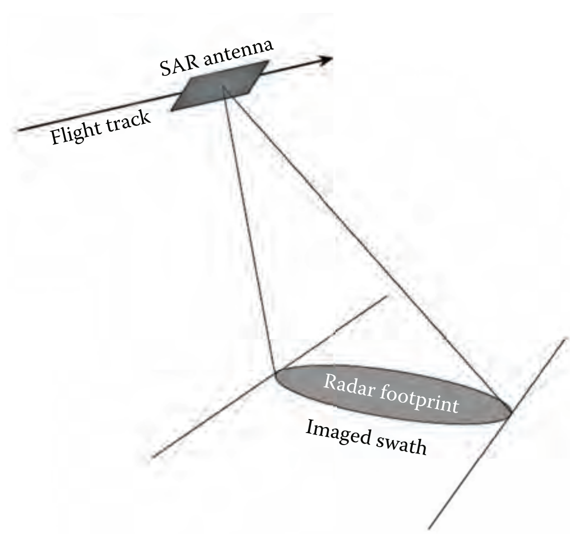

FIGURE 5.1 Typical side-looking imaging geometry of a SAR sensor. Unlike nadir-looking optical sensors, which resolve objects based on spatial (angular) separation of them, radar sensors differentiate objects based on the arrival time of backscattered echo.

TABLE 5.1
Summary of How the Five Different Radar Measurements Discussed in This Chapter Could Be Applied to the Study of Different Natural Hazards

	Amplitude	Phase	Pixel Tracking	DEMs	Coherence
Floods	X	X		X	X
Deformation before earthquakes and eruptions		X			
Wildfires	X				X
Deformation before river ice breakup		X			
Sea ice			X		
Landslides		X	X	X	X
Volcano eruptions and deposits (ash, lava and lahars)	X	X		X	X
Glacier change		X	X	X	
Building damage	X				X
Earthquake fault slip		X	X		X
Liquefaction					X
Water defence structures		X			X
Permafrost change		X			
Deformation before sinkhole collapse		X			
Subsidence – Coastal or human caused		X			

5.2 WHAT DOES RADAR MEASURE THAT IS USEFUL FOR NATURAL HAZARDS?

Change detection on the ground surface plays an essential role for natural hazard studies in both prediction and after-the-fact assessment. There are at least five different ways that SAR can be used to detect these changes. All these methods require at least two radar images acquired at different times (usually days to weeks apart) in order to determine the change between them. The power of imaging radar is that the change detection can usually occur on a pixel-by-pixel basis across the image, providing high spatial resolution maps (1–100 m/pixel) of changes over large areas spanning tens to hundreds of kilometres. In addition, for most applications, the calculation of change detection is done automatically, with little human intervention, and so can be applied over large regions to thousands of images or rapidly after a disaster. In the next sections, we provide overviews of the methods of change detection and some of their applications.

5.3 CHANGE IN THE AMPLITUDE OF THE RADAR SIGNAL

Each pixel in the SAR image records the amplitude of the radar signal returned to the satellite after being scattered by the ground. The amplitude signal will change over time if any of the following change: roughness, slope or dielectric constant (which depends on water content, among other things). Some ways that amplitude change can be used for natural hazards include the following:

- Detecting natural or man-made oil slicks on water (Jones et al. 2011; Leifer et al. 2012). The amplitude is lower on a smooth oil slick than on the rougher water surrounding the slick.

- Mapping the extent of flooding from rivers, tsunamis and storm surges. The surface roughness changes due to inundation – rough land surfaces are covered with a smooth water surface – causing flooded areas to often appear darker in a post-flood amplitude image compared with a pre-flood image (Figure 5.2). The existence of waves in the flood zone can complicate the interpretation, but the use of additional radar measurements like phase change (Section 5.4) or coherence change (Section 5.5) can isolate the wind effect (Strozzi et al. 2000). Flooding also tends to be accompanied by clouds, and thus can benefit from SAR observations. However, flood mapping is one of the most time-sensitive applications in natural disaster response, because the floodwaters drain away on a timescale of hours to days – often too short a time for SAR images to be acquired. The ephemeral character of the events also makes it challenging to find ground truth surveys or independent observations for validation of the SAR flood maps.
- Mapping the extent of flooding in areas with vegetation (Alsdorf et al. 2000). The amplitude in vegetated flooded areas is higher than that in dry conditions because the radar signal undergoes a 'double bounce' off the water and the vegetation to return with a larger amplitude to the satellite.
- Radar amplitude change can detect building devastation (Brunner et al. 2010). Buildings are often good radar signal reflectors, especially when their facades are parallel to satellites' flight direction.
- Radar energy is double or triple bounced on the ground and building facades and reflected back to satellites. Significant damage to building structures can reduce the amount of such energy reflection, reducing the radar amplitude. On the other hand, however, massive debris from damaged buildings can increase the roughness of the buildings, increasing the scattered energy (Arciniegas et al. 2007). Thus, care needs to be taken when interpreting amplitude change for building damage assessment, and other measurements (like coherence change) may be necessary to robustly map the damage.
- Areas that are recently burned in a wildfire can have different radar amplitude than pre-burned areas (Figure 5.3), although whether the amplitude increases or decreases from the fire can depend on the angle of the radar beam and the characteristics of the burned area (Lu et al. 2010b). An advantage of using SAR is that it can 'see' through the smoke.

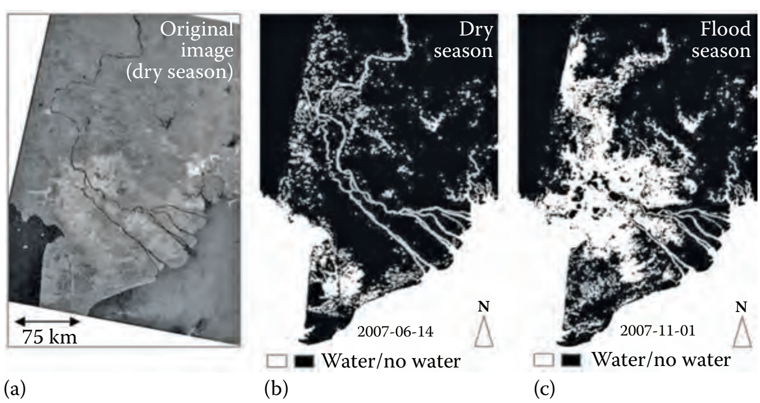

FIGURE 5.2 Mapping flood extent in the Mekong delta of south Vietnam using Envisat ScanSAR data. (a) Original radar image from 14 June 2007. (b) Interpretation of left image in terms of water and dry land. (c) Interpretation of radar image from 1 November 2007 at the end of the rainy season. (From Kuenzer, C. et al., *Remote Sens.*, *5*(2), 687–715, 2013.)

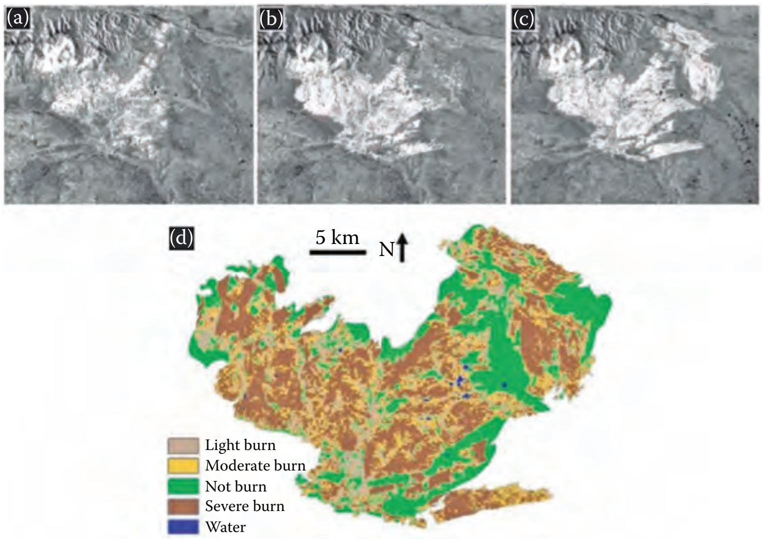

FIGURE 5.3 Radar amplitude images taken during a fire in the Yukon River Basin, Alaska, on sequential dates: (a) 17 August 2003, (b) 10 September 2003 and (c) 4 October 2003. (d) Once the fire was over, the amplitude and coherence change was used to determine a fire severity map. (All from Lu, Z. et al., *Int. J. Image Data Fusion*, 1(3), 217–242, 2010.)

- Fresh volcanic deposits – Lava, ash and mudflows (lahars) – can cause a change in amplitude. In some cases, the deposit absorbs more radar energy than before the deposition occurs (the amplitude decreases as for fine-grained lahars at Mt. Pinatubo, Philippines) (Chorowicz et al. 1997) or the deposit could scatter more radar energy than before – becoming radar bright like most lava flows (Wadge et al. 2012).

5.4 CHANGE IN THE DISTANCE FROM SATELLITE TO GROUND: INTERFEROMETRY

In addition to the amplitude of the returned radar signal, each pixel in a radar image records the returned phase of the radar signal with a value in radians between 0 and 2π. The phase values in an individual SAR image appear as white noise, because the pixel-to-pixel values of phase vary significantly depending on the scattering elements in a pixel. But when the phase difference between two images is calculated, systematic trends in the phase change are visible, creating an interferogram (Figure 5.4). This technique is generically called interferometric synthetic aperture radar (InSAR), and its power lies in the ability to measure phase changes of a fraction of a radar wavelength – a few millimetres to centimetres of distance change between the satellite and the ground (including a combination of both vertical and horizontal motion). While a single interferogram can provide precise observations of surface displacements on a pixel-by-pixel basis that can be valuable for natural hazards studies (e.g. providing information on ground motion during an earthquake), additional value is obtained by combining several interferograms spanning different time intervals together to calculate how deformation is changing with time. There are numerous reviews of the applications and limits of InSAR (Massonnet and Feigl 1998; Bürgmann et al. 2000; Rosen et al. 2000; Simons and Rosen 2015), including time-series methods (Ferretti et al. 2001; Berardino et al. 2002; Hooper et al. 2012), so we provide only a few illustrative examples, focusing on hazards:

- InSAR can measure slow deformation near faults, indicating that strain is building up that will probably be released in a future earthquake (Figure 5.5). Although the time of a future earthquake cannot be determined, the rate of deformation and how quickly the deformation decays with distance from the fault indicate how fast the fault is accumulating strain and how much of the fault might move – useful information for forecasting the earthquake magnitude (Fialko 2006).
- When an earthquake occurs, the pattern of ground deformation reveals which portions of a fault slipped (Figure 5.6). The detailed estimates of the location of a fault slip from InSAR are useful for several reasons, especially in the first few hours after the earthquake – the earthquake fault may not have been previously recognized (Talebian et al. 2004), seismic catalogues may place the earthquake in the wrong location (Lohman and Simons 2005), or depending on the details of the fault slip, the earthquake may make additional earthquakes on nearby faults more or less likely in the near term (Stramondo et al. 2011).
- Volcano uplift can indicate that magma is accumulating and an eruption may be possible within months to years (Chaussard and Amelung 2012; Lundgren et al. 2013). Not all volcanoes deform before eruption, and some volcanoes deform without eruption, but the vast majority of volcanoes that are not deforming are also not erupting (Biggs et al. 2014). Surface deformation before, during and after volcanic eruption has been observed with

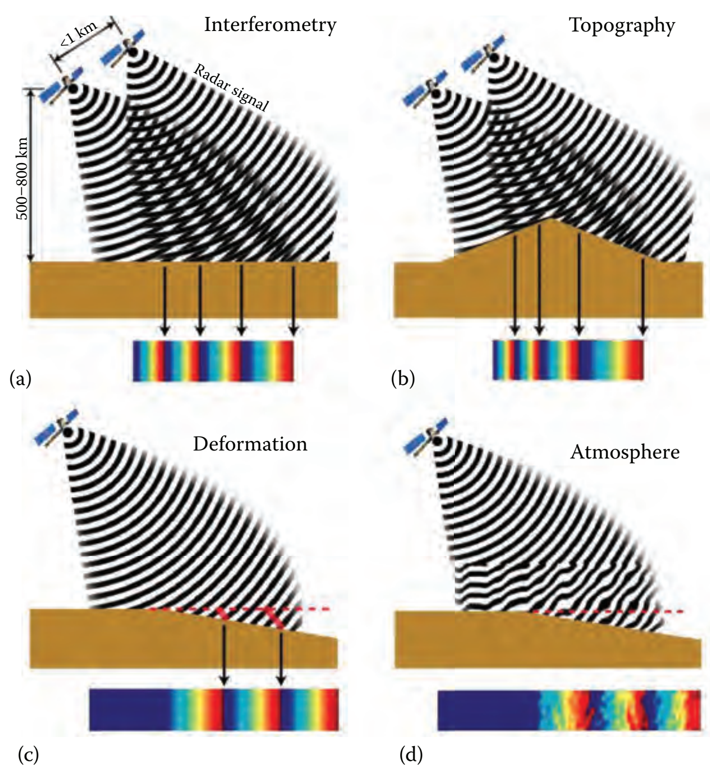

FIGURE 5.4 SAR interferometry. (a) Interference of two radar echoes from two sensors (or one sensor at different times) produces colour fringes. (b) Topography distorts the fringe pattern. (c) Ground deformation between two SAR acquisitions produces colour fringes. (d) Atmosphere (ionosphere and troposphere) distorts radio wavefronts. Satellites are flying into this page. (From Yun, S. H., A mechanical model of the large-deformation 2005 Sierra Negra volcanic eruption derived from InSAR measurements, PhD thesis, Stanford University, 147 pp, 2007.)

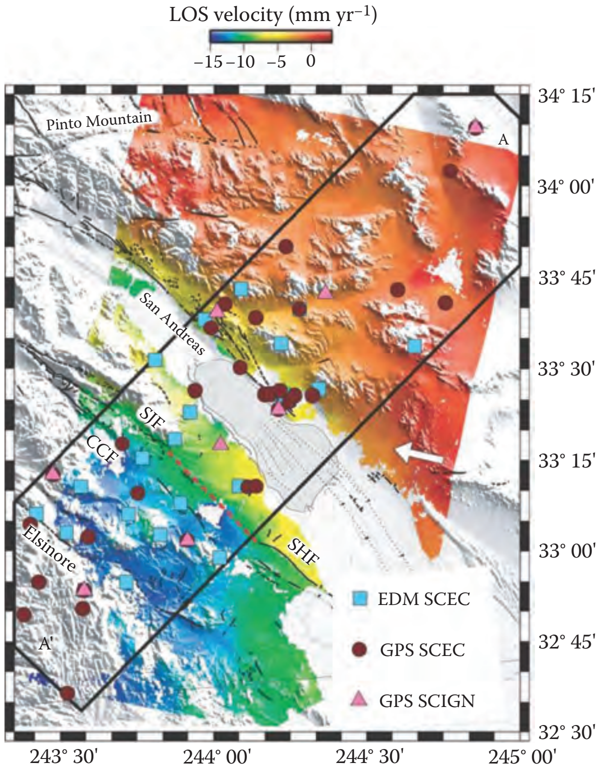

FIGURE 5.5 Ground velocity in the direction of the satellite line of sight (LOS) between the years 1992 and 2000 along the southern San Andreas Fault showing the interseismic strain accumulation that will be released in an earthquake in the future. The location of ground-based global positioning system (GPS) and electronic distance measurements (EDMs) from the Southern California Earthquake Center (SCEC) and Southern California Integrated Geodetic Network (SCIGN) are also shown. Fault locations are shown as solid and dashed black lines are labelled. SJF, San Jacinto Fault; CCF, Coyote Creek Fault; SHF, Superstition Hills Fault. (From Fialko, Y., *Nature*, 441(7096), 968–971, 2006.)

InSAR measurements (Figure 5.7). Once a volcanic eruption begins, InSAR deformation observations could indicate where the magma is coming from, if the magma chamber is refilling and possibly the length of the eruption (Lundgren et al. 2013).

- Sinkholes are formed either naturally in karst regions where carbonate rock is dissolved into groundwater or due to human activities, such as mining. Many sinkholes occur rapidly over a small region, so it is difficult to capture precursory deformation using remote sensing techniques. In some cases, however, there may be slow deformation before sinkholes collapse catastrophically, indicating where a future collapse is possible (Castañeda et al. 2009; Paine et al. 2012; Jones and Blom 2014).
- Slow-moving landslides or mass movements pose numerous hazards and can be mapped using advanced InSAR techniques called persistent scatterers (also known as PSInSAR) (Hilley et al. 2004; Colesanti and Wasowski 2006; Delacourt et al. 2007) or small baseline subset (Calò et al. 2014), as in Figure 5.8. To date, satellite observations have been too infrequent to detect precursors before large catastrophic landslides.
- When levees (or other water defence structures) subside, there is a high risk of catastrophic flooding. Such subsidence was observed by PSInSAR before the Hurricane Katrina floods in New Orleans (Dixon et al. 2006). InSAR also detected the motion of embankments

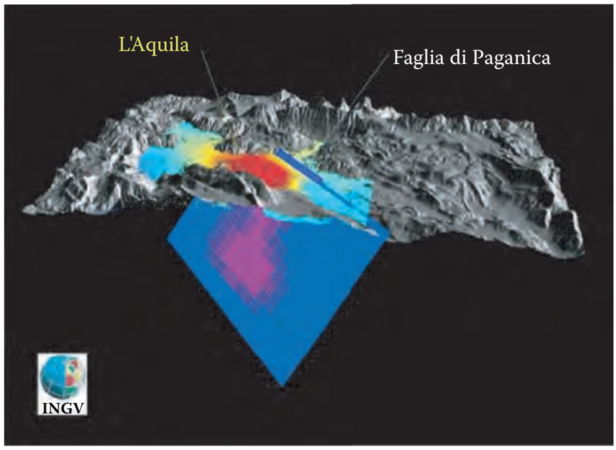

FIGURE 5.6 Ground displacement from the 6 April 2009 L'Aquila, Italy, earthquake (magnitude 6.3) observed by InSAR from the COSMOSkyMed satellite shown in colour on the Earth's surface, with red showing the maximum subsidence of 25 cm. Below the surface in blue is the fault plane inferred to have caused the earthquake (bottom of the fault is 12 km), with purple colours showing the amount of fault slip (maximum 90 cm at 4 km depth) determined by inversion of the surface displacements. The fault that caused the earthquake (Faglia di Paganica) is shown as a blue line at the Earth's surface and is about 20 km long, and the city of L'Aquila is also labelled. (From Salvi, S. et al., Measurement and modeling of co-seismic deformation during the L'Aquila Earthquake, preliminary results, Istituto Nazionale di Geofisica e Vulcanoligia, Rome, 2009, http://portale.ingv.it/primo-piano-1/news-archive/2009-news/april-6-earthquake/sar-prelimina ry-results/view?set_language=en.)

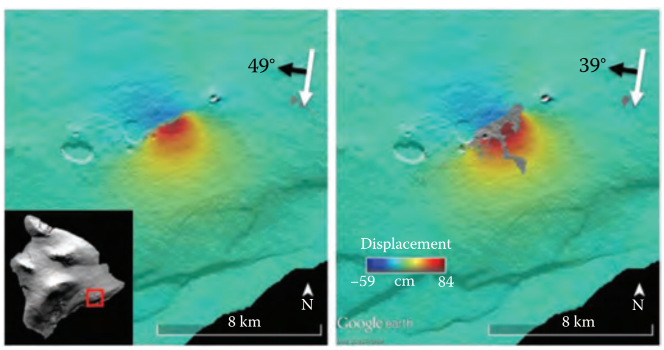

(a) 2011.01.19–2011.03.06 (b) 2011.01.24–2011.03.11

FIGURE 5.7 Ground deformation maps of the eastern part of Kilauea Volcano, Hawaii, observed by the PALSAR sensor mounted on the ALOS satellite. The varying colour represents the amount of ground surface displacement in the radar line of sight. The deformation was caused by magma intrusion, followed by fissure eruption on 5–9 March 2011. The white and black arrows indicate the satellite heading and look directions, respectively, and the approximate incidence angle, from vertical, in the centre of the image. Panel (a) includes only the first day of eruption, and panel (b) spans the entire eruption period, where part of the deformation signal was obscured due to the lava flow and localized large deformation. (Adapted from Lundgren, P. et al., *J. Geophys. Res. Solid Earth*, 118(1018), 897–914, 2013.)

before they failed catastrophically in Hungary, creating the worst environmental disaster in that country's history (Grenerczy and Wegmüller 2011).

- Subsidence along coastlines, often combined with sea level rise, is of special interest because it leads to increased flooding. InSAR has been used to detect and map coastal subsidence in several areas (Finnegan et al. 2008; Wang et al. 2012).

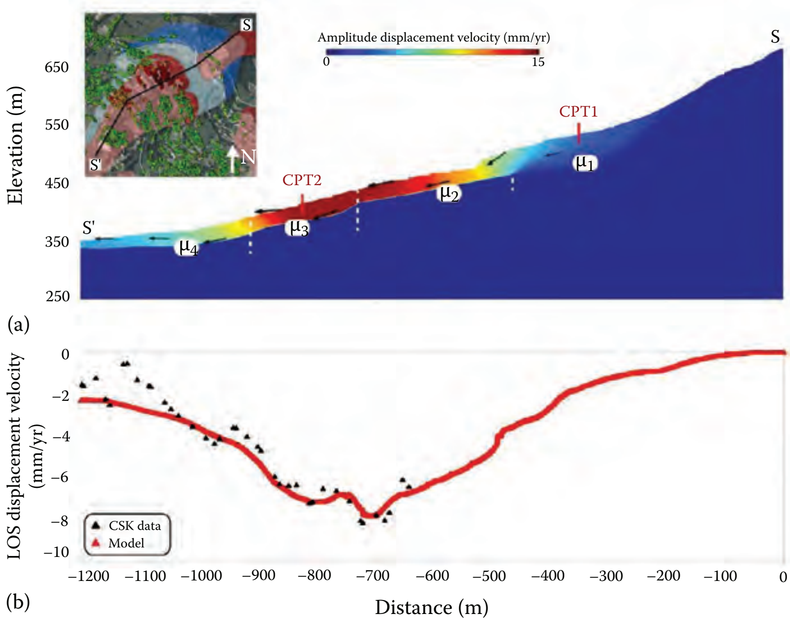

FIGURE 5.8 (a) Two-dimensional displacement field obtained from numerical modelling along the longitudinal cross section S-S′ of the Ivancich landslide in Assisi, Italy. μ1, μ2, μ3 and μ4 are the dynamic viscosities for the four shear band sectors. CPT1 and CPT2 indicate direction changes of the profile trace. The inset shows the modelled longitudinal cross section S-S′, superimposed on the full-resolution, ground deformation velocity map obtained processing COSMO-SkyMed data. (b) Comparison between the modelled velocity profile (red triangles) and the COSMO-SkyMed measurements (black triangles) along the longitudinal cross section of the landslide. (From Calò, F. et al., *Remote Sens. Environ.*, 142(0), 69–82, 2014.)

- Changes to permafrost causes coastal erosion, mass movements in mountainous areas (Kääb et al. 2005) and damage to human infrastructure. InSAR is capable of measuring long-term changes in the permafrost active layer thickness and its spatial variations – essential measurements for the state of health of the permafrost (Liu et al. 2012).
- The breakup of ice in rivers or along coastlines poses several hazards, and deformation that precedes the breakup can be detected by InSAR (Smith 2002; Vincent et al. 2004). River ice breakup can be hazardous for navigation (Vincent et al. 2004) and cause flooding (Smith 2002). Coastal ice also presents problems for navigation (both travelling over the ice and ships avoiding the ice) and increased storm damage when it is absent (Eicken et al. 2011).
- Glacier motions and/or melting can cause hazards to populations living near glaciers, as well as contribute to global sea level rise (Kääb et al. 2005). Glacier advance can threaten infrastructure, while glacier-controlled dams (usually below the surface) can fail catastrophically, causing glacial lake outburst floods (GLOFs). Glacier motions can be tracked with InSAR when satellites make repeat overflights within a few days or weeks (Goldstein et al. 1993; Joughin 2002). Subglacial lakes have been detected and monitored by InSAR (Capps et al. 2010), but observations are unlikely to be frequent enough to provide immediate warning for GLOFs.
- During flooding, in addition to mapping changes in radar amplitude that can be a proxy for flood extent (see Section 5.3 on amplitude change), the phase change measurement is related to changes in height–important for assessing flood stage (Alsdorf et al. 2000; Smith 2002). However, the height measurement is not absolute–only the change in height between measurements is possible, unless additional ground or space observations are

available (Alsdorf et al. 2001). Phase change measurements are only possible in flooded areas with vegetation where the radar signal undergoes a double bounce that also increases the radar amplitude in these areas. But as few as one or two emergent tree trunks within a radar pixel might be sufficient for the double-bounce effect (Alsdorf et al. 2001).

Various types of human activities can cause surface deformation (sometimes including catastrophic collapse) that can have an impact on infrastructure. While this deformation could be considered human-made instead of a natural disaster, it is not always simple to draw the line between the two – for example, are changes in permafrost due to anthropogenic global warming (human-made) or natural hazards? Examples of anthropogenic deformation that has been detected by InSAR and PSInSAR include mining (Lu and Wicks 2010; Ismaya and Donovon 2012), oil and gas production (Fielding et al. 1998), groundwater pumping (Amelung et al. 1999), geothermal production (Carnec and Fabriol 1999) and carbon sequestration (Vasco et al. 2010).

5.5 ALONG-TRACK DISPLACEMENT AND SUBPIXEL MOVEMENTS

Sometimes the ground motion from an earthquake or landslide, for example, is so large that it can be detected with a simple visual inspection of images before and after the event. More sophisticated analysis can be applied to hundreds or thousands of pixels to even detect motions that are a fraction of a pixel (Brown 1992), and this has been demonstrated for both SAR and optical images (Scambos et al. 1992; Michel et al. 1999) – we will call these subpixel displacement measurements pixel tracking. Thus, depending on the pixel size, ground motion as small as 1–100 cm could be detected. While these measurements are not as precise as InSAR, they have several advantages, including that they are often successful in areas of large change where InSAR fails (e.g. on glaciers that have significant melting or snowfall), and they are more sensitive to certain horizontal motions (particularly along the track of the satellite orbit).

Pixel tracking has been used to study earthquakes (Michel et al. 1999; Simons et al. 2002), volcanic eruptions (e.g. Yun et al. 2007), landslides (Raucoules et al. 2013) and glaciers (Joughin 2002), and are a critical tool for monitoring sea ice (Kwok et al. 1990). Time series of the pixel tracking (or pixel offsets) can be made to monitor temporal change of large ground deformation (Casu et al. 2011). Pixel tracking produces both across-track and along-track displacement measurements. This means that from a pair of SAR data, one can generate a two-dimensional ground displacement map – radar line of sight and along-track direction.

Another way of measuring along-track displacement is called multiple aperture interferometry (MAI) or along-track beam splitting. This analysis creates two intreferograms – one forward looking and the other backward looking. Differencing the two interferograms produces the along-track displacements (Bechor and Zebker 2006; Jung et al. 2009). The quality of MAI results depends on the quality of the regular InSAR – MAI produced poor results where InSAR quality is poor. The technique is not as sensitive as InSAR, but because of the differencing, the noise from the atmosphere is lessened with MAI. However, in the presence of ionospheric noise, MAI can be severely affected. This means that MAI can be used to correct for ionospheric noise in InSAR observations (Jung et al. 2013; Liu et al. 2013). Modern SAR missions tend to have higher resolution than their predecessors, and both pixel tracking and MAI benefit from high-resolution SAR.

5.6 CHANGES IN TOPOGRAPHY: DIGITAL ELEVATION MODELS

When comparing phase change in two radar images, if the satellites are not in the exact same location, part of the phase change is caused by topography on the ground (aka the parallax effect). This phase change from topography is usually removed with topographic maps (called digital elevation models [DEMs]). In fact, the InSAR sensitivity to topography can be used to create DEMs, particularly if the data acquisitions are taken close in time so that there is little chance for the ground to deform or for the atmosphere to change between satellite overflights. The best InSAR DEMs are created when two antennas are used to measure topography at the exact same time, as was done by the U.S. space shuttle in 2000 (the Shuttle Radar Topography Mission [SRTM]) (Farr et al. 2007) or between 2010 and 2014 by the German TanDEM-X twin satellites (Moreira et al. 2004). Useful DEMs can also be created when the overflights are separated by short time periods, especially when several images can be combined to reduce errors caused by changes in the atmosphere (Rufino et al. 1998; Lu et al. 2010a,b). For example, during the tandem phase of the European ERS-1 and ERS-2 satellites in 1995–1996, when there was 1 day between overflights. Improved DEMs can also be created in PSInSAR and other methods that use multiple interferograms (Lu et al. 2010b) and can be combined with DEMs made from LIDAR and stereo-optical images.

Several types of natural hazards require high-quality topographic maps (landslides, floods and wildfires), and InSAR is one method for mapping the change in topography related to the natural disaster. InSAR-created DEMs have been used to measure erosion from flooding (Smith 2002), emplacement of lava flows (Lu et al. 2010a,b), mining (Bhattacharya et al. 2012), landslides and glaciers (Kääb et al. 2005). In addition, DEMs are needed to correct for geometric distortions and convert imagery (optical, radar or other) to geographic coordinates. In other words, if a disaster causes a significant change in topography, a new DEM is necessary to properly interpret imagery.

5.7 COHERENCE CHANGE

We can quantify how similar the amplitudes and phases are between pairs of SAR images by calculating the coherence (Zebker and Villasenor 1992). Coherence has a value between zero (no coherence) and 1 (identical signal in the two images). Bare rock with no vegetation will maintain high coherence, while an area that just had a large landslide or was covered by a fresh lava flow will have low coherence. Coherence decrease, or decorrelation, was observed, for example, along the pathway of lava flows on the flank of the Kilauea volcano (Zebker et al. 1996) and along the surface rupture of an earthquake, where the ground was most severely disturbed (Simons et al. 2002). Other examples of the utility of coherence change are listed below:

- Large earthquakes often cause building damage, which is a major component of economic loss. Thus, a map of building damage can be very useful for early assessment of loss and fatality. The potential of interferometric coherence change has been tested with the 1995 Kobe earthquake in Japan (Yonezawa and Takeuchi 2001) and the 2003 Bam earthquake in Iran (Talebian et al. 2004; Fielding et al. 2005; Hoffmann 2007) by comparing two pairs of SAR images – the pair including the earthquake and the pair before the earthquake. This approach requires that the imaging conditions of the two pairs, specifically the separation of the satellites in space and time, be similar to each other. This requirement is later mitigated by equalizing the coherence statistics of the two pairs (Yun et al. 2011a). In principle, buildings damaged by windstorms (hurricanes or tornadoes) or other disasters could be measured by coherence change as well. While there are other ways to assess building damage (using satellite optical images), they usually underestimate the damage (Lemoine et al. 2013), and so additional methods, like coherence-based damage mapping, may improve damage assessment.
- Volcanic eruptions can cause ground surface change with lava flows and ash deposits. The resurfacing with fresh lava completely changes the radar scattering properties of the surface and often appears as a distinct low-coherence band along the path of lava flow (Zebker et al. 1996; Dietterich et al. 2012). Ash fall damage can spread and affect wider areas than lava. Depending on the depth of the ash deposit, the sensitivity of the radar signal to detect such change varies with radar wavelength (Yun et al. 2011b). Even without eruption, volcanoes can produce mudflows (lahars) that are deadly and damaging to infrastructure (Kerle and Oppenheimer 2002). Because these flows cause a loss of radar coherence, they can

be mapped rapidly after the event to assess their impact. In some cases, the flows can be detected by amplitude change (like after the 1991 Mt. Pinatubo, Philippines, eruption), but not always, so coherence change might be the best way to detect them. However, if images are not acquired frequently, coherence can be lost in vegetated areas, making it impossible to map the lahar (Kerle and Oppenheimer 2002).

- Unlike slow-moving landslides, the ground deformation due to catastrophic landslides cannot be imaged with InSAR observations due to the complete loss of coherence. Because of this disturbance, however, such events can be detected in a coherence change map. However, it is often challenging to produce such a map of mountain terrain because of (1) steep slopes, which cause the landslides, which also cause distortions and shadows in SAR images, and (2) dense vegetation that causes decorrelation even when there are no landslides.
- Earthquakes sometimes induce liquefaction, a phenomenon where sediments lose stiffness and behave like a liquid due to applied sudden stress change (Green et al. 2011; Cox et al. 2013). During earthquakes, liquefied soil, or silt, often oozes out of the ground, replacing the dry land with a wet silty surface. Such change in the surface material, along with the moisture content, was mapped with coherence change (Yun et al. 2011a), as in Figure 5.9.
- Both natural and man-made levees can be breached suddenly by weather events, earthquakes or human activities, or gradually by subsurface weakening processes due to hydraulic pressure. The breakage of levees can lead to substantial inundation of land, and sometimes also poses a significant threat to water resources for drinking and irrigation, if the flooding in river deltas reverses the water flow and shifts the saltwater boundary inland (Shwartz 2006). Levees usually maintain high coherence along their crowns (Hanssen and van Leijen 2008), so if coherence is lost, it could indicate damage to the structure.

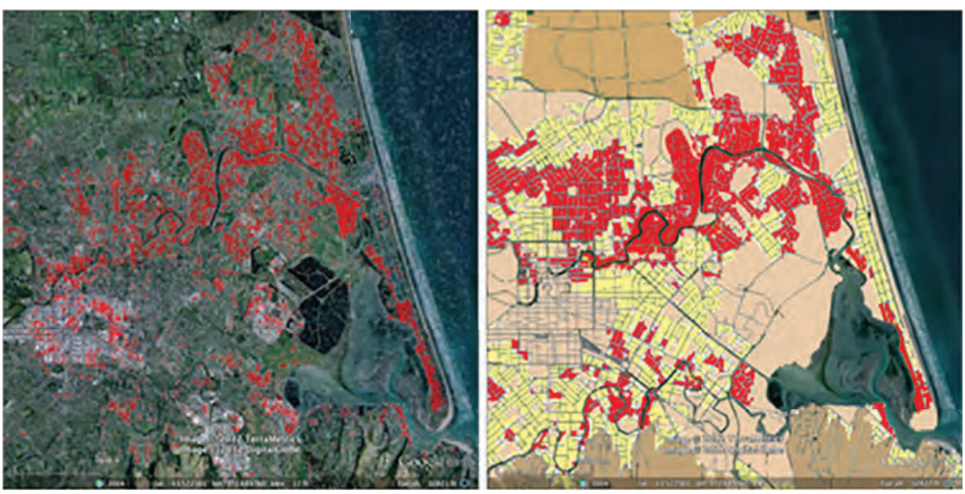

(a) (b)

FIGURE 5.9 (a) Damage proxy map of Christchurch area, New Zealand, derived from ALOS PALSAR data acquired on 10 October 2010, 10 January 2011 and 25 February 2011. The red pixels represent change due to the February 2011 Christchurch earthquake. (b) Damage zone map released by the New Zealand government, where red polygons indicate significant damage on buildings or land. This ground truth map was produced 8 months after the earthquake, whereas the damage proxy map (a) was produced from remotely sensed radar data acquired 3 days after the earthquake. (From Yun, S. et al., Damage proxy map of M6.3 Christchurch Earthquake using InSAR coherence [abstract], presented at Fringe 2011 Workshop: Advances in the Science and Applications of SAR Interferometry from ESA and 3rd Party Missions, Frascati, Italy, 19–23 September, 2011, 2011a.)

However, the width of levees is often small, so high-resolution SAR imagery is usually required to monitor changes in levees (Jones et al. 2012).

- In addition to the changes in radar amplitude mentioned in Section 5.1, wildfires cause changes in coherence because of changes in water content, the number and type of vegetation and other factors (Lu et al. 2010b). By combining the radar amplitude and coherence changes, the severity of the fire burn can be assessed (Figure 5.3).

5.8 PRACTICAL CONSIDERATIONS: WHAT DATA TYPE WILL BE OF MOST UTILITY?

When considering whether an imaging radar will be useful for a specific study, several characteristics of the radar need to be considered:

- The wavelength of the radar – Existing systems (Table 5.2) have wavelengths that span 3–24 cm (corresponding to frequencies of 1–10 GHz), but most satellite systems fall into three categories: X-band (about 3 cm), C-band (about 5.6 cm) and L-band (about 23.5 cm). Each band has different advantages, in part related to the fact that the radar energy is scattered off the ground and back to the satellite by scatterers that are about the same size as the radar wavelength. Thus, short-wavelength X-band radar signals interact with the leaves at the tops of trees, while the longer L-band radar signals scatter off the larger parts of the trees – the trunks and branches. Because the leaves are more likely to change their orientation between SAR acquisitions than the branches, the coherence of the radar signal is higher in vegetated areas at L-band than X-band over the same time interval. Thus, to maintain coherence between observations, observations at short radar wavelengths must be more frequent than those at longer radar wavelengths. On the other hand, shorter radar wavelengths are less affected than longer radar wavelengths by distortions caused by changes in the ionosphere that occur in polar areas or near the magnetic equator. While longer-wavelength radars should be less sensitive to ground deformation than short-wavelength radars (i.e. L-band should be less sensitive than C-band), this effect is smaller than expected and may be overcome by the higher coherence of longer-wavelength systems (Sandwell et al. 2008).
- Spatial resolution of the radar image – This property can vary between about 1 and 100 m even for a given satellite (Table 5.1), depending on the type of observation mode for the radar. One of the lowest-resolution modes is called ScanSAR, and it can be often combined with the intermediate-mode Stripmap data. The highest-resolution mode is typically called Spotlight, and it cannot be combined with the other modes. The Spotlight, Stripmap and ScanSAR modes are often subdivided even further into high- and low-resolution modes. For all modes, the resolution trades off with swath width – the lower spatial resolution corresponds to wider coverage, and only a small area can be imaged using the highest spatial resolution. For some applications, the highest-resolution modes are necessary for change detection – for example, individual buildings, small landslides or domes inside volcano craters – while the lower-resolution modes are better to see large areas affected by great earthquakes or floods. The general trend in recent years has been that newer systems have higher resolution – for example, a new mode on TerraSAR-X called Staring Spotlight has a spatial resolution of 0.25 m.
- Polarization. Most radar signals used for satellite remote sensing are linearly polarized – either horizontally or vertically. When these signals encounter objects on the ground, electric currents are induced in the objects. Depending on the dominant orientation of the object, the scattered radio wave back to the satellite may contain vertically polarized energy even when the original transmitted signal was purely horizontal. The polarization in a radar image can affect the coherence, particularly in vegetated areas (Alsdorf et al. 2000).

As polarization changes the amplitude and phase, only images with the same polarization should be compared for change detection.

- Repeat time between measurements. For the specific techniques and applications described here, a strong constraint is that the radar images should be taken from the same location in space by the same radar system. Thus, observations can only be made as frequently as the satellite repeats the same flight path over a given area (called the repeat time) – usually several weeks to more than a month (Table 5.2). It is increasingly common for constellations of satellites with the same radar system (like COSMO-SkyMed or Sentinel) to follow each other in orbit so that repeat observations can be made within a few days to about a week. But even without constellations, observations are more frequent than the repeat time would suggest for several reasons:
  - A given spot is imaged by the satellite as it travels in its orbit from north to south (called descending orbits) and south to north (ascending orbits).

TABLE 5.2

List of Civilian SAR Satellites

Mission	Agency	Life	Repeat Cycle (days)	Band	Wavelength (cm)	Resolution (m)
ERS1	ESA	July 1991–March 2000	3, 168, 35	C	5.66	20
JERS1	JAXA	March 1992–October 1998	44	L	23.5	20
ERS2	ESA	April 1995–September 2011	35	C	5.66	20
Radarsat1	CSA	November 1995–March 2013	24	C	5.66	10–100
Envisat	ESA	March 2002–April 2012	35, 30	C	5.63	20–100
ALOS1	JAXA	January 2006–April 2011	46	L	23.6	10–100
TerraSARX (TSX), TanDEMX	DLR	June 2007–present, June 2010–present	11	X	3.1	1–16
Radarsat2	CSA	December 2007–present	24	C	5.4	3–100
COSMOSkyMed	ASI	June 2007– present, December 2007–present, October 2008–present, November 2010–present	1, 3, 4, 8	X	3.1	1–100
KOMPSAT5	KARI	August 2013–present	28	X	3.2	1–20
PAZ	INTA/His deSAT	2017 (planned)	11 (5.5 days in constellation with TSX)	X	3.1	1–16
Sentinel 1a, 1b	ESA	April 2014–present, April 2016–present	12, 6	C	5.66	5–40
ALOS2	JAXA	May 2014–present	14 (selected tracks)	L	23.6	1–100
SAOCOM 1a, 1b	CONAE	2017, 2018 (planned)	16, 8	L	23.5	7–100
NISAR	ISRO/ NASA	2021 (planned)	12	L, S	23.8, 9.3	3–12

Note: ASI, Agenzia Spaziale Italiana (Italy); CONAE, Comisión Nacional de Actividades Espaciales (Argentina); CSA, Canadian Space Agency; DLR, Deutsches Zentrum für Luft- und Raumfahrt e.V. (Germany); ESA, European Space Agency; INTA, Instituto Nacional de Técnica Aeroespacial (Spain); ISRO, Indian Space Research Organization; JAXA, Japanese Aerospace Exploration Agency; KARI, Korea Aerospace Research Institute (South Korea).

- The orbital tracks start to converge near the poles so the tracks increasingly overlap at higher latitudes – thus, the frequency of imaging a certain patch of ground is latitude dependent.
- On many satellites, the radar antenna is steerable so that it can be focused on an area of interest – particularly over isolated ocean islands like Hawaii at the expense of imaging the open ocean.
- On many satellites, the swath width of the imaging radar overlaps with other swaths.

Through the combination of multiple satellite tracks (ascending and descending orbits, partly overlapping orbits and steerable beams), more dense time series of observations can be created, albeit with some added complexity of interpretation.

5.8.1 Data Availability

By 2018, there should be at least 14 functioning civilian radar satellites, from eight different space programmes, with data prices ranging from no cost to thousands of U.S. dollars per image. Each satellite has different mission objectives, ranging from a focus on specific geographic regions, to targeted commercial applications, to global monitoring. Thus, the amount of data available for a given area on the Earth varies a lot – in some areas, data are collected during every overpass, while in others, data may never have been acquired by certain satellites. But the good news is that with so many satellite systems, after a large disaster it should be possible to acquire an image by at least one of the satellites within 24 hours to assist with emergency response. After a disaster, the International Charter can be invoked to facilitate satellite data collection and access (www.disasterscharter.org). Furthermore, the Global Earth Observation System of Systems (GEOSS) seeks to coordinate and improve international satellite observations to prepare and respond to disasters (Lautenbacher 2006). This coordination of efforts is critical considering that all satellites have limited duty cycles and cannot collect data over all global areas that have natural hazards.

5.8.2 Data Latency

Latency is one of the most critical parameters for disaster response, as the utility of images after the event diminishes with time. Data acquisition latency is the time interval between the disaster event and data acquisition by a radar sensor. This latency is completely controlled by satellite orbits and space agencies' data acquisition plan. Data discovery latency is the time interval between data acquisition and a data user's awareness of the existence of such data. This may be affected by the space agencies' cataloguing efficiency. Data access latency is defined as the time interval between such awareness and the moment of gaining access to the data. This may involve obtaining credentials for such access and file transfer speed. Data processing latency is the time interval between data access and the production of a high-level decision support product for response. This latency depends on the processing algorithm and automation level of the data system.

In response to superstorm Sandy, for example, a damage proxy map of New York City was produced by the Advanced Rapid Imaging and Analysis (ARIA) team at the Jet Propulsion Laboratory and California Institute of Technology. The COSMO-SkyMed constellation imaged the affected area in Stripmap mode 5 days after the landfall of Sandy on the East Coast of the United States. It took 3 days for the information about the data to appear in the online catalogue. The ARIA team contacted the Italian Space Agency and gained access to the data a day later.

The processing took 2 days until the product was delivered to responding agencies. Thus, data acquisition, discovery, access and processing latencies added up to 11 days, with every step implemented manually. This demonstrates the importance of coordinated effort to establish an end-to-end system that automatically handles all intermediate processes. Especially important are background observations in critical areas by all satellites, so that a pre-event image is available after a disaster.

Once the radar data are acquired, they must be processed and useful data products created. While there is an impression that radar data are difficult to interpret and process (Voigt et al. 2007), there are now several commonly used open-source and commercial software packages to process the data (ISCE, GMTSAR, ROI_PAC, Gamma, NEST, DORIS, SARScape and DIAPASON) and commercial companies that are generating data products. As the number of SAR satellites increases, the resources available to aid in interpretation of the data will continue to grow.

5.9 CONCLUSION

We have highlighted the variety of uses of imaging radar, from anticipating earthquakes, ice breakup and volcanic eruptions, to mapping the extent of floods in progress, to assessing building damage from earthquakes and windstorms (summarized in Table 5.1). While interpreting radar images can be non-unique – for example, damaged buildings or lahars can both increase and decrease radar signal amplitudes – because radar images can be analyzed in several ways, including phase and coherence change, some of the non-uniqueness can be removed at the expense of additional time and analysis. Thus, there is a critical need to find effective, efficient algorithms that take full advantage of the myriad types of imaging radar observables to maximize the full potential of the international constellation of more than a dozen radar satellites to reduce the impact of natural hazards. Yet, even with the large international constellation of satellites, they are still limited in the amount of data that can be collected – SAR data files are large and downlink capabilities are insufficient to download data over all land areas where natural hazards exist. International coordination and additional satellite missions are necessary to routinely monitor all areas of potential natural disasters.

ACKNOWLEDGEMENTS

We thank Paul Lundgren for providing the data used in Figure 5.6. M. P. was partly supported by the NASA Science Mission Directorate (Grant Number NNX12AO13G). S.-H.Y. was partly supported by the NASA Applied Sciences Program (Grant Number NNN13D788T).

REFERENCES

Alsdorf, D., Birkett, C., Dunne, T., Melack, J., and Hess, L. (2001). Water level changes in a large Amazon lake measured with spaceborne radar interferometry and altimetry. *Geophysical Research Letters*, *28*(14), 2671–2674.

Alsdorf, D. E., Melack, J. M., Dunne, T., Mertes, L. A., Hess, L. L., and Smith, L. C. (2000). Interferometric radar measurements of water level changes on the Amazon flood plain. *Nature*, *404*(6774), 174–177.

Amelung, F., Galloway, D. L., Bell, J. W., Zebker, H. A., and Laczniak, R. J. (1999). Sensing the ups and downs of Las Vegas: InSAR reveals structural control of land subsidence and aquifer-system deformation. *Geology*, *27*(6), 483–486.

Arciniegas, G. A., Bijker, W., Kerle, N., and Tolpekin, V. A. (2007). Coherence- and amplitude-based analysis of seismogenic damage in Bam, Iran, using Envisat ASAR data. *IEEE Transactions on Geoscience and Remote Sensing*, *45*(6), 1571–1581.

Bechor, N., and Zebker, H. (2006). Measuring two-dimensional movements using a single InSAR pair. *Geophysical Research Letters*, *33*, L16311. doi: 10.1029/2006GL026883.

Berardino, P., Fornaro, G., Lanari, R., and Sansosti, E. (2002). A new algorithm for surface deformation monitoring based on small baseline differential SAR interferograms. *IEEE Transactions on Geoscience and Remote Sensing*, *40*(11), 2375–2383.

Bhattacharya, A., Arora, M. K., and Sharma, M. L. (2012). Usefulness of synthetic aperture radar (SAR) interferometry for digital elevation model (DEM) generation and estimation of land surface displacement in Jharia coal field area. *Geocarto International*, *27*(1), 57–77.

Biggs, J., Ebmeier, S. K., Aspinall, W. P., Lu, Z., Pritchard, M. E., Sparks, R. S. J., and Mather, T. A. (2014). Global link between deformation and volcanic eruption quantified by satellite imagery. *Nature Communications*, *5*, 3471. doi: 10.1038/ncomms4471.

Brown, L. G. (1992). A survey of image registration techniques. *ACM Computing Surveys*, *24*(4), 325–376.

Brunner, D., Lemoine, G., and Bruzzone, L. (2010). Earthquake damage assessment of buildings using VHR optical and SAR imagery. *IEEE Transactions on Geoscience and Remote Sensing*, *48*(5), 2403–2420.

Bürgmann, R., Rosen, P. A., and Fielding, E. J. (2000). Synthetic aperture radar interferometry to measure Earth's surface topography and its deformation. *Annual Review of Earth and Planetary Sciences*, *28*(1), 169–209.

Calò, F., Ardizzone, F., Castaldo, R., Lollino, P., Tizzani, P., Guzzetti, F., Lanari, R., Angeli, M.-G., Pontoni, F., and Manunta, M. (2014). Enhanced landslide investigations through advanced DInSAR techniques: The Ivancich case study, Assisi, Italy. *Remote Sensing of Environment*, *142*(0), 69–82.

Capps, D. M., Rabus, B., Clague, J. J., and Shugar, D. H. (2010). Identification and characterization of alpine subglacial lakes using interferometric synthetic aperture radar (InSAR): Brady Glacier, Alaska, USA. *Journal of Glaciology*, *56*(199), 861–870.

Carnec, C., and Fabriol, H. (1999). Monitoring and modeling land subsidence at the Cerro Prieto geothermal field, Baja California, Mexico, using SAR interferometry. *Geophysical Research Letters*, *26*(9), 1211–1214.

Castañeda, C., Gutiérrez, F., Manunta, M., and Galve, J. P. (2009). DInSAR measurements of ground deformation by sinkholes, mining subsidence, and landslides, Ebro River, Spain. *Earth Surface Processes and Landforms*, *34*(11), 1562–1574.

Casu, F., Manconi, A., Pepe, A., and Lanari, R. (2011). Deformation time-series generation in areas characterized by large displacement dynamics: The SAR amplitude pixel-offset SBAS technique. *IEEE Transactions on Geoscience and Remote Sensing*, *49*(7), 2752–2763.

Chaussard, E., and Amelung, F. (2012). Precursory inflation of shallow magma reservoirs at west Sunda volcanoes detected by InSAR. *Geophysical Research Letters*, *39*(21), L21311. doi: 10.1029/2012GL053817.

Chorowicz, J., Lopez, E., Garcia, F., Parrot, J. F., Rudant, J. P., and Vinluan, R. (1997). Keys to analyze active lahars from Pinatubo on SAR ERS imagery. *Remote Sensing of Environment*, *62*(1), 20–29.

Colesanti, C., and Wasowski, J. (2006). Investigating landslides with space-borne synthetic aperture radar (SAR) interferometry. *Engineering Geology*, *88*(3–4), 173–199.

Cox, B. R., Boulanger, R. W., and Tokimatsu, K. (2013). Liquefaction at strong motion stations and in Urayasu city during the 2011 TohokuOki earthquake. *Earthquake Spectra*, *29*(Suppl. 1), S55–S80.

Delacourt, C., Allemand, P., Berthier, E., Raucoules, D., Casson, B., Grandjean, P., Pambrun, C., and Varel, E. (2007). Remote-sensing techniques for analysing landslide kinematics: A review. *Bulletin de la Societe Geologique de France*, *178*(2), 89–100.

Dietterich, H. R., Poland, M. P., Schmidt, D. A., Cashman, K. V., Sherrod, D. R., and Espinosa, A. T. (2012). Tracking lava flow emplacement on the east rift zone of Kīlauea, Hawai'i, with synthetic aperture radar coherence. *Geochemistry, Geophysics, Geo*systems, *13*(5), Q05001. doi: 10.1029/2011GC004016.

Dixon, T. H., Amelung, F., Ferretti, A., Novali, F., Rocca, F., Dokka, R., Sella, G., Kim, S.-W., Wdowinski, S., and Whitman, D. (2006). Space geodesy: Subsidence and flooding in New Orleans. *Nature*, *441*(7093), 587–588.

Eicken, H., Jones, J., Meyer, F., Mahoney, A., Druckenmiller, M. L., Rohith, M. V., and Kambhamettu, C. (2011). Environmental security in Arctic ice-covered seas: From strategy to tactics of hazard identification and emergency response. *Marine Technology Society Journal*, *45*(3), 37–48.

Farr, T. G., Rosen, P. A., Caro, E., Crippen, R., Duren, R., Hensley, S., Kobrick, M. et al. (2007). The Shuttle Radar Topography Mission. *Reviews of Geophysics*, *45*(2), RG2004. doi: 10.1029/2005RG000183.

Ferretti, A., Prati, C., and Rocca, F. (2001). Permanent scatterers in SAR interferometry. *IEEE Transactions on Geoscience and Remote Sensing*, *39*(1), 8–20.

Fialko, Y. (2006). Interseismic strain accumulation and the earthquake potential on the southern San Andreas Fault system. *Nature*, *441*(7096), 968–971.

Fielding, E. J., Blom, R. G., and Goldstein, R. M. (1998). Rapid subsidence over oil fields measured by SAR interferometry. *Geophysical Research Letters*, *25*(17), 3215–3218.

Fielding, E. J., Talebian, M., Rosen, P. A., Nazari, H., Jackson, J. A., Ghorashi, M., and Walker, R. (2005). Surface ruptures and building damage of the 2003 Bam, Iran, earthquake mapped by satellite synthetic aperture radar interferometric correlation. *Journal of Geophysical Research: Solid Earth*, *110*(B3), B03302. doi: 10.1029/2004JB003299.

Finnegan, N. J., Pritchard, M. E., Lohman, R. B., and Lundgren, P. R. (2008). Constraints on surface deformation in the Seattle, WA, urban corridor from satellite radar interferometry time-series analysis. *Geophysical Journal International*, *174*(1), 29–41.

Goldstein, R. M., Engelhardt, H., Kamb, B., and Frolich, R. M. (1993). Satellite radar interferometry for monitoring ice sheet motion: Application to an Antarctic ice stream. *Science*, *262*, 1525–1530.

Green, R. A., Wood, C., Cox, B., Cubrinovski, M., Wotherspoon, L., Bradley, B., Algie, T., Allen, J., Bradshaw, A., and Rix, G. (2011). Use of DCP and SASW tests to evaluate liquefaction potential: Predictions vs. observations during the recent New Zealand earthquakes. *Seismological Research Letters*, *82*(6), 927–938.

Grenerczy, G., and Wegmüller, U. (2011). Persistent scatterer interferometry analysis of the embankment failure of a red mud reservoir using ENVISAT ASAR data. *Natural Hazards*, *59*(2), 1047–1053.

Hanssen, R. F., and van Leijen, F. J. (2008). Monitoring water defense structures using radar interferometry. In *IEEE Radar Conference 2008 (RADAR '08)*, Rome, Italy, 26–30 May, 2008, pp. 1–4.

Hilley, G. E., Bürgmann, R., Ferretti, A., Novali, F., and Rocca, F. (2004). Dynamics of slow-moving landslides from permanent scatterer analysis. *Science*, *304*(5679), 1952–1955.

Hoffmann, J. (2007). Mapping damage during the Bam (Iran) earthquake using interferometric coherence. *International Journal of Remote Sensing*, *28*(6), 1199–1216.

Hooper, A., Bekaert, D., Spaans, K., and Arıkan, M. (2012). Recent advances in SAR interferometry time series analysis for measuring crustal deformation. *Tectonophysics*, *514–517*(0), 1–13.

Ismaya, F., and Donovan, J. (2012). Applications of DInSAR for measuring mine-induced subsidence and constraining ground deformation model. In *GeoCongress 2012: State of the Art and Practice in Geotechnical Engineering*, Oakland, CA, 25–29 March, 2012, pp. 3001–3010.

Jones, C. E., Bawden, G., and Deverel, S. (2012). Study of movement and seepage along levees using DINSAR and the airborne UAVSAR instrument. In *SPIE Remote Sensing*. Bellingham, WA: International Society for Optics and Photonics, edited by C. Notarnicola, S. Paloscia, and N. Pierdicca, p. 85360E.

Jones, C. E., and Blom, R. G. (2014). Bayou Corne, Louisiana, sinkhole: Precursory deformation measured by radar interferometry. *Geology*, *42*(2), 111–114.

Jones, C. E., Minchew, B., Holt, B., and Hensley, S. (2011). Studies of the Deepwater Horizon oil spill with the UAVSAR radar. In *Monitoring and Modeling the Deepwater Horizon Oil Spill: A Record-Breaking Enterprise*, ed. Liu, Y., Macfadyen, A., Ji, Z.-G., Weisberg, R. H. AGU Geophysical Monograph Series 195. Washington, DC: American Geophysical Union, pp. 33–50.

Joughin, I. (2002). Icesheet velocity mapping: A combined interferometric and speckle-tracking approach. *Annals of Glaciology*, *34*(1), 195–201.

Jung, H., Lee, D., Lu, Z., and Won, J. (2013). Ionospheric correction of SAR interferograms by multiple-aperture interferometry. *IEEE Transactions on Geoscience and Remote Sensing*, *51*(5), 3191–3199.

Jung, H., Won, J., and Kim, S. (2009). An improvement of the performance of multiple-aperture SAR interferometry (MAI). *IEEE Transactions on Geoscience and Remote Sensing*, *47*(8), 2859–2869.

Kääb, A., Huggel, C., Fischer, L., Guex, S., Paul, F., Roer, I., Salzmann, N. et al. (2005). Remote sensing of glacier- and permafrost-related hazards in high mountains: An overview. *Natural Hazards and Earth System Science*, *5*(4), 527–554.

Kerle, N., and Oppenheimer, C. (2002). Satellite remote sensing as a tool in lahar disaster management. *Disasters*, *26*(2), 140–160.

Kuenzer, C., Guo, H., Huth, J., Leinenkugel, P., Li, X., and Dech, S. (2013). Flood mapping and flood dynamics of the Mekong Delta: ENVISATASARWSM based time series analyses. *Remote Sensing*, *5*(2), 687–715.

Kwok, R., Curlander, J. C., McConnell, R., and Pang, S. S. (1990). An ice-motion tracking system at the Alaska SAR facility. *IEEE Journal of Oceanic Engineering*, *15*(1), 44–54.

Lautenbacher, C. C. (2006). The Global Earth Observation System of Systems: Science serving society. *Space Policy*, *22*(1), 8–11.

Leifer, I., Lehr, W. J., Simecek-Beatty, D., Bradley, E., Clark, R., Dennison, P., Hu, Y. et al. (2012). State of the art satellite and airborne marine oil spill remote sensing: Application to the BP Deepwater Horizon oil spill. *Remote Sensing of Environment*, *124*(0), 185–209.

Lemoine, G., Corbane, C., Louvrier, C., and Kauffmann, M. (2013). Intercomparison and validation of building damage assessments based on post-Haiti 2010 earthquake imagery using multisource reference data. *Natural Hazards and Earth System Sciences Discussions*, *1*(2), 1445–1486.

Liu, L., Schaefer, K., Zhang T., and Wahr, J. (2012). Estimating 1992–2000 average active layer thickness on the Alaskan North Slope from remotely sensed surface subsidence. *Journal of Geophysical Research: Earth Surface*, *117*, F01005. doi: 10.1029/2011JF002041.

Liu, Z., Jung, H., and Lu, Z. (2013). Joint correction of ionosphere noise and orbital error in L-band SAR interferometry on interseismic deformation in Southern California. *IEEE Transactions on Geoscience and Remote Sensing*, *52*(6), 3421–3427.

Lohman, R. B., and Simons, M. (2005). Locations of selected small earthquakes in the Zagros Mountains. *Geochemistry, Geophysics, Geosystems*, *6*, Q03001. doi: 10.1029/2004GC000849.

Lu, Z., Dzurisin, D., Jung, H.-S., Zhang, J., and Zhang, Y. (2010a). Radar image and data fusion for natural hazards characterisation. *International Journal of Image and Data Fusion*, *1*(3), 217–242.

Lu, Z., and Wicks Jr., C. (2010). Characterizing 6 August 2007 Crandall Canyon mine collapse from ALOS PALSAR InSAR. *Geomatics, Natural Hazards and Risk*, *1*(1), 85–93.

Lu, Z., Zhang, J., Zhang, Y., and Dzurisin, D. (2010b). Monitoring and characterizing natural hazards with satellite InSAR imagery. *Annals of GIS*, *16*(1), 55–66.

Lundgren, P., Poland, M., Miklius, A., Orr, T., Yun, S., Fielding, E., Liu, Z., Tanaka, A., Szeliga, W., Hensley, S., and Owen, S. (2013). Evolution of dike opening during the March 2011 Kamoamoa fissure eruption, Kilauea volcano, Hawaii. *Journal of Geophysical Research: Solid Earth*, *118*(1018), 897–914. doi: 10.1002/jgrb.50108.

Massonnet, D., and Feigl, K. L. (1998). Radar interferometry and its application to changes in the earth's surface. *Reviews of Geophysics*, *36*, 441–500.

Michel, R., Avouac, J. P., and Taboury, J. (1999). Measuring ground displacements from SAR amplitude images: Application to the Landers earthquake. *Geophysical Research Letters*, *26*(7), 875–878.

Moreira, A., Krieger, G., Hajnsek, I., Hounam, D., Werner, M., Riegger, S., and Settelmeyer, E. (2004). TanDEM-X: A TerraSAR-X add-on satellite for single-pass SAR interferometry. In *2004 IEEE International Proceedings of the Geoscience and Remote Sensing Symposium (IGARSS '04)*, Anchorage, AK, 20–24 September, 2004, vol. 2, pp. 1000–1003.

Paine, J. G., Buckley, S. M., Collins, E. W., and Wilson, C. R. (2012). Assessing collapse risk in evaporite sinkhole-prone areas using microgravimetry and radar interferometry. *Journal of Environmental Engineering and Engineering Geophysics*, *17*, 75–87.

Raucoules, D., de Michele, M., Malet, J. P., and Ulrich, P. (2013). Time-variable 3D ground displacements from high-resolution synthetic aperture radar (SAR). Application to La Valette landslide (South French Alps). *Remote Sensing of Environment*, *139*, 198–204. http://dx.doi.org/10.1016/j.rse.2013.08.006.

Rosen, P. A., Hensley, S., Joughin, I. R., Li, F. K., Madsen, S. N., Rodriguez, E., and Goldstein, R. M. (2000). Synthetic aperture radar interferometry. *Proceedings of the IEEE*, *88*(3), 333–382.

Rufino, G., Moccia, A., and Esposito, S. (1998). DEM generation by means of ERS tandem data. *IEEE Transactions on Geoscience and Remote Sensing*, *36*(6), 1905–1912.

Salvi, S., Salvi, S., Stramondo, S., Hunstad, I., Chini, M., Atzori, S., Moro, M. et al. (2009). Measurement and modeling of coseismic deformation during the L'Aquila Earthquake, preliminary results. Rome: Istituto Nazionale di Geofisica e Vulcanoligia. http://portale.ingv.it/primo-piano-1/new-archive/2009-news/april-6-earthquake/sar-preliminary-results/view?set_language=en (accessed 29 September 2014).

Sandwell, D. T., Myer, D., Mellors, R., Shimada, M., Brooks, B., and Foster, J. (2008). Accuracy and resolution of ALOS interferometry: Vector deformation maps of the Father's Day intrusion at Kilauea. *IEEE Transactions on Geoscience and Remote Sensing*, *46*(11), 3524–3534.

Scambos, T. A., Dutkiewicz, M. J., Wilson, J. C., and Bindschadler, R. A. (1992). Application of image cross-correlation to the measurement of glacier velocity using satellite image data. *Remote Sensing of Environment*, *42*(3), 177–186.

Shwartz, M. (2006). Experts fear impacts of quake on Delta. Stanford report, May 17.

Simons, M., Fialko, Y., and Rivera, L. (2002). Coseismic deformation from the 1999 Mw 7.1 Hector Mine, California, earthquake as inferred from InSAR and GPS observations. *Bulletin of the Seismological Society of America*, *92*(4), 1390–1402.

Simons, M., and Rosen, P. A. (2015). Interferometric synthetic aperture radar geodesy. In *Treatise on Geophysics*, ed. Shubert, G. 2nd ed., vol. 3. Amsterdam: Elsevier, pp. 339–385.

Smith, L. C. (2002). Emerging applications of interferometric synthetic aperture radar (InSAR) in geomorphology and hydrology. *Annals of the Association of American Geographers*, *92*(3), 385–398.

Stramondo, S., Kyriakopoulos, C., Bignami, C., Chini, M., Melini, D., Moro, M., Picchiani, M., Saroli, M., and Boschi, E. (2011). Did the September 2010 (Darfield) earthquake trigger the February 2011 (Christchurch) event? *Scientific Reports*, *1*, 98. doi: 10.1038/srep00098.

Strozzi, T., Dammert, P. B., Wegmuller, U., Martinez, J. M., Askne, J. I., Beaudoin, A., and Hallikainen, N. T. (2000). Landuse mapping with ERS SAR interferometry. *IEEE Transactions on Geoscience and Remote Sensing*, *38*(2), 766–775.

Talebian, M., Fielding, E. J., Funning, G. J., Ghorashi, M., Jackson, J., Nazari, H., Parsons, B., Priestley, K., Rosen, P. A., Walker, R., and Wright, T. J. (2004). The 2003 Bam (Iran) earthquake: Rupture of a blind strike-slip fault. *Geophysical Research Letters*, *31*(11), L11611. doi: 10.1029/2004GL020058.

Tralli, D. M., Blom, R. G., Zlotnicki, V., Donnellan, A., and Evans, D. L. (2005). Satellite remote sensing of earthquake, volcano, flood, landslide and coastal inundation hazards. *ISPRS Journal of Photogrammetry and Remote Sensing*, *59*(4), 185–198.

Vasco, D. W., Rucci, A., Ferretti, A., Novali, F., Bissell, R. C., Ringrose, P. S., Mathieson, A. S., and Wright, I. W. (2010). Satellite-based measurements of surface deformation reveal fluid flow associated with the geological storage of carbon dioxide. *Geophysical Research Letters*, *37*(3), L03303. doi: 10.1029/2009GL041544.

Vincent, F., Raucoules, D., Degroeve, T., Edwards, G., and Abolfazl Mostafavi, M. (2004). Detection of river/sea ice deformation using satellite interferometry: Limits and potential. *International Journal of Remote Sensing*, *25*(18), 3555–3571.

Voigt, S., Kemper, T., Riedlinger, T., Kiefl, R., Scholte, K., and Mehl, H. (2007). Satellite image analysis for disaster and crisismanagement support. *IEEE Transactions on Geoscience and Remote Sensing*, *45*(6), 1520–1528.

Wadge, G., Saunders, S., and Itikarai, I. (2012). Pulsatory andesite lava flow at Bagana volcano. *Geochemistry, Geophysics, Geosystems*, *13*(11), Q11011. doi: 10.1029/2012GC004336.

Wang, H., Wright, T. J., Yu, Y., Lin, H., Jiang, L., Li, C., and Qiu, G. (2012). InSAR reveals coastal subsidence in the Pearl River Delta, China. *Geophysical Journal International*, *191*(3), 1119–1128.

Yonezawa, C., and Takeuchi, S. (2001). Decorrelation of SAR data by urban damages caused by the 1995 Hyogoken-Nanbu earthquake. *International Journal of Remote Sensing*, *22*(8), 1585–1600.

Yun, S., Agram, P., Fielding, E., Simons, M., Webb, F., Tanaka, A., Lundgren, P., Owen, S., Rosen, P. A., and Hensley, S. (2011b). Damage proxy map from InSAR coherence applied to February 2011 M6.3 Christchurch earthquake, 2011 M9.0 Tohoku-oki earthquake, and 2011 Kirishima volcano eruption [abstract NH31A1533]. Presented at AGU Fall Meeting, San Francisco, CA, 5–9 December, 2011.

Yun, S., Fielding, E., Simons, M., Rosen, P. A., Owen, S. E., and Webb, F. (2011a). Damage proxy map of M6.3 Christchurch earthquake using InSAR coherence [abstract]. Presented at Fringe 2011 Workshop: Advances in the Science and Applications of SAR Interferometry from ESA and 3rd Party Missions, Frascati, Italy, 19–23 September, 2011.

Yun, S., Zebker, H. A., Segall, P., Hooper, A., and Poland, M. (2007). Interferogram formation in the presence of complex and large deformation. *Geophysical Research Letters*, *34*, L12305. doi: 10.1029/2007GL02974.

Zebker, H. A., Rosen, P. A., Hensley, S., and Mouginis-Mark, P. J. (1996). Analysis of active lava flows on Kilauea volcano, Hawaii, using SIRC radar correlation measurements. *Geology*, *24*(6), 495–498.

Zebker, H. A., and Villasenor, J. (1992). Decorrelation in interferometric radar echoes. *IEEE Transactions on Geoscience and Remote Sensing*, *30*(5), 950–959.

12 On SAR Image Processing
From Focusing to Target Recognition

Kun-Shan Chen and Yu-Chang Tzeng

CONTENTS

12.1 INTRODUCTION

Synthetic aperture radar (SAR) image understanding and interpretation are essential for remote sensing of Earth environment and target detection [1–12]. In the development of aided target recognition and identification system, the SAR image database with rich information content plays important roles. It is well recognized that these image base volumes are enormous and it is impractical to acquire them solely by *in situ* measurements. Hence, SAR simulation is one potential alternative to alleviating the problem. However, it is highly desirable to develop a full-blown SAR image simulation scheme with high verisimilitude including the sensor and target geolocation relative to the Earth, movement of the SAR sensor, SAR system parameters, radiometric and geometric characteristics of the target, and environment clutter. The simulation should at least include the computation of radar cross section (RCS) of targets, orbital parameters estimation, SAR echo signal generation, image focusing, and so on. Such a simulation scheme is also well suited for satellite SAR mission planning. Nevertheless, the simulation apparently is of high computational complexity and is heavy computational resource demanding. To release the heavy computational burden, a graphic processing unit (GPU)-based algorithm that explores and makes use of the graphic computation power is developed. As an application example of the simulated SAR images, the second part of this chapter deals with target recognition. Before doing so, feature enhancement and extraction are presented. It is well known that good feature enhancement is essential for target identification and recognition of

SAR images [13–18]. Novel algorithm proposed for spotlight mode SAR involves the formation of a cost function containing nonquadratic regularization constraints [19–20]. In stripmap mode, neither the radar antenna nor the target being mapped rotates, and the radar flight track is almost perpendicular to the look direction with a small squint angle. By reformulating the projection kernel and using it in an optimization equation form, an optimal estimate of the target's reflectivity field may be obtained [21]. As a result, the image fuzziness may be reduced and image fidelity was preserved. Thus, the target's features were adequately enhanced, and dominant scatterers could be well separated. Finally, target recognition from various commercial aircrafts was demonstrated by means of a simulated database and a neural classifier. The neural network is structured to allow its training by the Kalman filtering technique [22–26]. Performance evaluation was done from simulated images and various real images by Radarsat-2 and TerraSAR-X in stripmap mode.

12.2 SATELLITE SAR IMAGES SIMULATION

Figure 12.1 illustrates a functional block diagram of a satellite SAR image simulation and a follow-up target recognition. The simulation processing flow is basically adapted from Refs. [9,27,28]. Generally, the inputs include satellite and radar parameters setting, the target's computer aided design (CAD) model, and also the clutter model. The computation includes satellite orbit estimation, imaging geometry, target RCS, SAR echo, and raw signal generation. Also included is Doppler centroid and rate estimation, a critical step for image focusing. The most time-consuming part is echo and raw

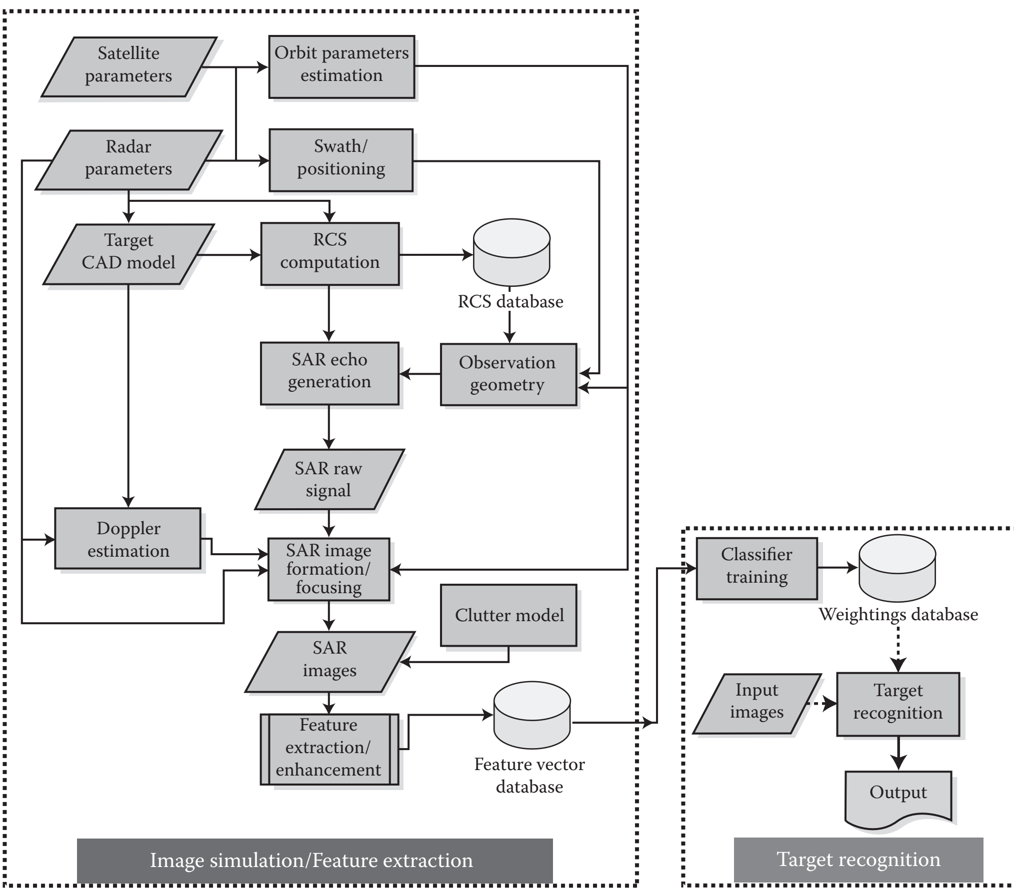

FIGURE 12.1 SAR image simulation and target recognition flowcharts.

signal generation, which is illustrated in Figure 12.1. Then a refined range-Doppler (RD) method is applied to perform the SAR image focusing. The outputs include sets of image for a desired target for a range of radar looking angles and orientation angles. Once the image database is built and made available, feature extraction and enhancement are performed, followed by a target recognition stage that includes a neural classifier training, neural weights storage for a later operation stage.

12.2.1 SAR Signal Model

A typical side-looking SAR observation geometry is shown in Figure 12.2 where the slant range between SAR and target, R, is a function of satellite moving time or slow time η or equivalently depends on the squint angle away from the zero-Doppler plane which corresponds to the slant range R_0. In SAR processing, it is essential to project R onto R_0.

An SAR transmits a linear frequency-modulated signal of the form

$$s_t(\tau) = w_r\left(\tau, T_p\right)\cos\left(2\pi f_c \tau + \pi\alpha_r \tau^2\right) \tag{12.1}$$

where α_r is the chirp rate, T_p is the pulse duration, f_c is the carrier frequency, τ is the ADC sampling time or fast time, and $w_r(\cdot)$ is a rectangular function

$$w_r\left(\tau, T_p\right) = \mathrm{rect}\left(\frac{\tau}{T_p}\right) = \begin{cases} 1, & \left|\dfrac{\tau}{T_p}\right| \le 0.5 \\ 0, & \text{else.} \end{cases} \tag{12.2}$$

The received signal or raw data is a delayed version of the transmitted signal (Equation 12.1) [16],

$$\begin{aligned} s_r(\tau) &= A_0 s_t\left(\tau - \frac{2R}{c}\right) \\ &= A_0 w_r\left(\tau - \frac{2R}{c}, T_p\right) w_a(\eta)\cos\left\{2\pi f_0\left(\tau - \frac{2R}{c}\right) + \pi\alpha_r\left(\tau - \frac{2R}{c}\right)^2 + \varphi\right\}, \end{aligned} \tag{12.3}$$

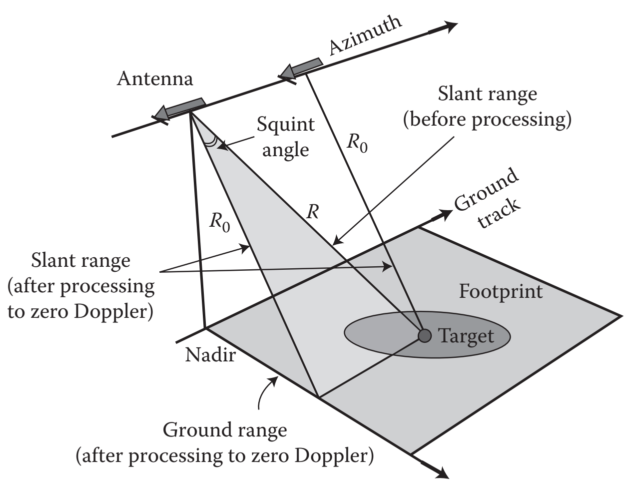

FIGURE 12.2 A typical stripmap SAR observation geometry. (From I. Cumming and F. Wong, *Digital Signal Processing of Synthetic Aperture Radar Data: Algorithms and Implementation*, Artech House, 2004. With permission.)

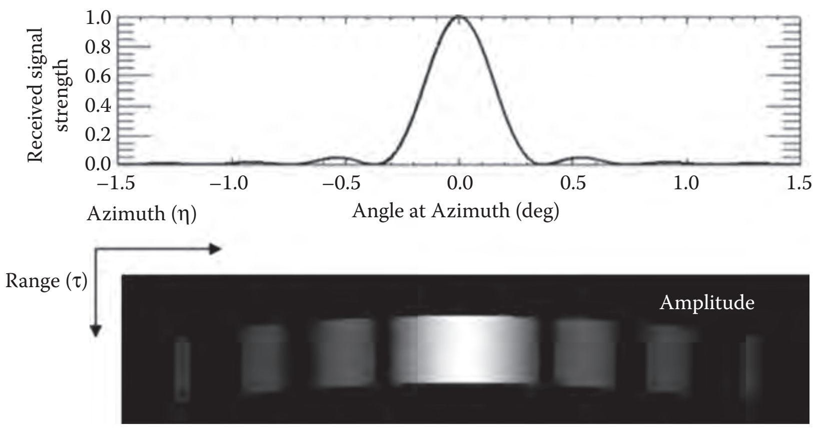

FIGURE 12.3 A typical antenna pattern along the azimuth direction and the received signal.

where R is the distance from the antenna to the target being observed, A_0 is the slant range backscatter coefficient of the target, φ is the phase term, and $w_a(\eta)$ is the antenna pattern and is a function of slow time. A commonly used pattern is of the form

$$w_{\mathrm{a}}(\eta) \cong \mathrm{sinc}^2\left\{\frac{\sqrt{3}\theta(\eta)}{2\beta_{\mathrm{az}}}\right\}, \tag{12.4}$$

where β_{az} is the azimuth beamwidth and $\theta(\eta)$ is the angle measured from boresight in the slant range plane. Figure 12.3 displays such an antenna pattern (upper) and received echo (lower) along the azimuth direction. The echo strength is varied according to antenna gain and is changed with flight time η. Note that the echo still comes with the carrier frequency that contains no target information and needs to be removed before further processing.

After demodulation, the received signal is given as [22]

$$s_0(\tau,\eta) = A_0 w_{\mathrm{r}}\left(\tau - \frac{2R(\eta)}{c}, T_{\mathrm{p}}\right) w_{\mathrm{a}}(\eta) \exp\left\{-j\frac{4\pi f_{\mathrm{c}} R(\eta)}{c} + \mathrm{j}\pi\alpha_r\left(\tau - \frac{2R(\eta)}{c}\right)^2 + \varphi''\right\}, \tag{12.5}$$

where φ'' is the lumped sum of phase noise from the atmosphere, satellite altitude error, terrain, and so on, and is only of interest for interferometric SAR. Equation 12.5 serves as the fundamental signal model for the working process that follows.

12.2.2 RCS Computation

To facilitate the radar response from a target, we need the target's radar cross section under a radar observation scenario. The radar backscattering characteristics is taken into account. The coherent scattering process between a target and its background is neglected for the sake of simplicity. Also, fully polarimetric response is not considered, however. Radar Cross Section Analysis and Visualization System [29] is a powerful algorithm that utilizes the physical optics (PO), physical diffraction theory (PDT), and shooting and bouncing rays (SBRs) to compute the RCS of complex radar targets [30–34]. Single scattering and diffraction from a target are first computed by PO and PDT, followed by SBRs to account for multiple scattering and diffraction. The system outputs for a given three-dimensional (3D) CAD model of the target of interest. The CAD model contains

FIGURE 12.4 **(See color insert.)** Computed RCS of commercial aircrafts for C-band HH polarization (left) and X-band VV polarization (right).

numerous grids or polygons, each associated with computed RCS as a function of incident and aspect angles for a given set of radar parameters. The number of polygons is determined by the target's geometry complexity and its electromagnetic size. To realize the imaging scenario, each polygon must be properly oriented and positioned based on ECR coordinates. Figure 12.4 displays the computed RCSs of these aircraft for the cases of Radarsat-2 and TerraSAR-X.

12.2.3 Clutter Model

Although the coherent scattering process between a target and its background is neglected for the sake of simplicity, the clutter from background is incoherently integrated into the radar echo. Extensive studies on SAR speckle and its reduction have been documented [12,35–37]. Many studies [38–41] suggest that for surface-like clutter such as vegetation canopy [42,43] and airport runway, the radar signal statistics follows the Weibull distribution fairly well. For our aircraft targets of interest, we applied the Weibull distribution for the runway clutter model. Other models can be easily adopted in the simulation chain.

$$p(x) = \frac{\kappa}{\lambda}\left(\frac{x}{\lambda}\right)^{\kappa-1} \exp\left[-(x/\lambda)^{\kappa}\right], \tag{12.6}$$

where the shape parameter k and the scale parameter λ may be estimated from real SAR images over the runway with mean amplitude A [37]:

$$k = \frac{\pi}{\mathrm{std}\left[\ln(A)\right]\sqrt{6}} \tag{12.7}$$

$$\lambda = \exp\left\{\left[<\ln(A)>\right] + \frac{0.5722}{\kappa}\right\} \tag{12.8}$$

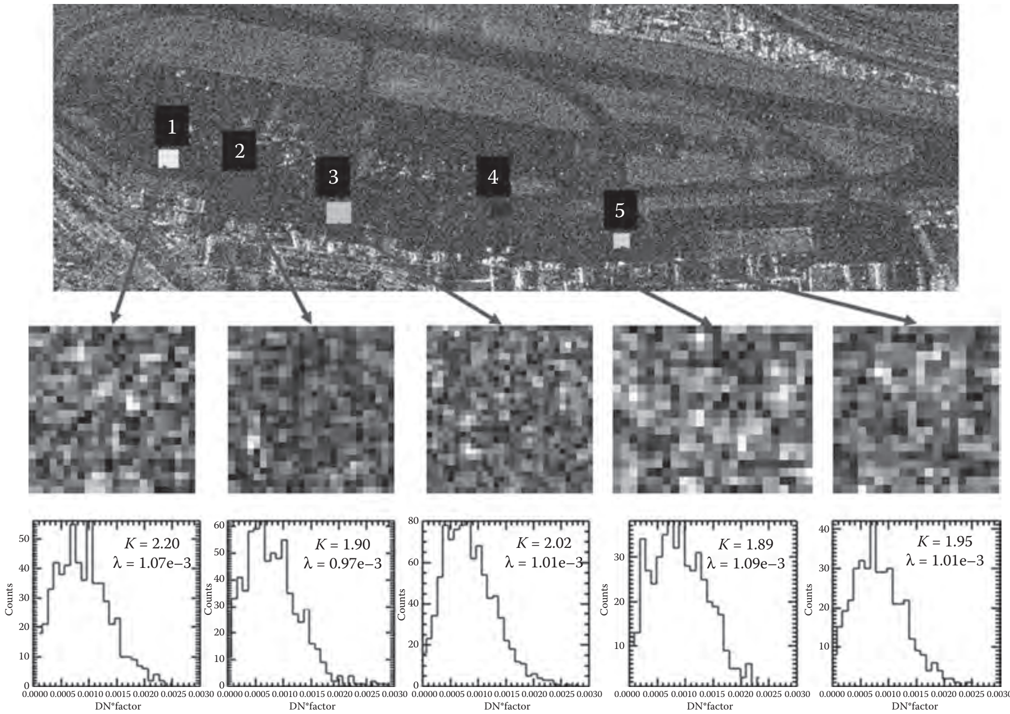

FIGURE 12.5 Samples of clutter and estimated model parameters on a TerraSAR-X image.

Figure 12.5 displays sample regions of clutter and estimated model parameters on a TerraSAR-X image. The model parameters are obtained by averaging several samples.

12.2.4 Satellite Orbit Determination

In applying Equation 12.5, the range between a satellite in space and a target being imaged on the ground must be precisely determined for matched filtering. That is to say, we need to know the satellite and target position vectors in order to estimate the Doppler frequency and its rate. Before doing so, we have to define and then determine the reference systems for time and geodetic. Six fundamental parameters required to determine the orbital position include the semimajor axis a, eccentricity e, inclination angle i, right ascension of ascending node Ω, argument of perigee ω, and true anomaly v. Three of the parameters determine the orientation of the orbit or trajectory plane in space, while three locate the body in the orbital plane [44,45]. These six parameters are uniquely related to the position and velocity of the satellite at a given epoch.

To deduce the orbital elements of a satellite, at least six independent measurements are needed [44]. In this chapter, we adopted simplified perturbations models (SPM) [46–48] to estimate the orbital state vectors of satellite in the Earth Centered Inertial coordinate system. A C++ version program code by Henry [46] was used. Once the orbit parameters are determined, we can transform it to Earth Centered Rotation coordinate system, as described below. The transformation matrix is of the form [44]

$$\mathbf{U}_{\mathrm{ECR}}^{\mathrm{ECI}} = \Pi\Theta\mathbf{NP}, \tag{12.9}$$

where matrices Π, Θ, **N**, and **P** represent, respectively, polar motion, Earth rotation, nutation, and precession matrices:

$$\Theta(t) = \mathbf{R_z}(\mathrm{GAST}), \tag{12.10}$$

$$\mathbf{P}(T_1, T_2) = \mathbf{R_z}\left(-z(T,t)\right)\mathbf{R_y}\left(\vartheta(T,t)\right)\mathbf{R_z}\left(-\xi(T,t)\right), \tag{12.11}$$

where GAST is Greenwich apparent sidereal time. Referring to Figure 12.6, the nutation matrix is

$$\mathbf{N}(T) = \mathbf{R_x}(-\varepsilon - \Delta\varepsilon)\mathbf{R_z}(-\Delta\psi)\mathbf{R_z}(\varepsilon) \tag{12.12}$$

Note that from Ref. [44], in computing the derivative of the transformation, the precession, nutation, and polar motion matrices may be considered as constant.

$$\frac{\mathrm{d}\mathbf{U}_{\mathrm{ECR}}^{\mathrm{ECI}}}{\mathrm{d}t} \approx \Pi \frac{\mathrm{d}\Theta}{\mathrm{d}t}\mathbf{NP}. \tag{12.13}$$

Then the state vectors in the transformation are

$$\boldsymbol{r}_{\mathrm{ECR}} = \mathbf{U}_{\mathrm{ECR}}^{\mathrm{ECI}}\mathbf{r}_{\mathrm{ECI}}, \tag{12.14}$$

$$\mathbf{v}_{\mathrm{ECR}} = \mathbf{U}_{\mathrm{ECR}}^{\mathrm{ECI}}\mathbf{v}_{\mathrm{ECI}} + \frac{\mathrm{d}\mathbf{U}_{\mathrm{ECR}}^{\mathrm{ECI}}}{\mathrm{d}t}\mathbf{r}_{\mathrm{ECI}}, \tag{12.15}$$

$$\boldsymbol{r}_{\mathrm{ECI}} = \left(\mathbf{U}_{\mathrm{ECR}}^{\mathrm{ECI}}\right)^{\mathrm{T}}\mathbf{r}_{\mathrm{ECR}}, \tag{12.16}$$

and

$$\mathbf{v}_{\mathrm{ECI}} = \left(\mathbf{U}_{\mathrm{ECR}}^{\mathrm{ECI}}\right)^{\mathrm{T}}\mathbf{v}_{\mathrm{ECR}} + \frac{\mathrm{d}\left(\mathbf{U}_{\mathrm{ECR}}^{\mathrm{ECI}}\right)^{\mathrm{T}}}{\mathrm{d}t}\mathbf{r}_{\mathrm{ECR}}. \tag{12.17}$$

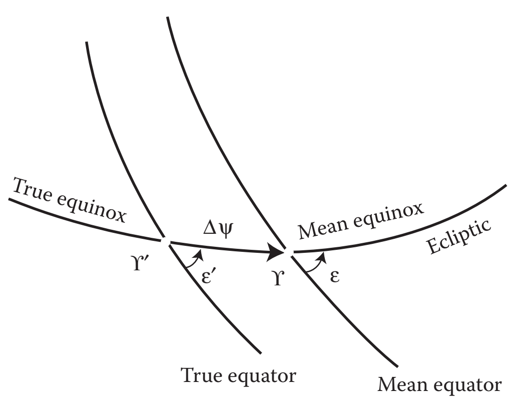

FIGURE 12.6 Illustration of nutation.

In summary, four key steps are needed:

1. Find the satellite position: calculated from two-line elements data and imaging time duration.
2. Find the radar beam pointing vector derived from the satellite attitude (pitch, roll, and yaw angle).
3. Locate the target center position derived from the satellite position and the line of sight.
4. Locate each target's polygon position derived from the target center position and the target aspect angle.

12.2.5 Image Focusing

Several focusing algorithms have been proposed, including RD, omega-K, chirp-scaling, and so on [27,49,50] and their improved versions, with each bearing pros and cons. We adopted the refined RO algorithm with secondary range compression because of its fast computation while it maintains reasonably good spatial resolution and a small defocusing error. Figure 12.7 outlines the functional block diagram of processing steps in the refined RD algorithm.

The power balance method in conjunction with the average cross-correlation coefficient method was used to obtain a rough estimate of baseband Doppler frequency [51]. To obtain absolute Doppler centroid frequency, f_{DC}, algorithms such as multilook cross-correlation, multilook beat frequency, and wave number domain algorithm may be utilized to determine the ambiguity number [27]:

$$f_{DC} = f_{DC,base} + M_{amb}PRF, \tag{12.18}$$

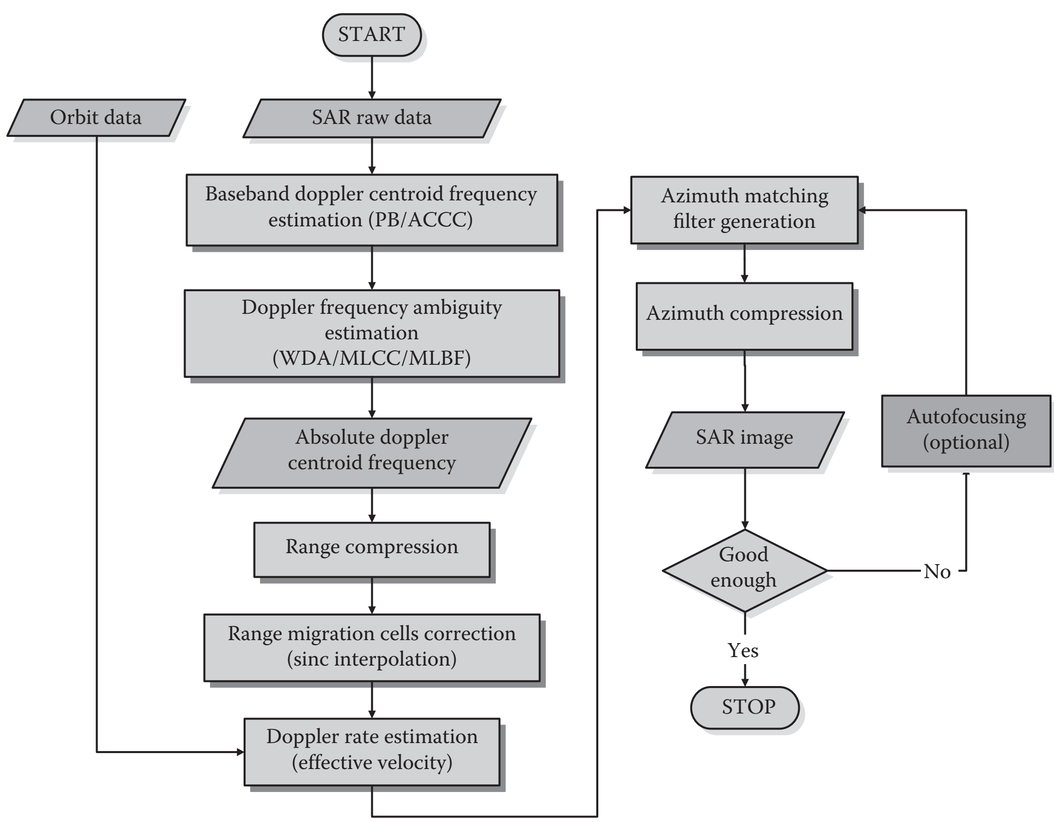

FIGURE 12.7 SAR image-focusing flowchart of an RD-based algorithm.

where $f_{DC,base}$ is the baseband part of PRF, M_{amb} is the ambiguity number, and PRF is the pulse repetition frequency.

After an effective satellite velocity, V_r, is estimated from orbit state vectors, the Doppler rate estimation can be computed via

$$f_R(R_0) = \frac{2V_r^2(R_0)\cos(\theta_{sq,c})}{R_0}, \tag{12.19}$$

where $\theta_{sq,c}$ is the squint angle and R_0 is referred to as the zero-Doppler plane (see Figure 12.2). Note that in some cases, Equation 12.19 is just a rough estimate, and then autofocus via the phase gradient algorithm [27] may be further applied to refine the Doppler rate given above.

12.3 COMPUTATION COMPLEXITY AND VALIDATION

An SAR image is sensitive to the target's geometry, including orientation and aspects angles. For target recognition and identification, a more complete database for feature extraction is preferable to achieve better performance and reduce the false alarm rate. In SAR image simulation, suppose that n samples (incident angles and aspect angles) are desired; then, the computation complexity is $\theta(n^3)$. Table 12.1 lists CPU hours to complete one TerraSAR-X image simulation of MD80 aircraft using 25672 polygons representing RCS for just a pose (one incident angle and one aspect angle). It would take about 11 months to complete all poses for incident angles from 20° to 50° with 5° a step and aspect angles from −180° to ~+180° with 1° a step (total 2520 poses). Apparently, finding methods to speed up the computation time is essential for practical use.

As for a GPU, work load is assumed to be highly parallel—many data to be processed by the same algorithm. Recently, applications of GPUs to SAR simulation are reported [52–53]. Based on that assumption, each processing unit is designed to handle many threads. Processing units work as a group to maximize throughput of all threads. Latency can be hidden by skipping stalled threads, if there are few compared to the number of eligible threads. Grouping means shared control logics and cache. The GPU-based SAR simulation is divided into a grid of blocks. Each block consists of a number of *threads*, which are executed in a *multiprocessor* (also named as *stream multiprocessor* or *block*). Compute unified device architecture (CUDA) developed by NVIDIA [54] is used for the proposed GPU-based implementation on a Linux operating system. The usage of the shared memory implemented in the proposed method is applied to the data-intensive computational tasks of the GPU-based computations [55]. The data with high dependency are assigned into the same block of the shared memory with a finer granularity of parallel implementation. To make use of this highly efficient memory architecture, we devised local variables and parameters by using these registers. The GPU-based experiments were performed on a low-cost 960 (240)-core NVIDIA Tesla personal supercomputer with one Intel Xeon 5504 quad-core CPU and four NVIDIA GTX295 (240 core) GPUs. Figure 12.8 shows the speed-up performance using the GPU algorithm against a CPU one, as a function of the number of samples

TABLE 12.1
CPU Hours to Complete a TerraSAR-X Simulated Image of MD80 for One Pose (with 25672 RCS Polygons)

OS	RAM (GB)	CPU (GHz)	Multithreading	CPU Time (Hours)
Win-XP 64 bits	1.97	2.4 (4 cores)	OFF	20.1
			ON	18.7
Win-XP 32 bits	3.24	2.8 (2 cores)	OFF	21.1

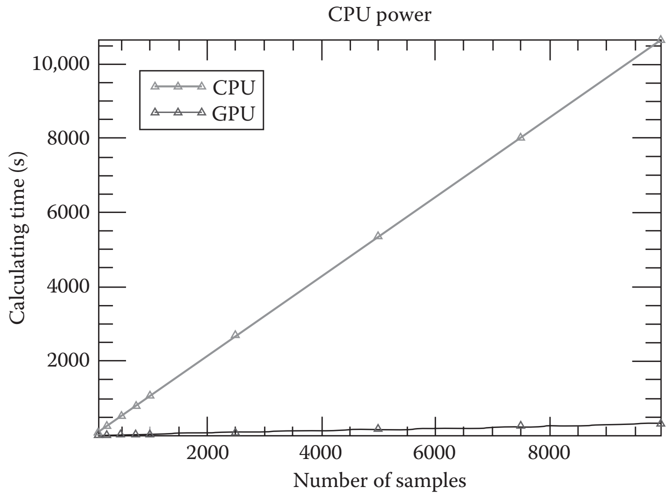

FIGURE 12.8 Speedup performance as a function of number of polygons using a GPU algorithm.

(polygons in target's RCS) for one pose. As the number of samples increases, CPU time grows very fast. The required computation time is absorbed by GPUs, as obviously seen from the chart. The average speed-up ratio to CPU is about 32. With a dual-GPU configuration, 65 times speed-up was boosted.

12.4 APPLICATION TO TARGET RECOGNITION

The proposed working flows and algorithms were validated by evaluating the image quality, including geometric and radiometric accuracy using simple point targets first, followed by simulating four types of commercial aircraft : A321, B757-200, B747-400, and MD80. The satellite SAR systems for simulation include ERS-1, ERS-2, Radarsat-2, TerraSAR-X, and ALOS PALSAR, but others can be easily realized. Table 12.2 lists the key image quality indices for a simulated image of TerraSAR-X and PLASAR satellite SAR systems. Quality indices include 3 dB azimuth beamwidth (m), peak-to-side lobe ratio (dB), integrated side lobe ratio (dB), and scene center accuracy in different coordinate systems. As can be seen from the table, the simulated images are all well within the nominal specifications for different satellite systems.

12.4.1 Feature Enhancement

The essential information for target classification, detection, recognition, and identification is through feature selection for the training phase. For our interest, depending on the spatial resolution offered by Radarsat-2 and TerraSAR-X in stripmap mode, we aim at target recognition. Before feature extraction, feature enhancement is performed first. To enhance the stripmap mode data using the nonquadratic regularization method [19,20], one has to modify the projection operator kernel accordingly. The received signal $\mathbf{s}_o$ in Equation 12.5 may be expressed as [19–21]:

$$\mathbf{s}_o = \mathbf{Tf} + \mathbf{s}_n, \tag{12.20}$$

where $\mathbf{s}_n$ represents noise, and $\mathbf{T}$ is the projection operation kernel with dimension $MN \times MN$ which plays a key role in contrast enhancement if the signal in Equation 12.5 is of dimension $M \times N$. It has

TABLE 12.2
Comparison of Simulated Image Quality for a Point Target

		ALOS PALSAR		TerraSAR-X	
Index		**Simulation**	**Nominal**	**Simulation**	**Nominal**
3 dB Azimuth beamwidth (m)		4.26	5.10	3.49	4.51
PSLR (dB)	Slant range	−24.85	−20.5	−22.85	−13
	Azimuth	−25.42		−31.16	
ISLR (dB)	Slant range	−30.62	−15.0	−31.62	−17
	Azimuth	−25.62		−43.98	
Scene center	Long, Lat (°)	121.49927°E, 24.764622°N	121.49930°E, 24.764477°N	119.395090°E, 24.894470°N	119.39506°E, 24.894620°N
	ECR (x,y,z) (m)	−3027814.2, 4941079.3, 2655407.1	−3027808.4, 4941075.0, 2655421.7	−2817396.77, 5608995.60, 2830631.97	−2817397.45, 5608996.11, 2830630.29
	Long/Lat difference (°)	-3×10^{-5}, 1.45×10^{-4}		-3×10^{-6}, 1.5×10^{-4}	
	ECR difference (ground range, azimuth) (m)	0.98, −16.26		0.06, 16.97	

been shown that [3,4] nonquadratic regularization is practically effective in minimizing the clutter while emphasizing the target features via

$$\hat{\mathbf{f}} = \arg\min\left\{\left\|\mathbf{s}_{\mathrm{r}} - \mathbf{T}\mathbf{f}\right\|_2^2 + \gamma^2 \left\|\mathbf{f}\right\|_p^p\right\}, \tag{12.21}$$

where $\|\ \|_p$ denotes ℓ_p-norm ($p \le 1$), γ^2 is a scalar parameter, and $\left\{\left\|\mathbf{s}_{\mathrm{o}} - \mathbf{T}\mathbf{f}\right\|_2^2 + \gamma^2 \left\|\mathbf{f}\right\|_p^p\right\}$ is recognized as the cost or objective function.

To easily facilitate the numerical implementation, both $\mathbf{s}_{\mathrm{o}}$ and $\mathbf{f}$ may be formed as long vectors, with $\mathbf{T}$ being a matrix. Then, from Equations 12.5 and 12.20, we may write the projection operation kernel for the stripmap mode as [21]

$$\mathbf{T} = \exp\left\{-i\left[\omega_0 \frac{2\left(\mathbf{r} + \frac{(\mathbf{x}-\mathbf{x}_0)^2}{2\mathbf{r}}\right)}{c} - \alpha\left(\mathbf{t} - \frac{2\left(\mathbf{r} + \frac{(\mathbf{x}-\mathbf{x}_0)^2}{2\mathbf{r}}\right)}{c}\right)^2\right]\right\}, \tag{12.22}$$

where $\mathbf{t}$, $\mathbf{r}$, $\mathbf{x} - \mathbf{x}_0$ are matrices to be described below by first defining the following notations to facilitate the formation of these matrices:

N : the number of discrete sampling points along the slant range direction
M : the number of discrete sampling points along the azimuth direction
Δt : the sampling interval along the slant range
ℓ_{r} : the size of the footprint along the slant range
ℓ_{x} : the size of the footprint along the azimuth direction
$\mathbf{1}_l$: the column vector of dimension $l \times 1$ and all elements equal to one, in which $l = M$ or $l = MN$

With these notions, we can obtain explicit $\mathbf{t}$, $\mathbf{r}$, $\mathbf{x} - \mathbf{x}_0$ forms, after some mathematical derivations [21].

$$\mathbf{t} = [\mathbf{1}_M \otimes \mathbf{M}_1]_{MN \times MN}, \tag{12.23}$$

$$\mathbf{v}_1 = \begin{bmatrix} 0 \\ 1 \\ \vdots \\ N-1 \end{bmatrix} \Delta t = \begin{bmatrix} 0 \\ \Delta t \\ \vdots \\ (N-1)\Delta t \end{bmatrix}_{N \times 1}, \tag{12.24a}$$

$$\mathbf{M}_1 = \mathbf{V}_1 \cdot \mathbf{1}_{MN}^T = \begin{bmatrix} 0 & \cdots & 0 \\ \Delta t & & \Delta t \\ \vdots & & \vdots \\ (N-1)\Delta t & \cdots & (N-1)\Delta t \end{bmatrix}_{N \times MN}, \tag{12.24b}$$

$$\mathbf{r} = [\mathbf{M}_2 \otimes \mathbf{V}_2^T]_{MN \times MN}, \tag{12.25}$$

$$\mathbf{V}_2 = \begin{bmatrix} \dfrac{-\ell_r}{2} + r_0 \\ \dfrac{-\ell_r}{2} + r_0 + \Delta\ell \\ \vdots \\ \dfrac{-\ell_r}{2} + r_0 + (N-1)\Delta\ell \end{bmatrix}_{N \times 1}, \quad \Delta\ell = \frac{\ell_r}{N}, \tag{12.26a}$$

$$\mathbf{M}_2 = \mathbf{1}_M^T \otimes \mathbf{1}_{MN} = \begin{bmatrix} \mathbf{1}_{MN} & \cdots & \mathbf{1}_{MN} \end{bmatrix}_{MN \times MN}, \tag{12.26b}$$

$$\mathbf{x} - \mathbf{x}_0 = [\mathbf{M}_3 \otimes \mathbf{M}_4]_{MN \times MN}, \tag{12.27}$$

$$\mathbf{V}_3 = \begin{bmatrix} 0 \\ 1 \\ \vdots \\ M-1 \end{bmatrix} \frac{\ell_x}{M} - \frac{\ell_x}{2} = \begin{bmatrix} \dfrac{-\ell_x}{2} \\ \dfrac{\ell_x}{M} - \dfrac{\ell_x}{2} \\ \vdots \\ (M-1)\dfrac{\ell_x}{M} - \dfrac{\ell_x}{2} \end{bmatrix}_{M \times 1}, \tag{12.28a}$$

$$\mathbf{V}_4 = \begin{bmatrix} \mathbf{V}_3[\delta - 1 : (M-1)]_{\delta \times 1} \\ \mathbf{0}_{(M-\delta) \times 1} \end{bmatrix}_{M \times 1}; \quad \delta = \left\lfloor \frac{M-1}{2} \right\rfloor + 1, \tag{12.28b}$$

$$\mathbf{V}_5 = \begin{bmatrix} \mathrm{Mirror}(\mathbf{V}_3[0 : \delta - 1])_{\delta \times 1} \\ \mathbf{0}_{(M-\delta) \times 1} \end{bmatrix}_{M \times 1}, \tag{12.28c}$$

$$\mathbf{M}_3 = \left[\mathrm{Toep}(\mathbf{V}_5^T, \mathbf{V}_4^T) \right]_{M \times M}, \tag{12.28d}$$

$$\mathbf{M}_4 = \left[\mathbf{1}_{N\times 1} \cdot \mathbf{1}_{N\times 1}^T\right]_{N\times N}, \tag{12.28e}$$

In the above equations, each of the bold-faced letters denotes a matrix and ⊗ represents the Kronecker product. The operation $\mathbf{V}[m : n]$ takes element m to element n from vector $\mathbf{V}$, and Toep(·) converts the input into a Toeplitz matrix [56,57]. Note that in Equation 12.28c, by Mirror $[a : b, c : d]_{p\times q}$ we mean taking elements a to b along the rows and elements c to d along the columns, so that the resulting matrix is of size $p \times q$.

12.4.2 Feature Vectors and Extraction

The feature vector contains two types: fractal geometry and scattering characteristics. In the fractal domain, the image is converted into a fractal image [58]. It has been explored that SAR signals may be treated as a spatial chaotic system because of the chaotic scattering phenomena [59–63]. Applications of fractal geometry to SAR analysis are studied in Refs. [64,65]. There are many techniques proposed to estimate the fractal dimension of an image. Among them, the wavelet approach proves both accurate and efficient. It stems from the fact that the fractal dimension of an N-dimensional random process can be characterized in terms of fractional Brownian motion (fBm) [58]. The power spectral density of the fBm is written as

$$P(f) \propto f^{-(2H+D)} \tag{12.29}$$

where $0 < H < 1$ is the persistence of the fBm and D is the topological dimension (= 2 in the image). The fractal dimension of this random process is given by $D = 3 - H$. As image texture, an SAR fractal image is extracted from SAR imagery data based on local fractal dimension. Therefore, wavelet transform can be applied to estimate the local fractal dimension of an SAR image. From Equation 12.29, the power spectrum of an image is therefore given by

$$P(u,v) = \upsilon\left(\sqrt{u^2 + v^2}\right)^{-2H-2}, \tag{12.30}$$

where υ is a constant. Based on the multiresolution analysis, the discrete detailed signal of an image I at a resolution level j can be written as [66–67]

$$\begin{aligned} D_j I &= \left\langle I(x,y), 2^{-j}\Psi_j\left(x - 2^{-j}n, y - 2^{-j}m\right)\right\rangle \\ &= \left(I(x,y) \otimes 2^{-j}\Psi_j(-x,-y)\right)\left(2^{-j}n, 2^{-j}m\right) \end{aligned} \tag{12.31}$$

where ⊗ denotes a convolution operator, $\Psi_j(x,y) = 2^{2j}\Psi\left(2^j x, 2^j y\right)$ and $\Psi(x,y)$ is a two-dimensional wavelet function. The discrete detailed signal, thus, can be obtained by filtering the signal with $2^{-j}\Psi_j(-x,-y)$ and sampling the output at a rate 2^{-j}. The power spectrum of the filtered image is given by [67]

$$P_j(u,v) = 2^{-2j} P(u,v)\left|\tilde{\Psi}_j(u,v)\right|^2, \tag{12.32}$$

where $\tilde{\Psi}_j(u,v) = \tilde{\Psi}(2^{-j}u, 2^{-j}v)$ and $\tilde{\Psi}(u,v)$ is the Fourier transform of $\Psi(u,v)$. After sampling, the power spectrum of the discrete detailed signal becomes

$$P_j^d\left(u,v\right) = 2^j \sum_k \sum_l P_j\left(u + 2^{-j}2k\pi, v + 2^{-j}2l\pi\right). \tag{12.33}$$

Let σ_j^2 be the energy of the discrete detailed signal:

$$\sigma_j^2 = \frac{2^{-j}}{\left(2\pi\right)^2} \iint P_j^d\left(u,v\right) \mathrm{d}u\, \mathrm{d}v. \tag{12.34}$$

By inserting Equations 12.32 and 12.33 into Equation 12.34 and changing variables in this integral, Equation 12.34 may be expressed as $\sigma_j^2 = 2^{-2H-2}\sigma_{j-1}^2$.

Therefore, the fractal dimension of an SAR image can be obtained by computing the ratio of the energy of the detailed images:

$$D = \frac{1}{2}\log_2 \frac{\sigma_j^2}{\sigma_{j-1}^2} + 2 \tag{12.35}$$

A fractal image indeed represents information regarding spatial variation; hence, its dimension estimation can be realized by sliding a preset size window over the entire image. The selection of the window size is subject to reliability and homogeneity considerations with the center pixel of the window replaced by the local estimate of the fractal dimension. Once fractal image is generated, features of angle, target area, long axis, short axis, and axis ratio are extracted from the target of interest. As for scattering center, features of major direction [X], major direction [Y], minor direction [X], minor direction [Y], major variance, and minor variance are selected, in addition to radar look angle and aspect angle. Figure 12.9 displays such a feature vector from simulated MD80 and B757-200 aircrafts from Radarsat-2. Finally, the recognition is done by a dynamic learning neural classifier [22–26]. This classifier is structured using a polynomial basis function model. A digital Kalman filtering scheme [68] is applied to train the network. The necessary time to complete the

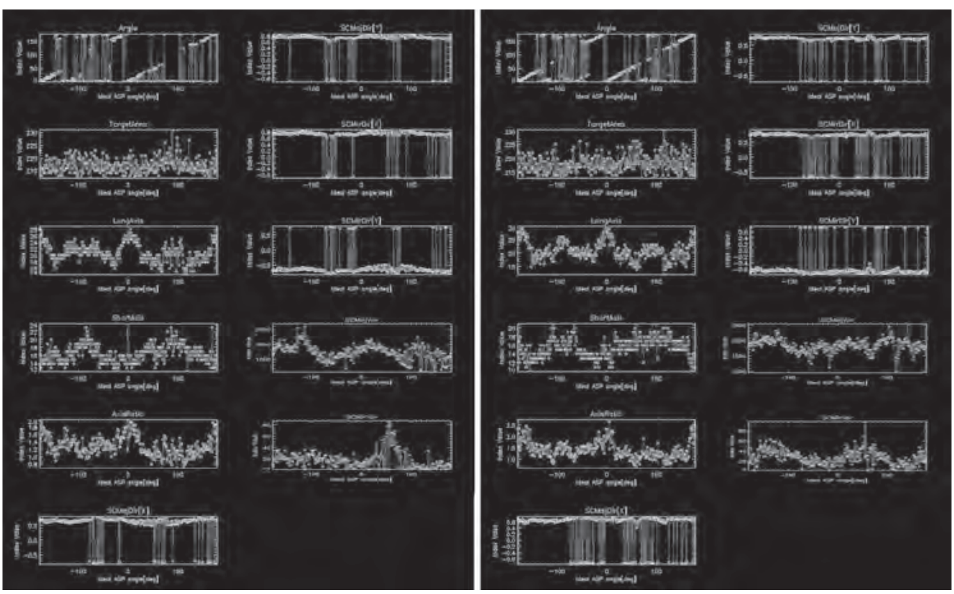

FIGURE 12.9 Selected features of simulated Radarsat-2 images of A321 (left) and B757-200 (right) for incidence angle of 35° and aspect angle from –180° ~ +180° (1° step).

training basically is not sensitive to the network size and is fast. Also, the network allows recursive training when new and updated training data sets are available without revoking training from scratch. The classifier is structured with 13 input nodes to feed the target features, 350 hidden nodes in each of the four hidden layers, and four output nodes representing four aircraft targets (A321, B757-200, B747-400, and MD80).

12.4.3 Performance Evaluation

12.4.3.1 Simulated SAR Images

Both simulated Radarsat-2 and TerraSAR-X images for four targets, as described above, are used to evaluate the classification and recognition performance. For this purpose, Radarsat-2 images with an incidence angle of 45° and TerraSAR-X with 30° of incidence were tested. Both are with a spatial resolution of 3 m in stripmap mode. The training data contain all 360 aspect angles (1° a step); among them 180 samples were randomly taken to test. Fast convergence of neural network learning is observed. The confusion matrix for Radarsat-2 and TerraSAR-X in classifying four targets is given in Tables 12.3 and 12.4, respectively. The overall accuracy and kappa coefficient are very satisfactory. Higher confusion between B757-200 and MD80 was observed. It is also noted that with Radarsat-2 and TerraSAR-X systems, comparable results were obtained as long as classification rate is concerned.

12.4.3.2 Real SAR Images

Data acquisition on May 8, 2008 from TerraSAR-X over an airfield was processed into four looks images with a spatial resolution of 3 m in stripmap mode. Feature enhancement by an operator kernel in Equation 12.22 was performed. Meanwhile, ground truth collections were conducted to identify the targets. Figure 12.10 displays such acquired images where the visually identified targets are marked and their associated image chips were later fed into neural classifier that is trained by the simulated image database. Among all the targets, three types of them are contained in simulated

TABLE 12.3
Confusion Matrix of Classifying Four Targets from Simulated Radarsat-2 Images

		A321	**B747-400**	**B757-200**	**MD80**	**Producer Accuracy**
Target	A321	165	2	6	7	0.917
	B747-400	0	175	3	2	0.972
	B757-200	4	1	164	11	0.911
	MD80	4	2	11	163	0.906
User accuracy		0.954	0.972	0.891	0.891	

Overall accuracy: 0.926, kappa coefficient: 0.902

TABLE 12.4
Confusion Matrix of Classifying Four Targets from Simulated TerraSAR-X Images

		A321	**B747-400**	**B757-200**	**MD80**	**Producer Accuracy**
Target	A321	166	0	5	9	0.922
	B747-400	0	179	0	1	0.994
	B757-200	2	0	168	10	0.933
	MD80	1	0	8	171	0.950
User accuracy		0.982	1.000	0.928	0.895	

Overall accuracy: 0.950, kappa coefficient: 0.933

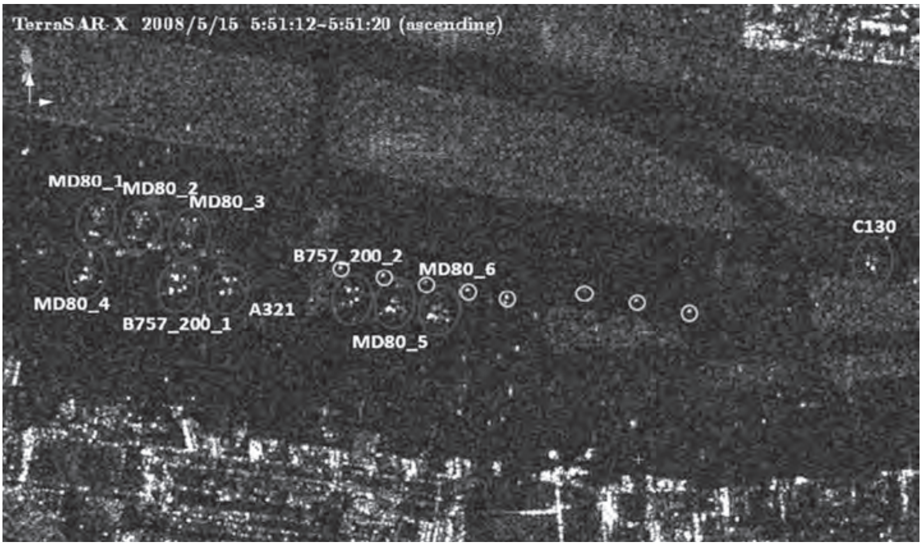

FIGURE 12.10 A TerraSAR-X image over an airfield acquired on May 15, 2008. The identified targets are marked from ground truth.

database: MD80, B757-200, and A321. From Table 12.5, these targets are well recognized, where the numeric value represents membership. Winner-takes-all approach was taken to determine the classified target and whether these targets are recognizable. More sophisticated schemes such as type-II fuzzy may be adopted in the future. It is realized that for certain poses, there exists confusion between MD80 and B757-200, as already demonstrated in the simulation test above. It was not able to recognize target C130, as expected.

As another example, a blind test was performed. Here, blind means the targets to be recognized are not known to the tester, nor is the image acquisition time. The ground truth was collected by the third party and was only provided after recognition operation was completed. This is very close to the real situation for recognition operation. A total of 12 targets (T1–T12) were chosen for the test, as indicated in Figure 12.11. Unlike in Figure 12.10, this image was acquired in descending mode but was unknown at the time of test. Table 12.6 gives the test results, where the recognized targets and truth are listed. It is readily indicated that all the MD80 targets were successfully recognized,

TABLE 12.5
Membership Matrix for Target Recognition on TerraSAR-X Image of Figure 12.10

	Output				
Input	**A321 (%)**	**B747-400 (%)**	**B757-200 (%)**	**MD80 (%)**	**Recognizable**
MD80_1	16.61	7.26	0	76.12	Yes
MD80_2	0	9.63	18.50	71.85	Yes
MD80_3	0	3.63	8.78	87.58	Yes
MD80_4	0	3.64	23.08	73.27	Yes
MD80_5	17.88	12.28	0	69.82	Yes
MD80_6	5.64	0	46.72	47.63	Yes
B757-200_1	12.05	11.84	76.09	0	Yes
B757-200_2	0	19.41	78.55	2.03	Yes
A321	63.28	15.09	0	21.61	Yes
C130	—	—	—	—	—

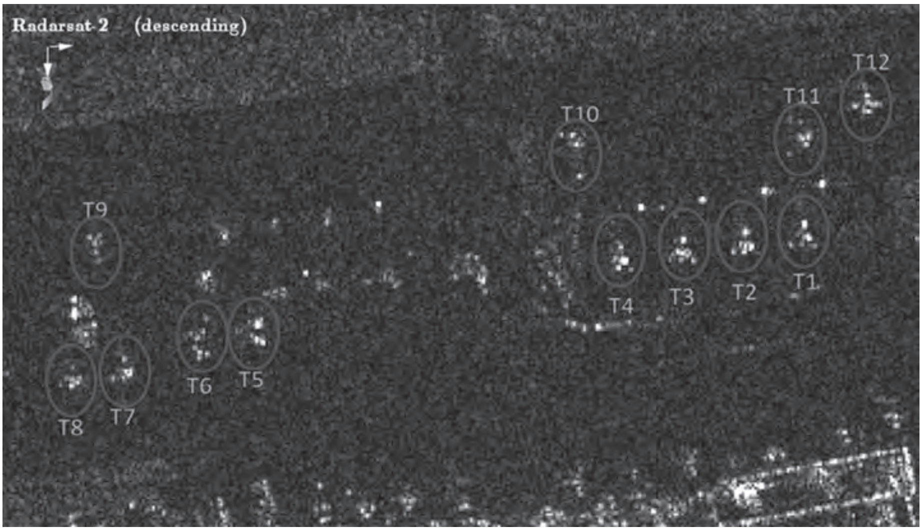

FIGURE 12.11 A Radarsat-2 image over an airfield. The identified targets are marked.

TABLE 12.6
Membership Matrix for Target Recognition on Raradsat-2 Image of Figure 12.11

	A321 (%)	B747-400 (%)	B757-200 (%)	MD80 (%)	Recognized	Truth
T1	19.25	0	22.88	57.86	MD80	MD80
T2	0.01	0	0	99.98	MD80	MD80
T3	14.99	0	11.59	73.40	MD80	MD80
T4	21.31	10.81	15.27	52.60	MD80	MD80
T5	0	3.09	95.10	1.79	B757-200	E190
T6	96.82	1.70	0	1.46	A321	B737-800
T7	0.13	0	0.17	99.69	MD80	MD80
T8	0.10	0.04	0	99.84	MD80	MD80
T9	63.28	15.09	0	21.61	A321	FOKKER-100
T10	6.48	2.26	0	91.24	MD80	MD80
T11	43.61	15.59	40.59	0	A321	DASH-8
T12						C130

while four types of target were wrongly recognized. This is mainly attributed to the lack of database. Again, the T12 target was not completely recognizable by the system for the same reason. Enhancement and updation of the target database are clearly essential.

12.5 CONCLUSIONS

In this chapter, we presented a full-blown satellite SAR image simulation scheme based on the GPU computation algorithm. The simulation steps included orbit state vector estimation, imaging scenario setting, target RCS computation, and clutter model, all specified by an SAR system specification. As an application example, target recognition has been successfully demonstrated using the simulated image database as training sets. Extended tests on both the simulated image and real images were conducted to validate the proposed algorithm. To this end, it is suggested that a more powerful target recognition scheme be explored for high-resolution SAR images. Extension to fully polarimetric SAR image simulation seems highly desirable as more such data are being available for much better target discrimination capability. In this aspect, further improvement on the computational efficiency by taking advantage of GPU power is critical.

REFERENCES

1. F. T. Ulaby, R. K. Moore, and A. K. Fung, *Microwave Remote Sensing: Active and Passive*, *Vol. 2*, *Radar Remote Sensing and Surface Scattering and Emission Theory*, Norwood, MA: Artech House, 1982.
2. A. W. Rihaczek and Steven J. Hershkowitz, *Radar Resolution and Complex-Image Analysis*, Norwood, MA: Artech House, 1996.
3. A. W. Rihaczek and Steven J. Hershkowitz, *Theory and Practice of Radar Target Identification*, Boston, MA: Artech House, 2000.
4. C. H. Chen, ed., *Information Processing for Remote Sensing*, Singapore: World Scientific Publishing Co., 2000.
5. J. C. Leachtenauer and R. G. Driggers, *Surveillance and Reconnaissance Systems: Modeling and Performance Prediction*, Boston, MA: Artech House, 2001.
6. C. Oliver and S. Quegan, *Understanding Synthetic Aperture Radar Images*, Raleigh, NC: SciTech Publishing, 2004.
7. J. R. Schott, *Remote Sensing: The Image Chain Approach*, Oxford, UK: Oxford University Press, 2007.
8. M. Skolnik, *Radar Handbook*, 3rd edition, New York, NY: McGraw-Hill, 2008.
9. J.-S. Lee and E. Pottier, *Polarimetric Radar Imaging: From Basics to Applications*, Boca Raton, FL: CRC Press, 2009.
10. G. Margarit, J.-J. Mallorqui, J. M. Rius, and J. Sanz-Marcos, On the usage of GRECOSAR, an orbital polarimetric SAR simulator of complex targets, to vessel classification studies, *IEEE Trans. Geosci. Remote Sens.*, 44, 3517–3526, 2006.
11. D. Lemoine Brunner, G. Bruzzone, and H. Greidanus, Building height retrieval from VHR SAR imagery based on an iterative simulation and matching technique, *IEEE Trans. Geosci. Remote Sens.*, 48, 1487–1504, 2010.
12. J. S. Lee, Digital image enhancement and noise filtering by use of local statistics, *IEEE Trans. Pattern Anal. Mach. Intell.*, 2, 165–168, 1980.
13. S. Musman, D. Kerr, and C. Bachmann, Automatic recognition of ISAR ship images, *IEEE Trans. Aerosp. Electron. Syst*., 32, 1392–1404, 1996.
14. M. Migliaccio, G. Ferrara, A. Gambardella, F. Nunziata, and A. Sorrentino, A physically consistent speckle model for marine SLC SAR images, *IEEE J. Ocean. Eng*., 32, 837, 2007.
15. G. Margarit, Mallorqui, J. J. Fortuny-Guasch, and C J. Lopez-Martinez, Phenomenological vessel scattering study based on simulated inverse SAR imagery, *IEEE Trans. Geosci. Remote Sens.*, 47, 1212–1223, 2009.
16. J. Wang and L. Sun, Study on ship target detection and recognition in SAR imagery, in *CISE '09 Proceedings of the 2009 First IEEE International Conference on Information Science and Engineering*, Nanjing, China, pp. 1456–1459, 2009.
17. B. Bhanu and G. Jones, Object recognition results using MSTAR synthetic aperture radar data, in *Proceedings of IEEE Workshop on Computer Vision Beyond the Visible Spectrum: Methods and Applications*, Hilton Head, South Carolina, pp. 55–62, 2000.
18. M. Nishimoto, X. Liao, and L. Carin., Target identification from multi-aspect high range-resolution radar signatures using a hidden Markov model, *IEICE Trans. Electron E Series C*, 87, 1706–1714, 2004.
19. M. Çetin and W. C. Karl, Feature-enhanced synthetic aperture radar image formation based on nonquadratic regularization, *IEEE Trans. Image Process.*, 10, 623–631, 2001.
20. M. Çetin, W. C. Karl, and A. S. Willsky, Feature-preserving regularization method for complex-valued inverse problems with application to coherent imaging, *Opt. Eng.*, 45, 017003-1 ~ 11, 2006.
21. C. Y. Chiang, K. S. Chen, C. T. Wang, and N. S. Chou, Feature enhancement of stripmap-mode SAR images based on an optimization scheme, *IEEE Geosci. Remote Sens. Lett.*, 6, 870–874, 2009.
22. Y. Tzeng, K. S. Chen, W. L. Kao, and A. K. Fung, A dynamic learning neural network for remote-sensing applications, *IEEE Trans. Geosci. Remote Sens.*, 32, 1096–1102, 1994.
23. K. S. Chen, Y. C. Tzeng, C. F. Chen, and W. L. Kao, Land-cover classification of multispectral imagery using a dynamic learning neural network, *Photogramm. Eng. Remote Sens*., 61, 403–408 1995.
24. K. S. Chen, W. L. Kao, and Y. C. Tzeng, Retrieval of surface parameters using dynamic learning neural network, *Int. J. Remote Sens.*, 16, 801–809, 1995.

25. K. S. Chen, W. P. Huang, D. W. Tsay, and F. Amar, Classification of multifrequency polarimetric SAR image using a dynamic learning neural network, *IEEE Trans. Geosci. Remote Sens.*, 34, 814–820, 1996.
26. Y. C. Tzeng and K. S. Chen, A fuzzy neural network to SAR image classification, *IEEE Trans. Geosci. Remote Sens.*, 36, 301–307, 1998.
27. I. Cumming and F. Wong, *Digital Signal Processing of Synthetic Aperture Radar Data: Algorithms and Implementation*, Boston, MA: Artech House, 2004.
28. J. C. Curlander and R. N. McDonough, *Synthetic Aperture Radar: Systems and Signal Processing*, New York, NY: Wiley-Interscience, 1991.
29. Ching-Chian Chen, Ya Cheng, and Ming Ouhyoung, Radar cross section analysis and visualization system, in *Proceedings of Computer Graphics Workshop 1995*, pp. 12–16, Taipei, Taiwan, 1995.
30. S. W. Lee, H. Ling, and R. Chou, Ray-tube integration in shooting and bouncing ray method, *Microw. Opt. Technol. Lett.*, 1, 286–289, 1988.
31. H. Lee, R. C. Chou, and S. W. Lee, Shooting and bouncing rays: Calculating the RCS of an arbitrarily shaped cavity, *IEEE Trans. Antennas Propag.*, 37, 194–205, 1989.
32. R. Bhalla and H. Ling, 3D scattering center extraction using the shooting and bouncing ray technique, *IEEE Trans. Antennas Propag.*, 44, 1445–1453, 1996.
33. S. K. Jeng, Near-field scattering by physical theory of diffraction and shooting and bouncing rays, *IEEE Trans. Antennas Propag.*, 46, 551–558, 1998.
34. S. H. Chen and S. K. Jeng, An SBR/image approach for indoor radio propagation in a corridor, *Trans. IEICE Electron.*, E78-C(8), 1058–1062, 1995.
35. J. S. Lee, Refined filtering of image noise using local statistics, *Comput. Vis. Graph. Image Process.*, 15, 380–389, 1981.
36. J. S. Lee, M. R. Grunes, and R. Kwok, Classification of multi-look polarimetric SAR imagery based on complex Wishart distribution, *Int. J. Remote Sens.*, 15, 2299–2311, 1994.
37. J. S. Lee, P. Dewaele, P. Wambacq, A. Oosterlinck, and I. Jurkevich, Speckle filtering of synthetic aperture radar images: A review, *Remote Sens. Rev.*, 8, 313–340, 1994.
38. J. I. Marcum, A statistical theory of target detection by pulsed radar, *IEEE Trans. Inf. Theory*, IT-6, 59–267, 1960.
39. G. V. Trunk and S. F. George, Detection of targets in non-Gaussian clutter, *IEEE Trans. Aerosp. Electron Syst.*, AES-6, 620–628, 1970.
40. D. C. Schleher, Radar detection in Weibull clutter, *IEEE Trans. Aerosp. Electron. Syst*., 12, 136–143, 1976.
41. Boothe, R. R., The Weibull distribution applied to the ground clutter backscattering coefficient, in Schleher, D. C., ed. *Automatic Detection and Radar-Data Processing*, pp. 435–450, Artech House, 1980.
42. A. K. Fung, *Microwave Scattering and Emission Models and Their Applications*, Artech House, 1994.
43. K. S. Chen and A. K. Fung, Frequency dependence of signal statistics from vegetation components, *IEEE Proc. Radar Sonar Navig.*, 142(6), 301–305, 1996.
44. O. Montenbruck and E. Gill, *Satellite Orbits: Models, Methods, and Applications*, Berlin, Germany: Springer-Verlag, 2000.
45. D. A. Vallado and W. D. McClain, *Fundamentals of Astrodynamics and Applications*, 3rd edition, Hawthorne, CA: Microcosm Press/Springer, 2007.
46. M. F. Henry, NORAD SGP4/SDP4 Implementations, Available at http://www.zeptomoby.com/satellites/.
47. D. Vallado, P. Crawford, R. Hujsak, and T. S. Kelso, Revisiting spacetrack report# 3, AIAA, vol. 6753, pp. 1–88, 2006.
48. N. Z. Miura, Comparison and design of simplified general perturbation models, California Polytechnic State University, San Luis Obispo 2009. Earth Orientation Centre. Available at http://hpiers.obspm.fr/eop-pc/.
49. C. Cafforio, C. Prati, and F. Rocca, SAR data focusing using seismic migration techniques, *IEEE Trans. Aerosp. Electron. Syst.*, 27, 194–207, 1991.
50. A. Moreira, J. Mittermayer, and R. Scheiber, Extended chirp scaling algorithm for air- and spaceborne SAR data processing in stripmap and scanSAR imaging modes, *IEEE Trans. Geosci. Remote Sens.*, 34, 1123–1136, 1996.
51. F.-K. Li, D. N. Held, J. C. Curlander, and C. Wu, Doppler parameter estimation for spaceborne synthetic-aperture radars, *IEEE Trans. Geosci. Remote Sens.*, GE-23, 47–56, 1985.
52. M. Lambers, A. Kolb, H. Nies, and M. Kalkuhl, GPU-based framework for interactive visualization of SAR data, in *Proceedings of IEEE Geoscience and Remote Sensing Symposium (IGARSS)*, Barcelona, Spain, pp. 4076–4079, July 2007.

53. T. Balz and U. Stilla, Hybrid GPU based single- and double-bounce SAR simulation, *IEEE Trans. Geosci. Remote Sens.*, 47, 3519–3529, 2009.
54. NVIDIA CUDA Compute unified device architecture programming guide 1.1. Internet draft, NVIDIA Corporation, 2008.
55. J. Sanders and E. Kandrot, *CUDA by Example: An Introduction to General-Purpose GPU Programming*, Reading, MA: Addison-Wesley, 2010.
56. G. Strang, *Introduction to Applied Mathematics*, Cambridge, MA: Wellesley-Cambridge Press, 1986.
57. D. Bini, *Toeplitz Matrices, Algorithms and Applications*, ECRIM News Online Edition, No. 22, July 1995.
58. A. B. Mandelbrolt and J. W. Van Ness, Fractional Brownian motion, fractional noises and applications, *IEEE Trans. Med. Imag.* 10, 422–437, 1968.
59. E. Ott, *Chaos in Dynamical Systems*, Cambridge, UK: Cambridge University Press, 1993.
60. R. C. Hilborn, *Chaos and Nonlinear Dynamics*, Oxford, UK: Oxford University Press, 1994.
61. H. Leung and T. Lo, A spatial temporal dynamical model for multipath scattering from the sea, *IEEE Trans. Geosci. Remote Sens.* 33, 441–448, 1995.
62. H. Leung, N. Dubash, and N. Xie, Detection of small objects in clutter using a GA-RBF neural network, *IEEE Trans. Aerosp. Electron. Syst.* 38, 98–117, 2002.
63. H. D. I. Abarbanal, *Analysis of Observed Chaotic Data*, Berlin, Germany: Spring-Verlag, 1996.
64. Y. C. Tzeng and K. S. Chen, Change detection in synthetic aperture radar images using a spatially chaotic model, *Opt. Eng.* 46, 086202, 2007.
65. N. S. Chou, Y. C. Tzeng, K. S. Chen, C. T. Wang, and K. C. Fan, On the application of a spatial chaotic model for detecting landcover changes in synthetic aperture radar images, *J. Appl. Remote Sens.*, 3, 033512, 1–16, 2009.
66. S. G. Mallat, A theory for multiresolution signal decomposition: The wavelet representation, *IEEE Trans. Pattern Anal. Mach. Intell.* 11, 674–693, 1989.
67. S. Mallat, *A Wavelet Tour of Signal Processing*, 2nd edition, New York, NY: Academic Press, 1999.
68. R. Brown and P. Hwang, *Introduction to Random Signal Analysis and Kalman Filtering*, New York, NY: Wiley, 1983.

6 Tropical Cyclone Activities

Asia-Pacific Region

Lindsey M. Harriman

CONTENTS

6.1 INTRODUCTION

The Asia-Pacific region is known to experience many tropical cyclones during the summer and autumn months with two primary basins of tropical cyclone origin and activity: the western North Pacific Ocean (WNP) and the North Indian Ocean (NIO). Subregions of these basins in which there is also frequent tropical cyclone activity include the South China Sea and the Bay of Bengal. The WNP basin experiences more tropical cyclones, or typhoons as they are known in this region, per year than any other region worldwide, affecting island nations such as the Philippines and vulnerable coastlines of Vietnam. Tropical cyclones in the NIO affect countries such as India when a tropical cyclone forms over the Bay of Bengal. This chapter explains the characteristics of tropical cyclones, the impacts these systems can have on humans and the environment and provides insight on the recent trends of activity in the Asia-Pacific region with primary focus on the WNP and NIO basins. Two of the most intense storms in history, Very Severe Cyclonic Storm Phailin and Super Typhoon Haiyan, both of which struck land in 2013, are profiled.

6.2 CYCLONES AND TYPHOONS

6.2.1 What Is a Cyclone or Typhoon?

The terms cyclones and typhoons, and even the term hurricanes, all refer to the same general natural phenomenon: a tropical cyclone. A tropical cyclone is an organized, rotating storm system that forms over tropical or sub-tropical waters (National Hurricane Center, n.d.(a)). Tropical cyclones are warm-core, non-frontal, low-pressure systems that pull their energy from the ocean surface, as opposed to being a cold-core system that forms along fronts in higher latitudes (Hobgood, 2005). The vernacular distinction between a cyclone, typhoon and hurricane lies in regional application and severity of the storm, the latter being based upon sustained wind speed. Over the Atlantic, these storms are referred to as hurricanes, in the WNP, they are typhoons, and in the NIO they are referred to as cyclones (National Hurricane Center, n.d.(a)). In its weakest form, a tropical cyclone is termed a 'tropical depression', and is distinguished by sustained winds of less than 60 kilometres per hour (km/h) (34 knots). When winds surpass 60 km/h, the disturbance is then referred to as a tropical storm in the WNP and a cyclonic storm in the NIO. Continued increases in wind speed define the severity of the storm and regional vernacular influences what the storm is called (Table 6.1).

Cyclogenesis is the term used to describe the process of cyclone formation from an existing disturbance. The existing disturbance needs to be over warm ocean surface temperatures (≥ 26°C) with enough moisture above the surface, and unstable atmospheric conditions so that the storm can intensify, ultimately becoming a tropical cyclone (Hobgood, 2005). A tropical cyclone is composed of three main parts: the eye, the eyewall and rain bands (National Weather Service, n.d.(a)). A well-formed eye is distinct in the centre of the storm (Figure 6.1) and is usually an area of weak horizontal temperature and pressure gradients, which strongly contrast with the high-speed winds and thick clouds that surround it (Jordan, 1961). A well-defined eye is indicative of a very strong storm – a Category 4 or 5 hurricane or a super typhoon. Another indicator of the storm's intensity is when there are changes to the structure of the eye and eyewall, which can lead to changes in wind speed (National Weather Service, n.d.(a)). The eyewall is made up of a ring of tall

TABLE 6.1
Tropical Cyclone Classifications

	Maximum Sustained Winds	
Basin	119–220 km/h (64–119 knots)	≥220 km/h (≥119 knots)
WNP	Typhoon	Super typhoon[a]
NIO	Very severe cyclonic storm	Super cyclonic storm

Source: National Weather Service (n.d.(b)). Tropical Cyclone Classification. http://www.srh.noaa.gov/jetstream/tropics/tc_classification.htm (accessed 28 March, 2017).

[a] When winds reach ≥ 241 km/h.

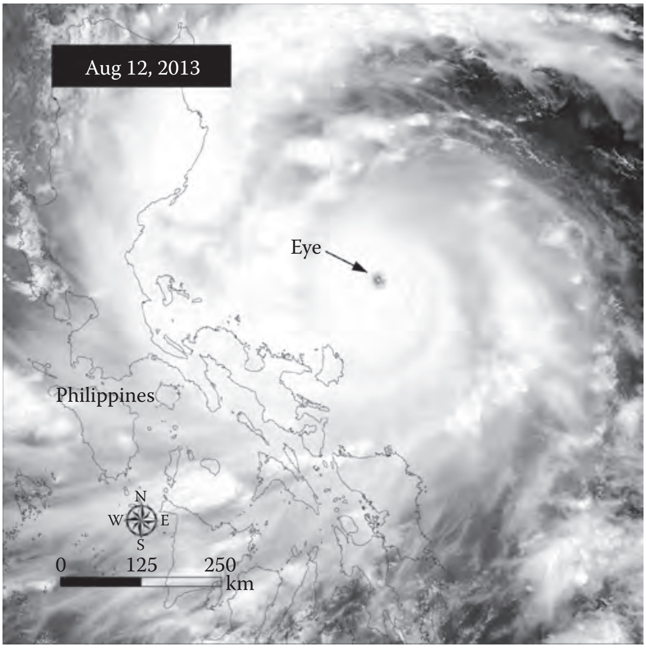

FIGURE 6.1 In this satellite image of Super Typhoon Utor captured by Terra Moderate Resolution Imaging Spectroradiometer (MODIS) on August 12, 2013, the eye of the storm is clearly visible. (From NASA Earth Observatory, http://earthobservatory.nasa.gov/NaturalHazards/view.php?id=81837, accessed January 31, 2014.)

thunderstorms and usually this is where the strongest winds can be found. The rain bands extend out from the eyewall, bending in a spiral manner (Barcikowska et al., 2013). The tropical cyclone itself can extend for hundreds of kilometres, typically around 480 km, but size is not necessarily an indicator of intensity (National Weather Service, n.d.(b)).

The warm sea surface temperatures of the Asia-Pacific region, such as in the Bay of Bengal in the NIO basin and the South China Sea of the WNP basin, are common areas for cyclogenesis and tropical cyclone activity. In the WNP, cyclogenesis primarily occurs between latitudes 10° and 30°N and longitudes 120° and 150°E (Barcikowska et al., 2013) (Figure 6.2). Tropical cyclones cannot form within 500 km of the equator (Hobgood, 2005). It is very possible for a tropical cyclone to form in the WNP, but migrate westward toward the NIO basin, like Very Severe Cyclonic Storm Phailin did in October 2013 (CWD-IMD, 2013).

As a cyclone leaves these warmer latitudes and areas of converging winds, the storm typically loses strength. For example, Super Typhoon Guchol began as a disturbance off the southeast coast of Guam in June 2012 and rapidly intensified to a super typhoon when it moved north of 10°N latitude. When it surpassed 30°N latitude, cooler sea surface temperatures, among other factors, weakened the typhoon before it made landfall in Japan (Evans and Falvey, 2012).

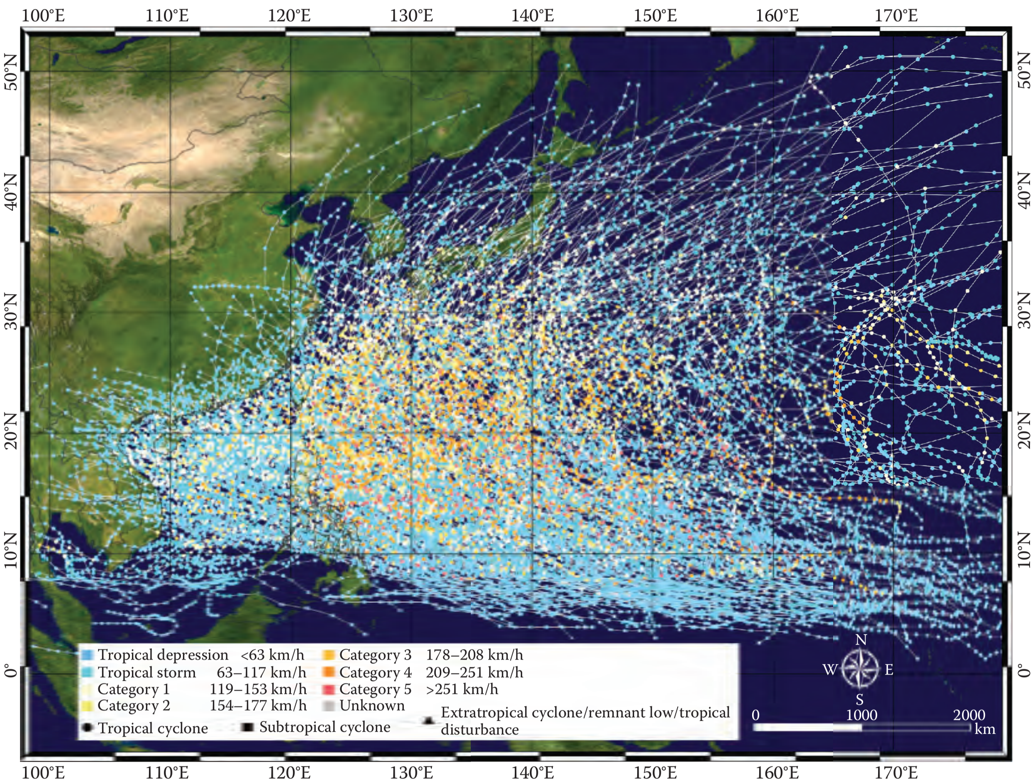

FIGURE 6.2 A map of tropical cyclone tracks, in 6-hour intervals, over the northwest Pacific Ocean from 1980 to 2005 based on data from the Joint Typhoon Warning Center and laid over a Terra MODIS image from the National Aeronautics and Space Administration (NASA). (http://en.wikipedia.org/wiki/File:Pacific_typhoon_tracks_1980-2005.jpg via Wikimedia Commons.)

6.3 METEOROLOGICAL INFLUENCES ON TROPICAL CYCLONES

Meteorological patterns such as the Asia–Pacific Oscillation (APO) and the El Niño–Southern Oscillation (ENSO) can have an impact on tropical cyclone formation and intensity in the Asia–Pacific region. A strong APO is indicated by warmer upper-tropospheric eddy air temperatures over Asia and cooler temperatures over the North Pacific. According to Zhou et al. (2008), tropical cyclone frequency tends to increase if the APO is stronger than normal in the summer, and decreases in response to a weaker APO than normal. For example, prior to 1975, the APO was stronger than normal and after 1975, the APO weakened. Following this trend, the frequency of tropical cyclones in the WNP was higher before the mid-1970s when compared to later in the decade (Zhou et al., 2008).

The terms El Niño and La Niña refer to phenomena surrounding the equatorial Pacific, where years with sea surface temperatures warmer than normal are considered to be El Niño years and, alternatively, when sea surface temperatures are cooler than normal, are considered to be La Niña years (Philander, 1985). On average, an El Niño period can last 12 to 18 months at a time and occur every 3 or 4 years. ENSO refers to the influence of the Southern Oscillation (SO), which induces variability in tropical sea level pressure between the eastern and Western Hemispheres. In El Niño years, this influence typically results in high pressures in the western tropical Pacific and Indian Ocean basins and lower pressures in the southeast tropical Pacific Ocean (Pacific Marine Environmental Laboratory, n.d.). Studies have found that in El Niño years, the average tropical storm and typhoon genesis region has a southward displacement in the WNP (Carmargo and Sobel, 2005) and other studies have found that the frequency of tropical cyclones with varying intensity (such as typhoons and super typhoons) changes based on influences from El Niño or La Niña (Li and Zhou, 2012).

Li and Zhou (2012) use upper-ocean heat content as a proxy for ENSO, to determine the influences on three different types of tropical cyclone frequency: (1) tropical storms and depressions, (2) typhoons and (3) super typhoons. They conclude that the changes incurred in upper ocean heat content vary according to the phase of the ENSO cycle. For example, the frequency of super typhoons increases during the mature phase of El Niño and the frequency of typhoons increases when La Niña transitions to El Niño.

6.4 IMPACTS

No matter the basin of origin, tropical cyclones are known for heavy rainfall, high winds and ensuing floods when and if they hit land (Nguyen-Thi et al., 2012). The World Meteorological Organization (WMO) has established a network of Regional Specialized Meteorological Centres (RSMCs), specifically dedicated to understanding and managing the impacts of tropical cyclones (Obasi, 1974). Of these, the RSMC located in Tokyo, Japan, has the regional responsibility for monitoring tropical cyclones and providing forecasts and warnings in the WNP and the South China Sea, and the RSMC in New Delhi, India, is responsible for the NIO, which includes the Bay of Bengal (WMO, n.d.(b); Tyagi et al., 2010). The Saffir–Simpson hurricane

TABLE 6.2

Saffir–Simpson Hurricane Wind Scale Categories and Potential Damage That Could Occur Because of Winds

Category	Sustained Winds	Types of Damage due to Winds
1	119–153 km/h (64–82 knots)	Well-constructed frame homes could have damage to roof, shingles, vinyl siding and gutters. Large branches of trees will snap, and shallowly rooted trees may be toppled. Extensive damage to power lines and poles likely will result in power outages that could last a few to several days.
2	154–177 km/h (83–95 knots)	Well-constructed frame homes could sustain major roof and siding damage. Many shallowly rooted trees will be snapped or uprooted and block numerous roads. Near-total power loss is expected with outages that could last from several days to weeks.
3	178–208 km/h (96–112 knots)	Well-built framed homes may incur major damage or removal of roof decking and gable ends. Many trees will be snapped or uprooted, blocking numerous roads. Electricity and water will be unavailable for several days to weeks after the storm passes.
4	209–251 km/h (113–136 knots)	Well-built framed homes can sustain severe damage with loss of most of the roof structure and/or some exterior walls. Most trees will be snapped or uprooted and power poles downed. Fallen trees and power poles will isolate residential areas. Power outages will last weeks to possibly months. Most of the area will be uninhabitable for weeks or months.
5	>252 km/h (> 137 knots)	A high percentage of framed homes will be destroyed, with total roof failure and wall collapse. Fallen trees and power poles will isolate residential areas. Power outages will last for weeks to possibly months. Most of the area will be uninhabitable for weeks or months.

Source: Adapted from National Hurricane Center (n.d,(b)). Saffir–Simpson Hurricane Wind Scale. http://www.nhc.noaa.gov/aboutsshws.php (accessed 28 March, 2017).

wind scale (Table 6.2) breaks storms down into categories based upon wind speed and the estimated property damage they could cause (Schott et al., 2012; National Hurricane Center, n.d.(b)).

According to the Emergency Events Database (EM-DAT) and the Centre for Research on the Epidemiology of Disasters (CRED) International Disaster Database, both based in Belgium (www.cred.be), and the U.S. Office of Foreign Disaster Assistance (OFDA), some of the deadliest storms that have occurred worldwide since 1900 have all been of tropical cyclone origin and have occurred in the Asia-Pacific region (Table 6.3). The Asia-Pacific region is vulnerable to some of the most severe impacts because of the extent of coastline, the number of island nations present and the heavily populated coastal areas. The mere infrastructure of many communities, such as buildings made of clay or mud, unpaved roads and weak power and water networks can exacerbate any immediate effects of a tropical cyclone (Dube et al.,

TABLE 6.3
Top 10 Most Important Tropical Cyclones for 1900–2014, Based on Fatalities

Country	Date (mm/dd/yyyy)	Number of Fatalities
Bangladesh	11/12/1970	300,000
Bangladesh	4/29/1991	138,866
Myanmar	5/2/2008	138,366
China	7/27/1922	100,000
Bangladesh	10/1942	61,000
India	1935	60,000
China	8/1912	50,000
India	10/14/1942	40,000
Bangladesh	5/11/1965	36,000
Bangladesh	5/28/1963	22,000

Source: International Disaster Database EM-DAT: The Emergency Events Database – Université Catholique de Louvain (UCL) – CRED, D. Guha-Sapir - www.emdat.be, Brussels, Belgium.

2006; UN-ESCAP and UNISDR, 2012), especially in rural areas (Peduzzi et al., 2012). Furthermore, the prevalence of poverty can be an inhibiting factor to financing for both preparedness and hazard mitigation and this creates economic vulnerability (UN-ESCAP and UNISDR, 2012).

The total population of the Asia-Pacific region increased from 2.2 billion in 1970 to 4.2 billion in 2010 and during this time, the number of people living in cyclone-prone areas increased approximately 68% from 71.8 million to 120.7 million (UN-ESCAP and UNISDR, 2012). Some impacts of tropical cyclones can include flooding, erosion and destruction of dykes and sand dunes, harm to crops and saltwater intrusion of agricultural land (Nguyen et al., 2012). Coastal populations are especially vulnerable as they bear the brunt of the initial landfall of a tropical cyclone. Tropical cyclones can have direct impact on daily activities such as fishing, transportation and tourism (Kotal et al., 2014) in addition to destroying homes, roads and utility infrastructures. These impacts can lead to lasting damage on the environment, economies and livelihoods; it is estimated that more than 85% of global economic exposure to tropical cyclones occurs in the Asia-Pacific region (UN-ESCAP and UNISDR, 2012). Future forecasting of tropical cyclone activity in response to climate change could be of practical value (Stowasser et al., 2006) and help to contribute to already improving forecasting abilities of current tropical cyclone events (WMO, 2014).

Storm surge, especially for island nations or nations with exposed and heavily developed coastlines, is a considerable concern when anticipating a tropical cyclone. The magnitude of storm surge depends on factors such as speed, angle of approach toward the coast, size and spread of the tropical cyclone. Geomorphology of the land, including positioning and structure of bays and estuaries, near-shore bathymetry and width and slope of the continental shelf can also be determining factors for magnitude of storm surge (Lin et al., 2013). In many cases, natural barriers such as wetlands and mangroves can help to mitigate some impacts of storm surge, breaking the waves and absorbing much of the rush of water (McIvor et al., 2012).

The strong winds of a tropical cyclone can stir up nutrients in the ocean and when these nutrients reach the surface and become exposed to sunlight, a massive phytoplankton bloom can result (Lin et al., 2003). Phytoplankton are tiny marine plants that contain chlorophyll, requiring sunlight for survival, much like plants on land (National Ocean Service, 2014). The size, speed of movement and preconditions determining where cold, nutrient-rich water lies are also factors in whether a plankton bloom can be induced by a tropical cyclone (Lin, 2012). For example, in the WNP basin, slow moving, large-diameter tropical cyclones with intense winds moving over cooler waters can cause a plankton bloom to occur (Lin, 2012). In other cases, such as in 1999 over what is now the state of Odisha in India, intense rains from a super cyclone caused rivers and streams to flood, dumping a considerable amount of nutrients into the ocean, resulting in a plankton bloom (Kundu et al., 2001). Plankton blooms can remove greenhouse gases from the atmosphere and provide an ample feeding ground for fish and other marine life (National Ocean Service, 2014). However, very thick blooms can also act as a barrier to sunlight, which is necessary to most marine life below the ocean's surface. Fish mortality and negative impacts to human health, among other issues, can result from excessive plankton blooms.

In 2000, off the coast of Taiwan, Japan and the Philippines, a major plankton bloom occurred when Cyclone Kai-Tak stirred up nutrients from below the surface of the South China Sea; the plankton accounted for 2–4% of the total new phytoplankton production in the South China Sea that year (Lin et al., 2003). Plankton blooms can have long-lasting residual effects such as the two plankton blooms that lingered for about 2 weeks following two of the eleven typhoons the WNP experienced in 2003 (Lin, 2012).

There is also evidence of the influence of cyclones on dissolved oxygen (DO) levels of the open oceans and estuaries. DO levels were measured by Lin et al., (2014) after the passage of Super Typhoon Nanmadol over the western Pacific Ocean and the South China Sea in August 2011. They found that DO concentrations increased between the surface and 40-metre (m) depth, an indication that oxygen from the air was entrained after the typhoon passed. The maximum DO concentration was found at 5–50 m higher than the average summer DO depth in the South China Sea – providing further evidence that the strong typhoon winds affected DO concentrations by uplifting the maximum level. An increase of chlorophyll levels was also observed during this study. Estuaries are vulnerable to intrusion of ocean water due to high winds, altering the chemical composition of the water and harming coastal resources. Mitra et al., (2011) monitored conditions of the Hooghly–Matla estuarine system after Severe Cyclonic Storm Aila passed over the Bay of Bengal in May 2009. They observed an intrusion of saline water into the estuarine system from the Bay of Bengal, which resulted in an increase of salinity levels in surface water. Increased salinity levels can lead to harmful algae blooms, which can also lead to fish kills.

6.5 RECENT TRENDS OF TROPICAL CYCLONE ACTIVITY

6.5.1 Tropical Cyclone Activity in the WNP Basin

As previously stated, the WNP is one of the primary basins of tropical cyclone development and experiences the most tropical cyclone activity in the world (D'Asaro et al., 2011; Lin, 2012; Barcikowska et al., 2013). Tropical cyclones in the WNP most frequently form between July and October and although tropical cyclones can form over the southern Indian Ocean and the southwestern Pacific Ocean at any time, most tropical cyclones form in the summer months (Hobgood, 2005). Over the central North Pacific Ocean, the average number of tropical cyclone occurrence is low, only 6 per year, but the inter-annual variability is much higher, with some years experiencing upward of 10 tropical cyclones (Clark and Chu, 2002).

Trends in changes of frequency and intensity of tropical cyclone activity in the WNP have been ambiguous over the past three decades (Barcikowska et al., 2013). A review of literature in Liu and Chan (2012) indicates a decrease in tropical cyclone activity between 1998 and 2011 in the WNP based upon reports of tropical cyclone occurrence of at least a tropical storm intensity (where winds are greater than or equal to 60 km/h) from the Joint Typhoon Warning Center (JTWC). Cycles of active and inactive years are typical, with a normal year consisting of between 25 and 29 tropical cyclones (Liu and Chan, 2012). The inactive period of 1998 to 2011 had an average of 23.2 tropical cyclones per year, making it the lowest average of noted cycle periods since 1960 (active periods = 1960–1974; 1989–1997; inactive periods = 1975–1988, 1998–2011) and two of the years, 1998 (UN-ESCAP and UNISDR, 2012) and 2010 (WMO, n.d.(b)), had the least number of tropical cyclones since 1960 (Liu and Chan, 2012). Liu and Chan (2012) attribute the decrease in observed tropical cyclone activity to a decrease in instances of formation in the southeastern WNP (0°N–20°N, 140°E–180°E) and an overall northward shift in formation between longitudes 120°E and 160°E.

In 2012, the JTWC issued warnings on 27 tropical cyclones in the WNP basin, four of which intensified to super typhoons (Evans and Falvey, 2012). The number of total tropical cyclone occurrences for 2012 was below the long-term average of 31 (Evans and Falvey, 2012), but can be considered within the normal range of occurrences (Liu and Chan, 2012). However, the Philippines experienced its second deadliest typhoon in history when Super Typhoon Bopha struck the island of Mindanao on December 3, 2012, and then continued onto central Visayas and Palawan the next day, leaving a total of 1901 people dead (Masters, 2013). Super Typhoon Bopha exhibited maximum wind speeds of 278 km/h and sustained winds of at least 213 km/h when it first made landfall in the Philippines (Evans and Falvey, 2012).

For the WNP basin, 2013 was the most active tropical cyclone season since 2004 (WMO, 2014), with the area experiencing not only more tropical cyclones than average, but also the most intense tropical cyclone in history, Super Typhoon Haiyan. Super Typhoon Haiyan brought 315 km/h winds to the Philippines, resulting in over 6000 deaths and impacting 16 million people (NDRRMC, 2014; NOAA National Centres for Environmental Information, 2014); the storm also had residual effects on southern China and Vietnam. The following year, the World Meteorological

Organization (WMO) reported 31 storms in the WNP, which was also well above the average of 26, with 13 of these storms intensifying to typhoon strength (WMO, 2014).

6.5.1.1 Philippines, Vietnam and South China: Super Typhoon Haiyan in 2013

On average, the Philippines experience 20 tropical cyclones that form or pass through the area surrounding the country each year (PAGASA, 2011). Super Typhoon Haiyan (or 'Yolanda' as it is better known in the Philippines) is the most powerful storm to ever hit land worldwide, based upon sustained wind speed (WMO, 2014). The first signs of Haiyan were thunderstorms that occurred in Micronesia on November 4, 2013, and warnings of intensification were issued throughout November 5, with indications that the storm would transform from a tropical storm to a typhoon headed for the Philippines by November 8 (NASA, 2013). Maximum sustained winds prior to reaching the Philippines were recorded at almost 315 km/h, classifying Haiyan as a super typhoon. Winds slightly subsided to 269 km/h when the storm first made landfall (NASA, 2013). Haiyan initially made landfall early on November 8 in the Philippines, not once, but six times by the end of the day and at super typhoon strength (NDRRMC, 2014). The dense populations of low-lying Tacloban City saw storm surges of up to 7.5 m, swallowing the city as most of it lies below 5 m (NASA, 2013). The island of Leyte received as much as 685 mm of rain over the course of the storm (NASA, 2013). Haiyan continued past the islands of the Philippines, weakening as it approached the West Philippine Sea. The system left the Philippines Area of Responsibility in the afternoon of November 9 (NDRRMC, 2014) and continued toward Vietnam (Figure 6.3).

Haiyan made landfall over Vietnam in the early morning hours of November 11, gusts of wind up to 157 km/h near Ha Long Bay (BBC, 2013). Although the storm had been downgraded to a tropical depression by this time (Haeseler and Lefebvre, 2013), Haiyan was still the most severe storm many coastal cities of Vietnam had experienced in years, causing power outages, uprooting large trees and destroying roofs (ABC, 2013). Storm surge estimates were placed at 3–5 m and measurements of up to 100 mm of rain in 24 hours were reported (WMO, n.d.(a)). As Haiyan progressed inland, it changed course and headed toward China with winds exceeding 70 km/h; the system finally weakened to a tropical storm by November 11 (WMO, n.d.(a)).

The Philippines National Disaster Risk Reduction and Management Council (NDRRMC) recorded a total cost of damages in the Philippines at more than US$840 million (PhP36.7 billion) with upward of 1.1 million homes damaged. Although the super typhoon resulted in more than 6000 deaths, more than 4 million people were able to be sheltered in evacuation centres (NDRRMC, 2014).

6.5.2 Tropical Cyclone Activity in the North Indian Ocean Basin

In the North Indian Ocean (NIO) basin in 2012, the JTWC recorded four tropical cyclones, with two having formed in the Persian Sea and two in the Bay of Bengal, and none of which had peak winds that exceeded 93 km/h (CWD-IMD, 2013). Only two of

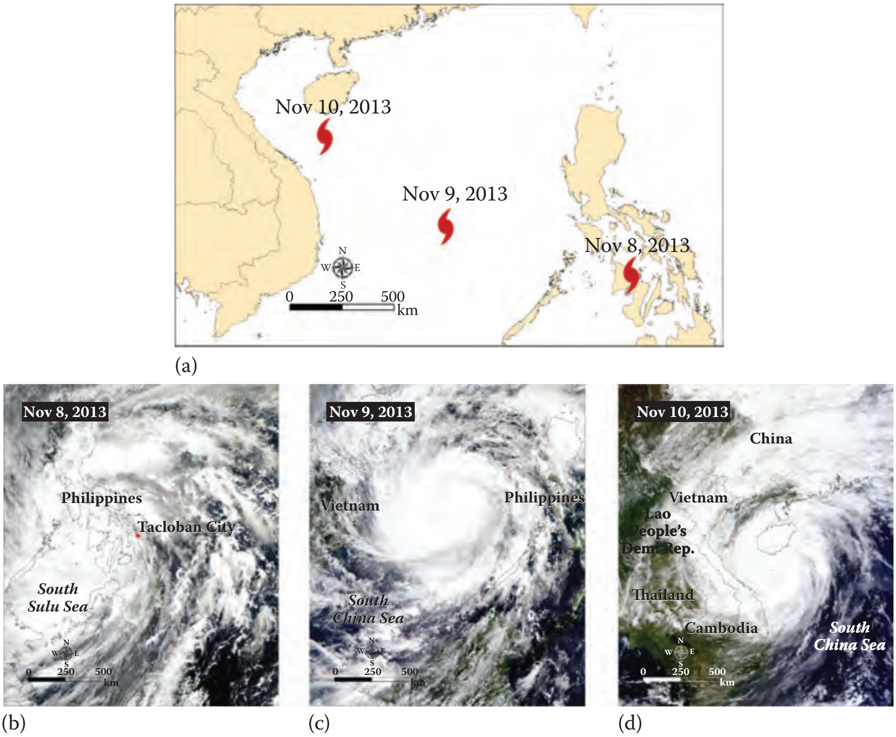

FIGURE 6.3 Path of Super Typhoon Haiyan. (a) Map of the relative location of the eye of the storm as it corresponds with the MODIS images in b, c, d. (b) Aqua MODIS image from November 8, 2013, of Super Typhoon Haiyan as it made landfall over the Philippines. (c) Aqua MODIS image from November 9, 2013, as Typhoon Haiyan passed over the Philippines, weakening slightly and continuing over the South China Sea toward Vietnam. (d) Terra MODIS image from November 10, 2013, as the eye of the typhoon approached Vietnam and southern China. (MODIS imagery retrieved from NASA EOSDIS Worldview, https://worldview.earthdata.nasa.gov/.)

these cyclonic storms made landfall; this number was three tropical cyclones below the normal range of occurrences in the NIO (Kotal et al., 2014).

The NIO experienced five tropical cyclones with an intensity of a tropical storm or greater in 2013, and three of the five storms were categorized as very severe cyclonic storms; no super cyclones were reported (Kotal et al., 2014). The most significant of these, Very Severe Cyclonic Storm (VSCS) Phailin, is profiled in detail below.

6.5.2.1 Bay of Bengal, North Indian Ocean: Very Severe Cyclonic Storm Phailin in 2013

VSCS Phailin was the worst storm to strike India since October 1999, when a super cyclone over Orissa (now Odisha) had left more than 10,000 people dead and caused US$2.5 billion in damage (Kalsi, 2006). When VSCS Phailin intensified to similar strength of this super cyclone, worries spread that it might have the same impact. However, the 1999 super cyclone had reaffirmed the value of knowing what effects a tropical cyclone can have on inland areas as well as at the coast, as it had maintained its intensity as a cyclonic storm for 30 hours after reaching land (Kotal et al., 2014); and it also reaffirmed the need for early warning and forecasting to prevent such losses in the future, a lesson that was heeded during preparations for VSCS Phailin (Mühr, 2013; Ghosh, 2014; WMO, 2014).

According to a comprehensive report from the Cyclone Warning Division of the India Meteorological Division (CWD-IMD, 2013), VSCS Phailin formed from remnants of a cyclonic circulation over the South China Sea on 6 October 2013. The system intensified over the North Andaman Sea, becoming a depression by 8 October and a cyclonic storm by the evening of 9 October. Continuing to progress northwestward over the Bay of Bengal, Phailin evolved into a very severe cyclonic storm less than 24 hours later by the afternoon of 10 October. VSCS Phailin made landfall on 12 October, first passing over the Indian states of Odisha (Ganjam and Puri Districts) and then Andhra Pradesh with maximum sustained winds of 210 km/h and gusts up to 220 km/h (CWD-IMD, 2013; Mühr et al., 2013).

Due to early warnings, approximately 1 million people from Puri and Ganjam Districts were able to evacuate to safe shelters within 3 days before VSCS Phailin made landfall (ADB et al., 2013). After the storm passed, 21 deaths were attributed to the cyclone and 17 caused by flooding were recorded (CWD-IMD, 2013).

Regardless, extensive damage was caused to agricultural land, resulting in a 50% loss to nearly 1.3 million hectares of crops due to impacts from the storm. Approximately 90,000 homes in Ganjam District were damaged to some extent, if not lost completely. The estimated cost of reconstruction for all sectors including infrastructure, housing and agriculture and others, totalled US$1.45 billion (ADB et al., 2013).

The fragile coastline also sustained damage because of VSCS Phailin. The coastal Chilika Lake flooded and experienced sedimentation (Figure 6.4) (Hindustan Times, 2013). Excessive winds that accompanied VSCS Phailin wreaked havoc on the mangroves around the lake, which serve as a coastal barrier, protecting against erosion and minimizing intrusion of saltwater from the Bay of Bengal (Hindustan Times, 2013). Impacts from VSCS Phailin also affected wildlife in the area. Chilika Lake is a favoured location for many species of migratory birds and the aftermath of VSCS Phailin has inhibited the return of some of these migratory birds. In November 2013, the Bombay Natural History Society (BNHS) reported that it would begin a study on the impact of VSCS Phailin on the migratory bird populations and migration patterns (ENVIS Centre, 2013). In early 2014, approximately 158,000 fewer birds than normal were observed as reported by local ornithologists, experts and organizations such as the BNHS, possibly because the storm had removed much of the vegetation that the birds tend to feed on (Zee News, 2014).

6.6 FUTURE OUTLOOK

Several studies have investigated the potential future impact of various climate change implications on storm surge, tropical cyclone frequency and tropical cyclone intensity in the Asia-Pacific region (Chan and Liu, 2004; Stowasser et al., 2006; Mase et al., 2013). Some studies assessing the impacts of warming climate scenarios indicate that the intensity and frequency of storms could increase in parts of the

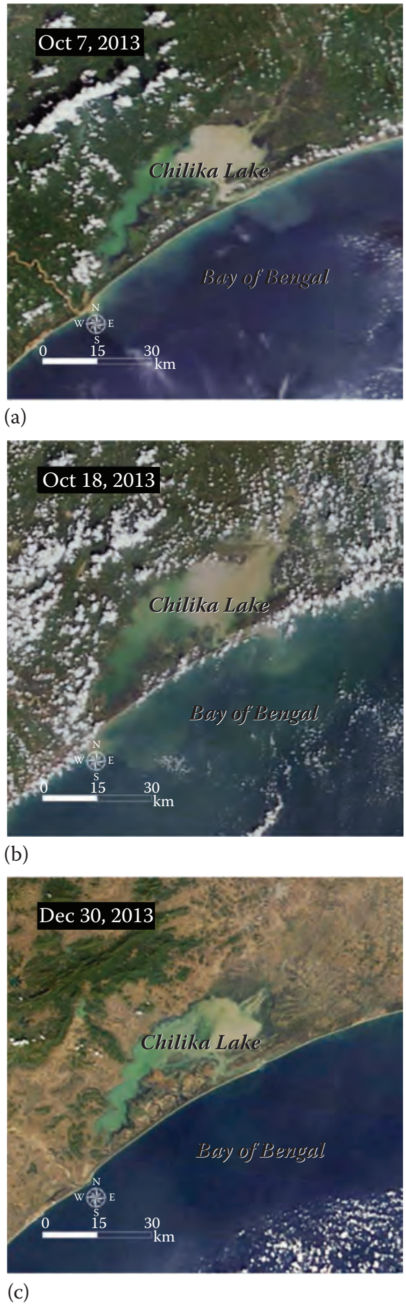

FIGURE 6.4 Status of Chilika Lake and the coastline (a) on October 7, 2013, before VSCS Phailin struck; (b) 6 days after VSCS Phailin made landfall; (c) approximately 2 months after VSCS Phailin made landfall. (MODIS imagery retrieved from NASA EOSDIS Worldview, https://worldview.earthdata.nasa.gov/.)

Asia-Pacific region (Stowasser et al., 2006). Likewise, the Intergovernmental Panel on Climate Change (IPCC) finds that climate variability, including patterns such as ENSO, is 'very likely' to continue to influence tropical cyclone frequency, intensity and global distribution (Kirtman et al., 2013). Furthermore, the IPCC finds that tropical cyclones will continue to vary on an annual and decadal scale (Kirtman et al., 2013) with the general thought that though frequency may decrease or remain the same, intensity of individual storms, in terms of wind speed and precipitation, may increase (Christensen et al., 2013). An increase in intensity could lead to an increase in damage to the rapidly growing Asia-Pacific region if exposure to risks and vulnerability to tropical cyclone impacts is not reduced (Peduzzi et al., 2012; UN-ESCAP and UNISDR, 2012).

6.7 CONCLUSION

Favourable conditions for tropical cyclogenesis exist in the Asia-Pacific region. Variations in intensity and frequency are typical, as has been exhibited recently with years of below average activity, which have been observed in the past decade. However, the intense tropical cyclones that the Asia-Pacific region experienced in 2013 are a reminder that continued monitoring of oceanic and atmospheric conditions remains necessary to mitigate impacts to the more than 120 million people vulnerable in the region, and to increase the certainty of climate change projections.

ACKNOWLEDGEMENTS

Many thanks to Alyson Kauffman, Sean Miller and James Rowland for their insight, review and comments.

REFERENCES

ABC. (2013). Weakened Typhoon Haiyan sweeps over Vietnam and into China. http://www.abc.net.au/news/2013-11-11/typhoon-haiyan-sweeps-over-vietnam-and-china/5084232 (accessed 12 July, 2017).

ADB, GoO, WB. (2013). *India: Cyclone Phailin in Odisha. Rapid Damage and Needs Assessment Report*, Asian Development Bank (ADB), Government of Odisha (GoO) and the World Bank (WB), Odisha.

Barcikowska, M., Feser, F. and von Storch, H. (2013). Changes in Tropical Cyclone activity for the western North Pacific during the last decades, derived from a regional model simulation. *27th Conference on Hydrology American Meteorology Society.* Austin, 2013.

BBC. (2013). Severe Tropical Storm Haiyan makes landfall in Vietnam. http://www.bbc.com/news/world-asia-24890114 (accessed 10 January, 2014).

Camargo, S.J. and Sobel, A.H. (2005). Western North Pacific tropical cyclone intensity and ENSO. *Journal of Climate.* 18, 2996–3006.

Chan, J.C.L. and Liu, K.S. (2004). Global warming and Western North Pacific typhoon activity from an observational perspective. *Journal of Climate.* 17, 4590–4602.

Christensen, J.H., Krishna Kumar, K., Aldrian, E., An, S.-I., Cavalcanti, I.F.A., de Castro, M., Dong, W. et al. (2013). Climate phenomena and their relevance for future regional climate change. In *Climate Change 2013: The Physical Science Basis. Contribution of Working Group I to the Fifth Assessment Report of the Intergovernmental Panel on Climate Change*; Stocker, T.F., Qin, D., Plattner, G.-K., Tignor, M., Allen, S.K., Boschung, J., Nauels, A. et al., Eds.; Cambridge University Press, Cambridge and New York, 1217–1308.

Clark, J.D. and Chu, P.-S. (2002). Interannual variation of tropical cyclone activity over the Central North Pacific. *Journal of the Meteorological Society of Japan*. 80(3), 403–418.

CWD-IMD. (2013). *Very Severe Cyclonic Storm Phailin over the Bay of Bengal (08-14 October 2013): A Report.* Cyclone Warning Division India Meteorological Department, New Delhi.

D'Asaro, E., Black, P., Centurioni, L., Harr, P., Jayne, S., Lin, I.-I., Lee, C. et al. (2011). Typhoon-ocean interaction in the western North Pacific: Part 1. *Oceanography*. 24(4), 24–31.

Dube, S.K., Mazumder, T. and Das, A. (2006). An approach to vulnerability assessment for tropical cyclones: A case study of a coastal district in West Bengal. *ITPI Journal*. 3(4), 15–27.

ENVIS Centre. (2013). http://www.orienvis.nic.in/searchdisplay.aspx?st=1&lid=384&langid=1&mid=4 (accessed 28 March, 2014).

Evans, A.D. and Falvey, R.J. (2012). *Annual Tropical Cyclone Report 2012*. Annual Report, Joint Typhoon Warning Center (JTWC), Pearl Harbor, HI.

Ghosh, S., Vidyasagaran, V. and Sandeep, S. (2014). Smart cyclone alerts over the Indian subcontinent. *Atmospheric Science Letters* 15, 157–158. (Published online in Wiley Online Library). DOI: 10.1002/asl2.486.

Haeseler, S. and Lefebvre C. (2013). Super typhoon HAIYAN crossed the Philippines with high intensity in November 2013. Deutscher Wetterdienst (Published online: https://www.dwd.de/EN/ourservices/specialevents/storms/20131213_taifun_haiyan_philippinen_en.pdf?__blob=publicationFile&v=3).

Hindustan Times. (2013). http://www.hindustantimes.com/india/odisha-phailin-hit-chilika-may-take-years-to-recover/story-aEN6BWnRAXvFVEjYTmgYMN.html (accessed 28 March, 2014).

Hobgood, J. (2005). Tropical cyclones. In *Encyclopedia of World Climatology*, Oliver, J.E., Ed., Springer, the Netherlands, 750–756.

EM-DAT: The Emergency Events Database. (n.d.). Université Catholique de Louvain (UCL) – CRED, D. Guha-Sapir, www.emdat.be, Brussels, Belgium (accessed 3 March, 2014).

http://www.rsmcnewdelhi.imd.gov.in/images/pdf/cyclone-awareness/terminology/faq.pdf (accessed 12 July, 2017).

Jordan, C.L. (1961). Marked changes in the characteristics of the eye of intense typhoons between the deepening and filling stages. *J. Meteor.* 18, 779–789.

Kalsi, S.R. (2006). Orissa super cyclone – A Synopsis. *Mausam*. 57, 1–20.

Kirtman, B., Power, S.B., Adedoyin, J.A., Boer, G.J., Bojariu, R., Camilloni, I., Doblas-Reyes, F.J. et al. (2013). Near-term climate change: Projections and predictability. In *Contribution of Working Group I to the Fifth Assessment Report of the Intergovernmental Panel on Climate Change 2013: The Physical Science Basis,* Stocker, T.F., Qin, D., Plattner, G.-K., Tignor, M., Allen, S.K., Boschung, J., Nauels, A. et al., Eds., Cambridge University Press, Cambridge and New York, 953–1028.

Kotal, S.D., Bhattacharya, S.K., Bhowmik, S.K.R., Rao, Y.V.R. and Sharma, A. (2014). *NWP Report on Cyclonic Storms Over the North Indian Ocean During 2013.* India Meteorological Department Numerical Weather Prediction Division, New Delhi.

Kundu, S.N., Sahoo, A.K., Mohapatra, S. and Singh, R.P. (2001). Change analysis using IRS-P4 OCM data after the Orissa super cyclone. *International Journal of Remote Sensing*. 22(7), 1383–1389.

Li, R.C.Y. and Zhou, W. (2012). Changes in Western Pacific tropical cyclones associated with the El Nino-southern oscillation cycle. *Journal of Climate*. 25, 5864–5878.

Lin, I., Liu, W.T., Wu, C.-C., Wong, G.T.F., Hu, C., Chen, Z., Liang, W. et al. (2003). New evidence for enhanced ocean primary production triggered by tropical cyclone. *Geophysical Research Letters*. 30(13), 51–54.

Lin, I.I. (2012). Typhoon-induced phytoplankton blooms and primary productivity increase in the western North Pacific subtropical ocean. *Journal of Geophysical Research*. 117, C03039.

Lin, I.-I., Goni, G.J., Knaff, J.A., Forbes, C., and Ali, M.M. (2013). Ocean heat content for tropical cyclone intensity forecasting and its impact on storm surge. *Natural Hazards*. 66(3), 1481–1500.

Lin, J., Tang, D., Alpers, W. and Wang, S. (2014). Response of dissolved oxygen and related marine ecological parameters to a tropical cyclone in the South China Sea. *Advances in Space Research*. 53, 1081–1091.

Liu, K.S. and Chan, J.C.L. (2012). Inactive period of Western North Pacific tropical cyclone activity in 1998–2011. *Journal of Climate*. 26, 2614–2630.

Mase, H., Mori, N. and Yasuda, T. (2013). Climate change effects on waves, typhoons and storm surges. *Journal of Disaster Research*. 8, 145–146.

Masters, J. (2013). Category 5 Super Typhoon Haiyan heads towards the Philippines (Blog entry). http://www.wunderground.com/blog/JeffMasters/category-5-super-typhoon-haiyan-headed-towards-the-philippines (accessed 29 March, 2017).

McIvor, A., Spencer, T., Möller, I. and Spalding, M. (2012). Natural Coastal Protection Series: Report 2. *Cambridge Coastal Research Unit Working Paper 41*, The Nature Conservancy and the Department of Zoology, University of Cambridge, Cambridge.

Mitra, A., Halder, P. and Banerjee, K. (2011). Changes of selected hydrological parameters in Hooghly estuary in response to a severe tropical cyclone (Aila). *Indian Journal of Geo-Marine Sciences*. 40(1), 32–36.

Mühr, B., Köbele, D., Bessel, T., Fohringer, J., Lucas, C. and Girard, T. (2013). *2nd Report on Super Cyclonic Storm "Phailin"*. Centre for Disaster Management and Risk Reduction Technology (CEDIM). (Available online at http://www.cedim.de/download/CEDIM-Phailin_Report2.pdf; accessed 28 March, 2017.)

NASA. (2013). Haiyan (Northwestern Pacific Ocean) http://www.nasa.gov/content/goddard/haiyan-northwestern-pacific-ocean/#.UzrHzPldXA0 (accessed 29 March, 2017).

National Hurricane Center. (n.d.(a)). Tropical cyclone climatology. http://www.nhc.noaa.gov/climo/(accessed 29 March, 2017).

National Hurricane Center. (n.d.(b)). Saffir–Simpson hurricane wind scale. http://www.nhc.noaa.gov/aboutsshws.php (accessed 28 March, 2017).

National Ocean Service. (2014). http://oceanservice.noaa.gov/facts/phyto.html (accessed 29 March, 2017).

National Weather Service. (n.d.(a)). Tropical cyclone structure. http://www.srh.noaa.gov/jetstream/tropics/tc_structure.htm (accessed 28 March, 2017).

National Weather Service. (n.d.(b)). Tropical cyclone classification. http://www.srh.noaa.gov/jetstream/tropics/tc_classification.htm (accessed 28 March, 2017).

NDRRMC. (2014). *SitRep No. 90 Effects of Typhoon Yolanda (Haiyan). Update, Quezon City*, Republic of the Philippines National Disaster Risk Reduction and Management Council.

Nguyen-Thi, H.A., Matsumoto, J., Ngo-Duc, T. and Endo, N. (2012). Long-term trends in tropical cyclone rainfall in Vietnam. *J. Agrofor. Environ.* 6(2), 89–92.

NOAA National Centers for Environmental Information. (2014). *State of the Climate: Hurricanes and Tropical Storms for Annual 2013* (accessed 29 March, 2017 from https://www.ncdc.noaa.gov/sotc/tropical-cyclones/201313).

Obasi, G.O.P. (1994). WMO's role in the international decade for natural disaster reduction. *Bulletin of the American Meteorological Society*. 75(9), 1655–1661. DOI: http://dx.doi.org/10.1175/1520-0477(1994)075<1655:WRITID>2.0.CO;2.

Pacific Marine Environmental Laboratory. (n.d.). https://www.pmel.noaa.gov/elnino/faq#what (accessed July 12, 2017).

PAGASA. (2011). *Climate Change in the Philippines*. Philippine Atmospheric, Geophysical and Astronomical Services Administration, Quezon City.

Peduzzi, P., Chatenoux, B., Dao, H., De Bono, A., Herold, C., Kossin, J., Mouton, F. and Nordbeck, O. (2012). Global trends in tropical cyclone risk. *Nature Climate Change*. 2, 289–294.

Philander, S.G.H. (1985). El Niño and La Niña. *Journal of the Atmospheric Sciences* 42(23), 2652–2662. DOI: http://dx.doi.org/10.1175/1520-0469(1985)042<2652:ENALN>2.0.CO;2.

RMSC. (n.d.). Regional Specialized Meteorological Centre (RSMC) for Tropical Cyclones over North Indian Ocean (http://www.rsmcnewdelhi.imd.gov.in/images/pdf/cyclone-awareness/terminology/faq.pdf).

Schott, T., Landsea, C., Hafele, G., Lorens, J., Taylor, A., Thurm, H., Ward, B., Willis, M. and Zaleski, W. 2012. The Saffir–Simpson hurricane wind scale. *National Weather Services, National Hurricane Centre, National Oceanic and Atmospheric Administration (NOAA) factsheet*. http://www.nhc.noaa.gov/pdf/sshws.pdf.

Stowasser, M., Wang, Y. and Hamilton, K. (2006). Tropical cyclone changes in the Western North Pacific in a global warming scenario. *Journal of Climate*. 20, 2378–2396.

Tyagi, A., Bandyopadhyay, B.K. and Mohapatra, M. (2010). Monitoring and prediction of cyclonic disturbances over North Indian Ocean by Regional Specialised Meteorological Centre, New Delhi (India): Problems and prospective. In Y. Charabi (Ed.), *Indian Ocean Tropical Cyclones and Climate Change*. pp. 93–103. Springer Science + Business Media BV. DOI 10.1007/978-90-481-3109-9_13.

UN-ESCAP and UNISDR. (2012). *Reducing Vulnerability and Exposure to Disasters: The Asia-Pacific Disaster Report*. United Nations Economic and Social Commission for Asia and the Pacific (UN-ESCAP) and the United Nations Office for Disaster Risk Reduction (UNISDR), Bangkok.

WMO. (2014). WMO statement on the status of the global climate in 2013. World Meteorological Organization, Geneva.

WMO. (n.d.(a)). https://public.wmo.int/en/media/news/wmo-community-mobilizes-haiyan-yolanda (accessed July 12, 2017).

WMO. (n.d.(b)). Latest advisories on current tropical cyclones, hurricanes, typhoons. http://www.wmo.int/pages/prog/www/tcp/Advisories-RSMCs.html (accessed 29 March, 2017).

Zee News. (2014). Drop in the number of migratory birds visiting Chilika Lake. Online at http://zeenews.india.com/news/eco-news/drop-in-the-number-of-migratory-birds-visiting-chilika-lake_903951.html (accessed 29 March, 2017).

Zhou, B., Cui, X. and Zhao, P. (2008). Relationship between the Asian-Pacific oscillation and the tropical cyclone frequency in the western North Pacific. *Science in China Series D: Earth Sciences*. 51(3), 300–385.

7 Monitoring and Interpreting the Tropical Oceans by Satellite Altimetry

Tong Lee, J. Thomas Farrar, Sabine Arnault, Benoit Meyssignac, Weiqing Han, and Theodore Durland

7.1 INTRODUCTION

The tropical oceans, which are responsible for meridional and zonal heat transports that are comparable to or larger than those carried by the tropical atmosphere, have significant influence on the Earth's climate. The interactions between the tropical oceans and atmosphere and their impact on intraseasonal to multidecadal timescales result in climate variability that has regional to global impact. This variability includes the impact of the Madden-Julian Oscillations (MJO) on intraseasonal timescales, the monsoons on seasonal timescales, El Niño-Southern Oscillation (ENSO), Indian Ocean Zonal/Dipole Mode (IOZDM), and Tropical Atlantic Niño on interannual timescales, and the Pacific Decadal Oscillation (PDO). Variability associated with tropical-ocean currents influences the geographical distribution of large-scale upper-ocean heat content. Under the influence of global warming, the climate of the tropical region will probably undergo significant changes. The tropical Pacific easterly trade winds are expected to weaken under the global warming scenario, leading to a slower equatorial oceanic circulation (including equatorial upwelling) (Vecchi and Soden 2007). In response, the surface ocean temperatures are expected to warm fastest near the equator and more slowly farther away, the equatorial thermocline is expected to shoal, and the temperature gradients across the thermocline are expected to become steeper (e.g., Collins et al. 2010). The climate modes such as ENSO and IOZDM, which are controlled by a delicate balance of amplifying and damping feedback, depend on these thermocline features, and thus they will probably be modified under global warming. Understanding how they will change, however, remains a challenge.

The stratification of the tropical oceans is characterized by a relatively shallow pycnocline with an averaged depth ranging from 50 to 200 m depending on longitudes, and most of the variability occurs above the pycnocline (Hastenrath and Merle 1987; Durand and Delcroix 2000; Schott et al. 2009). A two-layer system is a reasonably good approximation of the tropical oceans where the response to wind forcing is dominated overall by the first baroclinic mode. Consequently, sea surface height (SSH) variability provides a good proxy for changes of pycnocline geostrophic flow and upper-ocean heat content. Altimeter-derived SSH anomalies thus have been providing critical measurements for the study of tropical ocean variability and the related ocean-atmosphere interaction.

The equatorial oceans provide a waveguide that hosts a suite of large-scale oceanic waves that are important to ocean dynamics and ocean-atmosphere interactions, such as the oceanic equatorial Kelvin and Rossby waves and tropical instability waves (TIWs). In particular, Kelvin and Rossby waves transmit the oceanic response to wind forcing zonally across the equatorial oceans, thereby modulating sea surface temperature (SST) and the feedback to the atmosphere (e.g., through the so-called Bjerknes feedback) and providing the oceanic memory associated with seasonal-to-interannual climate variability such as ENSO. Prior to the early 1990s, the limited observational capability to monitor these waves relied primarily on the sparsely distributed tide gauges and moorings (Knox and Halpern 1982; Lukas et al. 1984). Furthermore, in the Atlantic and Indian oceans, there was no equivalent to the

Tropical Atmosphere Ocean (TAO) mooring array of the Pacific back then. Altimeter-derived SSH measurements have greatly enhanced our ability to observe the variability of the tropical oceans, and they have been fundamental to the study of tropical ocean dynamics and air-sea interaction.

Following the proof-of-concept missions such as Skylab, GEOS 3, and Seasat, in the 1980s, GEOSAT brought a noticeable improvement in terms of altimeter accuracy (Tai 1988; Cheney et al. 1989). Tropical ocean studies using GEOSAT SSH data were first dedicated to comparisons with *in situ* data or models on basin scales (Arnault et al. 1989; Carton 1989; Arnault et al. 1990; Picaut et al. 1990; Arnault and LeProvost 1997) or on more regional scales (Carton and Katz 1990; Cheney and Miller 1990; Forristall et al. 1990; Wyrtki and Mitchum 1990; Arnault et al. 1992; Carton et al. 1993; Didden and Schott 1993; Arnault and Cheney 1994; Minster et al. 1995; Verstraete and Park 1995; Arnault et al. 1999). These comparisons showed that altimetric observations were mature enough to depict the seasonal cycle and to detect the interannual variability of Tropical Ocean SSH. Applications to study oceanographic physical processes were emerging (e.g., Miller and Cheney 1990; Périgaud 1990; Périgaud and Delecluse 1992) especially those concerning wave propagation associated with ENSO (Delcroix et al. 1991). The famous picture from Miller et al. (1988) showing, for the first time, propagating Kelwin and Rossby waves along the whole Pacific basin during 1987 to 1988 El Niño was a remarkable milestone in altimetry history.

TOPEX/Poseidon (T/P), launched in 1992, represented a major improvement in high-precision satellite altimetry. Jason-1, Jason-2, and Jason-3 missions continue the precision altimeter records. Besides the CalVal studies inherent to each new satellite mission (Busalacchi et al. 1994; Giese et al. 1994; Mitchum 1994; Picaut et al. 1995; Verstraete and Park 1995; Mayer et al. 2003; Arnault et al. 2004; Provost et al. 2004; Arnault et al. 2011; Liu et al. 2014), altimetry began to be used as an independent source of information to improve knowledge of tropical dynamics, allowing new insights into mesoscale activity, wave propagation, and low-frequency variability from seasonal to decadal timescales.

Much of the efforts describing the utility of altimetry measurements to study intraseasonal to interannual tropical ocean variability and the related climate variability prior to 2000 has been described in Chapter 4, "Tropical Ocean Variability" (authored by J. Picaut and A. Busalacchi), of the *Altimetry and Earth Sciences: A Handbook of Techniques and Applications* (Fu and Cazenave 2000). Since then, significant progress has been made toward understanding and predicting such variability. Moreover, the nearly two-and-half decades of precision satellite altimetry measurements have enabled the studies of decadal variability of the tropical ocean and coupled ocean-atmosphere system. This chapter mostly focuses on the contributions of altimetry-derived SSH measurements in these areas of studies since 2000. However, some related studies in the late 1990s that have not been discussed by Picaut and Busalacchi (2000) in the previous altimetry book are also highlighted here to provide a more complete scope and context.

Section 7.2 of this chapter focuses on the Atlantic Ocean variability. Variability of the tropical Pacific and Indian Ocean as well as their linkages (e.g., the Indonesian Throughflow) are described in Sections 7.3, 7.4, and 7.5, respectively. The discussions in these sections are generally organized by subsections that focus on intraseasonal, seasonal, interannual, and decadal timescales. Hereafter, SSH measurements generally refer to altimetry-derived SSH anomalies from various missions since 1992 (e.g., T/P, Jason-1 and Jason-2), including the SSH products derived by merging data from two or more altimeter missions such as the Archiving, Validation, and Interpretation of Satellite Oceanographic (AVISO) gridded data products (see Pujol et al. 2016 and references therein).

7.2 TROPICAL ATLANTIC OCEAN

7.2.1 Intraseasonal and Eddy Activities

7.2.1.1 Eddy Structures

Eddy activities have been identified from altimetry along the African coast, in the Mauritania-Sénégal and the Benguela upwelling systems (Chaigneau et al. 2009), and in the Gulf of Guinea

(Djakoure et al. 2014). However, the mesoscale eddy activity in the tropical Atlantic is mostly located in the western basin associated with the North Brazil Current (NBC) and its retroflection into the North Equatorial Countercurrent (NECC) (e.g., Goni and Johns 2001) (Figure 2.1). These eddies may account for more than 25%–50% of the inter-hemispheric transports of mass and heat within the Atlantic meridional overturning cell (Didden and Schott 1993; Frantantoni et al. 1995; Goni and Johns 2001; Garzoli et al. 2003). Following previous work by Didden and Schott (1993), Nystuen and Andrade (1993), and Fratantoni et al. (1995) based on GEOSAT SSH data, Pauluhn and Chao (1999) tracked 16–20 anticyclonic eddies using T/P SSH data between October 1992 and June 1997. Goni and Johns (2001) depicted approximately six rings per year between 1993 and 1998, nearly twice that previously thought from *in situ* observations. Extending the series up to 2001, Goni and Johns (2003) found a weak tendency for rings to form during the first half of the year, suggesting that a formation mechanism other than the NBC retroflection also exists, with important year-to-year variability. Castelao and Johns (2011) questioned the altimetric underestimation of the rings' intensity due to the inexact crossing of the ring centers during individual satellite passes.

7.2.1.2 Tropical Instability Waves

TIWs play a role in climate variability as they can influence, for instance, the phase of the seasonal cycle, the position of the equatorial cold tongue and of the Intertropical Convergence Zone (ITCZ), the oxygen and salinity front along the equator, and the plankton and nutrient distribution (Menkes et al. 2002; Jochum and Malanotte-Rizzoli 2003; Lee et al. 2012). Away from the equator (3°N–5°N), where Kelvin and Rossby waves play a key role (see the following), SSH and thermocline variations in the 40- to 60-day band in the tropical Atlantic are caused largely by TIWs (Katz 1997; Han et al. 2008). Strong seasonal variations of tropical Atlantic TIW activities have been identified in SSH as well as in SST and SSS associated with seasonal variations of the equatorial current system (e.g., Lee et al. 2014) (Figure 2.2). This is in contrast to tropical Pacific TIWs that have stronger interannual than seasonal variations.

Von Schuckmann et al. (2008) used altimetry SSH data to validate a numerical eddy-resolving model and investigated the spatial and temporal distributions of these TIWs and the role of baroclinic versus barotropic instabilities to generate these waves. Grodsky et al. (2005) used temperature, salinity, velocity, and wind from a mooring at 0°N, 23°W along with satellite data for SST and SSH to examine the contribution of TIWs to the energy and heat balance of the equatorial Atlantic mixed layer. The TIW intensification occurs in phase with strengthening of the southeasterly trade winds and the seasonal appearance of the equatorial cold tongue. The waves contribute to a net warming of the mixed layer by 0.35°C during the summer months, and they are maintained by both barotropic and baroclinic conversions that are of comparable size. They also showed that salinity fluctuations, previously neglected, increase the magnitude of baroclinic energy conversion, a result expanded on by Lee et al. (2014) in an analysis of satellite measurements including SSH, SSS, and SST. Perez et al. (2012) developed metrics based on SST and SSH fluctuations to examine interannual TIW variability in the Atlantic. They found that in contrast to the near equatorial region, years with low TIW variance along the off-equatorial latitude bands are associated with anomalously warm SSTs in the cold tongue region, weak wind stress divergence and curl in the equatorial region, and weak zonal current shear in the NECC/South Equatorial Current (SEC) region.

7.2.2 The Seasonal Cycle

The seasonal cycle is the dominant source of variability in the tropical Atlantic Ocean. Its main features—including the annual strengthening/weakening of the surface currents, the retroflection of the NBC, the zonal pressure gradient along the equator, and the annual and semiannual upwelling and downwelling cycle in the Gulf of Guinea—were apparent even in the early satellite altimetry missions. They suggested that the annual cycle accounts for at least 60% of the total SSH variance in the Tropical Atlantic. However, the limited accuracy of these early missions prevented a precise quantification of this seasonal cycle.

Two decades of high-precision altimetry from T/P and subsequent missions have confirmed these early findings (Schouten et al. 2005; Aman et al. 2007; Ding et al. 2010). They offer the opportunity to obtain a detailed picture of the tropical Atlantic equatorial upwelling (Schlundt et al. 2014) and surface circulation (Arnault et al. 1999; Arnault and Kestenaere 2004; Fonseca et al. 2004; Stramma et al. 2005; Artamonov 2006; Urbano et al. 2008; Goes et al. 2013). For instance, Fonseca et al. (2004) showed that the NBC retroflection exhibits a mean position of 6.6°N ± 2.0°N, with a strong annual signal that follows the meridional migration of the ITCZ and the strength of the wind stress curl over the equatorial Atlantic. Yang and Joyce (2005) found that the seasonal variation of the NECC geostrophic transport in the tropical Atlantic Ocean is dominated by changes in the southern flank of the current and hypothesized that the wind stress forcing along the equator is the leading driver for the seasonal cycle of the NECC transport. The wind stress curl in the NECC region is an important but smaller contributor.

7.2.3 Equatorial Waves

Equatorially trapped waves are an important component of tropical ocean variability because they are efficient carriers of information along the equator and can lead to remote effects on ocean-atmosphere interaction. Prior to the altimeter era, the existence of Kelvin and Rossby waves in the tropical Atlantic was questioned on the basis of narrow width of the basin, the typical length scales of the wind forcing, and the high propagation speed of these waves. Katz (1997) was one of the first to identify in the 1993–1995 T/P data eastward propagations as first-mode Kelvin waves. Franca et al. (2003) explained much of the variance of the T/P data during 1992–1999 as a combination of the Kelvin and first two Rossby mode waves. Schouten et al. (2005) found that the seasonal adjustment of the tropical Atlantic to the wind leads to a cycle of consecutive Kelvin and Rossby waves, with the African coastal signal partially forced by the equatorial waves (Figure 2.3). However, Bunge and Clarke (2009) argued that the phase speed of the propagation found by Schouten et al. (2005) is too slow. They concluded that this annual eastward propagating signal in SSH at the equator is not the result of waves but rather the superposition of two independent modes of variability: variations in the warm water volume above the 20°C isotherm and a tilt in the thermocline. But Polo et al. (2008a) presented an intraseasonal climatology of T/P data that reveals regular boreal autumn-winter equator to coast propagations with phase speeds varying from 1.5 to 2 m s^{-1} in good agreement with the theory. A remote forcing effect of the Kelvin waves was evidenced over coastal regions as far as 10–15 degrees latitude and have no counterpart in the hypothesis put forth by Bunge and Clarke (2009). Furthermore, the modeling results of Ding et al. (2009), validated using SSH data, show that Kelvin and Rossby waves are both important at the equator, with the Kelvin wave being most important. Additionally, there is an important contribution of boundary reflections equal to that of the wind-forced response.

More studies on the role of Kelvin and Rossby waves during particular events in the tropical Atlantic Ocean have been conducted. Illig et al. (2006) detailed the 1996 warm event from a numerical investigation associated with SSH data and argued for an essential role of equatorial waves triggered by distinct wind events. A possible teleconnection with the tropical Pacific Ocean through the modification of the Walker Circulation has been suggested. Han et al. (2008) found that the 40- to 60-day Sea Surface Height Anomaly (SSHA) was dominated in 2002–2003 by the equatorially symmetric Kelvin waves driven by intraseasonal winds within the 3°S–3°N equatorial belt. Interestingly, if the 10- to 40-day periods are dominated by TIWs west of 10°W, east of it, SSHA variations result almost entirely from wind-driven equatorial waves. During the boreal spring of 2002, when TIWs were weak, Kelvin waves dominated the SSHA across the equatorial basin (2°S–2°N). Hormann and Brandt (2009) continued analysis of the 2002 warm event, comparing it to the 2005 strong cold event using moored and satellite observations. Prior to the warm event in 2002, equatorial easterly winds in the western to central Atlantic, covarying with the equatorial

Kelvin wave mode, relax. In response, the thermocline shoals in the west and the basin-wide adjustment of the equatorial thermocline slope via downwelling Kelvin waves results in a deeper thermocline in the east. In contrast, such a zonal wind mechanism could not be established for the strong cold event in 2005. Hormann et al. (2012), using surface currents derived from altimetry, suggested that alongshore winds in the northeastern tropical Atlantic generate Rossby waves that propagate westward from the eastern boundary and are responsible for a large part of the NECC interannual variability. These studies dedicated to specific years showed that besides the intense annual cycle, the tropical Atlantic also presents interannual variations but of comparatively small amplitude.

7.2.4 Interannual Variability

Interannual variations in the early 1990s have been identified through their signature on SST (Servain 1991; Houghton and Tourre 1992). An attempt using GEOSAT altimetry was conducted (Arnault and Cheney 1994), but the analysis of their signature on SSH began in earnest in the 2000s, enabled by the longer record of precise satellite altimetry (Arnault and Kestenaere 2004; Schouten et al. 2005; Handoh et al. 2006a, 2006b; Foltz and McPhaden 2010; Arruda et al. 2011; Arnault and Mélice 2012). These studies revealed that the interannual variability of the tropical Atlantic basin-scale SSH is dominated by two modes of variability: (1) an equatorial mode akin to ENSO but with a weaker magnitude and (2) a meridional mode varying between north (10°N–20°N) and south (along 20°S) of the equator.

The equatorial mode is characterized by changes in the east-west SSH slope along the equator in response primarily to changes in the zonal wind stress (Provost et al. 2006; Ding et al. 2010; Foltz and McPhaden 2010; Arnault and Mélice 2012) or by the emergence of a cold tongue in the Gulf of Guinea (such as in 1997 or 2002). The positive feedback among SST, zonal wind, and thermocline depth or SSH (i.e., Bjerknes feedback) tends to prolong this equatorial mode (Keenlyside and Latif 2007; Ding et al. 2010).

The meridional mode variability has also been attributed to variability in the trade winds. In the northern and southern tropics, the variations of SSH are in phase with the variations in SST because both are a response to the thermosteric variations generated by the wind variability: As trade winds intensify, SSH and SST decrease (Ruiz-Barradas et al. 2000; Handoh et al. 2006a, 2006b; Arnault and Mélice 2012). Foltz and McPhaden (2010) analyzed SST and SSH observations to conclude that the meridional and equatorial modes of the tropical Atlantic are linked through anomalous changes in equatorial winds.

The possible teleconnection of the Atlantic tropical modes of variability with the Pacific ENSO mode is intensely debated. Several studies have shown an influence of ENSO on the northern tropical Atlantic SST with warming in the North Atlantic occurring 4–5 months later than in the Pacific (Enfield and Mayer 1997; Huang et al. 2005; Arnault and Mélice 2012) (Figure 2.4). This ENSO-related warming seems to have a signature on SSH in the Gulf of Guinea as well, with a longer lag of the latter (Andrew et al. 2006; Arnault and Mélice 2012). Other climate modes such as the IOZDM and the North Atlantic Oscillation (NAO) do not seem to influence the tropical Atlantic sea level variability (Andrew et al. 2006).

The role of equatorial Kelvin and Rossby waves in interannual variability has also been suggested in the Angola/Benguela area, south of 15°S. Shannon et al. (1986) suggested that wind stress anomalies to the north, and possibly in the equatorial Atlantic, are the dominant factor of SST variations in that area. Polo et al. (2008a, 2008b) point out that the influence of Kelvin waves triggered by equatorial wind stress anomalies might not reach further poleward than 12°S, while other studies have articulated the importance of remote equatorial influences (Florenchie et al. 2003, 2004; Grodsky et al. 2006; Huang and Hu 2007; Rouault et al. 2007). Richter et al. (2010) argued that meridional wind anomalies along the southwest African coast contribute substantially. These wind anomalies form part of a basin-scale weakening of the subtropical anticyclone that extends to the equator. Results also indicate that the close correlation between Benguela and Atlantic Niños in observations might result from the large spatially coherent wind stress anomalies associated with the weakened anticyclone.

Very recently, the tropical Atlantic has raised special interest in the climate community because the particularly low interannual variability in SSH in this region makes it an area where the SSH signal due to greenhouse gas (GHG) emissions might be detected over the signals generated by the natural climate variability. Indeed, recent detection and attribution studies based on satellite altimetry and atmosphere-ocean general circulation models or Earth system models suggest that the SSH signal forced by the GHG emissions may be detectable above the level of unforced internal variability in the tropical Atlantic within the next decade (Jordà 2014; Richter et al. 2014; Carson et al. 2015; Fernandez Bilbao et al. 2015; Lyu et al. 2015).

7.3 TROPICAL INDO-PACIFIC OCEAN

7.3.1 Tropical Pacific

SSH measurements by satellite altimeters have proven especially useful for allowing insight into the dynamics of the tropical Pacific Ocean. Unlike variability seen in SST or SSS, the SSH anomalies detected from altimetry directly reflect the upper-ocean pressure fluctuations associated with ocean dynamical variations, and, because of a strong correlation of SSH and thermocline depth in the tropical Pacific (Rebert et al. 1985), SSH anomalies provide important information about thermocline depth and ocean heat content. The enormous size of the tropical Pacific, combined with a dearth of shipping lanes south of the equator, has made it a challenge to adequately resolve the broad spectrum of spatiotemporal variability of the tropical Pacific with *in situ* measurements. Although much was learned about tropical Pacific dynamics in the pre-satellite years, satellite altimetry has given us the first opportunity to observe the entire region in great detail, to confirm or refute previous conjectures, and to find new aspects of the equatorial dynamics that were previously unavailable to us.

7.3.1.1 Intraseasonal Variability

Several distinct types of variability with intraseasonal periods (20 to 100 days) coexist in the tropical Pacific Ocean, including eastward propagating Kelvin waves and shorter-wavelength, westward-propagating variability, such as TIWs.

TIWs were first discovered in satellite infrared SST measurements in the Pacific (Legeckis 1977). They arise from instabilities of the equatorial current system (Philander 1976; Luther and Johnson 1990; Lyman et al. 2005) and are clearly visible in satellite SST measurements as a meandering of the northern side of the equatorial cold tongue near 2°N. The discovery of TIWs in the late 1970s stimulated a great deal of subsequent theoretical and observational work to understand their generation mechanisms, properties, and consequences.

A relatively clear separation of TIWs and intraseasonal Kelvin waves can be achieved by examining the spectrum of SSH variability in the zonal-wavenumber-frequency domain, which allows separation of the eastward-propagating Kelvin waves from the westward-propagating TIWs. Examination of the zonal-wavenumber/frequency spectrum is also helpful because the most common theoretical approaches to Kelvin waves and TIWs are carried out in the zonal-wavenumber/frequency domain (e.g., Matsuno 1966; Moore and Philander 1977; Philander 1978).

The zonal-wavenumber/frequency spectrum of SSH in the equatorial Pacific exhibits two broad regions of elevated SSH variance, one corresponding to eastward propagating Kelvin waves at small, positive zonal wavenumbers (wavelengths exceeding 50° longitude) and one corresponding to TIWs and other westward-propagating variability with zonal wavelengths of about 9°–30° (Figure 7.1; Perigaud 1990; Zang et al. 2002; Wakata 2007; Farrar 2008; Shinoda et al. 2009; Farrar 2011). The SSH spectrum shown in Figure 7.1 (after Farrar 2011) was estimated using data from the DT2014 AVISO gridded altimetry product (Pujol et al. 2016) over the period 1993–2014 and almost the full width of the equatorial Pacific (149°E–88°W) and has been averaged over 7°S–7°N.

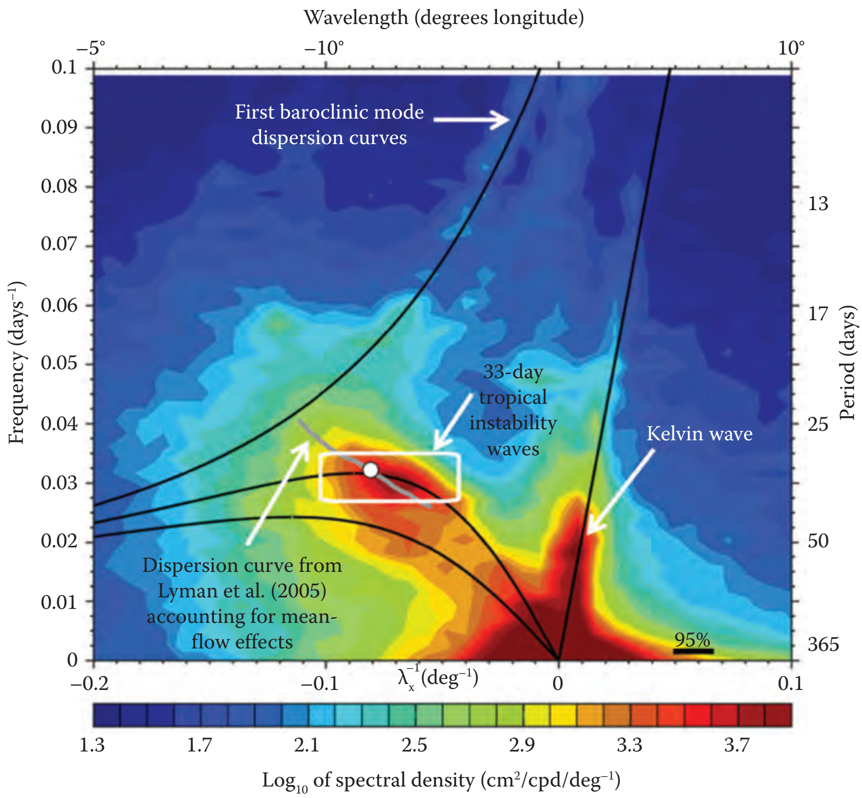

FIGURE 7.1 Zonal-wavenumber/frequency spectrum of SSH, averaged over 7°S–7°N (after Farrar, J. T., *J. Phys. Oceanogr.*, 41, 1160–1181, 2011. With permission), using data from 1993–2014 and almost the full width of the Pacific (149°E–88°W). At periods of 20–100 days, there are two broad regions of elevated SSH variance, one corresponding to eastward propagating Kelvin waves at small, positive wavenumbers (wavelengths exceeding 50°), and one corresponding to TIWs and other westward-propagating variability having zonal wavelengths of about 9°–30°. The TIW spectral peak in SSH near 33-day periods (white box) has wavelengths of 12°–17°. The four black curves are the theoretical dispersion curves for the first-baroclinic-mode Kelvin, Rossby, and mixed Rossby-gravity waves. The grey line depicts a theoretical dispersion curve for the unstable TIW mode, and the white circle indicates the fastest growing wavelength (from Lyman, J., et al., *J. Phys. Oceanogr.*, 35, 232–254, 2005. With permission). The 95% confidence interval should be measured against the color scale; a difference of two contour intervals is significant at 95% confidence.

There is a well-defined spectral peak in the SSH wavenumber-frequency spectrum near periods of 33 days (frequency of 0.03 days^{-1}) and wavelengths of 12°–16° (zonal wavenumbers of 0.06–0.08 degrees^{-1}). This is close to the period and wavelength (33 days and 12.4°) found for the most unstable mode of the equatorial current system in a linear stability analysis by Lyman et al. (2005). The ridge of high power in the 25- to 40-day period band roughly follows the dispersion curve of this most unstable mode (Farrar 2008, 2011; Figure 7.1). The SSH variability in this wavenumber-frequency band also has a spatial structure that closely resembles the structure of the most unstable mode predicted by the linear stability analysis (Farrar 2008, 2011). However, the linear stability analysis of Lyman et al. (2005) predicted many unstable modes that grew more slowly than the most unstable mode, and the SSH spectrum in Figure 7.1 suggests there is in fact a broad spectrum of instabilities.

Descriptions of the properties of TIWs have varied widely: TIWs have been reported to occur at periods of 14–50 days, at zonal wavelengths of 7° to 25°, and to have maximum amplitude at locations ranging from the equator to 6°N (Qiao and Weisberg 1995, provide a helpful review). Observational studies of TIWs have typically characterized them as a fairly narrowband phenomenon, but this apparently conflicts with the broad range of wavenumbers and frequencies reported. For example, Halpern et al. (1988) characterized the TIW signal in meridional velocity measurements on the equator as a narrowband fluctuation with a period of 20 days, while Lyman et al. (2005) and Farrar (2008) found a clear maximum in SSH variability at periods of about 33 days.

When the various wavenumbers and frequencies that have been reported or theoretically predicted for TIWs are plotted over the spectrum shown in Figure 7.1, it becomes apparent that the various estimates collectively span the range of wavenumber-frequency space that exhibits energetic SSH variability in the 7°S–7°N latitude band (Figure 7.2). Figure 7.2 includes the wavenumber-frequency estimates summarized in Table 1 of Qiao and Weisberg (1995) and some more recent estimates from Chelton et al. (2000), Donohue and Wimbush (1998), McPhaden (1996), Lyman et al. (2005, 2007), and Lee et al. (2012). The figure shows boxes, lines, and points depending on whether a study provided a range of wavenumbers and/or frequencies or simply stated a single wavenumber and frequency. Studies using SSH measurements (Perigaud 1990; Lyman et al. 2005; Farrar 2008, 2011) identified TIW wavenumbers and frequencies around the spectral peak in SSH seen near 33-day periods, consistent with the well-defined spectral peak in the SSH wavenumber-frequency spectrum near periods of 33 days. Those studies and Shinoda et al. (2009) also determined the peak TIW SSH variability to occur near 5°N. At the other extreme of the reported frequency range,

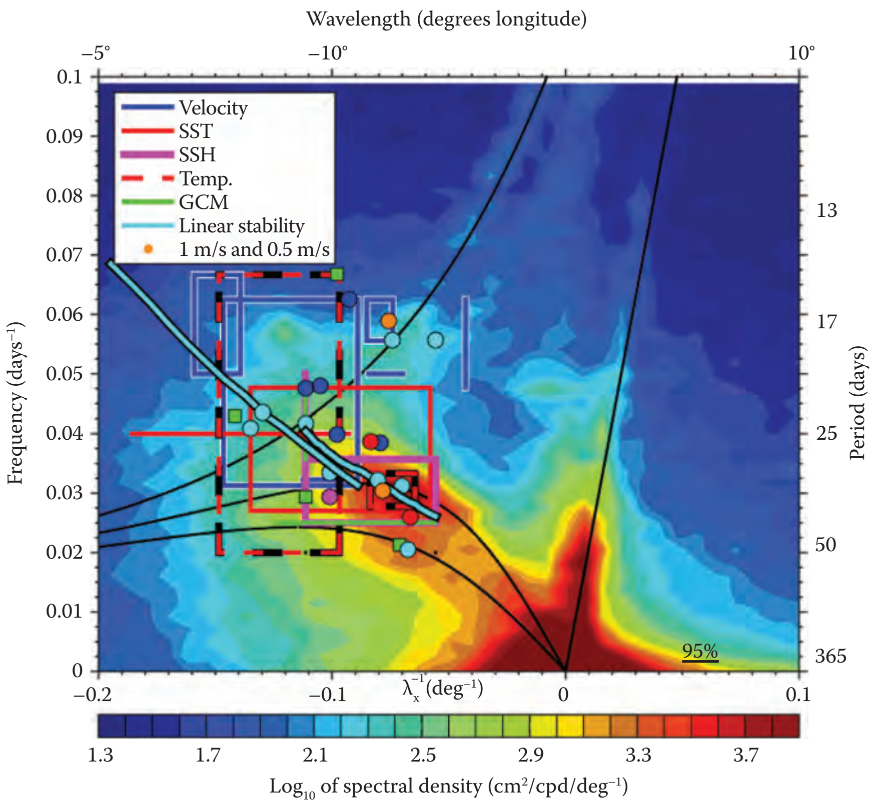

FIGURE 7.2 Previous estimates of the wavenumbers and frequencies of tropical instability waves (TIWs). (The contoured field is the zonal-wavenumber/frequency spectrum of SSH from Figure 7.1). A box indicates that a particular study provided a range of wavenumbers and frequencies, a line indicates a range of frequencies or wavenumbers, and a point indicates that a single wavenumber-frequency value was given. “SST” and “SSH” are from satellite observations, and “Velocity” and “Temp.” are from moored in situ measurements.

in situ equatorial velocity measurements have yielded shorter periods, near 20 days, with the strongest signals on the equator being seen in meridional velocity (e.g., Halpern et al. 1988). Satellite SST and *in situ* temperature measurements have tended to yield estimates in between these two extremes and have also tended to identify maximum variability as occurring near 2°N.

One interpretation of these disparate observations is that some of the TIW variability resembles mixed Rossby-gravity waves, which have a relatively weak SSH signal and a strong signal in equatorial meridional velocity, and other TIW variability resembles first-meridional-mode (and perhaps second-meridional-mode) equatorial Rossby waves, with a stronger off-equatorial SSH signal (Lyman et al. 2007). In SSH, the TIW signal is largest near 5°N, where the SSH signal of the Rossby-wave-like theoretical most unstable mode is largest (Lyman et al. 2005; Farrar 2008). Equatorial current meter measurements tend to emphasize the unstable modes that resemble mixed Rossby-gravity waves, which have a maximum meridional velocity signal at the equator.

This interpretation is supported by the analysis of Lee et al. (2012), who used SSS and SST to estimate propagation speeds of about 1 m/s for TIWs near the equator and of about 0.5 m/s near 5°N, which roughly spans the range of propagation speeds that have been reported in the literature and that dominate the westward-propagating part of the SSH spectrum (Figure 7.2). TIWs produce signals in variables like SSS and SST largely through advection, with meridional velocity fluctuations deforming the sharp meridional gradients of these quantities. SSS has its strongest propagating signature of tropical Pacific TIWs near the equator where the salty South Pacific waters meet the fresher waters under the ITCZ, forming a relatively large meridional SSS gradient. In contrast, the meridional gradient of SST is weaker at the equator and is the strongest near the northern edge of the cold tongue near 2°N, where TIW signature in SST is strongest. If the meridional velocities contributing to meridional advection of SST near 2°N are from a combination of the Rossby-wave-like and mixed Rossby-gravity-wave-like unstable modes, this could explain the fact that a broader range of frequencies of TIWs have been reported from temperature observations.

Kelvin waves are the other major form of intraseasonal variability in the tropical Pacific Ocean. These waves are visible in Figures 7.1 and 7.2 as a low-wavenumber band of high variance along the first-baroclinic-mode Kelvin wave dispersion curve. They dominate the variance of SSH and other fields at 40- to 90-day periods and have received considerable attention (e.g., Enfield 1987; McPhaden and Taft 1988; Johnson 1993; Johnson and McPhaden 1993; Kessler et al. 1995; Kessler and McPhaden 1995; Hendon et al. 1998; Kutsuwada and McPhaden 2002; Zang et al. 2002; Cravatte et al. 2003; Roundy and Kiladis 2006; Farrar 2008). The waves are forced by intraseasonal wind fluctuations in the western and central Pacific (Kessler et al. 1995; Hendon et al. 1998). Interestingly, altimetry observations and numerical simulations indicate that intraseasonal Kelvin waves affect the propagation and energetics of TIWs by modulating the mean flow that produces the TIWs (Holmes and Thomas 2016).

7.3.1.2 Seasonal Variability

Before satellite altimetry, investigations into the seasonal cycle of thermocline depth or dynamic topography in the equatorial Pacific were mostly based on hydrographic and current measurements that were sparsely and irregularly distributed in time and space; lack of good data coverage (primarily south of the equator) was invoked more than once as a possible explanation for puzzling results. The completion of the TAO/TRITON mooring array at about the same time that satellite altimetry was becoming available greatly improved the subsurface sampling characteristics, although the two- to three-degree meridional spacing of the moorings is barely able to resolve the relatively short meridional scales of equatorially trapped phenomena, and the 15-degree zonal spacing barely resolves important features of the seasonal cycle near the western and eastern boundaries.

Following is a review of major features of the seasonal cycle as understood before the modern satellite altimetry record, based primarily on Wang et al. (2000), Yu and McPhaden (1999), and Johnson et al. (2002). This is followed by an overview of papers that have advanced our knowledge through the use of satellite altimetry, focusing on those published since 2000.

7.3.1.2.1 Background

On the northern and southern flanks of the mean ITCZ and the South Pacific Convergence Zone (SPCZ), high annual thermocline variability is coincident with zones of elevated annual Ekman pumping produced by the annual march of the convergence zones. A basin-wide strip of high variability between 10°N and 15°N is intensified in the east where the annual march of the ITCZ is greatest, but it is non-propagating. Within 10 degrees of the equator, the maximum oceanic variability is collocated with the Ekman pumping maximum on the southern flank of the ITCZ in the east-central Pacific (170°W–110°W); with a peak near 4°N, 140°W, and extending across the equator with a smaller amplitude. The annual minimum and maximum thermocline depth propagate westward at both 5°N and 6°S with a phase speed close to the theoretical speed for a first baroclinic, first meridional mode Rossby wave. Mitchum and Lukas (1990) concluded that this wave is resonantly forced by a westward-propagating easterly wind pattern, which spans the wave guide but is obscured in climatologies by stronger stationary winds everywhere except near the equator.

Near the equator, thermocline anomalies propagate eastward in the central and eastern Pacific, and westward with a strong semiannual signal in the western Pacific (Yu and McPhaden 1999). Wang et al. (2000) found the eastward propagation of the maximum thermocline depth to proceed at close to the first baroclinic mode Kelvin wave speed, with a timing that suggested excitation by the Western Pacific Monsoon westerlies. This monsoon also contributes to elevated annual variability centered at 5°N near the western boundary. The eastward propagation of the minimum thermocline depth on the equator was found to be quite a bit slower, and Yu and McPhaden concluded that the annual Kelvin wave was a mix of first and second baroclinic modes.

In the central equatorial Pacific, Wang et al. (2000) found the seasonal cycle to be unimodal, with the annual harmonic explaining more than 90% of the variance. Near the western and eastern boundaries, and along the mean positions of the convergence zones, they found the seasonal cycle to be bimodal and explained this as an overlap between two distinct annual forcing regimes.

The far eastern equatorial Pacific is a dynamically complex place, and even a cursory description is beyond the scope of this work. An excellent review of this region and its seasonal cycle is given in Kessler (2006), including discussion of altimetry studies that have helped to define it.

Johnson et al. (2002) estimated the annual cycle of the equatorial Pacific currents from 15 years of hydrographic and ADCP sections, and we present here a summary of their conclusions for the major surface geostrophic currents. The NECC flows eastward between about 3°N and 10°N, with a maximum in August in the eastern Pacific, October in the central Pacific, and December in the western Pacific. Between the NECC and the equator, the northern branch of the westward-flowing South Equatorial Current (or NSEC) peaks in June to October in the east and in December in the central and western Pacific. South of the equator, the southern branch of the South Equatorial Current (or SSEC) peaks in October to December in the east and in February to April in the west, with a weak seasonal cycle in the central Pacific. The westward propagation of peak currents is consistent with the dominant westward propagation of thermocline depth noted earlier. Near the equator, the SEC in the eastern Pacific reverses direction in late spring and early summer, and this reversal propagates westward in concert with the annual Rossby wave but in contradiction to the eastward thermocline propagation. Yu and McPhaden (1999) showed that this unusual pattern could result from a superposition of the aforementioned Rossby and Kelvin waves.

Johnson et al. (2002) showed that La Niña conditions tend to strengthen all of the surface currents and push the NECC northward in the central and western Pacific. El Niño conditions tend to weaken the SEC and the NECC in the eastern Pacific.

7.3.1.2.2 Contributions from Altimetry: The Seasonal SSH Anomaly Field

Work done with altimetry data prior to 2000 is well covered in Fu and Cazenave (2000), and we focus on subsequent work. As a sole exception, we note that Stammer (1997) analyzed the global annual cycle of SSH anomalies from 3 years of T/P measurements (October 1992 to

November 1995). The results were plotted on a global scale, but even at that scale, some of the features described here for the equatorial Pacific were visible in the signal of SSH minus steric height. Stammer (1997) noted that the amplitude of interannual variability was similar to that of the annual cycle in the Pacific, “rendering a climatological annual cycle nearly nonexistent.” This is worth keeping in mind, but we note that the Niño 3.4 index was positive throughout all but a few months of Stammer’s 3-year measurement period and was above the El Niño threshold during two of the years (Figure 7.3), a period during the prolonged ENSO event (1990 to 1995) (Trenberth and Hoar 1996). This was not a representative period for climatology of the equatorial Pacific but was part of the 1990 to 1995 prolonged ENSO that was noted by Trenberth and Hoar (1996) to be the “longest on record.”

Wakata and Kitaya (2002) examined the annual cycle in Pacific SSH anomalies for the time period January 1992 to December 1997—the period of Stammer’s analysis plus the two following years. They thus encountered one weak La Niña but also the buildup and peak of the strong 1997 to 1998 El Niño, so even this 5-year period would be biased heavily toward El Niño conditions (Figure 7.3). Their Figure 1 is the first good view of the SSH annual cycle in the equatorial Pacific, and it is reproduced in our Figure 7.4.

The equatorial features in Figure 7.4 are consistent with the description of Wang et al. (2000), with some exceptions. The SSH anomaly maximum near 4°N peaks near 120°W, roughly 20° further east than the peak reported by Wang et al. The local maximum reported by Wang et al. near 5°N at the western boundary is not evident in the results of Wakata and Kitaya. The eastward phase propagation on the equator reported by Wang et al. and Yu and McPhaden (1999) is also not evident in Figure 7.4, although it is possible that latitudinal smoothing has obscured this feature.

Qu et al. (2008) analyzed 13 years of merged satellite altimetry (1993 to 2005) and demonstrated that the bimodal seasonal signal noted by Wang et al. (2000) near the western boundary is in part due to a semiannual complement to the annual Rossby wave. The amplitude and phase of their annual and semiannual harmonics are shown in Figure 7.5. The maximum of SSH anomalies near 5°N is further west than the maximum of Wakata and Kitaya (2002) and more in line with

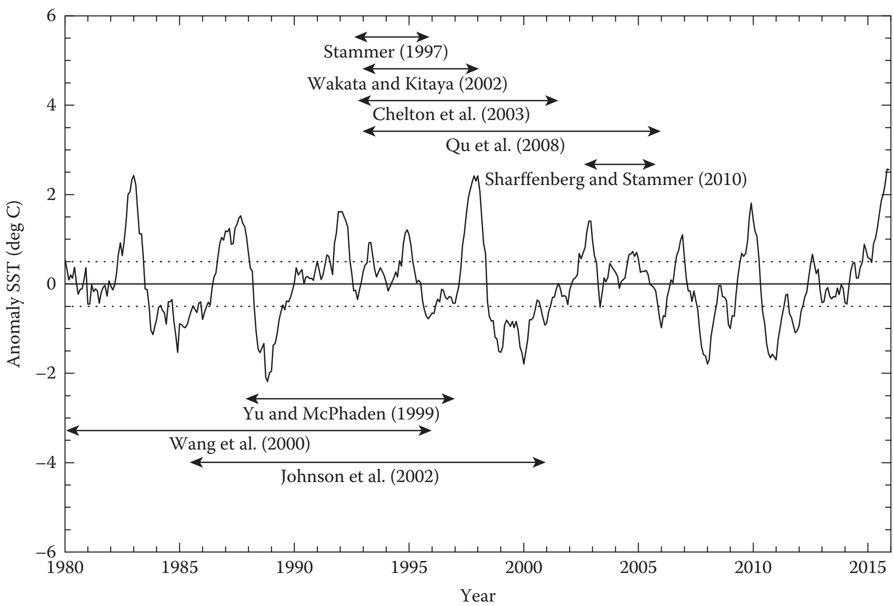

FIGURE 7.3 Niño 3.4 index with measurement spans of cited analyses. Studies shown below the index curve analyzed subsurface thermal data. Studies above the curve analyzed satellite altimetry data. Dotted lines are the ± 0.5C El Niño and La Niña thresholds.

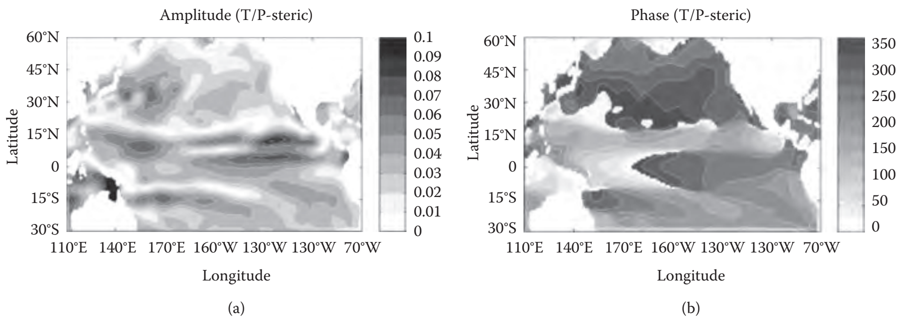

FIGURE 7.4 Amplitude (a: cm) and phase (b: year day) of annual harmonic from 5 years of T/P SSHa measurements (1/1993–12/1997). (From Wakata, Y., and Kitaya, S., *J. Oceanogr.*, 58, 439–450, 2002. With permission.)

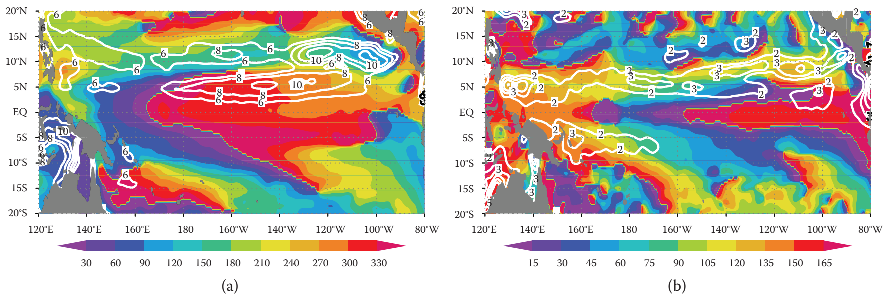

FIGURE 7.5 Amplitude (contours: cm) and phase (colors: year day) of the annual (a) and semiannual (b) harmonics from analysis of 13 years of merged satellite altimetry data sets (1/1993–12/2005) by Qu et al. (2008). From their Figure 1.

the results of Wang et al. (2000). The westward propagation at 5°N and 5°S can be seen for both harmonics. On the equator, eastward propagation can be seen for the annual harmonic east of about 130°W, with westward propagation to the west of 130°W. For the semiannual harmonic, propagation on the equator is westward to the east of the dateline and eastward to the west of the dateline.

The contribution that the semiannual harmonic makes to the variability near 5°N at the western boundary may explain why that feature was not evident in the annual harmonic plot of Wakata and Kitaya (2002). Other differences between Figures 7.4 and 7.5 (e.g., the longitude of the 4–5°N maximum, and the ratio of amplitude at 4–5°N to that on the equator) may be due to the dominant El Niño conditions of the Wakata and Kitaya study versus the longer time series incorporated in the Qu et al. study.

In a study of the SECC near 10°S, Chen and Qiu (2004) displayed the basin-wide amplitude and phase of the annual harmonic between 4°S and 20°S, from an analysis of 10 years of satellite altimetry (1992–2003). They used a dynamical model to demonstrate that the annual variability of the SECC was due to an interplay between different Rossby wave regimes north and south of 10°S. Their representation of the annual harmonic of SSH in the southern part of the equatorial waveguide (4–10°S) is consistent with that of Qu et al. (2008).

7.3.1.2.3 Contributions from Altimetry: Geostrophic Currents

Bonjean and Lagerloef (2002) estimated equatorial Pacific surface currents using satellite measurements of SSHA (T/P), winds (SSM/I speed and QuikSCAT wind vectors), and SST (AVHRR). Their current anomalies included geostrophic, Ekman, Stommel shear, and thermal wind shear components, averaged over the upper 30 m. The annual cycle, as represented by climatologies for the months of January, April, July, and October, over the years 1993–1996 and 1999 (i.e., without the 1997 to 1998 El Niño period) compared well with coincident cycles of 15-m drifter data and TAO array current measurements. From this effort, sprang the Ocean Surface Current Analyses Real-Time (OSCAR) product that has been used in subsequent analyses of the annual cycle.

Scharffenberg and Stammer (2010) used data from the 3-year tandem T/P and Jason-1 mission (September 2002 to September 2005) to calculate geostrophic velocity anomalies everywhere outside ±1° from the equator. They analyzed global distributions of the annual harmonics of both zonal and meridional current anomalies. Their findings for the equatorial Pacific were in general agreement with those of Johnson et al. (2002). Westward propagation is evident (in their Figure 9) north of the equator (NECC and NSEC) but not south of the equator (SSEC). There is a hint of phase propagation on the equator in the far eastern Pacific, but with results plotted from 65°S to 65°N, it is difficult to say anything about this feature. Scarffenberg and Stammer noted only minor discrepancies between their annual cycle phases and those of Johnson et al. (with 165°W in their paragraph 45 apparently intended to be 165°E). They noted one major discrepancy between their phase and that reported by Yu and McPhaden (1999) at 5°N in the eastern Pacific. The significance of this is unclear, but it may be simply a phase difference between the currents analyzed by Scharffenberg and Stammer and the thermocline anomalies reported by Yu and McPhaden. The 3-year period of the tandem mission examined by Scharffenberg and Stammer (2010) was another that contained 2 years during which the Niño 3.4 index exceeded the El Niño threshold, and the index was positive for all but a few months. Once again, these results would be biased toward El Niño conditions, and this may also have contributed to phase discrepancies in the eastern Pacific.

Hsin and Qiu (2012) used 18 years (October 1992 to September 2010) of OSCAR surface currents to construct monthly climatologies of zonal current anomalies north of the equator in order to define the seasonal cycle of the NECC. Although the OSCAR currents contain Ekman currents and thermal wind shear in addition to the geostrophic component, Hsin and Qiu showed that the OSCAR-derived climatologies compared well with those constructed from only geostrophic current anomalies calculated from AVISO SSHA during the same time span. Their analysis was able to show that the annually varying transport of the NECC does not propagate; it remains in phase across the width of the basin. What does propagate westward is the meridional march of the current centerline. Complementing the observations with a process model, they showed that the seasonal cycle of the NECC east of the dateline is controlled by both Ekman pumping and the annual Rossby wave, while west of the dateline it is controlled primarily by the latter.

7.3.1.2.4 The Annual Rossby Wave

Historical studies of the annual Rossby wave in the equatorial Pacific (e.g., Lukas and Firing 1985; Kessler and McCreary 1993) noted a meridional asymmetry in the thermal signature that is in contrast to classical equatorial theory (Moore and Philander 1977) and that they could not satisfactorily explain. Chelton et al. (2003) showed that the meridional asymmetry (as revealed by analysis of 8.5 years of satellite altimetry, November 1992 to May 2001) is consistent with solutions of the shallow water equations linearized about the mean equatorial currents reported by Johnson et al. (2002). In the eigenvalue solutions, the current system slows the phase speed (consistent with observations) through eastward advection by the Equatorial Undercurrent and a decrease in the background potential vorticity gradient at the peaks of the NSEC and SSEC, which coincide with the latitudes where the Rossby wave's meridional velocity has extrema. The meridional structure of the wave appears to deform in a manner that reduces changes to the dispersion relation (Durland et al. 2011).

The studies cited here are representative of a larger group that we have not had room to cover but that have advanced our knowledge of the equatorial Pacific's seasonal cycle through analyses of satellite altimetry. The excellent spatial and temporal coverage of the satellite measurements has allowed investigation of details that were inaccessible to the pre-satellite studies, and it is apparent that the long altimetric SSH record we now have presents continued opportunities for improving our understanding of the seasonal cycle in this dynamically important region.

7.3.1.3 Interannual and Decadal Variability

Since the mid-1990s, SSH- and SSH-derived surface geostrophic currents have been used routinely to monitor equatorial Kelvin waves and Rossby waves, large-scale zonal slope of the thermocline, equatorial upper-ocean heat content, and surface currents in the tropical Pacific associated with ENSO as well as to test and improve ENSO forecast models for studies. Picaut and Busalacchi (2000) provided an overview of the related studies prior to 2000. Here we focus on major areas of studies of interannual variability of the tropical Pacific Ocean in relation to studies since the 2000s, especially regarding the additional understanding of the roles of Kelvin and Rossby waves in ENSO cycle, the related physics in association with ENSO theories, and ENSO diversity that was not discussed by Picaut and Busalacchi (2000).

7.3.1.3.1 ENSO-Related SSH Variability

Dominant SSH fluctuations associated with classical El Niño/La Niña reflect the variations in the zonal tilt of the thermocline associated with the variation in the strength of the trade wind, with increasing (decreasing) SSH in the eastern (or western) equatorial Pacific during El Niño (e.g., McPhaden et al. 1998) vice versa during La Niña. During the peak of the 1997–1998 El Niño, the positive SSH in the eastern equatorial Pacific exceeded 30 cm, with negative SSH anomalies in the western equatorial Pacific being about half this magnitude (Picaut et al. 2002) (Figure 7.6). The SSH signature associated with this strong El Niño, fortuitously captured within the first few years of the T/P altimeter, provided researchers with significant insights about processes associated with El Niño development and challenged models to reproduce the observed changes.

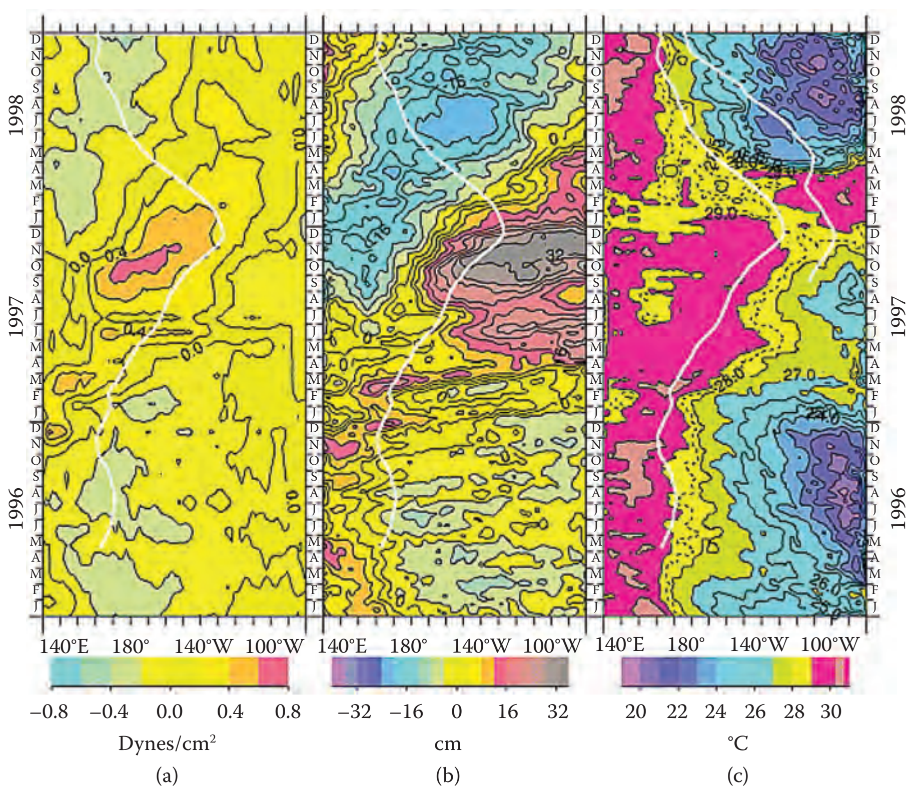

FIGURE 7.6 Longitude-time distribution of the following parameters averaged within 2_N–2_S: (a) SSM/I zonal wind stress anomaly, (b) TOPEX/Poseidon sea level anomaly, and (c) sea surface temperature. The thick lines represent the trajectory of a hypothetical drifter moved by the h2_N–2_Si zonal total geostrophic current.

In particular, the SSH observations together with other measurements illustrated that the delayed action oscillator mechanism was active during the onset of the 1997 El Niño, while both delayed oscillator and the recharge/discharge oscillator mechanisms were at work during the transition to the 1998 La Niña.

Altimeter-derived SSH has significantly advanced our knowledge of how the combined effects of wind-forced equatorial Pacific Kelvin and Rossby waves and their reflections at the eastern and western boundaries regulate the zonal displacement of the eastern edge of the western Pacific warm pool and thermocline depth fluctuations that are important to the development and decay of El Niño and La Niña events (e.g., Delcroix et al. 2000). The reflection of Rossby waves at western boundaries is key to the termination of El Niño in the Delayed Oscillator theory. Although such reflection was found to have 80%–90% efficiency, based on altimeter SSH, the resultant upwelling Kelvin waves during the peak of the 1997–1998 El Niño was insufficient to terminate the event without the upwelling Kelvin waves generated by easterly wind anomalies during the peak of that event (Boulanger et al. 2003, 2004). It suggests that reflected Rossby waves and wind-forced Kelvin waves are both important to the ENSO cycle. The equatorial Kelvin and Rossby waves also influence the stretching of upper-ocean isopycnals and barrier layer thickness that have implications in air-sea interactions (Bosc et al. 2009).

ENSO-related SSH variations are not limited to the zonal seesaw of SSH about the dateline associated with the Delayed Oscillation theory but also are associated with a meridional fluctuation of SSH (or warm water volume, WWV) with a fulcrum near 5°N that is dominated by geostrophic advection across 5°N (Alory and Delcroix 2002). The Recharge/Discharge Oscillator theory that describes the fluctuations of tropical Pacific WWV cannot explain the hemispheric asymmetry of the observed meridional SSH changes. The tropical Pacific WWV changes were attributed to the residual of opposing effects of meridional Ekman and geostrophic transports (Bosc and Delcroix 2008).

In the tropical Pacific, the OSCAR current estimates described previously have greatly facilitated diagnostic analysis of ENSO events. In the equatorial Pacific, surface current anomalies typically lead SST anomalies about 3 months with a magnitude that scales with the SST anomaly magnitude (Figure 7.7, Lumpkin et al. 2013). These features suggest the importance of surface current in regulating ENSO SST. Near the equator, accurate representation of ocean surface currents based on altimeter and scatterometer data (e.g., OSCAR) remains challenging because both the geostrophic and Ekman theories become invalid as the Coriolis parameter approaches zero.

El Niño characteristics experience changes on multidecadal timescales. Since 2000, there has been more frequent occurrence of the so-called El Niño Modoki (Ashok et al. 2007) or central-Pacific El Niño (Kao and Yu 2009). Different from the classical eastern-Pacific El Niño where large positive SSH anomalies developed in the eastern-equatorial Pacific, El Niño Modoki events are generally associated with positive SSH anomalies and surface current convergence in the central-equatorial Pacific due to the anomalous zonal wind convergence associated with El Niño Modoki (e.g., Ashok et al. 2007; Singh et al. 2011). The recharge/discharge of WWV as inferred from SSH is also different between the two types of El Niño events (Singh and Delcroix 2013). The more frequent occurrence of El Niño Modoki in the early to mid-2000s resulted in a decadal trend of increasing SSH in the central-equatorial Pacific region during the 1998–2007 period (Behera and Yamagata 2010).

7.3.1.3.2 Decadal and Multidecadal SSH Changes

Large decadal fluctuations in SSH and ocean surface winds have been observed in the Indo-Pacific region since the early 1990s (Lee and McPhaden 2008). Large-scale trends of the SSH and wind fields during 1993–2000 were generally opposite to those during 2000 to 2006 over much of the Indo-Pacific domain, although the trends in the earlier period were generally larger. The 1993–2000 and 2000–2006 SSH trends for the tropical Indo-Pacific domain (Figure 7.8c and d) were associated with opposite trends of zonal wind stress between these two periods both in the tropical Pacific and Indian oceans (Figure 7.8a and b). The coherent decadal changes of SSH and wind fields in the

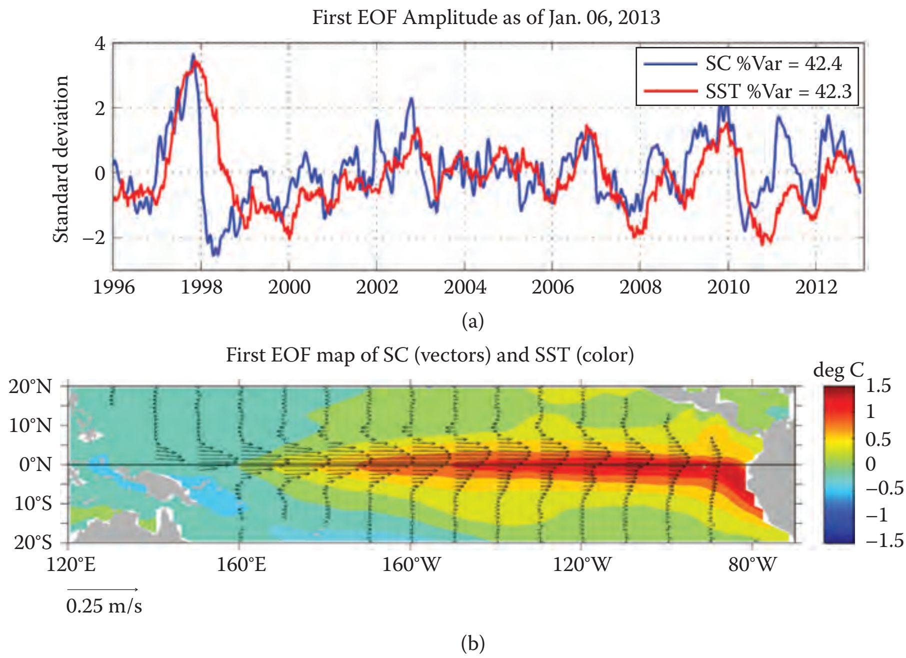

FIGURE 7.7 The time series (a) and spatial structure (b) of the first EOF of non-seasonal ocean surface current and SST in the tropical Pacific, showing the 2–3-month lead time of the surface current over SST. (After Lumpkin, R., et al., *Bull. Am. Meteorol. Soc.*, 94, S62–S65, 2013. With permission.)

Pacific and Indian oceans reflect oceanic and atmospheric linkages between the two basins caused by decadal oscillation of the Walker Circulation in the tropical Pacific and Indian sectors. These linkages are further discussed in the next subsection. The maximum net increase of SSH in the northwest tropical Pacific (as seen from Figure 7.8c) during 1993–2000 was 20 cm–25 cm, rivaling the magnitude of SSH changes in the eastern equatorial Pacific associated with strong El Niño events. It has been shown that the Interdecadal Pacific Oscillation (IPO), which is highly correlated with decadal variability of ENSO, can have a large influence on decadal variability of SSH patterns over the tropical Pacific (Frankcombe et al. 2015).

The SSH trend observed by altimetry during 1993 to 2009 in the Pacific was examined in the context of longer tide gauge records and wind stress patterns (Merrifield 2011). The dominant regional trends are also found to be associated with SSH rise in the western tropical Pacific (WTP), accompanied by weak SSH rise or fall in the eastern Pacific basin. This basin-scale SSH pattern is shown to be associated with the IPO (or decadal variability of ENSO; see Section 2.1 of Han et al. 2017 for a review and references therein). The rate of SSH rise in the WTP, however, has increased significantly since the early 1990s relative to the preceding 40 years, as revealed by tide gauge records. The IPO cannot explain this intensification because its strength did not intensify. Modeling studies suggest that warming of the tropical Indian Ocean enhances surface easterly trade winds and thus contributes to the intensified WTP SSH rise in the past few decades (Luo et al. 2012; Hamlington et al. 2014; Han et al. 2014). Also through numerical model experiments, it has been shown that warming of the Atlantic strengthens the equatorial easterlies and intensified SSH rise in the WTP since the early 1990s and plays an important role in causing the global warming “hiatus” since the early 2000s—a period when global mean surface temperature does not increase (McGregor et al. 2014). During this period, altimeter data however show a persistent rising trend of global mean SSH (Church et al. 2013). Because SSH represents an integral heating effect from both surface and subsurface ocean,

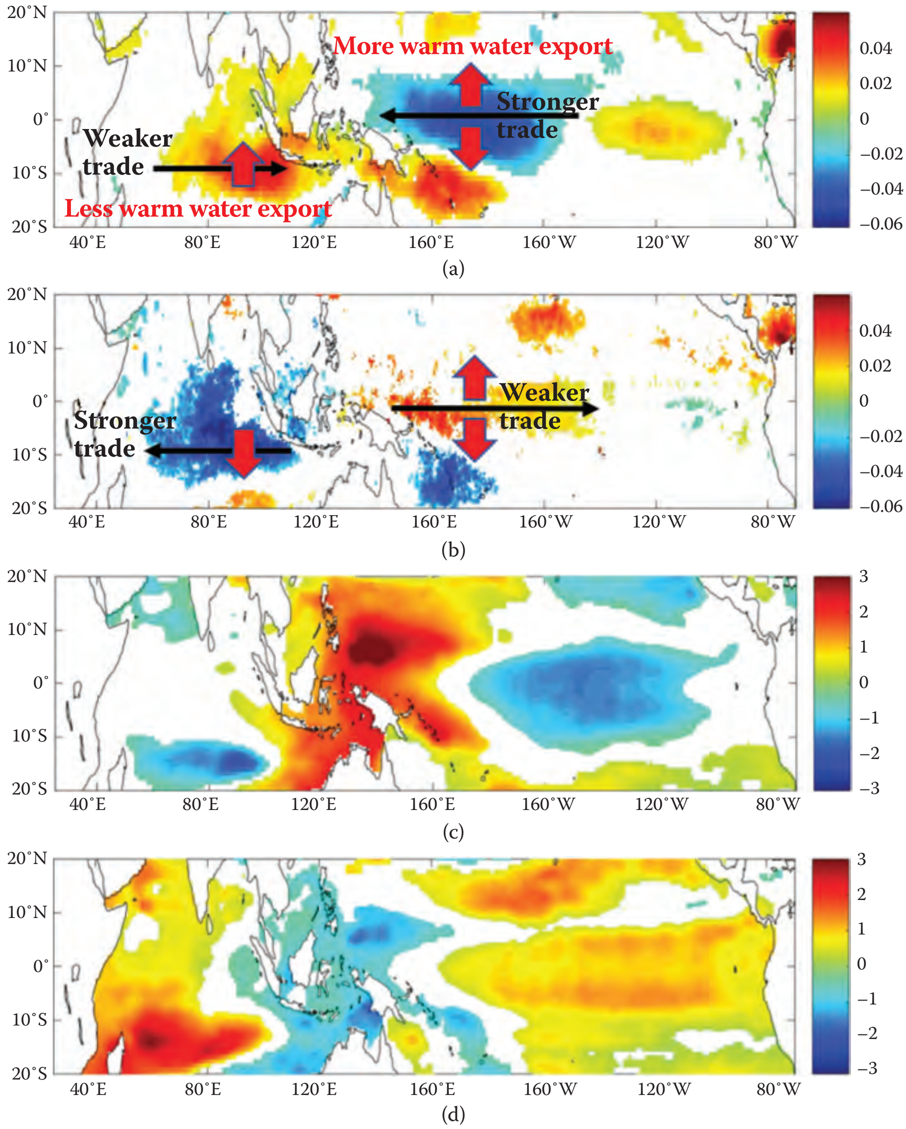

FIGURE 7.8 Trends of zonal wind stress during 1993–2000 estimated from ERS scatterometer data (a) and those during 2000–2006 estimated from QuikScat scatterometer data. SSH trends for the 1993–2000 (a) and 2000–2006 (b) periods estimated from altimeter data. These observations were also used to infer changes in the upper and lower branches of the shallow overturning circulations in the Pacific and Indian Oceans and their linkages as described in Indo-Pacific linkage subsection. (a) Trend of zonal wind stress: 1993–2000 (dyn/cm^2/yr), (b) Trend of zonal wind stress: 2000–2006 (dyn/cm^2/yr), (c) Trend of SSH: 1993–2000 (cm/yr), and (d) Trens of SSH: 2000–2006 (cm/yr). (After Lee, T., et al., *Dyn. Atmos. Oceans*., 2010; adapted from Lee, T., and McPhaden, M. J., *Geophys. Res. Lett*., 35, L01605, 2008.)

the SSH rise indicates that the excessive heat received by the Earth's surface has gone into the subsurface ocean.

Robust intensification also has been detected for decadal (10 to 20 years) SSH variability in the WTP since the early 1990s. This intensification results from the "out of phase" relationship of SST anomalies between the Indian Ocean and IPO since 1985, which produces "in phase" effects on the WTP SSH variability (Han et al. 2014). These results suggest that decadal and multidecadal SSH changes in the tropical Pacific also involve the linkage of the coupled ocean-atmosphere systems in the tropical Pacific and Indian Ocean sectors. From 1998 to 2007, the decadal trend of sea level shows a different spatial pattern: Sea level rises in the tropical central Pacific flanked by sea level fall in the western and eastern basins (Behera and Yamagata 2010). This abnormal condition is due to the frequent occurrence of central Pacific El Niño events during 2000 to 2004, which are associated with wind convergence to the dateline. Evidently, decadal changes in ENSO behavior will induce changes in the spatial patterns of decadal sea level variations. Note that interannual ENSO events may affect decadal trend calculations (Timmermann et al. 2010; Solomon and Newman 2012).

As mentioned earlier, SSH shows large interannual and decadal changes since 1992 in the Maritime Continent oceanic region that linked the western tropical Pacific and eastern tropical Indian Ocean warm pool (e.g., Lee and McPhaden 2008). Excluding SSH data in the Maritime Continent region reduced the estimated global mean SSH trend by 20% (7%) over the 2005 to 2010 (1992 to 2010) period (von Schuckmann et al. 2014). Because the trends of regional SSH over much of the global ocean to the first order resemble those of regional thermosteric height (e.g., Stammer et al. 2013), the lack of *in situ* observations in the Maritime Continent (especially from Argo) raises the question about its potential impact on the estimated interannual and decadal changes of global ocean steric height or heat content (von Schuckmann et al. 2014). This is among the examples highlighting the advantages of altimetry in sampling marginal seas.

7.3.1.3.3 Inference of Subtropical Cell Variability Using SSH

Meridional heat transport carried by the shallow meridional overturning circulations that connect the tropical and subtropical Pacific (i.e., the subtropical cells or STCs; McCreary and Lu 1994) plays an important role in regulating the climatological and decadal variation of tropical Pacific upper-ocean heat content, SST, and the related coupled ocean-atmosphere decadal climate variability (e.g., Kleeman et al. 1999; Schneider et al. 1999; Liu and Philander 2000; Hazeleger et al. 2001, McPhaden and Zhang 2002; Zhang and McPhaden 2006). SSH measurements provide a good proxy to study the variability of the lower branches of the Pacific STCs. The Northern and Southern Hemisphere STCs in the Pacific are somewhat symmetric about the equator. In a zonal average sense, the upper branches of the STCs (the poleward Ekman flows) carry warm surface waters from the tropics to the subtropics, while the lower branches (the pycnocline geostrophic flows) transport colder subsurface waters from the subtropics toward the tropics. The lower branches consist of an interior pathway and a western-boundary (WB) pathway in both hemispheres. The WB pathway is associated with low-latitude western-boundary currents (LLWBCs) in both hemispheres (i.e., the Mindanao Current in the north and New Guinea Coastal Undercurrent in the south). On average, they both carry pycnocline waters equatorward. Figure 2 in Lee and Fukumori (2003) illustrates the hemispheric asymmetry of the lower branches of the northern and southern STCs and the respective WB and interior pathways.

The SSH difference between the western and eastern boundaries of the tropical Pacific Ocean is found to be anticorrelated with that of thermocline depth difference and thus provides a good proxy for the variation of net meridional geostrophic transport in the pycnocline (i.e., the strength of the lower branches of the STCs; Lee and Fukumori 2003). On the other hand, meridional Ekman transport inferred from zonal wind stress is indicative of the strength of the upper branches of the STCs. Therefore, west-east SSH difference derived from altimeter measurements and zonally averaged zonal wind stress from scatterometer observations together are complementary to monitoring the lower and upper branches of the STCs on interannual and decadal timescales (e.g., Lee and Fukumori 2003; Lee and McPhaden 2008).

The zonal slope of the SSH anomalies across the WB and that across the interior (from the eastern side of the LLWBCs to the eastern boundary) also provide a good proxy for the variations of the WB and interior pycnocline transports (Lee and Fukumori 2003). Because of this, SSH measurements have offered insight into the zonal structure of the interannual and decadal variation of interior and WB pycnocline flows associated with the STCs. In contrast to the time mean picture where the interior and WB pycnocline flows reenforce each other (both being equatorward), the interannual and decadal anomalies of the interior and WB pycnocline transports counteract each other (Lee and Fukumori 2003). Therefore, they play opposite roles in regulating the tropical Pacific upper-ocean heat content. However, the variation of the interior pycnocline transport anomalies is more dominant than that of the WB transport anomalies. The compensation of the interior pycnocline transport by WB transport in the Southern Hemisphere is more significant (approximately 60%) than that in the Northern Hemisphere (approximately 30%). These features are robustly reproduced by various ocean models and data assimilation products (e.g., Hazeleger et al. 2004, Capotondi et al. 2005; Schott et al. 2007). The anticorrelated variability of WB transport and interior pycnocline transport is the result of the oscillation of the tropical gyres in the western Pacific caused by off-equatorial wind stress curl associated with the trade wind variations (Lee and Fukumori 2003).

The counteracting WB transport and interior pycnocline transport have important implications for the monitoring of the lower branch of the STC. Previous studies of decadal variation of the lower branch of the Pacific STC were mostly based on interior expandable bathythermograph (XBT) and conductivity-temperature-depth (CTD) observations and assumed that the WB transports do not change significantly (e.g., McPhaden and Zhang 2002, 2004). While broad-scale *in situ* observations in the interior ocean (e.g., from XBT, CTD, and Argo) provide observations to estimate the interior pycnocline transport, they do not have sufficient coverage near the LLWBCs to estimate their transports. Process-oriented experiments such as the Northwestern Pacific Ocean Climate Experiment (NPOCE) and the Southwest Pacific Ocean Circulation and Climate Experiment (SPICE) have developed the capability to study the LLWBCs based on measurements from gliders, moorings, and research vessels. However, the capability to develop sustained monitoring systems for the LLWBCs based on *in situ* instruments has not been established. SSH measurements from satellites provide a means to fill this observational gap, especially with sustained multiple altimeter missions operating simultaneously and with the upcoming Surface Waters Ocean Topography (SWOT) mission that will enhance the temporal and spatial samplings important to resolve the mesoscale variability associated with the LLWBCs. The contribution of satellite SSH in filling this observational gap is important to closing the volume, heat, and freshwater budget of the tropical Pacific Ocean. Altimeter data along with high-resolution ocean models have provided further insights about the variability of the South Pacific LLWBC in the Solomon Sea—in particular, the regional distributions of SSH anomalies and eddy kinetic energy and their relationships to ENSO (e.g., Melet et al. 2010, 2011).

7.3.2 Tropical Indian Ocean

7.3.2.1 Intraseasonal Variability

Over the tropical Indian and Pacific oceans, the large amplitude intraseasonal variability (20–90 days) in the troposphere is dominated by the MJO (Madden and Julian 1971, 1972), which exhibits strong spectral peaks at 30- to 60-day periods. The MJO propagates eastward during boreal winter and both eastward and poleward during boreal summer (see reviews by Zhang 2005; Lau and Waliser 2012). The summertime MJOs, together with the quasi-biweekly mode, are often referred to as the monsoon IntraSeasonal Oscillations (ISOs; Goswami 2012). The ISOs constantly interact with the underlying ocean and influence many weather and climate systems over the globe.

Compared to the MJO, oceanic intraseasonal variability was detected a decade later. Earlier *in situ* observations revealed 30- to 60-day variability in zonal currents at several locations in the equatorial Indian Ocean (Luyten and Roemmich 1982; McPhaden 1982; Schott et al. 1994; Reppin et al. 1999). Spectral peaks at 30- to 60-day and 26-day periods of meridional currents were observed in the western basin, but the maximum peak shifted to 12–15 days in the central and eastern basin (Mertz and Mysak 1984; Reverdin and Luyten 1986; Reppin et al. 1999; *review of* Schott and McCreary 2001). Numerical modeling studies suggested that the 30- to 60-day currents were forced by the 30- to 60-day oscillations of winds associated with the MJO (Moore and McCreary 1990), and the 26-day meridional current in the western basin resulted from oceanic instabilities (Kindle and Thompsen 1989; Woodberry et al. 1989; Tsai et al. 1992). Oceanic instabilities are not forced by the corresponding atmospheric variability (e.g., wind); rather, they arise from nonlinearity of the oceanic system. The sporadic *in situ* observations, however, could not depict the basin-scale structure and evolution associated with the intraseasonal currents.

Since the beginning of the twenty-first century, rapid advancement has been made in understanding the Indian Ocean intraseasonal variability, and satellite altimetry has played a vital role in this rapid development. Han et al. (2001) performed spectral analysis using the T/P altimeter data with 10-day resolution and model zonal surface current from 1993 to 1999 and showed that the strongest spectral peaks of SSH and zonal current occur at the 90-day period and secondary peaks occur at 40–70 days across the equatorial Indian Ocean (Figure 7.9), even though the MJO winds that force them peak at the 30- to 60-day periods. Similar spectral peaks are found using T/P and Jason data (Fu 2007), weekly AVISO SSH, and OSCAR zonal surface currents for various temporal periods (Iskandar and McPhaden 2011; Nagura and McPhaden 2012). Model experiments suggested that while the 40- to 70-day peaks are directly driven by the strong 30- to 60-day winds, the large 90-day peak is associated with the excitation of the basin resonance mode for the second baroclinic mode at the 90-day period in the equatorial Indian Ocean, which is established by the constructive interference between the eastward-propagating Kelvin wave directly forced by winds and the westward-propagating Rossby waves reflected from the eastern boundary (Han et al. 2001; Han 2005; Nagura and McPhaden 2012). While the T/P SSH showed an eastern basin concentration of the 90-day resonance (Han 2005; Fu 2007), the multiple-satellite merged AVISO SSH with finer spatial resolution showed a clear 90-day basin mode structure as theoretically predicted, with a significantly larger amplitude in the western basin (Han et al. 2011).

The strong intraseasonal variability of zonal current and SSH can significantly impact the spring and fall Wyrtki Jets (Masumoto et al. 2005), and can induce eastward monsoon jets during summer ISOs (Senan et al. 2003). The intraseasonal signals observed in the equatorial basin do not just stay there; they exert remote influence on intraseasonal variability in the Bay of Bengal and the Arabian Sea via coastal Kelvin waves that propagate around the perimeter of the North Indian Ocean (with the coasts to their right in the Northern Hemisphere) and through Rossby waves that radiate westward, as revealed by the AVISO SSH data (Girish Kumar et al. 2013; Suresh et al. 2013). They can also have large influence on the Indonesian Seas via eastward-propagating equatorial Kelvin waves, coastal Kelvin waves that propagate with the coast to their left in the Southern Hemisphere (Sprintall et al. 2000; Schouten et al. 2002; Iskandar et al. 2005, 2006; Zhou and Murtugudde 2010), and subsequently westward-radiating Rossby waves from the eastern basin, affecting the east Indian Ocean upwelling (Chen et al. 2015), impacting the IOZDM (Rao and Yamagata 2004; Han et al. 2006) and affecting the Indonesian Throughflow (Qiu et al. 1999; Drushka et al. 2010; Schiller et al. 2010; Pujiana et al. 2013; Shinoda et al. 2016).

In the central and western interior basin, analyses of the AVISO SSH together with *in situ* and other satellite observations showed that the arrival of downwelling intraseasonal Rossby waves might play an important role in triggering the primary MJO events, which were not immediately preceded by other MJO activities (Webber et al. 2012). Indeed, a downwelling intraseasonal Rossby wave reflected from the eastern Indian Ocean boundary was observed by SSH during the CINDY/DYNAMO field campaign period (Yoneyama et al. 2013; Zhang et al. 2013). Together with the analysis of *in situ* data from the Research Moored Array for African-Asian-Australian Monsoon Analysis and Prediction (RAMA) array (McPhaden et al. 2009) and from the CINDY/DANAMO field campaign, it was shown that this Rossby wave significantly influenced the upper ocean structure in the thermocline ridge region, where many MJO events were initiated (Shinoda et al. 2013).

In addition to the equatorial Kelvin and Rossby waves, satellite altimeter data were also used to identify Yanai waves at 20- to 30-day periods in the western equatorial basin and at approximately 14-day periods in the central and eastern basin, even though the weekly AVISO data appeared to

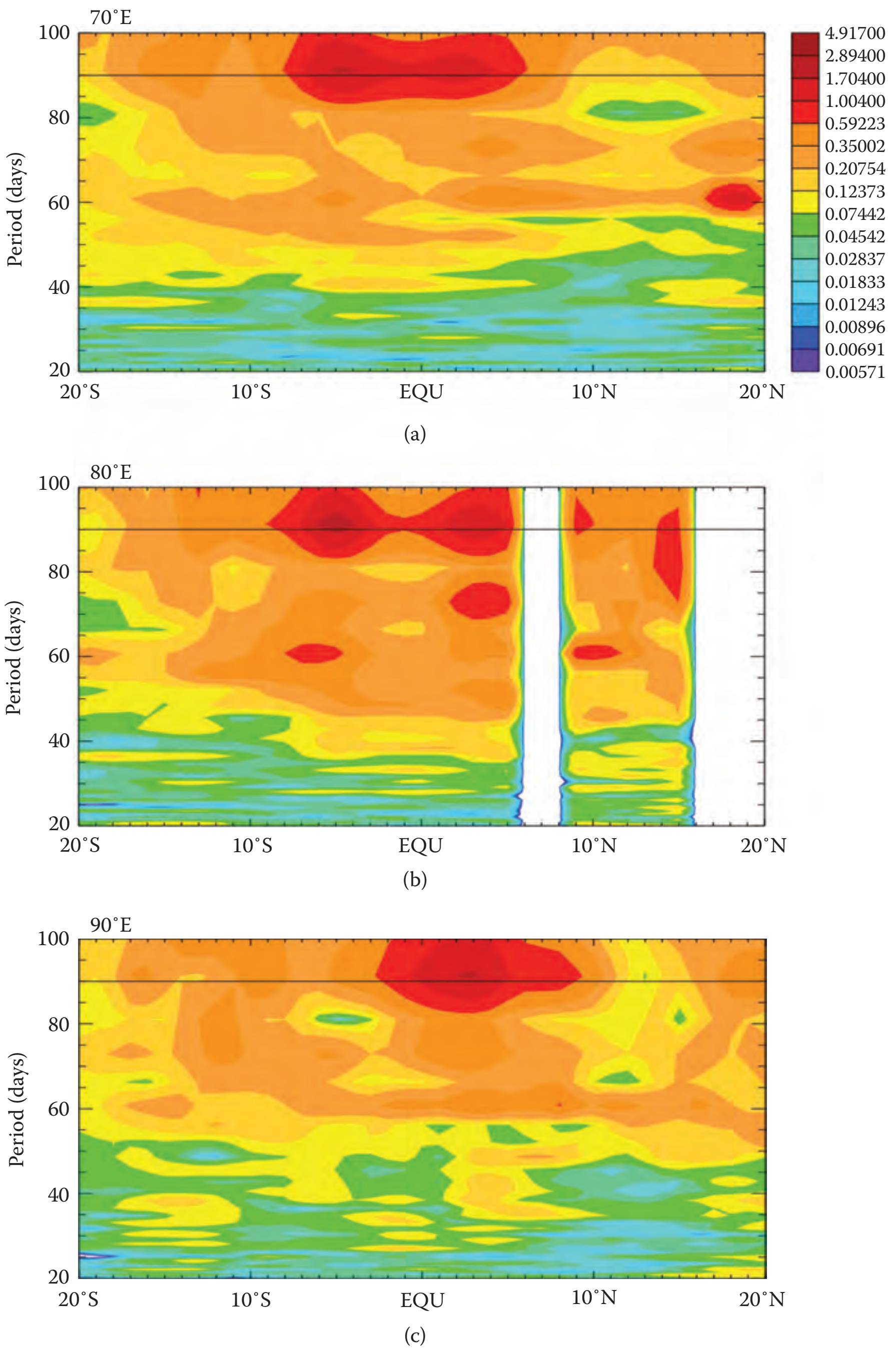

FIGURE 7.9 Meridional section for variance spectra (cm^2) of TOPEX/Poseidon SSH anomaly along (a) 70°E, (b) 80°E, and (c) 90°E of the Indian Ocean, based on an 8-year record (1993–2000) with a 10-day resolution. The 90-day and most 30- to 60-day spectral peaks are above 95% significance. (From Han, W., *J. Phys. Oceanogr.*, 35, 708–728, 2005.)

significantly underestimate the power of the approximately 14-day Yanai waves (Chatterjee et al. 2013). The Yanai waves (also referred to as "mixed Rossby-gravity waves") are antisymmetric about the equator and correspond to the *in situ* observed meridional currents at the equator discussed earlier. Modeling experiments suggested that the Yanai waves at the approximately 14-day period were forced by winds associated with the 10- to 20-day mode of monsoon ISOs, and those at 20- to 30-day periods in the western basin were influenced by western boundary reflection and oceanic instabilities (Miyama et al. 2006; Chatterjee et al. 2013). Furthermore, satellite altimeter data were also used to detect intraseasonal variability that resulted from oceanic instabilities in various regions of the Indian Ocean—for example, the western equatorial basin; the Somali, Omani, and Yemeni coasts (Brandt et al. 2003; Han 2005); the South Equatorial Current in the southeast tropical basin (Feng and Wijffels 2002; Yu and Potemra 2006; Ogata and Masumoto 2010, 2011; Trenary and Han 2012); and the subtropical south Indian Ocean (Palastanga et al. 2007).

7.3.2.2 Seasonal Cycle

The amplitudes of the annual cycle of SSH variation in the Indian Ocean are characterized by two local maxima in the South Indian Ocean between 5°S and 15°S as well as by local maxima in the Arabian Sea and the Bay of Bengal (Fu and Smith 1996) (Figure 7.10). In the South Indian Ocean, the two local maxima are centered near 60°E and 95°E (with amplitudes of approximately 9 and 12 cm) and a minimum near 75°E (with an amplitude of approximately 2 cm) (Wang et al. 2001). These observed features are reproduced reasonably well by ocean model simulations (e.g., Périgaud and Delecluse 1992; Fu and Smith 1996). Although these studies were based on just a couple of years of altimeter data, annual variations of the depth of the 20C isotherm based on over a decade of XBT data show a similar structure (Masumoto and Meyers 1998). These annual SSH variations were attributed to local wind-forced annual Rossby waves in the interior ocean superimposed on Rossby waves forced by winds in the east and those radiated from the eastern boundary near the exits of the Indonesian Throughflow (Périgaud and Delecluse 1992). The two local maxima and the minimum of annual SSH variations in the South Indian Ocean were explained through the constructive and

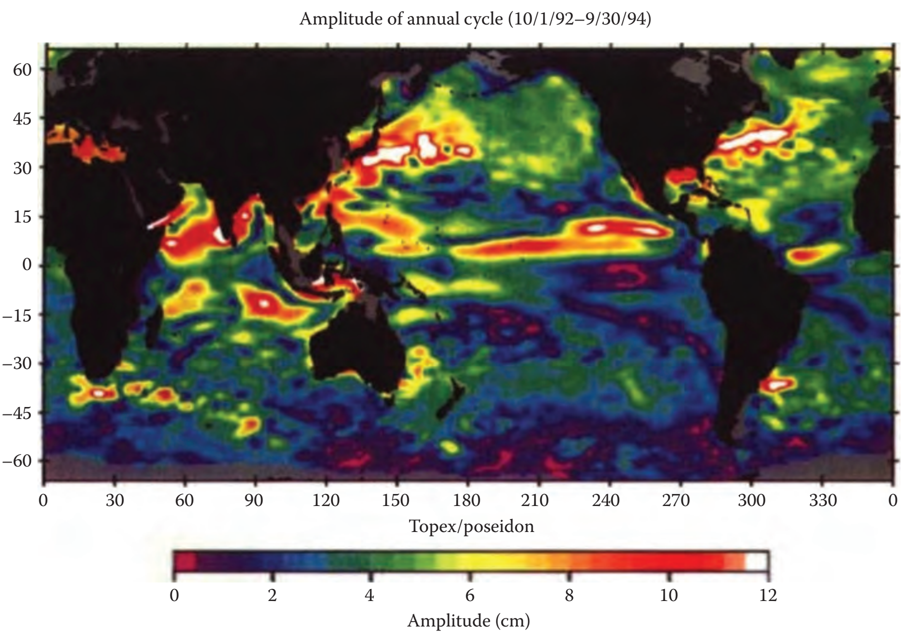

FIGURE 7.10 Amplitude of the annual cycle of SSH estimated from TOPEX/Poseidon altimeter data. (After Fu, L., and Smith, R., *Bull. Am. Meteorol. Soc.*, 77, 2625–2636, 1996. With permission.)

destructive interferences of the local response to Ekman pumping and Rossby wave propagation, respectively (Wang et al. 2001). Radiation of the Rossby waves from the ITF exit has some effects on annual SSH variations in the eastern part but not the western part of the basin (Wang et al. 2001; Trenary and Han 2012).

In the Arabian Sea, strong seasonal fluctuations of SSH (with an annual-harmonic amplitude of 10–15 cm) were observed between 6°N and 10°N and were associated with westward propagating annual Rossby waves radiated from the western side of the Indian subcontinent and continuously forced by the wind-stress curl over the central Arabian Sea (Brandt et al. 2002). These waves are related to a time-dependent meridional overturning cell that sloshes water northward and southward. Between 58°E and 68°E in the central Arabian Sea, Rossby waves induced up to 10 Sv of transport in the upper 500 m (southward in August 1993 and northward in January 1998) and a few Sv below 2000 m, as shown by hydrographic measurements. The annual SSH variations can be explained by the first- and second-mode annual Rossby waves. The reflection of annual Rossby waves also affects the western boundary currents.

In the Bay of Bengal, large-scale annual SSH variations reflect the oceanic response to seasonal wind stress curl over the bay (Schott and McCreary 2001). However, there are smaller-scale features in the bay, especially in the southwestern part. SSH-derived surface geostrophic currents suggest that during the peak of the summer monsoon, there is a western-boundary confluence near 10°N, with the East India Coastal Current (EICC) flowing northward to the north of 10°N and southward to the south (Eigenheer and Quadfasel 2000). This confluence is supplied mostly by the South Monsoon Current across 6°N that circulates cyclonically around an area of low SSH (i.e., the Sri Lanka Dome) (Vinayachandran et al. 1999). After the summer monsoon in late September, the EICC begins to flow southward, and by November, southward flow is seen everywhere along the east coasts of India and Sri Lanka. During this time, SSH suggests a slow cyclonic circulation around the Bay of Bengal, which breaks up into several cells as the monsoon season develops (Eigenheer and Quadfasel 2000).

7.3.2.3 Interannual Variability

A dominant mode of interannual climate variability of the coupled ocean-atmosphere system in the Indian Ocean sector is the IOZDM (Saji et al. 1999). During a positive IOZDM event, anomalous southeasterly winds in the equatorial Indian Ocean raise the thermocline depth and depress SSH in the southeastern equatorial Indian Ocean, reducing SST and triggering a coupled ocean-atmosphere interaction across the equatorial Indian Ocean that is akin to the Bjerknes feedback process associated with ENSO in the Pacific sector. The strongest IOZDM event occurred during 1997 to 1998 and associated with the El Niño event in the Pacific. During November 1997 to May 1998, negative anomalies of SSH in the southeastern equatorial Indian Ocean reached −30 cm, associated with approximately −2°C of SST anomaly (Webster et al. 1999; Yu and Reinecker 1999) (Figure 7.11). During this period, the SSH in the western equatorial Indian Ocean was higher than normal, but the magnitude of the anomaly was smaller than that in the east by a factor of three. Negative IOZDM events (e.g., in 1996 and 1998) are associated with opposite changes of SSH. The effects of the IOZDM on SSH are not limited to the equatorial band but extend northward into the western part of the Bay of Bengal and southward to the region off the west coast of Australia and to the southwest tropical Indian Ocean (SWTIO) (Han and Webster 2002; Rao et al. 2002).

The SWTIO region (5°S–15°S, 50°E–70°E), referred to as the Seychelles-Chagos thermocline ridge (Hermes and Reason 2008), is associated with a shallow thermocline and a unique region with open-ocean upwelling as evidenced by enhanced phytoplankton concentration (Murtugudde et al. 1999; Schott and McCreary 2001). The shallowness of the thermocline makes the SST in this region easily affected by the fluctuations of thermocline depth. This is well characterized by the highly correlated SSH and SST measurements (e.g., Xie et al. 2002; Rao and Behera 2005). Local Ekman pumping associated with the variability of IOZDM- or ENSO-related wind fields causes Rossby wave

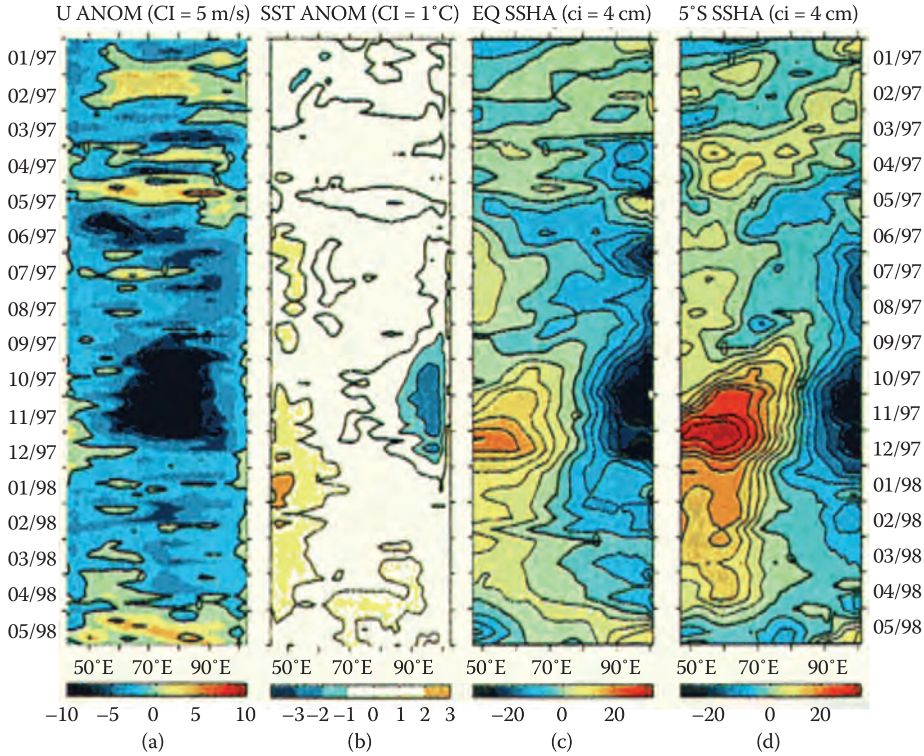

FIGURE 7.11 Time-longitude sections (an average over 2°S–2°N) of anomalous (a) zonal winds (5-day means) from NCEP reanalyses and (b) weekly-mean SST from Reynolds analyses; and time-longitude sections of anomalous SSH from TOPEX/Poseidon altimeter (10-day average) along (c) the equator and (d) 5°S. The anomalies are all derived from the 1981–1996 base period monthly means except the SSH anomalies which are deviations from the 1993–96 base period monthly means. (After Yu, L., and Rienecker, M. M., *Geophys. Res. Lett.*, 26, 735–738, 1999. With permission.)

propagation into this region that influences the thermocline depth (and thus SSH), thereby inducing feedback to the atmosphere (including precipitation) through its effect on SST (Xie et al. 2002). These processes, referred to as coupled ocean-atmosphere Rossby waves (Xie et al. 2002), offer potential predictability for SST and tropical cyclones in the western Indian Ocean.

In contrast to the IOZDM-related interannual maxima of SSH variations in the eastern and western equatorial Indian Ocean, the Seychelles-Chagos thermocline ridge, and the western Bay of Bengal, there are local minima of interannual SSH variations in the central equatorial Indian Ocean, Arabian Sea, and the eastern Bay of Bengal off the east coast of India and Sri Lanka. The minima (maxima) of interannual variability have been explained by the destructive (constructive) interference of the direct wind-forced response and reflected Rossby waves from the eastern boundaries (Shankar et al. 2010).

Shankar et al. (2010) also concluded that, on interannual timescales, the SSH adjustment to wind forcing in the Indian Ocean is less than that of the forcing, leading to a quasi-steady balance. This distinguishes the interannual minima from those at annual and semiannual timescales—for instance, the local minimum of annual Rossby wave amplitude in the middle of the southern tropical Indian Ocean (Wang et al. 2001).

McPhaden and Nagura (2014) examined whether SSH in the equatorial Indian Ocean could be used as a predictor of IOZDM development as it is for ENSO in the Pacific sector. They used SSH measurements and an analytical linear equatorial wave model to interpret the evolution of the

IOZDM in the context of the recharge oscillator theory. They found that, as in the Pacific, there are zonally coherent changes in SSH (heat content) along the equator prior to the onset of IOZDM events, an indication of a recharge oscillator being at work. These SSH changes are modulated by wind-forced westward propagating Rossby waves at 5°S–10°S, which at the western boundary reflect into Kelvin waves trapped at the equator. The biennial character of the IOZDM is affected by this cycling of wave energy between 5°S and 10°S and the equator. However, SSH changes are a weaker leading indicator of IOZDM-related SST anomalies than they are for ENSO. This is because IOZDM is also affected by ENSO through atmospheric teleconnection in addition to the recharge oscillator process in the Indian Ocean.

7.3.2.4 Decadal and Multidecadal Changes

The South Indian Ocean experienced large decadal changes from early 1993–2006 (Lee 2004; Lee and McPhaden 2008). During 1993–2000, SSH over much of the interior of the southern tropical Indian Ocean (8°S–20°S, 50°E–100°E) dropped by 10–20 cm while that in the east from the equator to 30°S (i.e., off the coasts of southern Sumatra and Java, near the ITF exit, and off the west coast of Australia) increased by similar amounts (Figure 7.8c). This pattern reversed during 2000–2006 (Figure 7.8d). These decadal changes of SSH were attributed to two factors. The SSH changes in the interior of the southern tropical Indian Ocean were caused by the wind stress curl forcing associated with decadal changes of the South Indian Ocean trade winds as well as the westward propagation of Rossby waves. In the east, the decadal SSH changes are largely due to the transmission of the SSH signals from the tropical Pacific through the Indonesian Seas via coastal Kelvin waves. The decadal SSH changes in the South Indian Ocean were associated with regional SSH changes in the entire Pacific Ocean that also had opposite trends between 1993 and 2000 and 2000 and 2006, as discussed in Section 7.3.2.2. The associated changes in SSH differences between the western and eastern boundaries have strong implications for the changes in the lower branches of the Indian and Pacific Ocean STCs. The linkages of the lower branches of the Pacific and Indian Ocean STCs through an oceanic tunnel and the relationship of the upper branches of the Pacific and Indian Ocean STCs through an atmospheric bridge are discussed in Section 7.5. In the equatorial and North Indian Ocean, SSH experienced a basin-wide decrease from 1993 to 2003 but a sharp increase from 2004 to 2013 (Srinivasu et al. 2017).

Both observational analyses and OGCM experiments suggest that winds over the Indian Ocean are the primary forcing for the basin-wide decadal sea level patterns, with the ITF having a significant contribution primarily in the eastern basin (e.g., Lee and McPhaden 2008; Trenary and Han 2012; Nidheesh et al. 2013, Zhuang et al. 2013; Wang et al. 2015). The observed North Indian Ocean basin-wide decadal reversal of SSH trends around 2003–2004 resulted from the combined effect of changing surface turbulent heat flux and cross-equatorial heat transport, both being associated with decadal changes of surface winds over the Indian Ocean (Srinivasu et al. 2017). Thermosteric effect is the primary contributor to the spatial patterns of decadal SSH variability (e.g., Fukumori and Wang 2013; Nidheesh et al. 2013; Srinivasu et al. 2017), while the halosteric effect is significant only in certain regions (Nidheesh et al. 2013). In particular, nearly two-thirds of the SSH rise in the southeastern-south-central tropical Indian Ocean in the past decade was due to a halosteric effect (Llovel and Lee 2015). In fact, this is the only region in the global ocean between approximately 66°S and 66°N (the domain sampled by most altimeters and Argo floats) where large-scale decadal SSH changes are primarily due to a halosteric instead of a thermosteric effect. The large halosteric effect in this region was associated with a freshening in this region in the upper 200–300 m as observed by Argo data. Possible causes for this freshening in the past decade include the relatively abrupt strengthening of the ITF since 2007 as observed by mooring observations in the Makassar Strait (the main branch of the ITF inflow from the Pacific; Gordon et al. 2012) and enhanced precipitation in the Maritime Continent region (Llovel and Lee 2015; Hu and Sprintall 2016).

The forcing that caused decadal SSH variability in the Indian Ocean is associated with various climate modes, including decadal changes in the IOZDM, the Decadal Indian Ocean Basin

(DIOB) mode, and the PDO, as well as decadal changes in ENSO. In particular, the basin-wide decadal SSH patterns over the tropical Indian Ocean (north of 20°S) are primarily forced by wind stress associated with climate modes, with the maximum amplitude occurring in the SCTR in the southwest tropical Indian ocean. Further studies are necessary to better decipher the relative contributions of different climate modes in forcing decadal SSH changes in the Indian Ocean. Given the dominant roles of wind forcing, the high correlation of decadal SSH variations near Mumbai with Indian monsoon rainfall (Shankar and Shetye 1999) may result from monsoon wind influence (Li and Han 2015) rather than the salinity effect associated with monsoon rainfall as suggested previously (Shankar and Shetye 1999). In addition to the effects of surface forcing, ocean internal variability also has large amplitudes near the Somali coast, western Bay of Bengal, and subtropical south Indian Ocean.

7.3.3 Indo-Pacific Linkage and Indonesian Throughflow

As mentioned in Sections 7.3.2.2 and 7.4.4, the variations of SSH differences between the western and eastern boundaries in the northern and southern tropical Pacific and southern tropical Indian Oceans reflect the variations of net meridional pycnocline transports associated with the lower branches of the STCs in these oceans. The rise (fall) of SSH at the western boundaries of the northern and southern tropical Pacific Ocean during 1993–2000 (2000–2006) (Figure 7.8c and d in Section 7.3.2.2) and the lack of significant SSH changes at the eastern boundaries implied an increased (reduced) equatorward convergence of pycnocline waters into the tropical Pacific (Lee and McPhaden 2008). The SSH signals at the western boundary of the tropical Pacific are transmitted through the Indonesian Seas via coastal Kelvin waves, affecting the SSH at the ITF exits and the eastern boundary of the southern tropical Indian Ocean off the west coast of western Australia. Therefore, the increase (decrease) of SSH at the western boundary of the northern tropical Pacific during 1993 to 2000 (2000 to 2006) caused similar SSH changes in the eastern Indian Ocean. This mechanism has in fact been at work throughout the entire period of the altimeter record since 1993 (Wang et al. 2015). Because the SSH at the western boundary of the southern tropical Indian Ocean did not experience significant changes, the SSH differences between the western and eastern boundary of the southern tropical Indian Ocean implied strengthening (weakening) of the northward pycnocline flow associated with the lower branch of the Indian Ocean STC. Therefore, the decadal anomalies of pycnocline transports associated with the Pacific and Indian Ocean STCs are anticorrelated, with the ITF region providing the oceanic tunnel that links the lower branches of the Pacific and Indian Ocean STCs.

Wind stress measurements from ERS and QuikSCAT scatterometers implied similarly opposite decadal changes of the upper branches of the Pacific and Indian Ocean STCs that were driven by anticorrelated decadal changes of the tropical Pacific and South Indian Ocean trade winds (Lee and McPhaden 2008). The anticorrelated changes in the Pacific and Indian Ocean trade winds were attributed to the decadal oscillation of the Walker Circulation, providing an atmospheric bridge that links the upper branches of the Pacific and Indian Ocean STCs. Therefore, the oscillation of the Walker circulation and the SSH signals transmitted through the Indonesian Seas provide an atmospheric bridge and oceanic tunnel that connect the Pacific and Indian Ocean STCs. As a result of these two mechanisms, the Pacific and Indian Ocean STCs play opposite roles in regulating the upper-ocean heat content of the Indo-Pacific domain.

Sustained, direct measurements of ITF transport are extremely challenging in large part because of the complicated geometry with many inflow and outflow passages (Sprintall et al. 2014). Systematic *in situ* measurements of transport at the main ITF inflow (Makassar Strait) and three main outflow passages were undertaken by the international program INSTANT but only for 3 years (2004 to 2006) (Sprintall et al. 2009). Only the Makassar Strait has mooring measurements that have encompassed decadal timescales (1996–1998 and 2004 onward) (Gordon et al. 2012). The ITF is known to be forced by the positive pressure difference between the tropical Pacific and tropical Indian oceans (Wyrtki 1987). Early attempts to infer ITF transport variations using SSH measurements from tide gauge stations in the islands of the tropical Pacific and Indian oceans or altimeter-derived SSH measurements showed that the resultant estimates were sensitive to the locations of reference points in the two oceans (e.g., Wyrtki 1987; Clarke and Liu 1994; Potemra et al. 1997; Potemra 2005). The lack of *in situ* measurements of ITF transport in the past has also made it difficult to validate the proxy estimates of ITF transport derived from SSH measurements. The extended record of satellite altimetry and gravimetry, along with estimates of upper-700 m ITF transport based on XBT data have provided an opportunity to identify the optimal locations in the tropical Pacific and Indian oceans where SSH from altimetry and ocean bottom pressure (OBP) can be used as a proxy to estimate ITF transport. The SSH and OBP differences between 11°N, 162°E in the Pacific and 0°E, 80°E in the Indian Ocean were found to provide optimal proxy estimates of the ITF transport when these measurements are used in a theoretical calculation that combined the "geostrophic control" theory (Garrett and Toulany 1982) and "hydraulic control" theory (Whitehead 1989) as proposed by Song (2006) and Qu and Song (2009). The derived proxy time series of ITF transport compared reasonably well (both for time mean and interannual variations) with estimated ITF transport derived from *in situ* measurements in the Makassar Strait (the main branch of the ITF inflow from the Pacific) during 1996–1998 and 2004–2011.

The large increase of SSH in the western tropical Pacific during 1993–2000 associated with the strengthening of the tropical Pacific trade winds implied a strengthening of the ITF transport. Although no direct measurements of ITF transports were available for this period, ITF transport estimates derived from a suite of ocean data assimilation products consistently depicted the strengthening of the ITF transport during this period (Figure 12 in Lee et al. 2010), which is also evident in the estimates derived from SSH by Susanto and Song (2015). This further supports the notation that SSH measurements can be used as a proxy to infer interannual and decadal changes of the ITF transport.

7.4 SUMMARY

Following the success of the T/P mission, sustained measurements of SSH from precision altimetry into the twenty-first century with the Jason series satellites have significantly advanced the understanding far beyond what was learned in the 1990s in terms of tropical ocean variability, its relationship with various climate variability, and inter-basin linkage, from intraseasonal to multidecadal timescales.

On intraseasonal timescales, SSH measurements have allowed in-depth understanding of the wavenumber-frequency characteristics associated with different behaviors of TIWs (e.g., mixed Rossby-gravity wave versus meridional-mode Rossby wave nature). The measurements have also enabled the detection of coastal Kelvin waves in various basins and marginal seas, including those transmitting through the Indonesian archipelago. On seasonal timescales, SSH measurements help identify and improve the understanding of annual Rossby waves and basin modes that have been identified in various basins as well as the dynamics of the Wyrtki Jet in the Indian Ocean.

The sustained altimeter measurements also have been essential to improving the understanding of interannual ocean variability and its relationships with interannual climate modes such as ENSO, IOZDM, and Tropical Atlantic Interannual climate variability. In particular, these measurements illustrate the importance of the combined effects of wind-forced equatorial Kelvin waves and the reflections of equatorial Rossby waves at boundaries to regulate the zonal movement of the eastern edge of the tropical Pacific warm pool and the thermocline depth fluctuations as well as the influence on the ENSO cycle in the context of the Delayed Oscillator theory. Altimeter measurements also characterize the meridional recharge/discharge of tropical Pacific warm water volume on ENSO timescales and reveal the hemispheric asymmetry of the recharge/discharge that was not described by the Recharge Oscillator theory. The continuing altimeter record has made it possible to examine the diversity of ENSO events such as the eastern- versus central-equatorial Pacific El Niño in terms of their distinct SSH and surface current signatures, which have significant implications for the interaction between the thermocline and the mixed-layer and thus the associated air-sea interaction.

Significant new knowledge about decadal to multidecadal SSH variability has been gained from the analysis of SSH measurements and the related ocean modeling effort. Studies of the nearly two-and-one-half decade SSH record derived from precision altimetry in the context of the longer record of the sparsely distributed tide gauge data help in the understanding of the processes responsible for enhanced decadal variability during the altimeter record and shed light on the relative contributions of natural decadal variability versus potential climate change forcing.

Satellite-derived SSH and wind measurements have been used to infer the variations in the strengths of the shallow meridional overturning cells that are the primary mechanisms for tropical-subtropical exchanges both in the Pacific and Indian oceans (i.e., the STCs). They also elucidated the linkages of the STCs in the Pacific and Indian oceans, including the oceanic tunnel of the Indonesia Seas (coastal Kelvin wave propagation and the Indonesian Throughflow) and the atmospheric bridge associated with the two branches of the Walker Circulation over the tropical Pacific and Indian oceans. SSH measurements have also revealed the zonal structure of the lower branch (pycnocline flow) of the STC in the Pacific Ocean, characterized by anticorrelated variability of the LLWBC transport and that of the interior pycnocline flow and a substantial compensation of the latter by the former. This has important implications for the closure of the volume, heat, and freshwater budgets of the tropical Pacific Ocean and supports the need for sustained observing systems in the LLWBC regions together with broad-scale observations in the ocean interior to close these budgets.

Finally, it is important to note that sustaining the climate data record of satellite SSH to monitor tropical ocean variability is critical to address the knowledge gaps in terms of the interplay among multidecadal variation of interannual climate modes such as ENSO, intrinsic multidecadal variability that may be linked to the extratropics, and climate change signals. Sustaining the SSH climate data record is also important to the continued improvement of ENSO forecast models, especially in light of the apparent degradation of ENSO forecast skills after the turn of the century. As the length of the SSH climate data record continues to increase, the measurements become increasingly useful for evaluating climate models. The current generation of altimeters still has limited capability for characterizing SSH variations in coastal regions and for sub-mesoscale variability (e.g., in the Solomon Sea and the Maritime Continent region). The upcoming SWOT mission will significantly improve this capability.

The ocean and climate research community has recognized the importance of sustaining and enhancing altimeter measurements of the world's ocean (including tropical oceans) to advance research and applications in the aforementioned areas. This was well described by several community whitepapers of the OceanObs'09 Conference (http://www.oceanobs09.net/proceedings/cwp/) as well as the Tropical Pacific Observing System 2020 (TPOS2020) First Report released recently (http://tpos2020.org/). Sustaining and enhancing satellite altimetry will continue to improve our understanding of tropical ocean and climate variability and predictions.

ACKNOWLEDGMENTS

The research by T. Lee was carried out at the Jet Propulsion Laboratory (JPL), California Institute of Technology, under a contract with NASA, supported by the NASA Physical Oceanography Program. J. T. Farrar and T. Durland acknowledge support from NASA grants NNX13AE46G and NNX14AM71G. W. Han is supported by NASA NNH16ZDA001N-OSTST.

REFERENCES

Alory, G., and T. Delcroix, (2002), Interannual sea level changes and associated mass transports in the tropical Pacific from TOPEX-Poseidon data and linear model results (1964–1999). *J. Geophys. Res.*, 107, C10, 3153, doi:101029/2001JC00106.

Aman, A., L. Testut, P. Woodworth, T. Aarup, and D. Dixon, 2007. Seasonal sea level variability in the Gulf of Guinea from altimetry and tide gauge, *Rev. Ivoir. Sci. Technol.*, 09 (2007) 105–118.

Andrew, J. A. M., H. Leach, and P. L. Woodworth, (2006), The relationships between tropical Atlantic sea level variability and major climate indices. *Ocean Dyn.*, 56, 452–463, doi:10.1007/s10236-006-0068-z.

Arnault, S., B. Bourlès, Y. Gouriou, and R. Chuchla, (1999), Intercomparison of the upper layer circulation of the western equatorial Atlantic ocean: In situ and satellite data, *J. Geophys. Res.*, 104, C9, 21171–21194, doi:10.1029/1999JC900124.

Arnault, S., and R.E. Cheney, (1994), Tropical Atlantic sea level variability from GEOSAT (1985–1989), *J. Geophys. Res.*, 99, C9, 18207–18223, doi:10.1029/94JC01301.

Arnault, S., G. Eldin, B. Bourlès, Y. Dupenhoat, Y. Gouriou, A. Aman, R. Chuchla, F. Gallois, E. Kestenaere, and F. Marin, (2004), In situ and satellite data in the tropical Atlantic ocean during the EQUALANT99 experiment, *Int. J. Remote Sens*., vol. 25, n°7-8, 1291–1296.

Arnault, S., L. Gourdeau, and Y. Ménard, (1992), Comparison of the altimetric signal with in situ measurements in the Tropical Atlantic Ocean, *Deep Sea Res.*, 39, 3/4, 481–499.

Arnault, S., and E. Kestenare, (2004), Tropical Atlantic surface current variability from 10 years of TOPEX/Poséïdon altimetry, *Geophys. Res. Lett.*, 31, L03308, doi:10.1029/2003GL019210.

Arnault, S., and C. LeProvost, (1997), Regional identification in the tropical Atlantic ocean of residual tide errors from an empirical orthogonal function analysis of the TOPEX/Poséïdon altimetric data, *J. Geophys. Res.*, 102, C9, 21011–21036, doi:10.1029/97JC00983.

Arnault, S., and J. L. Mélice, (2012), Investigation of the interannual variability of the tropical Atlantic Ocean from satellite data, *Mar. Geod*., vol. 35, n°1, 151–174, doi:10.1080/01490419.2012.718212.

Arnault, S., Y. Ménard, and J. Merle, (1990), Observing the Tropical Atlantic Ocean in 86-87 from altimetry, *J. Geophys. Res*., 95, C10, 17921–17945, doi:10.1029/JC095iC10p17921.

Arnault, S., Y. Ménard, and M. C. Roucquet, (1989), Variability of the Tropical Atlantic in 1986–1987 as observed by GEOSAT and in situ data. *Adv. In Space Res.*, 9, n°7, 7,383–7,386, doi:10.1016/0273-1177(89)90189-0.

Arnault, S., I. Pujol, and J. L. Mélice, (2011), In situ validation of Jason-1 and Jason-2 altimetry missions in the tropical Atlantic Ocean, *Mar. Geod.*, 34, 319–339, doi:10.1080/01490419.2011.584833.

Arruda, W. Z., and E. J. Campos, Sea level anomaly trends in the South Atlantic around 10°S, Anais XV Simpósio Brasileiro de Sensoriamento Remoto - SBSR, Curitiba, PR, Brasil, 30 de abril a 05 de maio de 2011, INPE p.7200.

Artamonov, Y. V., (2006), Seasonal variability of geostrophic currents in the Atlantic ocean according to the altimetry data. *Phys. Oceanogr.*, 16, 3, 60–71.

Ashok, K., S. K., Behera, S. A. Rao, H. Weng, and T. Yamagata, (2007), El Niño Modoki and its possible teleconnection, *J. Geophys. Res.*, 112, C11007, doi:10.1029/2006JC003798.

Behera, S., and T. Yamagata, (2010), Imprint of the El Niño Modoki on decadal sea level change. *Geophys. Res. Lett.*, 37, L23702, doi:10.1029/2010GL045936.

Bonjean, F., and G. S. E. Lagerloef, (2002), Diagnostic model and analysis of the surface currents in the tropical Pacific Ocean, *J. Phys. Oceanogr.*, 32(10), 2938–2954.

Bosc, C., and T. Delcroix, (2008), Observed equatorial Rossby waves and ENSO-related warm water volume changes in the equatorial Pacific Ocean. *J. Geophys. Res.*, 113, C06003, doi:10.1029/2007JC004613.

Bosc, C., T. Delcroix, and C. Maes, (2009), Barrier layer variability in the western Pacific warm pool from 2000–2007. *J. Geophys. Res.*, 114, C06023, doi:10.1029/2008JC005187.

Boulanger, J.-P., S. Cravatte, and C. Menkes, (2003), Reflected and locally wind-forced interannual equatorial Kelvin waves in the western Pacific Ocean. *J. Geophys. Res.*, 108, 3311, doi:10.1029/2002JC001760.

Boulanger, J.-P., C. Menkes, and M. Lengaigne, (2004), Role of high- and low-frequency winds and wave reflection in the onset, growth and termination of the 1997–1998 El Niño. *Clim. Dyn.*, 2, 267–280, doi:10.1007/s00382-003-0383-8.

Brandt, P., M. Dengler, A. Rubino, D. Quadfasel, and R. Schott, (2003), Intraseasonal variability in the southwestern Arabian Sea and its relation to the seasonal circulation, *Deep Sea Res. II*, 50, 2129–2141.

Brandt, P., L. Stramma, F. Schott, J. Fischer, M. Dengler, and D. Quadfasel, (2002). Annual Rossby waves in the Arabian Sea from TOPEX/POSEIDON altimeter and in situ data. *Deep-Sea Res. II*, 49, 1197–1210.

Bunge, L., and A. J. Clarke, (2009), Seasonal propagation of sea level along the Equator in the Atlantic, L., *J. Phys. Oceanogr.*, 39, 1069–1074. doi:10.1175/2008.4003.1.

Busalacchi, A.J., M. J. McPhaden, J. Picaut, (1994), Variability in the equatorial Pacific sea surface topography during the verification phase of the TOPEX/Poséïdon mission. *J. Geophys. Res.*, 99, C12, 24725–24738.

Capotondi, A., M. A. Alexander, C. Deser, et al., (2005), Anatomy and decadal evolution of the Pacific Subtropical-Tropical Cells (STCs). *J. Clim.*, 18, 3739–3758.

Carson, M., A. Köhl, and D. Stammer, (2015), The impact of regional multidecadal and century-scale internal climate variability on sea level trends in CMIP5 Models. *J. Clim.*, 28, 853–861, doi:10.1175/JCLI-D-14-00359.1.

Carton, J.A., (1989), Estimates of Sea Level in the Tropical Atlantic Ocean Using GEOSAT Altimetry, *J. Geophys. Res.*, 94, C6, 8,029–8,039, doi:10.1029/JC094iC06p08029.

Carton, J. A., and E. Katz, (1990), Estimates of the zonal slope and seasonal transport of the Atlantic North Equatorial Countercurrent, *J. Geophys. Res.*, 95, C3, 3,091–3,100, doi:10.1029/JC095iC03p03091.

Carton, J. A., G. A. Chepurin, G. K. Korotaev, and T. Zhu, (1993), Comparison of dynamic height variations in the tropical Atlantic during 1987–1989 as viewed in Sections hydrography and GEOSAT altimeter. *J. Geophys. Res.*, 98, 14369–14377, doi:10.1029/93JC01505.

Castelão, G. P., and W. E. Johns, (2011), Sea surface structure of North Brazil Current rings derived from shipboard and moored acoustic Doppler current profiler observations, *J. Geophys. Res.*, 116, C01010, doi:10.1029/2010JC006575.

Chaigneau, A., G. Eldin, and B. Dewitte, (2009), Eddy activity in the 4 major upwelling systems from satellite altimetry (1992–2007), *Prog. In Oceanogr.*, 83, 117–123, doi:10.1016/J.pocean.2009.07.012.

Chatterjee, A., D. Shankar, J. P. McCreary Jr., and P. N. Vinayachandran, (2013), Yanai waves in the western equatorial Indian Ocean, *J. Geophys. Res. Oceans*, 118, 1556–1570, doi:10.1002/jgrc.20121.

Chelton, D. B., M. G. Schlax, J. M. Lyman and G. C. Johnson, (2003), Equatorially trapped Rossby waves in the presence of meridionally sheared baroclinic flow in the Pacific Ocean. *Progr. Oceanogr.*, 56, 323–380.

Chelton, D. B., F. Wentz, C. Gentemann, R. deSzoeke, and M. Schlax, (2000), Satellite microwave SST observations of transequatorial tropical instability waves. *Geophys. Res. Lett.*, 27, 1239–1242.

Chen, S., and B. Qiu, (2004), Seasonal variability of the South Equatorial Countercurrent. *J. Geophys. Res.*, 109, C08003, doi:10.1029/2003JC002243.

Chen, G., W. Han, Y. Li, D. Wang, and T. Shinoda, 2015: Intraseasonal Variability of Upwelling in the Equatorial Eastern Indian Ocean. J. Geophys. Res.-Oceans, 120, 7598–7615, DOI: 10.1002/2015JC011223.

Cheney, R. E., B. C. Douglas, and L. Miller, (1989), Evaluation of GEOSAT altimeter data with applications to tropical Pacific sea level variability. *J. Geophys. Res.*, 94, C4, 4737–4747.

Cheney, R. E., and L. Miller, (1990), Recovery of the sea level signal in the western tropical Pacific from GEOSAT altimetry. *J. Gophys. Res.*, 95, C3, 2977–2984.

Church, J. A., P. U. Clark, A. Cazenave, et al., (2013), Sea Level Change. In: *Climate Change 2013: The Physical Science Basis. Contribution of Working Group I to the Fifth Assessment Report of the Intergovernmental Panel on Climate Change*, Stocker, T. F., D. Qin, G.-K. Plattner, M. Tignor, S. K. Allen, J. Boschung, A. Nauels, Y. Xia, V. Bex and P. M. Midgley (eds.). Cambridge University Press, Cambridge, United Kingdom and New York, NY.

Clarke, A. J., and X. Liu, (1994), Interannual sea level in the northern and eastern Indian Ocean, *J. Phys. Oceanogr.*, 24, 1224–1235, doi:10. 1175/1520-0485(1994)024<1224:ISLITN>2.0.CO;2.

Collins, M., S. An, W. Cai, et al., (2010), The impact of global warming on the tropical Pacific Ocean and ElNiño. *Nat. Geosci.*, 3, 391–397.

Cravatte, S., J. Picaut, and G. Eldin, (2003), Second and first baroclinic Kelvin modes in the equatorial Pacific at intraseasonal timescales. *J. Geophys. Res.*, 108, 3266, doi:10.1029/ 2002JC001511.

Delcroix, T., B. DwWitte, Y. duPenhaot, et al., (2000), Equatorial waves and warm pool displacements during the 1992–1998 El Niño Southern Oscillation events: Observation and modeling. *J. Geophys. Res.*, 105, 26045–26062.

Delcroix, T., J. Picaut, and G. Eldin, (1991), Equatorial Kelvin and Rossby waves evidenced in the Pacific ocean through GEOSAT sea level and surface current anomalies. *J. Geophys. Res.*, 96, 3249–3262.

Didden, N., and F. Schott, (1993), Eddies in the North Brazil Current retroflection region observed by GEOSAT altimetry. *J. Geophys. Res.*, 98, c11, 20121–20131.

Ding, H., N. S. Keenlyside, and M. Latif, (2009), Seasonal cycle in the upper equatorial Atlantic Ocean, *Geophys. Res. Lett.*, 114, C09016, doi:10.1029/2009JC005418.

Ding, H., N. S. Keenlyside, and M. Latif, (2010), Equatorial Atlantic interannual variability: Role of heat content, *J. Geophys. Res.*, 115, C09020, doi:10.1029/2010JC006304.

Djakoure, S., P. Penven, B. Bourles, J. Veitch, and V. Kone, (2014), Coastally trapped eddies in the north of the Gulf of Guinea, *J. Geophys. Res.*, 119, 6805–6819, doi:10.1002/2014JC010243.

Donohue, K., and M. Wimbush, (1998), Model results of flow instabilities in the tropical Pacific Ocean, *J. Geophys. Res.*, 103, 21401–21412.

Drushka, K., J. Sprintall, S. T. Gille, and I. Brodjonegoro, (2010), Vertical structure of Kelvin waves in the Indonesian throughflow exit passages, *J. Phys. Oceanogr.*, 40(9), 1965–1987. doi:10.1175/2010JPO4380.1.

Durand, F., and T. Delcroix, (2000), On the variability of the Tropical Pacific Thermal Structure during the 1979–96 period, as Deduced from XBT Sections. *J. Phys. Oceanogr.*, 30, 3261–3269.

Durland, T. S., R. M. Samelson, D. B. Chelton, and R. A. deSzoeke, (2011), Modification of long Rossby wave phase speeds by zonal currents. *J. Phys. Oceanogr.*, 41, 1077–1101.

Eigenheer, A., and D. Quadfasel, (2000), Seasonal variability of the Bay of Bengal circulation inferred from TOPEX/POSEIDON altimetry. *J Geophys. Res.*, 105, 3243–3252.

Enfield, D., (1987), The intraseasonal oscillation in eastern Pacific sea levels: How is it forced? *J. Phys. Oceanogr.,* 17, 1860–1876.

Enfield, D. B., and D. A. Mayer, (1997), Tropical Atlantic sea surface temperature variability and its relation to El Niño-Southern Oscillation. *J. Geophys. Res.: Oceans*, 102(C1), 929–945.

Farrar, J. T., (2008), Observations of the dispersion characteristics and meridional sea-level structure of equatorial waves in the Pacific Ocean. *J. Phys. Oceanogr.*, 38, 1669–1689.

Farrar, J. T., (2011), Barotropic Rossby waves radiating from tropical instability waves in the Pacific Ocean. *J. Phys. Oceanogr.*, 41, 1160–1181.

Feng, M., and S. Wijffels, (2002), Intraseasonal variability in the south equatorial current of the East Indian Ocean. *J. Phys. Oceanogr.*, 32 (2002), 265–277.

Fernandez Bilbao, R. A. F., J. M. Gregory, and N. Bouttes, (2015), Analysis of the regional pattern of sea level change due to ocean dynamics and density change for 1993–2099 in observations and CMIP5 AOGCMs. *Clim. Dyn.*, 45, 2647–2666, doi:10.1007/s00382-015-2499-z.

Florenchie, P., J. R. E. Lutjeharms, C. J. C. Reason, S. Masson, and M. Rouault, (2003), The source of Bengula Niños in the South Atlantic Ocean, *Geophys. Res. Lett.*, 30(10), 1505, doi:10.1029/2003GL017172.

Florenchie, P., C. J. C. Reason, J. R. E. Lutjeharms, M. Rouault, C. Roy, and S. Masson, (2004), Evolution of interannual warm and cold events in the southeast Atlantic Ocean, *J. Clim.*, 17, 2318–2334, doi:10.1175/1520-0442(2004)017<2318:EOIWAC>2.0.CO;2.

Foltz, G.R., and M. J. McPhaden, (2010), Interaction between the Atlantic meridional and Niño modes, *Geophys. Res. Lett.*, 37, L18604, doi:10.1029/2010GL044001.

Fonseca, G. A., G. J. Goni, W. E. Johns, and E. J. D. Campos, (2004), Investigation of the North Brazil Current retroflection and North Equatorial Countercurrent variability, *Geophys. Res. Lett.*, vol. 31, L21304, doi:10.1029/2004GL020054.

Forristall, G. Z., K. J. Schaudt, and J. Calman, (1990), Verification of GEOSAT altimetry for operational use in the Gulf of Mexico. *J. Gophys. Res.*, 95, C3, 2985–2989.

Franca, C. A. A., I. Wainer, and A. R. de Mesquita, (2003), Planetary equatorial trapped waves in the Atlantic ocean from Topex/Poseidon altimetry, In: Gustavo Jorge Goni, Paola Malanotte-Rizzoli. (org.). Interhemispheric water exchange in the Atlantic ocean. Amsterdam: Elsevier Science, 2003, v. 68, p. 213–232.

Frankcombe, L. M., S. McGregor, and M. H. England, (2015), Robustness of the modes of Indo-Pacific sea level variability, *Clim. Dyn.*, 45, 1281–1298, doi:10.1007/s00382-014-2377-0.

Fratantoni, D. M., W. E. Johns, and T. L. Townsend, (1995), Rings of the North Brazil Current: Their structure and behavior inferred from observations and a numerical simulation. *J. Geophys. Res.*, 100, C6, 10635–10654, doi:10.1029/95JC00925.

Fu, L., and R. Smith, (1996), Global ocean circulation from satellite altimetry and high-resolution computer simulation. *Bull. Am. Meteorol. Soc.*, 77, 2625–2636.

Fu, L.-L. and A. Cazanave (2000), Satellite Altimetry and Earth Science: a Handbook for Techniques and Applications, Academic Press, San Diego, California, USA. 463 pp.

Fu, L.-L., (2007), Intraseasonal variability of the equatorial Indian Ocean observed from sea surface height, wind, and temperature data. *J. Phys. Oceanogr.*, 37, 188–202, doi:10.1175/JPO3006.1.

Fukumori, I., and O. Wang, (2013), Origins of heat and freshwater anomalies underlying regional decadal sea level trends, *Geophys. Res. Lett.*, 40, 563–567, doi:10.1002/grl.50164.

Garrett, C. J. R., and B. Toulany (1982), Sea level variability due to meteorological forcing in the northeast of St. Lawrence, J. Geophys. Res., 87, 1968–1978.

Garzoli, S. L., A. Field, and Q. Yao, (2003), North Brazil current rings and the variability in the latitude of retroflection. In: *Interhemispheric Water Exchange in the Atlantic Ocean*, Goni G. J. and P. Malanotte-Rizzoli (Ed.), Elsevier Oceanography Series, Elsevier B.V., Amsterdam, The Netherlands. 68, pp. 357–373.

Giese, B. S., J. A. Carton, and L. J. Holl, (1994), Sea level variability in the eastern tropical Pacific as observed by TOPEX and Tropical Ocean Global Atmosphere, Tropical Atmosphere Ocean experiment. *J. Geophys. Res.*, 99, C12, 24739–24748.

Girish Kumar, M. S., M. Ravichandran, and W. Han, (2013), Observed intraseasonal thermocline variability in the Bay of Bengal. *JGR-Oceans*, 118, 3336–3349, doi:10.1002/jgrc.20245.

Goes, M., G. Goni, V. Hormann, and R. C. Perez, (2013), Variability of the Atlantic off-equatorial eastward currents during 1993–2010 using a synthetic method, *J. Geophys. Res.*, 118, 1–20, doi:10.1002/jgrc.20186.

Goni, G. J, and W.E. Johns, (2001), A census if North Brazil Current rings observed from Topex/Poseidon altimetry: 1993–1998, *Geophys. Res. Lett.*, 28, 1, 1–4.

Goni, G. J., and W. E. Johns, (2003), Synoptic study of warm rings in the North Brazil Current retroflection region using satellite altimetry, In: *Interhemispheric Water Exchange in the Atlantic Ocean, Elsevier Oceanogr. Ser.*, vol. 68, G. J. Goni, and P. Malanotte-Rizzoli, (Ed.), chap. 13, pp. 335–356, Elsevier, Amsterdam.

Gordon, A. L., B. A. Huber, E. J. Metzger, R. D. Susanto, H. E. Hurlburt, and T. R. Adi, (2012), South China Sea throughflow impact on the Indonesian throughflow, *Geophys. Res. Lett.*, 39, L11602, doi:10.1029/2012GL052021.

Goswami, B. N., (2012), South Asian monsoon. In Intraseasonal Variability in the Atmosphere-Ocean Climate System, Lau W. and D. Waliser (Eds.), Springer Fachmedien, Wiesbaden, 2012, ISBN 978 3 642 13913 0.

Grodsky, S. A., J. A. Carton, and F. M. Bingham, (2006), Low frequency variation of sea surface salinity in the tropical Atlantic, *Geophys. Res. Lett.*, 33, L14604, doi:10.1029/2006GL026426.

Grodsky, S. A., J. A. Carton, C. Provost, J. Servain, J. A. Lorenzzetti, and M. J. McPhaden, (2005), Tropical instability waves at 0°N, 23°W in the Atlantic: A case study using Pilot Research Moored Array in the Tropical Atlantic (PIRATA) mooring data, *J. Geophys. Res.*, 110, C08010, doi:10.1029/2005JC002941.

Halpern, D., R. A. Knox, and D. S. Luther, 1988: Observations of 20-day period meridional current oscillations in the upper ocean along the Pacific equator. J. Phys. Oceanogr., 18, 1514–1534.

Hamlington, B. D., M. W. Strassburg, R. Leben, W. Han, R. S. Nerem, and K. Y. Kim, (2014), Uncovering the anthropogenic warming-induced sea level rise signal in the Pacific Ocean, *Nat. Clim. Change*, *4*, 782–785.

Han, W., (2005), Origins and dynamics of the 90-day and 30–60-day variations in the equatorial Indian Ocean. *J. Phys. Oceanogr.*, 35, 708–728.

Han, W., D. M. Lawrence, and P. J. Webster, (2001), Dynamical response of the equatorial Indian Ocean to intraseasonal winds: Zonal flow. *Geophys. Res. Lett.*, 28, 4215–4218.

Han, W., J. P. McCreary, Y. Masumoto, J. Vialard, and B. Duncan, (2011), Basin resonances in the equatorial Indian Ocean. *J. Phys. Oceanogr.*, 41, 1252–1270.

Han, W., G. Meehl, D. Stammer, A. Hu, B. Hamlington, J. Kenigson, H. Palanisamy, and P. Thompson (2017), Spatial Patterns of Sea Level Variability Associated With Natural Internal Climate Modes. Surveys in Geophysics, 38(1), 217–250, DOI:10.1007/s10712-016-9386-y.

Han, W., G. Meehl, D. Stammer, A. Hu, B. Hamlington, J. Kenigson, H. Palanisamy, and P. Thompson, (2017), Spatial patterns of sea level variability associated with natural internal climate modes, *Surv. Geophys.*, 38(1), 217–250, doi:10.1007/s10712-016-9386-y.

Han, W., T. Shinoda, L.-L. Fu, and J. P. McCreary, (2006), Impact of atmospheric intraseasonal oscillations on the Indian Ocean dipole during the 1990s. *J. Phys. Oceanogr.*, 36, 670–690.

Han, W., J. Vialard, M. McPhaden, T. Lee, Y. Masumoto, M. Feng, and W. de Ruijter, (2014), Indian Ocean decadal variability: A review. *Bull. Amer. Meteorol. Soc.*, 95, 1679–1703. 10.1175/BAMS-D-13-00028.1.

Han, W., and P. J. Webster, (2002), Forcing mechanisms of sea-level interannual variability in the Bay of Bengal, *J. Phys. Oceanogr.*, 32, 216–239.

Han, W., P. J. Webster, J. L. Lin, W. T. Liu, R. Fu, D. Yuan, and A. Hu, (2008), Dynamics of intraseasonal sea level and thermocline variability in the equatorial Atlantic during 2002–03, *J. Phys. Oceanogr.*, 38, doi:10.1175/2008.3854.1.

Handoh, I. C., J. Matthews, G. R. Bigg, and D. P. Stevens, (2006a), Interannual variability of the tropical Atlantic independent of and associated with ENSO: Part 1. The north tropical Atlantic. *Int. J. Climatol.*, 26, 14, 1937–1956, doi:10.1002/joc.1343.

Handoh, I. C., J. Matthews, G. R. Bigg, and D. P. Stevens, (2006b), Interannual variability of the tropical Atlantic independent of and associated with ENSO: Part 2. The south tropical Atlantic. *Int. J. Climatol.*, 26, 14, 1957–1976, doi:10.1002/joc.1342.

Hastenrath, S., and J. Merle, (1987), Annual cycle of subsurface thermal structure in the Tropical Atlantic Ocean. *J. Phys. Oceanogr.*, 17, 1518–1537.

Hazeleger, W., R. Seager, M. A. Cane, and N. H. Naik, (2004), How can tropical Pacific ocean heat transport vary? *J. Phys. Oceanogr.*, 34, 320–333.

Hazeleger, W., M. Visbeck, M. Cane, A. Karspeck, and N. Naik, (2001), Decadal upper ocean temperature variability in the tropical Pacific. *J. Geophys. Res.*, 106, 8971–8988.

Hendon, H., B. Liebmann, and J. Glick, (1998), Oceanic Kelvin waves and the Madden–Julian oscillation. *J. Atmos. Sci.,* 55, 88–101.

Hermes, J. C., and C. J. C. Reason, (2008), Annual cycle of the south Indian Ocean (Seychelles-Chagos) thermocline ridge in a regional ocean model. *J. Geophys. Res.*, 113, C04035, doi:10.1029/ 2007JC004363.

Holmes, R. M., and L. N. Thomas (2016), Modulation of tropical instability wave intensity by equatorial Kelvin waves, J. Phys. Oceanogr., 46, 2623–2643.

Hormann, V., and P. Brandt, (2009), Upper equatorial Atlantic variability during 2002 and 2005 associated with equatorial Kelvin waves, *J. Geophys. Res.*, 114, C03007, doi:10.1029/2008JC005101.

Hormann, V., R. Lumpkins, and G. R. Foltz, (2012), Interannual North Equatorial Countercurrent variability and its relation to Tropical Atlantic climatic modes. *J. Geophys. Res.*, 117, c04035, doi:10:1029/2011jc007697.

Houghton, R. W., and Y. M. Tourre, (1992), Characteristics of low-frequency sea surface temperature fluctuations in the tropical Atlantic, *J. Clim.*, 5, 765–771.

Hsin, Y.-C., and B. Qiu, (2012), Seasonal fluctuations of the North Equatorial Countercurrent. *J. Geophys. Res.*, 117, C06001, doi:10.1029/2011JC007794.

Hu, S., and J. Sprintall, (2016), Interannual variability of the Indonesian Throughflow: The salinity effect. *J. Geophys. Res.*, 121, 2596–2615, doi:10.1002/2015JC011495.

Huang, B., and Z.-Z. Hu, (2007), Cloud-SST feedback in southeastern tropical Atlantic anomalous events, *J. Geophys. Res.*, 112, C03015, doi:10.1029/2006JC003626.

Illig, S., D. Gushchina, B. Dewitte, N. Ayoub, and Y. du Penhoat, (2006), The 1996 equatorial Atlantic warm event: Origin and mechanisms, *Geophys. Res. Lett.*, 33, L09701, doi:10.1029/2005GL025632.

Iskandar, I., W. Mardiansyah, Y. Masumoto, and T. Yamagata, (2005), Intraseasonal Kelvin waves along the southern coast of Sumatra and Java. *J. Geophys. Res.*, 110, C04013, doi:10.1029/ 2004JC002508.

Iskandar, I., and M. J. McPhaden, (2011), Dynamics of wind-forced intraseasonal zonal current variations in the equatorial Indian Ocean, *J. Geophys. Res.*, 116, C06019, doi:10.1029/2010JC006864.

Iskandar, I., T. Tozuka, H. Sasaki, Y. Masumoto, and T. Yamagata, (2006), Intraseasonal variations of surface and subsurface currents off Java as simulated in a high-resolution ocean general circulation model. *J. Geophys. Res.*, 111, C12015, doi:10.1029/2006JC003486.

Jochum, M., and P. Malanotte-Rizzoli, (2003), The flow of AAIW along the equator. In: *Interhemispheric Water Exchange in the Atlantic Ocean*, Goni G.J. and P. Malanotte-Rizzoli (Eds.), Elsevier Oceanography Series, Elsevier B.V., Amsterdam, The Netherlands. 68, 193–212.

Johnson, E., (1993), Effects of a mean three-dimensional flow on intraseasonal Kelvin waves in the equatorial Pacific Ocean. *J. Geophys. Res.,* 98, 10185–10194.

Johnson, E., and M. McPhaden, (1993), Structure of intraseasonal Kelvin waves in the equatorial Pacific Ocean. *J. Phys. Oceanogr.*, 23, 608–625.

Johnson, G. C., B. M. Sloyan, W. S. Kessler, and K. E. McTaggart, (2002), Direct measurements of upper ocean currents and water properties across the tropical Pacific during the 1990s. *Progr. Oceanogr.*, 52, 31–61.

Jordà, G., (2014), Detection time for global and regional sea level trends and accelerations. *J. Geophys. Res. Oceans,* 119, 7164–7174. doi:10.1002/2014JC010005.

Kao, H.-Y., and J.-Y. Yu, (2009), Contrasting Eastern-Pacific and Central-Pacific types of ENSO. *J. Clim.*, 22, 615–632.

Katz, E. J., (1997), Waves along the Equator, *J. Phys. Oceanogr.*, 27, 2536–2544.

Keenlyside, N. S., and M. Latif, (2007), Understanding equatorial Atlantic interannual variability, *J. Clim.*, 20,131–142, doi:10.1175/JCLI3992.1.

Kessler, W. S., (2006), The circulation of the eastern tropical Pacific: A review. *Progr. Oceanogr.*, 69, 181–217.

Kessler, W. S., and J. P. McCreary, (1993), The annual wind-driven Rossby wave in the sub-thermocline equatorial Pacific. *J. Phys. Oceanogr.*, 23, 1192–1207.

Kessler, W. S., and M. McPhaden, (1995), Oceanic Kelvin waves and the 1991–93 El Niño. *J. Clim.*, 8, 1757–1774.

Kessler, W. S., M. McPhaden, and K. Weickmann, (1995), Forcing of intraseasonal Kelvin waves in the equatorial Pacific. *J. Geophys. Res.*, 100, 10613–10631.

Kindle, J. C., and J. D. Thompson, (1989), The 26- and 50-day oscillations in the western Indian Ocean: Model results. *J. Geophys. Res.*, 94, 4722–4735.

Kleeman, R., J. P. McCreary, and B. Klinger, (1999), A mechanism for generating ENSO decadal variability. *Geophys. Res. Lett.*, 26, 1743–1746.

Knox, R. A., and D. Halpern, (1982), Long range Kelvin wave propagation of transport variations in Pacific Ocean equatorial currents. *J. Mar. Res.*, 40 Suppl., 329–339.

Kutsuwada, K., and M. McPhaden (2002), Intraseasonal variations in the upper equatorial Pacific Ocean prior to and during the 1997–98 El Niño. J. Phys. Oceanogr., 32, 1133–1149.

Lau, W. K. M., and D. E. Waliser (Editors), (2012), *Intraseasonal variability in the Atmosphere–Ocean Climate System* (Second Edition). Springer-Verlag, Berlin.

Lee, T., (2004), Decadal weakening of the shallow overturning circulation in the South Indian Ocean, *Geophys. Res. Lett.*, 31, L18305, doi:10.1029/2004GL020884.

Lee, T., T. Awaji, M. Balmaseda, et al., (2010), Consistency and fidelity of Indonesian-throughflow total volume transport estimated by 14 ocean data assimilation products. *Dyn. Atmos. Oceans*. 50, 201–223, doi:10.1016/j.dynatmoce.2009.12.004.

Lee, T., and I. Fukumori, (2003), Interannual to decadal variation of tropical-subtropical exchange in the Pacific Ocean: Boundary versus interior pycnocline transports. *J. Clim.,* 16, 4022–4042.

Lee, T., G. Lagerloef, H. Y. Kao, J. Mcphaden, J. Willis, and M. M. Gierach, (2014), The influence of salinity on tropical Atlantic instability waves, *J. Geophys. Res.*, 119, 8375–8394, doi:10.1002/2014jc010100.

Lee, T., and M. J. McPhaden, (2008), Decadal phase change in large-scale sea level and winds in the Indo-Pacific region at the end of the 20th century. *Geophys. Res. Lett.*, 35, L01605, doi:10.1029/2007GL032419.

Lee, T., B. Qiu, S. Hakkinen, et al., (2010), Satellite observations of ocean circulation changes associated with climate variability. *TOS, Oceanogr.*, 23(4), 70–81.

Legeckis, R. (1977), Long waves in the eastern equatorial Pacific Ocean: a view from a geostationary satellite. Science. 197, 1179–1181.

Li, Y., and W. Han, (2015), Decadal sea level variations in the Indian Ocean investigated with HYCOM: Roles of climate modes, Ocean internal variability and stochastic wind forcing, *J. Clim.*, 28, 9143–9165, doi:10.1175/JCLI-D-15-0252.1.

Liu, Z., and S. G. H. Philander, (2000), Tropical-extratropical oceanic exchange. Chapter 4.4 *of Ocean Circulation and Climate: Observing and Modeling the Global Ocean*, G. Siedler, J. Church, and J. Gould, (Eds.), AP International Geophys. Series, Academic Press, London, UK and San Diego, California. 77, pp. 247–257.

Liu, Y., R. H. Weisberg, S. Vignudelli, and G. T. Mitchum, (2014), Evaluation of altimetry-derived surface current products using Lagrangian drifter trajectories in the eastern Gulf of Mexico, *J. Geophys. Res.*, 119, doi:10.1002/2013JC009710.

Llovel, W., and T. Lee, (2015), Importance and origin of halosteric contribution to sea level change in the southeast Indian Ocean during 2005–2013, *Geophys. Res. Lett.*, 42, 1148–1157, doi:10.1002/2014GL062611.

Lukas, R., and E. Firing, (1985), The annual Rossby wave in the central equatorial Pacific Ocean. *J. Phys. Oceanogr.*, 11, 55–67.

Lukas, R., S. P. Hayes, and K. Wyrtki, (1984), Equatorial sea-level response during the 1982–1983 El Niño. *J. Geophys. Res.*, 89, 10425–10430.

Lumpkin, R., G. Goni, and K. Dohan, (2013), Surface currents, in "State of the Climate in 2012". *Bull. Amer. Meteor. Soc.*, 94, S62–S65.

Luo, J. J., W. Sasaki, and Y. Masumoto, (2012), Indian Ocean warming modulates Pacific climate change, *Proc. Natl. Acad. Sci.,* 109, 18701–18706.

Luther, D., and E. Johnson (1990), Eddy energetics in the upper equatorial Pacific during the Hawaii-to-Tahiti Shuttle Experiment. J. Phys. Oceanogr., 20, 913–944.

Luyten, J. R., and D. H. Roemmich, (1982), Equatorial currents at semiannual period in the Indian Ocean, *J. Phys. Oceanogr.*, 12, 406–413, doi:10.1175/1520-0485(1982)012<0406:ECASAP>2.0.CO;2.

Lyman, J., D. Chelton, R. deSzoeke, and R. Samelson, (2005), Tropical instability waves as a resonance between equatorial Rossby waves. *J. Phys. Oceanogr.,* 35, 232–254.

Lyman, J., G. Johnson, and W. Kessler, (2007), Distinct 17-day and 33- day tropical instability waves in subsurface observations. *J. Phys. Oceanogr.*, 37, 855–872.

Lyu, K., X. Zhang, J. A. Church, and J. Hu, (2015), Quantifying internally generated and externally forced climate signals at regional scales in CMIP5 models, *Geophys. Res. Lett.*, 42, 9394–9403, doi:10.1002/2015GL065508.

Madden, R. A., and P. R. Julian, (1971), Detection of a 40–50 day oscillation in the zonal wind of the tropical Pacific. *J. Atmos. Sci.,* 28, 702–708.

Madden, R. A., and P. R. Julian, (1972), Description of global-scale circulation cells in the tropics with a 40–50 day period. *J. Atmos. Sci.,* 29, 1109–1123.

Masumoto, Y., H. Hase, Y. Kuroda, H. Matsuura, and K. Takeuchi, (2005), Intraseasonal variability in the upper-layer currents observed in the eastern equatorial Indian Ocean, *Geophys. Res. Lett.*, 32, L02607, doi:10.1029/2004GL021896.

Masumoto, Y., and G. Meyers, (1998), Forced Rossby waves in the southern tropical Indian Ocean, *J. Geophys. Res.,* 103, 12287–12293.

Matsuno, T. (1966), Quasi-geostrophic motions in the equatorial area. J. Meteor. Soc. Japan, 44, 25–43.

Mayer, D. A., M. O. Baringer and G. J. Goni, (2003), Comparison of hydrographic and altimeter based estimates of sea level height variability in the Atlantic Ocean, In: Gustavo Jorge Goni, Paola Malanotte-Rizzoli. (org.). Interhemispheric water exchange in the Atlantic ocean. Amsterdam: Elsevier Science, 2003, v. 68, pp. 213–232.

McCreary, J. P., and P. Lu, (1994), On the interaction between the subtropical and the equatorial oceans: The subtropical cell. *J. Phys. Oceanogr.*, 24, 466–497.

McPhaden, M. J., (1982), Variability in the central equatorial Indian Ocean. Part 1: Ocean dynamics, *J. Mar. Res.*, 40, 157–176.

McPhaden, M. J., (1996), Monthly period oscillations in the Pacific North Equatorial Countercurrent. *J. Geophys. Res.*, 101, 6337–6359.

McPhaden, M. J., A. J. Busalacchi, R. Cheney, et al., (1998), The Tropical Ocean-Global Atmosphere observing system: A decade of progress. *J. Geophys. Res.*, 103, 14169–14240.

McPhaden, M. J., G. Meyers, K. Ando, Y. Masumoto, V. S. N. Murty, M. Ravichandran, F. Syamsudin, J. Vialard, L. Yu, and W. Yu, (2009), RAMA: The research moored array for African-Asian-Australian monsoon analysis and prediction. *Bull. Amer. Meteorol. Soc.*, 90, 459–635.

McPhaden, M. J., and M. Nagura, (2014), Indian Ocean Dipole interpreted in terms of Recharge Oscillator theory, *Clim. Dyn.*, 42*,* 1569–1586. doi:10.1007/s00382-013-1765-1.

McPhaden, M. J., and B. Taft, (1988), Dynamics of seasonal and intraseasonal variability in the eastern equatorial Pacific. *J. Phys. Oceanogr.*, 18, 1713–1732.

McPhaden, M. J., and D. Zhang, (2002), Slowdown of the meridional overturning circulation in the upper Pacific Ocean. *Nature*, 415, 603–608.

McPhaden, M. J., and D. Zhang, (2004), Pacific Ocean circulation rebounds, *Geophys. Res. Lett.*, 31, L18301, doi:10.1029/2004GL020727.

Melet, A., L. Gourdeau, and J. Verron, (2011), Variability in the Solomon Sea circulation derived from altimeter sea level data, *Ocean Dyn.*, 60, 833–900. doi:10.1007/s10236-010-0302-6.

Melet, A., J. Verron, L. Gourdeau, et al., (2011), Equatorward pathways of Solomon Sea water masses and their modifications. *J. Phys. Oceanogr.*, 41, 810–826. doi:10.1175/2010JPO4559.1.

Menkes, C. E., S. C. Kennan, P. Flament, et al., (2002), A whirling ecosystem in the equatorial Atlantic, *Geophys. Res. Lett.*, 29(11), 1553, doi:10.1029/2001GL014576.

Merrifield, M. A., (2011), A shift in Western Tropical Pacific Sea Level Trends during the 1990s. *J. Clim.*, 24, 4126–4136, doi:10.1175/2011JCLI3932.1.

Mertz, G. L., and L. A. Mysak, (1984), Evidence for a 40–60 day oscillation over the western Indian Ocean during 1976 and 1979, *Mon. Weather Rev.*, 112, 383–386.

Miller, L., and R. E. Cheney, (1990), Large scale meridional transport in the tropical Pacific Ocean during 1986–1987 El Niño from GEOSAT. *J. Gophys. Res.*, 95, C10, 17905–17919.

Miller, L., R. E. Cheney, and B. C. Douglas, (1988), GEOSAT Altimeter Observations of Kelvin Waves and the 1986–87 El Niño, *Science,* 239, 52–54.

Minster, J. F., M. l. Genco, and C. Brossier, (1995), Variations of the sea level in the Amazon estuary, *Continental Shelf Res.*, 15(10), 1287–1302.

Mitchum, G., (1994), Comparison of TOPEX Sea Surface Heights and tide gauges levels. *J. Geophys. Res.*, 99, C12, 24541–24553.

Mitchum, G. T., and R. Lukas, (1990), Westward propagation of annual sea level and wind signals in the western Pacific Ocean. *J. Clim.*, 3, 1102–1110.

Miyama, T., J. P. McCreary, D. Sengupta, and R. Senan, (2006), Dynamics of biweekly oscillations in the equatorial Indian Ocean. *J. Phys. Oceanogr.*, 36(5), 827–846. doi:10.1175/JPO2897.1.

Moore, D. W., and J. P. McCreary, (1990), Excitation of intermediate-frequency equatorial waves at a western ocean boundary: With application to observations from the Indian Ocean, *J. Geophys. Res.*, 95, 5219–5231.

Moore, D. W., and S. G. H. Philander, (1977), Modeling of the tropical ocean circulation, *The Sea*, 6, 319–361. New York, John Wiley and Sons.

Murtugudde, R., S. Signorini, J. Christian, A. Busalacchi, C. McClain, and J. Picaut, (1999), Ocean color variability of the tropical Indo-Pacific basin observed by SeaWiFS during 1997–98. *J. Geophys. Res.*, 104, 18351–18366.

Nagura, M., and M. J. McPhaden, (2012), The dynamics of wind-driven intraseasonal variability in the equatorial Indian Ocean. *J. Geophys. Res.*, 115, C07009, doi:10.1029/2011JC007405.

Nidheesh, A. G., M. Lengaigne, J. Vialard, A. S. Unnikrishnan, and H. Dayan, (2013), Decadal and long-term sea level variability in the tropical Indo-Pacific Ocean, *Clim. Dyn.*, 41, 381–402, doi:10.1007/s00382-012-1463-4.

Nystuen, J. A., and C. A. Andrade, (1993), Tracking mesoscale ocean features in the Caribbean sea using GEOSAT altimetry. *J. Geophys. Res.*, 98, C5, 8389–8394.

Ogata, T., and Y. Masumoto, (2010), Interactions between mesoscale eddy variability and Indian Ocean dipole events in the south-eastern tropical Indian Ocean—Case studies for 1994 and 1997/ 1998, *Ocean Dyn*., 60, 717–730, doi:10.1007/s10236-010-0304-4.

Ogata, T., and Y. Masumoto, (2011), Interannual modulation and its dynamics of the mesoscale eddy variability in the southeastern tropical Indian Ocean. *J. Geophys. Res.*, 116, C05005, doi:10.1029/2010JC006490.

Palastanga, V., P. J. van Leeuwen, M. W. Schouten, and W. P. M. de Ruijter, (2007), Flow structure and variability in the subtropical Indian Ocean: Instability of the South Indian Ocean Countercurrent, *J. Geophys. Res.*, 112, C01001, doi:10.1029/2005JC003395.

Pauluhn, A., and Y. Chao, (1999), Tracking Eddies in the Subtropical North-Western Atlantic Ocean, *Phys. Chem. Earth (A)*, 24(4), 415–421.

Perez, R. C., R. Lumpkin, W. E. Johns, G. R. Foltz, and V. Hormann, (2012), Interannual variations of Atlantic tropical instability waves, *J. Geophys. Res.*, 117, C03011, doi:10.1029/2011JC007584.

Périgaud, C., (1990), Sea level oscillations observed with GEOSAT along the 2 shear fronts of the Pacific North Equatorial Countercurrent. *J. Gophys. Res.*, 95, C5, 7239–7248.

Périgaud, C., and P. Delecluse, (1992), Annual sea level variations in the southern tropical Indian Ocean from GEOSAT and shallow water simulations. *J. Geophys. Res.*, 97, 20169–20178.

Philander, S. G. H. (1976), Instabilities of zonal equatorial currents, J. Geophys. Res., 81, 3725–3735.

Philander, S. G. H. (1978), Instabilities of zonal equatorial currents, 2. J. Geophys. Res., 83, 3679–3682.

Picaut, J., A. J. Busalacchi, M. J. McPhaden, B. Camusat, (1990), Validation of the geostrophic method for estimating zonal currents at the equator from GEOSAT altimeter data. *J. Gophys. Res.*, 95, C3, 3015–3024.

Picaut, J., A. J. Busalacchi, M. J. McPhaden, M. McPhaden, L. Gourdeau, F. I. Gonzales, and E. C. Hackert, (1995), Open-ocean validation of TOPEX/Poseidon sea level in the western equatorial Pacific. *J. Geophys. Res.*, 100, 25109–25127. doi:10.1029/95JC02128.

Picaut, J. and A.J. Busalacchi (2000), Tropical ocean variability, Chpt. 4, 217-236 in "Satellite Altimetry and Earth Science: a Handbook for Techniques and Applications", L.-L. Fu and A. Cazanave (Eds), Academic Press, San Diego, California, USA. 463 pp.

Picaut, J., E. Hackert, A. J. Busalacchi, et al., (2002), Mechanisms of the 1997–1998 El Niño La Niña, as inferred from space-based observations. *J. Geophys. Res. – Oceans.*107, 5-1-5-18, doi:10.1029/2001JC000850.

Polo, I., A. Lazar, B. Rodriguez-Fronseca, S. Arnault, and G. Mainsaint, (2008a), Ocean Kelvin waves and tropical Atlantic intraseasonal variability: Part I: Kelvin wave characterization, *J. Geophys. Res*, 113(7), C07009.

Polo, I., B. Rodríguez-Fonseca, T. Losada, and J. García-Serrano, (2008b), Tropical Atlantic variability modes (1979–2002). Part I: time-evolving SST modes related to West African rainfall, *J. Clim.*, 21, 6457–6475, doi:10.1175/2008JCLI2607.1.

Potemra, J., (2005), Indonesian throughflow transport variability estimated from satellite altimetry, *Oceanography*, 18(4), 98–107, doi:10.5670/oceanog.2005.10.

Potemra, J. T., R. Lukas, and G. T. Michum, (1997), Large-scale estimation of transport from the Pacific to the Indian Ocean, *J. Geophys. Res.*, 102, 27795–27812, doi:10.1029/97JC01719.

Provost, C., S. Arnault, L. Bunge, N. Chouaib, and E. Sultan, (2006), Interannual variability of the zonal sea surface slope in the tropical Atlantic ocean in the 1990s, *Adv. Space Res.*, 4, 823–831.

Provost, C., S. Arnault, N. Chouaib, A. Kartavsteff, and L. Bunge, (2004), Equatorial pressure gradient in the Atlantic in 2002: TOPEX/Poséïdon and Jason versus the first PIRATA current measurements, *Mar. Geod.*, 27, n°1–2, 31–47.

Pujiana, K., A. L. Gordon, and J. Sprintall, (2013), Intraseasonal Kelvin Wave in Makassar Strait, *J. Geophys. Res.*, 118, 2023–2034 doi:10.1002/jgrc.20069.

Pujol, M.-I., Faugère, Y., Taburet, G., Dupuy, S., Pelloquin, C., Ablain, M., and Picot, N., (2016), DUACS DT2014: The new multi-mission altimeter data set reprocessed over 20 years, *Ocean Sci.*, 12, 1067–1090, doi:10.5194/os-12-1067-2016.

Qiao, L., and R. Weisberg, (1995), Tropical instability wave kinematics: Observations from the Tropical Instability Wave Experiment. *J. Geophys. Res.,* 100, 8677–8693.

Qiu, B., M. Mao, and Y. Kashino, (1999), Intraseasonal variability in the Indo-Pacific throughflow and regions surrounding the Indonesian seas, *J. Phys. Oceanogr.*, 29, 1599–1618.

Qu, T., J. Gan, A. Ishida, Y. Kashino and T. Tozuka, (2008), Semiannual variation in the western tropical Pacific Ocean. *Geophys. Res. Lett.*, L16602, 35, doi:10.1029/2008GL035058.

Qu, T., and Y. T. Song, (2009), Mindoro Strait and Sibutu Passage transports estimated from satellite data, *Geophys. Res. Lett.*, 36, L09601, doi:10.1029/2009GL037314.

Rao, S. A., and S. K. Behera, (2005), Subsurface influence on SST in the tropical Indian Ocean: Structure and interannual variability. *Dyn. Atmos. Oceans*, 39, 103–139.

Rao, S. A., S. K. Behera, Y. Masumoto, and T. Yamagata, (2002), Interannual variability in the subsurface tropical Indian Ocean, *Deep-Sea Res. II*, 49, 1549–1572.

Rao, S. A., and T. Yamagata, (2004), Abrupt termination of Indian Ocean dipole events in response to intraseasonal oscillations. *Geophys. Res. Lett.*, 31, L19306, doi:10.1029/2004GL020842.

Rebert, J. P., J. R. Donguy, G. Eldin, and K. Wyrtki, (1985), Relations between sea level, thermocline depth, heat content, and dynamic height in the tropical Pacific Ocean. *J. Geophys. Res.,* 90, 11719–11725.

Reppin, J., F. A. Schott, J. Fischer, and D. Quadfasel, (1999), Equatorial currents and transports in the upper central Indian Ocean: Annual cycle and interannual variability, *J. Geophys. Res.*, 104, 15495–15514.

Reverdin, G., and J. Luyten, (1986), Near-surface meanders in the equatorial Indian Ocean. *J. Phys. Oceanogr.*, 17, 903–927.

Richter, I., S. K. Behera, Y. Masumoto, B. Taguchi, N. Komori, and T. Yamagata, (2010), On the triggering of Benguela Niños: Remote equatorial versus local influences, *Geophys. Res. Lett.*, 37, L20604, doi:10.1029/2010GL044461.

Richter, K., and B. Marzeion, (2014), Earliest local emergence of forced dynamic and steric sea-level trends in climate models. *Environ. Res. Lett.*, 9, 114009, doi:10.1088/1748-9326/9/11/114009.

Rouault, M., S. Illig, C. Bartholomae, C. J. C. Reason, and A. Bentamy, (2007), Propagation and origin of warm anomalies in the Angola Benguela upwelling system in 2001, *J. Mar. Syst.*, 68, 473–488, doi:10.1016/j.jmarsys.2006.11.010.

Roundy, P., and G. Kiladis, (2006), Observed relationships between oceanic Kelvin waves and atmospheric forcing. *J. Clim.*, 19, 5253–5272.

Ruiz-Barradas, A., J. A. Carton, and S. Nigam, (2000), Structure of interannual-to-decadal climate variability in the tropical Atlantic sector. *J. Clim.*, 13, 3285–3297.

Saji, N. H., B. N. Goswami, P. N. Vinayachandran, and T. Yamagata, (1999), A dipole mode in the tropical Indian Ocean. *Nature*, 401, 360–363.

Servain, J., (1991), Simple climatic indices for the tropical Atlantic Ocean and some applications, *J. Geophys. Res.*, 96, C8, 15137–15146, doi:10.1029/91JC01046.

Scharffenberg, M. G., and D. Stammer, (2010), Seasonal variations of the large-scale geostrophic flow field and eddy kinetic energy inferred from the TOPEX/Poseidon and Jason-1 tandem mission data. *J. Geophys. Res.*, 115, C02008, doi:10.1029/2008JC005242.

Schiller, A., S. E. Wijffels, J. Sprintall, R. Molcard, and P. R. Oke, (2010), Pathways of intraseasonal variability in the Indonesian Throughflow region. *Dyn. Atmos. Oceans*, 50, 174–200, doi:10.1016/j.dynatmoce.2010.02.003.

Schlundt, M., P. Brandt, M. Dengler, R. Hummels, T. Fischer, K. Bumke, G. Krahmann, and J. Karstensen, (2014), Mixed layer heat and salinity budgets during the onset of the 2011 Atlantic cold tongue, *J. Geophys. Res.*, 119, 7882–7910. doi:10.1002/2014JC010021.

Schneider, N., A. J. Miller, M. A. Alexander, and C. Deser, (1999), Subduction of decadal North Pacific temperature anomalies: Observations and dynamics. *J. Phys. Oceanogr.*, 29, 1056–1070.

Schott, F., J. Reppin, J. Fischer, and D. Quadfasel, (1994), Currents and transports of the monsoon current south of Sri Lanka. *J. Geophys. Res.*, 99(C12), 25127–25141.

Schott, F., and J.P. McCreary (2001), The monsoon circulation of the Indian Ocean. Prog. Oceanogr., 51, 1–123.

Schott, F. A., W. Wang, D. Stammer, (2007), Variability of Pacific subtropical cells in the 50-year ECCO assimilation. *Geophys. Res. Lett.*, 34, L05604, doi:10.1029/2006GL028478.

Schott, F. A., S. P. Xie, and J. P. McCreary, (2009), Indian Ocean circulation and climate variability. *Rev. of Geophys.*, 47, RG1002, doi:10.1029/2007RG000245.

Schouten, M. W., W. P. M. de Ruijter, P. J. van Leeuwen, and H. A. Dijkstra, (2002), An oceanic teleconnection between the equatorial and southern Indian Ocean. *Geophys. Res. Lett.*, 29, 1812, doi:10.1029/2001GL014542.

Schouten, M. W., R. P. Matano, and T. P. Strub, (2005), A description of the seasonal cycle of the equatorial Atlantic from altimeter data. *Deep-Sea Res. I*, 52, 477–493.

Senan, R., D. Sengupta, and B. N. Goswami, (2003), Intraseasonal ‘‘monsoon jets’’ in the equatorial Indian Ocean, *Geophys. Res. Lett.*, 30(14), 1750, doi:10.1029/ 2003GL017583.

Shankar, D., S. G. Aparna, J. P. McCreary, I. Suresh, S. Neetu, F. Durand, S. S. C. Shenoi, M. A. Al Saafani, (2010), Minima of interannual sea-level variability in the Indian Ocean, *Prog. In Oceanogr.*, 84, 225–241.

Shankar, D., and S. R. Shetye, (1999), Are interdecadal sea level 1120 changes along the Indian coast influenced by variability of monsoon rainfall? *J. Geophys. Res.*, 104, 26031–26042.

Shannon, L. V., A. J. Boyd, G. B. Bundrit, and J. Taunton-Clark, (1986), On the existence of an El Niño–type phenomenon in the Benguela system, *J. Mar. Sci.*, 44, 495–520.

Shinoda, T., G. N. Kiladis, and P. E. Roundy, 2009: Statistical representation of equatorial waves and tropical instability waves in the Pacific Ocean. Atmos. Res., 94, 37–44.

Shinoda, T. J., M. Flatau, S. Chen, W. Han, and C. Wang, (2013), Large-scale oceanic variability during the CINDY/DYNAMO field campaign from satellite observations. *Remote Sensing*, 5, 2072–2092.

Shinoda, T., W. Han, T. Jensen, L. Zamudio, E. J. Metzger, and R.-C. Lien, (2016), Impact of the Madden-Julian Oscillation on the Indonesian Throughflow in Makassar Strait during the CINDY/DYNAMO field campaign. *J. Clim.* (DYNAMO/CINDY/AMIE/LASP special collection), 29, 6085–6108. doi:10.1175/JCLI-D-15-0711.1

Singh, A., and T. Delcroix, (2013), Eastern and central Pacific ENSO and their relationships to the recharge/discharge oscillator paradigm. *Deep Sea Res.*, 82, 32–43.

Singh, A., T. Delcroix, and S. Cravatte, (2011), Contrasting the flavors of El Niño Southern Oscillation using sea surface salinity observations. *J. Geophys. Res.*, 116, C06016, doi:10.1029/2010JC006862.

Solomon, A., and M. Newman, (2012), Reconciling disparate twentieth-century Indo-Pacific ocean temperature trends in the instrumental record. *Nat. Clim. Change*, 2, 691–699.

Song, Y. T., (2006), Estimation of interbasin transport using ocean bottom pressure: Theory and model for Asian marginal seas, *J. Geophys. Res.*, 111, C11S19, doi:10.1029/2005JC003189.

Sprintall, J., A. L. Gordon, T. Lee, J. T. Potemra, K. Pujiana, and S. E. Wijffels, (2014), The Indonesian seas and their role in the couple ocean climate system, *Nat. Geosci.*, 7, 487–492, doi:10.1038/ngeo2188.

Sprintall, J., A. L. Gordon, R. Murtugudde, and R. D. Susanto, (2000), An Indian Ocean Kelvin wave observed in the Indonesian seas in May 1997. *J. Geophys. Res.*, 105, 17217–17230.

Sprintall, J., S. E. Wijffels, R. Molcard, and I. Jaya, (2009), Direct estimates of the Indonesian throughflow entering the Indian Ocean: 2004–2006, *J. Geophys. Res.*, 114, C07001, doi:10.1029/2008JC005257.

Stammer, D., (1997), Steric and wind-induced changes in TOPEX/POSEIDON large-scale sea surface topography observations. *J. Geophys. Res.,* 102, No. C9, 20987–21009.

Stammer, D., A. Cazenave, R. M. Ponte, and M. E. Tamisiea, (2013), Causes for contemporary regional sea level changes, *Annu. Rev. Mar. Sci.*, 5, 21–46, doi:10.1146/annurev-marine-121211-172406.

Stramma, L., S. Huttl, and J. Schafstall, (2005), Water masses and currents in the upper tropical northeast Atlantic off northwest Africa, *J. Geophys. Res.*, 110, C12006, doi:10.1029/2005JC002939.

Srinivasu, U., Ravichandran, M., Han, W. et al. Clim Dyn (2017), Causes for decadal reversal of North Indian Ocean sea level in recent two decades, *Clim. Dyn.*, in revision. doi:10.1007/s00382-017-3551-y. https://link.springer.com/article/10.1007/s00382-017-3551-y

Suresh, I., J. Vialard, M. Lengaigne, W. Han, J. McCreary, F. Durand, P. M. Muraleedharan, (2013), Origins of wind-driven intraseasonal sea level variations in the North Indian Ocean coastal waveguide. *Geophys. Res. Lett.*, 40, 5740–5744, doi:10.1002/2013GL058312.

Susanto, R. D., and Y. T. Song, (2015), Indonesian throughflow proxy from satellite altimeters and gravimeters, *J. Geophys. Res. Oceans*, 120, 2844–2855, doi:10.1002/2014JC010382.

Tai, C. K., (1988), GEOSAT crossover analysis in the tropical pacific 1: Constrained sinusoidal crossover adjustment. *J. Geophys. Res.*, 93, 10621–10629.

Timmermann, A., S. McGregor, and F. F. Jin, (2010), Wind effects on past and future regional sea level trends in the southern Indo-Pacific, *J. Clim.*, 23, 4429–4437.

Trenary, L., and W. Han, (2012), Intraseasonal-to-interannual variability of South Indian Ocean sea level and thermocline: Remote versus local forcing. *J. Phys. Oceanogr.*, 42, 602–627.

Trenberth, K. E., and T. J. Hoar, (1996), The 1990-1995 El Niño-Southern Oscillation event: Longest on record. *Geophys. Res. Lett.*, 23(1), 57–60.

Tsai, P. T. H., J. J. O'Brien, and M. E. Luther, (1992), The 26-day oscillation observed in the satellite sea surface temperature measurements in the equatorial western Indian Ocean. *J. Geophys. Res.*, 97, 9605–9618.

Urbano, D. F., R. A. F. de Almeida, and P. Nobre, (2008), Equatorial undercurrent and North Equatorial Countercurrent at 38°W: A new perspective from direct velocity data, *J. Geophys. Res.*, 113, c04041, doi:10.1029/2007jc004215.

Vecchi, G.A., and B. J. Soden, (2007), Global warming and the weakening of the tropical circulation. *J. Clim.*, 20, 4316–4340. doi:10.1175/JCLI4258.1.

Verstraete, J. M., and Y. H. Park, (1995), Comparison of Topex Poseidon altimetry and in situ sea level data at Sao Tome island, Gulf of Guinea, *J. Geophys. Res.*, 100(12), 25129–25134, doi:10.1029/95JC01960.

Vinayachandran, P. N., Y. Masamoto, T. Mikawa, and T. Yamagata, (1999), Intrusion of the Southwest Monsoon Current into the Bay of Bengal. *J. Geophys. Res.*, 104, 11077–11085.

Von Schuckmann, K., P. Brandt, and C. Eden, (2008), Generation of tropical instability waves in the Atlantic Ocean, *J. Geophys. Res.*, 113, C08034, doi:10.1029/2007JC004712.

Von Schuckmann, K., J. B. Sallée, D. Chambers, et al., (2014), Consistency of the global ocean observing systems from an Argo perspective. *Ocean Sci.*, 10, 547–557. doi:10.5194/os-10-547-2014.

Wakata, Y., and S. Kitaya, (2002), Annual variability of sea surface height and upper layer thickness in the Pacific Ocean. *J. Oceanogr.*, 58, 439–450.

Wakata, Y., 2007: Frequency-wavenumber spectra of equatorial waves detected from satellite altimeter data. J. Oceanogr., 63, 483–490.
Wang, T. Y., Y. Dy, W. Zhuang, and J. B. Wang, (2015), Connection of sea level variability between the tropical western Pacific and the southern Indian Ocean during recent two decades. *Science China-Earth Sci.*, 58(8), 1387–1396. doi:10.1007/s11430-014-5048-4.
Wang, L.-P., C. J. Koblinksky, and S. Howden, (2001), Annual Rossby waves in the Southern Indian Ocean: Why does it appear to break down in the middle ocean? *J. Phys. Oceanogr.*, 31, 54–74.
Wang, B., R. Wu, and R. Lukas, (2000), Annual adjustment of the thermocline in the tropical Pacific Ocean. *J. Clim.*, 13, 596–616.
Webber, B. G., A. J. Matthews, K. J. Heywood, and D. P. Stevens, (2012), Ocean Rossby waves as a triggering mechanism for primary Madden–Julian events. *Q. J. R. Meteorol. Soc.*, 138, 514–527.
Webster, P. J., A. M. Moore, J. P. Loschnigg, and R. R. Leben, (1999), Coupled oceanic–atmospheric dynamics in the Indian Ocean during 1997–98. *Nature*, 401, 356–360.
Whitehead, J. A., (1989), Internal hydraulic control in rotating fluids: Applications to oceans, *Geophys. Astrophys. Fluid Dyn.*, 48, 169–192, doi:10.1080/03091928908219532.
Woodbery, K. E., M. E. Luther, and J. J. O'Brien, (1989), The wind-driven seasonal circulation in the southern tropical Indian Ocean. *J. Geophys. Res.*, 94, 17985–18002.
Wyrtki, K., (1987), Indonesian throughflow and the associated pressure gradient, *J. Geophys. Res.*, 92, 12941–12946, doi:10.1029/JC092iC12p12941.
Wyrtki, K., and G. Mitchum, (1990), Interannual differences of GEOSAT altimeter heights and sea level. *The importance of a datum. J. Geophys. Res.*, 95, C3, 2969–2975.
Xie, S.-P., H. Annamalai, F. A. Schott, and J. P. McCreary, (2002), Structure and mechanisms of south Indian Ocean climate variability. *J. Clim.*, 15, 864–878.
Yang, J., and T. M. Joyce, (2005), Local and Equatorial forcing of seasonal variations of the North equatorial Countercurrent in the Atlantic Ocean., *J. Phys. Oceanogr.*, 36, 238–254.
Yoneyama, K., C. Zhang, C. N. Long, (2013), Tracking pulses of the Madden-Julian oscillation. *Bull. Amer. Meteorol. Soc.*, 94, 1871–1891. doi:10.1175/BAMS-D-12-00157.1.
Yu, X., and M. J. McPhaden, (1999), Seasonal variability in the equatorial Pacific. *J. Phys. Oceanogr.*, 29, 925–947.
Yu, Z., and J. Potemra, (2006), Generation mechanism for the intraseasonal variability in the Indo-Australian basin. *J. Geophys. Res.-Oceans*, 111, C01013, doi:10.1029/2005JC003023.
Yu, L., and M. M. Rienecker, (1999), Mechanisms for the Indian Ocean warming during the 1997–98 El Niño. *Geophys. Res. Lett.*, 26, 735–738, 10.1029/1999GL900072.
Zang, X., L.-L. Fu, and C. Wunsch, (2002), Observed reflectivity of the western boundary of the equatorial Pacific Ocean. *J. Geophys. Res.*, 107, 3150, doi:10.1029/2000JC000719.
Zhang, C., (2005), Madden-Julian Oscillation, *Rev. Geophys.*, 43, RG2003, doi:10.1029/2004RG000158.
Zhang, C., J. Gottschalck, E. D. Maloney, M. W. Moncrieff, F. Vitart, D. E. Waliser, B. Wang, and M. C. Wheeler, (2013), Cracking the MJO nut, *Geophys. Res. Lett.*, 40, 1223–1230, doi:1210.1002/grl.50244.
Zhang, D., and M. J. McPhaden, (2006), Decadal variability of the shallow Pacific meridional overturning circulation: Relation to tropical sea surface temperatures in observations and climate change models. *Ocean Model.*, 15, 250–273.
Zhou, L., and R. Murtugudde, (2010), Influences of Madden-Julian oscillations on the eastern Indian Ocean and the maritime continent. *Dyn. Atmos. Oceans*, 50, 257–274.
Zhuang, W., M. Feng, Y. Du, A. Schiller, and D. Wang, (2013), Low-frequency sea level variability in the southern Indian Ocean and its impacts on the oceanic meridional transports, *J. Geophys. Res.*, 118, 1302–1315, doi:10.1002/jgrc.20129.

18 Radar Monitoring of Volcanic Activities

Zhong Lu and Daniel Dzurisin

CONTENTS

18.1 INTRODUCTION

Earth is home to about 1500 volcanoes that have erupted in the past 10,000 years, and today volcanic activity affects the lives and livelihoods of a rapidly growing number of people around the globe. About 20 volcanoes are erupting on Earth at any given time; 50–70 erupt each year, and about 160 erupt each decade. Impressive as these statistics are, they do not include a large but unspecified number of volcanic vents along submarine midocean ridges that girdle the globe (Smithsonian Institution, Global Volcanism Program, http://www.volcano.si.edu/faq.cfm#q3).

The nature of eruptive activity ranges from the quiet outpouring of fluid lava on the ocean floor and in places like Hawaii (http://hvo.wr.usgs.gov/) to the explosive ejection of volcanic ash, pumice and other fragmental material at volcanoes like Mount Fuji (Japan), Mount St. Helens (United States), Chaitén (Chile) and others along the Pacific Ring of Fire and elsewhere. Less frequent, larger events, like the 1912 eruption of Novarupta–Mount Katmai (Alaska) (Hildreth and Fierstein 2012) and the 1991 eruption of Mount Pinatubo (Philippines) (Newhall and Punongbayan 1996), produce local and regional impacts that can last for decades, and shorter-term effects on the average global temperature. At the extreme end of the spectrum, it has been suggested that a catastrophic eruption at Lake Toba on the Indonesian island of Sumatra about 74,000 years ago caused a decade-long 'volcanic winter', resulting in a genetic bottleneck that profoundly affected the course of human evolution—an idea that remains plausible but controversial (Robock 2013 and references therein).

The products of volcanic eruptions also vary widely, giving rise to a large range of associated hazards (Myers et al. 2008). Explosive eruptions produce ballistic ejecta (solid and molten rock fragments) that can impact the surface up to several kilometres away from the vent. Smaller fragments are carried upward in eruption columns that sometimes reach the stratosphere, forming eruption clouds that pose a serious hazard to aircraft. Large eruption clouds can extend hundreds to thousands of kilometres downwind, resulting in ash fall over large areas. Heavy ash fall can collapse buildings, and even minor amounts can cause significant damage and disruption to everyday life. Volcanic gases in high concentrations can be deadly. In lower concentrations, they contribute to health problems and acid rain, which causes corrosion and harms vegetation. Lava flows and domes extruded during mostly non-explosive eruptions can inundate property and infrastructure, and create flood hazards by damming streams or rivers. Pyroclastic flows – high-speed avalanches of hot pumice, ash, rock fragments and gas – can move at speeds in excess of 100 km/h and destroy everything in their path. In some cases, gravitational collapse of an unstable volcanic edifice results in a devastating debris avalanche; the most famous example is the 1980 debris avalanche at Mount St. Helens, which extended more than 20 km down the North Fork Toutle River Valley. Debris flows and lahars (volcanic mudflows) triggered by eruptions inundate valleys for distances approaching 100 km, causing long-term ecological impacts and increased flood hazards.

Assessment, monitoring and preparedness are three keys to mitigating the adverse impacts of volcanic activity. Radar can play a direct role in helping to monitor volcanoes and assess hazards, both during periods of unrest and during ensuing eruptions. For example, interferometric synthetic aperture radar (InSAR) images can be used to distinguish between deep and shallow sources of volcano deformation, and between the deformation pattern caused by magma accumulation in a subsurface reservoir and that caused by upward intrusion of a magma-filled dyke from the reservoir towards the surface. During the course of an eruption when the volcano is obscured by clouds or darkness, Synthetic Aperture Radar (SAR) intensity images might be the only means available to track hazardous developments, such as the emergence of a gravitationally unstable lava dome. Ground-based Doppler radars can track volcanic ash clouds and provide short-term warnings to aircraft and to areas downwind that are likely to receive ash fall. Insights gained from radar studies also can contribute to improved public awareness and preparedness for volcanic activity through proactive public information programmes. For additional information about volcano hazards, hazard assessments and eruption preparedness, see http://volcanoes.usgs.gov/.

18.2 RADAR

The term *radar* is derived from 'radio detection and ranging', a phrase that encapsulates some of radar's essential characteristics and capabilities. Radar systems make use of the radio and microwave portion of the electromagnetic spectrum, with wavelengths ranging from a few millimetres to 100 m or more. Most volcano applications, including SAR and InSAR, make use of wavelengths ranging from a few centimetres to a few tens of centimetres. All radar systems employ a radio transmitter that sends out a beam of microwaves either continuously or in pulses. By measuring the time it takes radio waves travelling at the speed of light to make the round trip from the radar to a target and back, a tracking radar system can determine the distance to the target. If the target is moving with respect to the radar, its velocity can be determined from the frequency of the return signal, which differs from that of the transmitted signal as a result of the Doppler effect. The distance to the target, strength of the return signal and Doppler shift are three fundamental parameters provided by tracking radars. Because of these capabilities, tracking radars are essential tools for air traffic control and weather monitoring.

A typical tracking radar employs a scanning strategy in which the beam sweeps through a range of azimuth and elevation angles in order to map a volume of interest. For example, the radar might transmit pulses while rotating 360° in azimuth at a fixed elevation angle, and then repeat the scan at progressively higher or lower elevation angles. Return echoes from targets are received by the radar antenna and processed by the receiver. Once the radar sweeps through all elevation slices, a volume scan is complete, which provides a three-dimensional view of the airspace around the radar site. Tracking radars equipped with Doppler capability, such as those used for air traffic control, can determine both the location and speed of targets (aircraft) within their range. Weather radars take advantage of the fact that the strength of the return signal depends on the size, density, state (e.g. solid hail and liquid rain) and shape of scatterers in the beam's path. Based on empirical relationships, the approximate rainfall rate at the ground can be estimated from observations made by weather radar (e.g. https://radar.weather.gov). Weather radars equipped with Doppler capability can peer inside thunderstorms and determine if there is rotation in the cloud, which often is a precursor to the development of tornadoes.

Two characteristics of radar that are important for volcano monitoring are (1) unlike optical and infrared systems that are inherently passive (i.e. they rely on natural reflected energy or radiated energy originating at the source), radar is an active sensor that provides its own illumination, and (2) owing to their longer wavelength, radar signals penetrate water clouds, diffuse ash clouds and sparse to moderate vegetation better than visible light, enabling limited 'see-through' capability for objects that are opaque at optical wavelengths. Because radar is an active microwave system, it is equally effective in darkness and daylight, and during bad weather or good. This is a tremendous advantage for volcano monitoring, which requires round-the-clock operations during periods of unrest.

Ground-based Doppler radars have been utilized to detect and track volcanic ash clouds (Harris and Rose 1983; Rose et al. 1995; Dubosclard et al. 1999; Lacasse et al. 2004; Houlié et al. 2005; Tupper et al. 2005; Marzano et al. 2006), which can pose a hazard to buildings, infrastructure, human health and aviation systems (Rose 1977; Miller and Casadevall 2000). Figure 18.1 shows time-series images of a developing ash cloud during the 2009 eruption at Redoubt volcano, Alaska

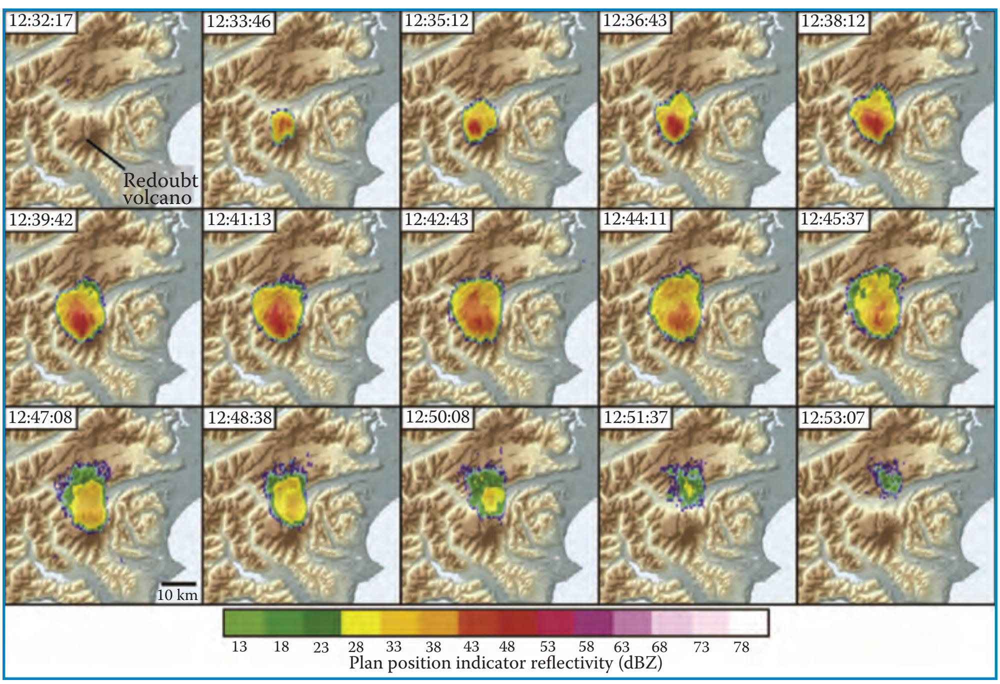

FIGURE 18.1 Sequence of radar reflectivity images at an altitude of 7.9 km above sea level over Redoubt volcano, Alaska, from a Doppler weather radar located about 82 km east of the volcano. The images show the growth and decline of an eruption cloud on 23 March 2009. Times are in Universal Time Coordinated for starts of volume scans, each of which take 90 seconds to complete. The colour bar at the bottom shows reflectivity values in decibels relative to Z (dBZ), a unit commonly used in weather radar to compare the equivalent reflectivity (Z) of a radar signal scattered from a remote object (volcanic ash, in this case) with the return from a droplet of rain with a diameter of 1 mm. For weather clouds, dBZ values can be converted to estimates of rainfall rate using an empirical formula. In this case, the greater dBZ values (warmer colours) correspond to denser parts of the ash cloud. (Modified from Schneider, D., and Hoblitt, R., *J. Volcanol. Geotherm. Res.*, 259, 133–144, 2013.)

(Schneider and Hoblitt 2013). The images show the extent and radar reflectivity of the cloud at an altitude of 7.9 km above sea level. The nearly circular cloud was characterized by a high reflectivity core and lasted at detectable levels for about 20 minutes (Schneider and Hoblitt 2013).

An imaging radar aboard the German Space Agency's TerraSAR-X satellite was used to track the growth, destruction and regrowth of a lava dome at Mount Cleveland volcano in the central Aleutian Islands, Alaska, during 2011–2013 (Lu and Dzurisin 2014, chap. 6, sect. 6.15.5). Mount Cleveland is remote, difficult to access and often obscured by clouds, so the SAR observations provided timely information about the eruption that would not have been available otherwise. Satellite SAR imagery provided similar information that aided hazard assessments during recent eruptions at the Merapi (2013) and Sinabung (2013–2014 ongoing) volcanoes in Indonesia (Smithsonian Institution Global Volcanism Program, http://volcano.si.edu/).

18.3 SYNTHETIC APERTURE RADAR

SAR is an imaging radar system designed, as the name implies, to take advantage of a large 'synthetic' antenna to produce images of much better resolution than would be possible otherwise. SAR systems operate on the same principles as Doppler radars, but have additional capability to distinguish among return signals from individual resolution elements within a target footprint. SARs are side looking, that is, they direct signals to the side of their path across the surface rather than straight down. As a result, the arrival path of the radar signal is oblique to the surface being imaged. Return signals from near-range parts of the target (the part closest to the ground track of the radar) generally arrive back at the radar sooner than return signals from far-range areas, so the relationship between round-trip travel time and range can be used to organize return signals in the across-track, or range, direction. In the along-track, or azimuth, direction, the Doppler principle comes into play. Signals returned from areas that are ahead of the radar as it travels along its path are shifted to slightly higher frequencies, while returns from trailing areas are shifted to slightly lower frequencies. An imaging radar uses the relationship between return signal frequency and relative velocity between radar and target to organize return signals in the azimuth direction. In this way, the returns from each resolution element on the ground can be assigned unique coordinates in range and azimuth. The resulting data can be processed into an image of the target area, which contains information about topography and radar reflective properties of the surface.

SAR systems take advantage of the fact that each point along the ground swath is illuminated for an extended period of time while the footprint of the radar beam moves across it. The resolution of an imaging radar is inversely proportional to the size (aperture) of the antenna, so a SAR is capable of much better resolution than is possible with a real aperture radar. Conceptually, a SAR image processor makes use of this fact to 'synthesize' a large virtual antenna, and thus achieves much higher spatial resolution than is practical with a real aperture radar. Most SAR systems designed for Earth orbit use an antenna that is 1–4 m wide and 10–15 m long, with a look angle in the range of 10°–60°, to illuminate a footprint 50–150 km wide in the range direction and 5–15 km wide in the azimuth direction. Such a SAR system is capable of producing a ground resolution of 1–10 m in azimuth and 1–20 m in range, which is an improvement by about three orders of magnitude over a comparable real aperture system. Because a SAR actively transmits and receives signals backscattered from the target area, and because radar wavelengths are mostly unaffected by weather clouds, a SAR can operate effectively during day and night under most weather conditions to produce images at times and under conditions that render most optical imaging systems useless for surface observations.

Using a sophisticated image processing technique called SAR processing (Curlander and McDonough 1991; Bamler and Hartl 1998; Henderson and Lewis 1998; Rosen et al. 2000; Massonnet and Souyris 2008), both the intensity and phase of the signal backscattered from each ground resolution element can be calculated and portrayed as part of a complex-valued SAR image. The intensity of a resulting single-look complex (SLC) image is controlled primarily by terrain slope, surface roughness and surface relative permittivity. Note that *dielectric constant* is the historical term often used to describe this property, but *surface relative permittivity* is more precise and currently accepted by the Institute of Electrical and Electronics Engineers (IEEE) Standards Board (IEEE Standard Definitions of Terms for Radio Wave Propagation 1997). The phase component is controlled mainly by the round-trip travel time from SAR to ground, which is affected by atmospheric conditions (water vapour in the troposphere slows the speed of electromagnetic waves, and electron density in the ionosphere shortens the propagation path) and by interaction of the radar signal with the ground surface.

18.4 INTERFEROMETRIC SYNTHETIC APERTURE RADAR

InSAR involves the use of two or more SAR images of the same area to extract the land surface topography plus any surface deformation that might have occurred during the interval between image acquisitions. The images can be created by spatially or temporally separated SARs (i.e. two SARs operating at the same time at slightly different locations, or a single SAR that images the same target area from similar vantage points at two different times). The spatial separation between two SAR antennas is called the baseline. The two antennas can be mounted on a single platform for simultaneous interferometry. This is the usual implementation for aircraft and space-borne systems such as the Topographic SAR (TOPSAR) and Shuttle Radar Topography Mission (SRTM) systems (Farr et al. 2007), which are used to generate digital elevation models (DEMs). Alternatively, InSAR images can be created by using a single antenna on an airborne or space-borne platform in nearly identical repeating flight paths or orbits for repeat-pass interferometry (Gray and Farris-Manning 1993; Massonnet and Feigl 1998). For the latter case, even though the antennas do not illuminate the same area at the same time, the two sets of signals recorded during the two passes will be highly correlated if the scattering properties of the ground surface remain undisturbed during the time between image acquisitions. This is the typical implementation for past and present space-borne sensors, such as the U.S. Seasat and Shuttle Imaging Radar-C (SIR-C); European Remote Sensing Satellites (ERS-1 and ERS-2), Environmental Satellite (Envisat) and Sentinel-1A/B; Canadian Radar Satellite (Radarsat-1 and Radarsat-2); and Japanese Earth Resources Satellite (JERS-1) and Advanced Land Observing Satellite (ALOS) and ALOS-2 – all of which operate at wavelengths ranging from a few centimetres (X-band and C-band) to tens of centimetres (L-band) (Table 18.1). This configuration enables InSAR measurements of surface deformation with millimetre to centimetre precision at a spatial resolution of a few tens of metres over a large region.

18.4.1 InSAR Processing Flow

A SAR image represents the intensity and phase of the reflected (or backscattered) signal from each ground resolution element in the form of a complex-valued data matrix (Figure 18.2). Generating an interferogram requires two SLC SAR images. Neglecting phase shifts induced by the transmitting and receiving antenna and SAR processing algorithms, the phase value of a pixel in an SLC SAR image (Figure 18.2b) can be represented as

$$\phi_1 = W\left\{-\frac{4\pi}{\lambda}r_1 + \varepsilon_1\right\} \tag{18.1}$$

where r_1 is the apparent range distance (including possible atmospheric delay) from the antenna to the ground target, λ is the radar wavelength, ε_1 is the sum of phase shifts due to the interaction between the incident radar wave and scatterers within the resolution cell and $W\{\}$ is a wrapping operator so that the observed ϕ_1 is wrapped into the interval of $(-\pi, \pi)$. Because the backscattering phase (ε_1) is a randomly distributed (unknown) variable, the phase value (ϕ_1) in a single SAR image

TABLE 18.1
Satellite SAR Sensors Capable of InSAR Mapping

Mission	Agency	Period of Operation	Orbit Repeat Cycle (days)	Band/ Frequency (GHz)	Wavelength (cm)	Incidence Angle (°) at Swath Centre	Resolution (m)
Seasat	NASA	June 1978–October 1978	17	L-band/1.275	23.5	23	25
ERS-1	ESA	July 1991–March 2000	3, 168 and 35[a]	C-band/5.3	5.66	23	30
JERS-1	JAXA	February 1992–October 1998	44	L-band/1.275	23.5	39	20
ERS-2	ESA	April 1995–July 2011	35 and 3[b]	C-band/5.3	5.66	23	30
Radarsat-1	CSA	November 1995–2013	24	C-band/5.3	5.66	10–60	10–100
Envisat	ESA	March 2002–April 2012	35 and 30[c]	C-band/5.331	5.63	15–45	20–100
ALOS	JAXA	January 2006–May 2011	46	L-band/1.270	23.6	8–60	10–100
TerraSAR-X	DLR	June 2007–present	11	X-band/9.65	3.11	20–55	0.24–260
Radarsat-2	CSA	December 2007–present	24	C-band/5.405	5.55	10–60	3–100
COSMO-SkyMed	ASI	June 2007–present	1, 4, 5, 7, 8, 9, 12 and 16[d]	X-band/9.6	3.12	20–60	1–100
RISAT-2	ISRO	April 2009–present	14	X-band/9.59	3.13	20–45	1–8
TanDEM-X[e]	DLR	June 2010–present	11	X-band/9.65	3.11	20–55	1–16
RISAT-1	ISRO	April 2012–present	25	C-band/5.35	5.61	15–50	3–50
Sentinel-1A	ESA	April 2014–present	12	C-band/5.405	5.55	20–47	5–40
ALOS-2	JAXA	May 2014–present	14	L-band/1.2575 (and more)	23.9 (and more)	8–70	1–100
Sentinel-1B	ESA	April 2016–present	12	C-band/5.405	5.55	20–47	5–40

Note: ASI, Italian Space Agency; CSA, Canadian Space Agency; ESA, European Space Agency; ISRO, Indian Space Research Organization; JAXA, Japan Aerospace Exploration Agency; RISAT-1, Radar Imaging Satellite-1; RISAT-2, Radar Imaging Satellite-2.

[a] To accomplish various mission objectives, the ERS-1 repeat cycle was 3 days from 25 July 1991 to 1 April 1992 and from 13 December 1993 to 9 April 1994; 168 days from 10 April 1994 to 20 March 1995; and 35 days at other times.

[b] The ERS-2 repeat cycle was mainly 35 days. During the few months before the end of the mission, the ERS-2 repeat cycle was changed to 3 days to match the 3-day-repeat ERS-1 phases in 1991–1992 and 1993–1994.

[c] The Envisat repeat cycle was 35 days from March 2002 to October 2010, and 30 days from November 2010 to April 2012.

[d] A constellation of four satellites, each of which has a repeat cycle of 16 days, can collectively produce repeat-pass InSAR images at intervals of 1, 4, 5, 7, 8, 9 and 12 days, respectively.

[e] TerraSAR add-on for digital elevation measurements.

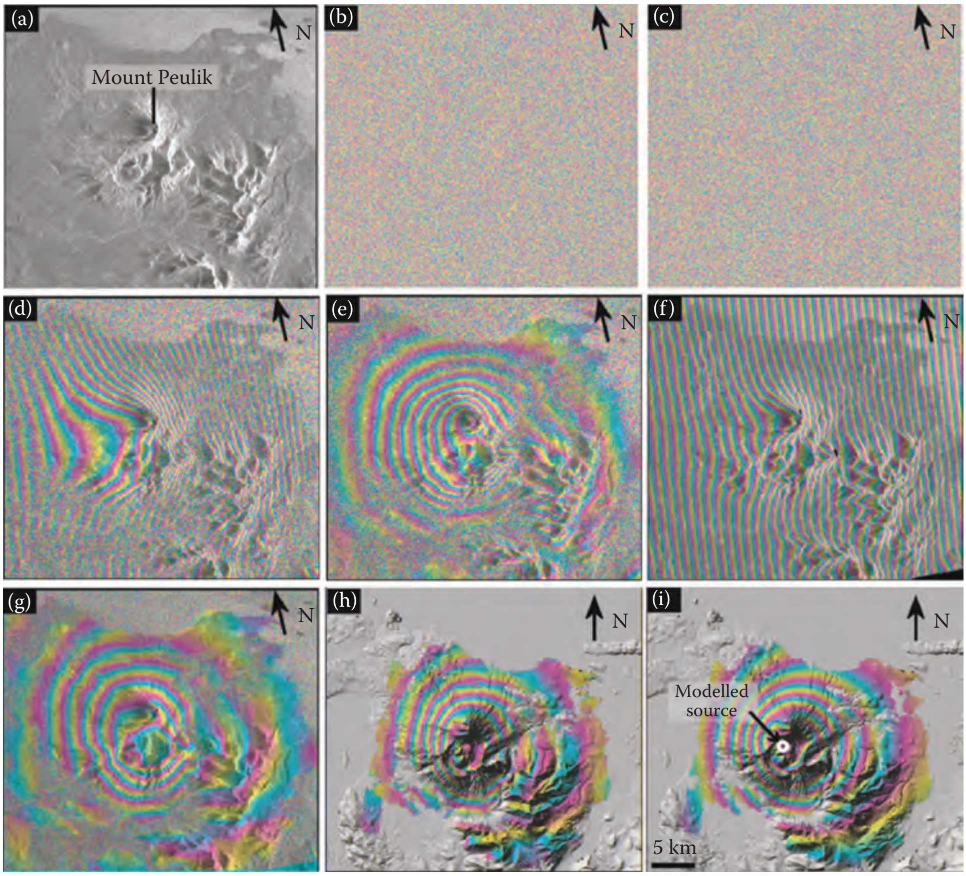

FIGURE 18.2 (a) Amplitude component of an ERS-1 SAR image acquired on 4 October 1995 over Mount Peulik volcano, Alaska. (b) Phase component of the SLC SAR image corresponding to the amplitude image in (a). (c) Phase component of an ERS-2 SAR image of Mount Peulik acquired on 9 October 1997. The amplitude component is similar to that in (a) and therefore is not shown. The phase values represented in (b) and (c) look spatially random but nonetheless contain useful information after InSAR processing. (d) Original interferogram formed by differencing the phase values of two co-registered SAR images, (b) and (c). The resulting InSAR image contains fringes produced by the differing viewing geometries, topography, any atmospheric delays, surface deformation and noise. The perpendicular component of the InSAR baseline is 35 m in this case. (e) Flattened interferogram produced by removing the effect of a flat Earth surface from the original interferogram (d). (f) Simulated interferogram representing the contribution of topography in the original interferogram (d) using knowledge of the InSAR imaging geometry and a DEM. (g) Topography-removed interferogram produced by subtracting the simulated interferogram (f) from the original interferogram (d). The resulting interferogram contains fringes produced by surface deformation, any atmospheric delays and noise. (h) Georeferenced topography-removed interferogram overlaid on a shaded relief image produced from a DEM. The concentric pattern of fringes indicates ~17 cm of uplift centred on the volcano, which occurred during an aseismic inflation episode between 1996 and 1998 prior to a strong earthquake swarm ~30 km to the northwest (Lu et al. 2002b). (i) Model interferogram produced using a best-fit inflationary point source at ~6.5 km depth with a volume change of ~0.043 km^3 overlaid on the shaded relief image (compare to (h)). Each interferometric fringe (full-colour cycle or band) represents 360° of phase change (b–f), or 2.83 cm of range change (g–i) between the ground and the satellite along the satellite look direction. Areas of loss of InSAR coherence are uncoloured in (h) and (i).

cannot be used to calculate the range (r_1) and is of no practical use. However, assume that a second SLC SAR image of the same area (with the phase image shown in Figure 18.2c) is obtained at a different time with a phase value represented by

$$\phi_2 = W\left\{-\frac{4\pi}{\lambda} r_2 + \varepsilon_2\right\} \tag{18.2}$$

Note that, by itself, the second SAR image cannot provide useful range information (r_2) either.

An interferogram (Figure 18.2d) is created by co-registering two SAR images and differencing the corresponding phase values (Figure 18.2b,c) on a pixel-by-pixel basis. The phase value of the resulting interferogram (Figure 18.2d) is

$$\phi = \phi_1 - \phi_2 = W\left\{-\frac{4\pi(r_1 - r_2)}{\lambda} + (\varepsilon_1 - \varepsilon_2)\right\} \tag{18.3}$$

The fundamental assumption in repeat-pass InSAR is that the scattering characteristics of the ground surface do not change during the interval between image acquisitions. The degree of change can be quantified by the interferometric coherence value, which is discussed in Section 18.5.3. Assuming that the interactions between radar waves and scatterers remain the same (i.e. $\varepsilon_1 = \varepsilon_2$), the interferometric phase value can be expressed as

$$\phi = W\left\{-\frac{4\pi(r_1 - r_2)}{\lambda}\right\} \tag{18.4}$$

Typical values for the range difference, $(r_1 - r_2)$, are from a few metres to several hundred metres. The SAR wavelength (λ) is of the order of several centimetres. Because the measured interferometric phase value (ϕ) is modulated by 2π, ranging from $-\pi$ to π, there is an ambiguity of many cycles (i.e. numerous 2π values) in the interferometric phase value. Therefore, the phase value of a single pixel in an interferogram is of no practical use. However, the change in range difference, $\delta(r_1 - r_2)$, between two neighbouring pixels that are a few metres apart is normally much smaller than the SAR wavelength. So the phase difference between two nearby pixels, $\delta\phi$, can be used to infer the range difference $(r_1 - r_2)$ to a precision that is a small fraction of the radar wavelength. This explains how the InSAR technique can determine range changes to within a few millimetres or centimetres based on observed phase differences between two co-registered images.

The phase (or range distance difference) in the original interferogram (Figure 18.2d) contains contributions from both the topography and any possible ground surface deformation. Therefore, the topographic contribution needs to be removed from the original interferogram in order to derive a deformation map. The most common procedure is to use an existing DEM and knowledge of the InSAR imaging geometry to produce a synthetic interferogram that represents the topographic effect and subtract it from the interferogram to be studied (Massonnet and Feigl 1998; Rosen et al. 2000). This is the so-called two-pass InSAR technique. Alternatively, a synthetic interferogram that represents the topographic contribution can be produced from a different interferogram of the same area that is either insensitive to deformation or does not span the deformation episode (if known by some other means). The procedures are then called three-pass or four-pass InSAR (Zebker et al. 1994). Because the two-pass InSAR method is commonly used for deformation mapping, we explain briefly how to simulate the effect of topography in an InSAR image based on an existing DEM.

Two steps are required to simulate a topography-only interferogram based on a DEM. In the first step, the DEM needs to be resampled to project heights from a map coordinate into the appropriate radar geometry via geometric simulation of the imaging process. The InSAR imaging geometry is shown in Figure 18.3. The InSAR system acquires two images of the same scene with SAR platforms located at A_1 and A_2. The baseline, defined as the vector from A_1 to A_2, has a length B and is tilted with respect to the horizontal by angle α. The slant range r from the SAR to a ground target T with an elevation value h is linearly related to the measured phase values in the SAR images by Equations 18.1 and 18.2. The look angle from A_1 to the ground point T is θ_1. For each ground resolution cell at ground range r_g with elevation h, the slant range value (r_1) should satisfy

$$r_1 = \sqrt{(H+R)^2 + (R+h)^2 - 2(H+R)(R+h)\cos\left(\frac{r_g}{R}\right)} \tag{18.5}$$

where H is the SAR altitude above a reference Earth surface, which is assumed to be a sphere with radius R. The radar slant range and azimuth coordinates are calculated for each point in the DEM. This set of coordinates forms a non-uniformly sampled grid in SAR coordinate space. The DEM

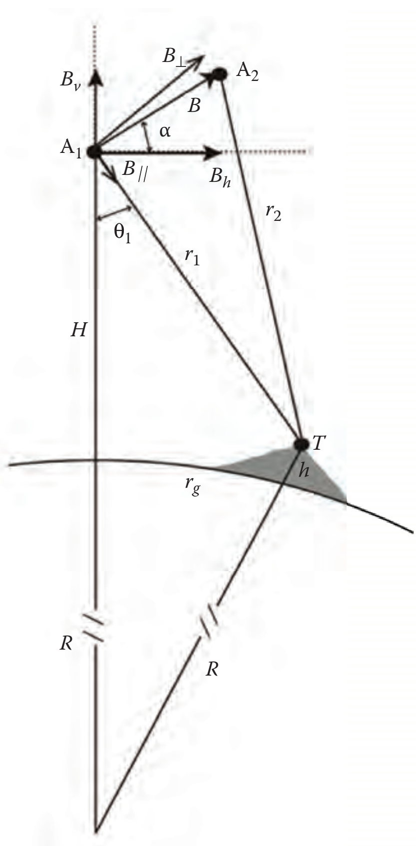

FIGURE 18.3 Schematic showing InSAR imaging geometry. Two SAR images of the same target area are acquired from vantage points A_1 and A_2. The baseline B (the spatial distance between SAR antennas A_1 and A_2) is tilted with respect to the horizontal by angle α, and can be represented by a pair of horizontal (B_h) and vertical (B_v) components, or by a pair of parallel ($B_{//}$) and perpendicular ($B_\perp$) components. The slant range distances from A_1 and A_2 to a ground target T with elevation above the ground surface h are r_1 and r_2, respectively. The altitude of A_1 is H, and the ground range from A_1 to T is r_g. The look angle from A_1 to T is θ_1. The radius of the spherical Earth is R.

height data are then resampled into a uniform grid in the radar coordinates using the values from the non-uniform grid.

In the second step, the precise look angle from A_1 to ground target T at ground range r_g, slant range r_1 and elevation h is calculated:

$$\theta_1 = \arccos\left[\frac{(H+R)^2 + r_1^2 - (R+h)^2}{2(H+R)r_1}\right] \tag{18.6}$$

Finally, the interferometric phase value due to the topographic effect at target T can be calculated:

$$\phi_{\text{dem}} = -\frac{4\pi}{\lambda}(r_1 - r_2) = \frac{4\pi}{\lambda}\left(\sqrt{r_1^2 - 2(B_h \sin\theta_1 - B_v \cos\theta_1)r_1 + B^2} - r_1\right) \tag{18.7}$$

where B_h and B_v are horizontal and vertical components of the baseline B (Figure 18.3).

Figure 18.2e shows the simulated topographic effect in the original interferogram (Figure 18.2d) calculated using an existing DEM and the InSAR imaging geometry (Figure 18.3). Removing the topographic effect (Figure 18.2e) from the original interferogram (Figure 18.2d) results in an interferogram that represents ground surface deformation during the time interval between image acquisitions, plus measurement noise (Figure 18.2f). The resulting phase value can be written as

$$\phi_{\text{def}} = W\{\phi - \phi_{\text{dem}}\} \tag{18.8}$$

In common practice, an ellipsoidal Earth surface characterized by its major axis, e_{maj}, and minor axis, e_{min}, is used instead of a spherical Earth model. The radius of the Earth at the imaged area is then

$$R = \sqrt{(e_{\min} \sin\beta)^2 + (e_{maj} \cos\beta)^2} \tag{18.9}$$

where β is the latitude of the centre of the imaged region.

If h is taken as zero, the procedure outlined in Equations 18.5 through 18.9 will remove the effect of an ellipsoidal Earth surface on the interferogram. This results in a flattened interferogram, in which phase values can be approximated as

$$\phi_{flat} = -\frac{4\pi}{\lambda}\frac{B\cos(\theta_1 - \alpha)}{r_1 \sin\theta_1}h + \phi_{def} = -\frac{4\pi}{\lambda}\frac{B_\perp}{H\tan\theta_1}h + \phi_{def} \tag{18.10}$$

where $B_\perp$ is the perpendicular component of the baseline with respect to the incidence angle θ_1 (Figure 18.3). Removing the effect of an ellipsoidal Earth surface from the original interferogram (Figure 18.2d) results in the flattened interferogram shown in Figure 18.2g.

If ϕ_{def} in Equation 18.10 is negligible (i.e. no deformation) or can be removed from an independent source (Lu et al. 2013), the phase value in Equation 18.10 can be used to calculate the surface height h. This explains how InSAR can be used to produce an accurate, high-resolution DEM for a large region. If the primary goal is to produce a DEM but the interferogram is also affected by ground deformation (i.e. ϕ_{def} is not negligible), the deformation effect can be calculated from a second interferogram that is less sensitive to topography, and then removed from the first interferogram (Lu and Dzurisin 2014).

For the ERS-1/2 satellites, H is about 800 km, θ_1 is about 23° ± 3°, λ is 5.66 cm and $B_\perp$ should be less than 1100 m for a coherent interferogram. Therefore, Equation 18.10 can be approximated as

$$\phi_{flat} \approx -\frac{2\pi}{9600} B_\perp h + \phi_{def} \tag{18.11}$$

For an interferogram with $B_\perp$ of 100 m, 1 m of topographic relief produces a phase value of about 4°. However, producing the same phase value requires only 0.3 mm of surface deformation. ϕ_{flat} in Equation 18.11 can be considered a function of two variables, h and ϕ_{def}. The coefficient (i.e. $2\pi B_\perp/9600$) for h is much less than 1, while the coefficient for ϕ_{def} is equal to 1. So for a given imaging geometry, the interferogram phase value is much more sensitive to changes in topography (i.e. surface deformation ϕ_{def}) than to the topography itself (h). This explains why repeat-pass InSAR is capable of mapping surface deformation with millimetre to centimetre precision.

With the two-pass InSAR technique, DEM errors can be incorrectly mapped into apparent surface deformation. The effect is characterized by the so-called 'altitude of ambiguity', which is the amount of DEM error required to generate one interferometric fringe in a topography-removed interferogram (Massonnet and Feigl 1998). Because the altitude of ambiguity is inversely proportional to the perpendicular baseline $B_\perp$, interferometric pairs with small baselines are better suited for deformation analysis. Conversely, pairs with larger baselines (within the constraint imposed by coherence; see Section 18.5.2) are preferable for DEM generation.

One significant error source in repeat-pass InSAR deformation measurements is inhomogeneity in the atmosphere that results in path-delay anomalies (Lu and Dzurisin 2014). Differences in atmospheric water vapour content (and temperature and pressure to a lesser extent) at two observation times can cause differing path delays and consequent anomalies in an InSAR deformation image. Atmospheric delay anomalies can reduce the accuracy of InSAR-derived deformation measurements from several millimetres under ideal conditions to a few centimetres under more typical conditions, thus obscuring subtle changes that could hold clues to the cause of the deformation. The difficulty with estimating water vapour conditions with the needed accuracy and spatial density is an important limiting factor in deformation monitoring with InSAR.

Four methods have been proposed to estimate the water vapour content and remove its effect from deformation interferograms. The first method is to estimate water vapour concentrations in the target area at the times of SAR image acquisitions using short-term predictions from operational weather models (Foster et al. 2006). The problem with this approach is that current weather models have much coarser resolution (a few kilometres) than InSAR measurements (tens of metres). This deficiency can be remedied to some extent by integrating weather models with high-resolution atmospheric measurements, but this approach requires intensive computation. The second method is to estimate water vapour concentration from continuous global positioning system (CGPS) observations in the target area (Li et al. 2005). The spatial resolution (i.e. station spacing) of local or regional CGPS networks at volcanoes is typically a few kilometres to tens of kilometres, which renders this method ineffective in most cases. The third approach to correcting atmospheric delay anomalies in InSAR observations is to utilize water vapour measurements from optical satellite sensors such as the Moderate Resolution Imaging Spectroradiometer (MODIS), Advanced Spaceborne Thermal Emission and Reflection Radiometer (ASTER) and European Medium Resolution Imaging Spectrometer (MERIS) (Li et al. 2003). The disadvantage of this method is the requirement of nearly simultaneous acquisitions of SAR and cloud-free optical images. The fourth and most promising technique is to correct atmospheric delay anomalies using a multitemporal InSAR technique (Section 18.6) (Ferretti et al. 2001; Lu and Dzurisin 2014). Because the atmospheric artefacts are generally spatially correlated and temporally random, they can be mitigated through temporal high-pass and spatial low-pass filtering of multitemporal interferograms.

Another significant error source in two-pass InSAR processing is baseline uncertainty due to inaccurate determination of the SAR antenna positions at the times of image acquisitions. Therefore, baseline refinement during InSAR processing is recommended. A commonly used method is to determine the baseline vector based on an existing DEM via a least-squares approach (Rosen et al. 1996). For this method, areas of the interferogram that are used to refine the baseline should have negligible deformation or deformation that is well characterized by an independent data source.

The final procedure in two-pass InSAR is to rectify the SAR images and interferograms into a geographic coordinate system, which is a backward transformation of Equation 18.5. The georeferenced interferogram (Figure 18.2h) and derived products can be readily overlaid with other data layers to enhance the utility of the interferograms and facilitate data interpretation. Figure 18.2h shows six concentric fringes that represent about 17 cm of range decrease (mostly uplift) centred on the southwest flank of Mount Peulik volcano, Alaska. The volcano inflated aseismically from October 1996 to September 1998, a period that included an intense earthquake swarm that started in May 1998 more than 30 km northwest of Peulik (Lu et al. 2002; Lu 2007; Lu and Dzurisin 2014).

Interferometric phase values need to be unwrapped to remove the modulo 2π ambiguity before estimating the topography or deformation source parameters (Goldstein et al. 1988; Costantini 1998; Chen and Zebker 2000). Phase unwrapping is the process of restoring the correct multiple of 2π to each pixel of the interferometric phase image. Interferograms are often spatially filtered before phase unwrapping (Goldstein and Werner 1998). Two popular phase unwrapping methods utilize branch cut (Goldstein et al. 1998) and minimum cost flow (Costantini 1998; Chen and Zebker 2000) algorithms.

In-depth descriptions of InSAR processing techniques are given by many (Zebker et al. 1994; Bamler and Hartl 1998; Henderson and Lewis 1998; Massonnet and Feigl 1998; Rosen et al. 2000; Hanssen 2001; Hensley et al. 2001; Lu and Dzurisin 2014).

18.5 InSAR PRODUCTS AND THEIR APPLICATIONS TO VOLCANOES

The InSAR processing techniques include a number of steps, precise registration of an InSAR image pair, interferogram generation, removal of the curved Earth phase trend, adaptive filtering, phase unwrapping, precise estimation of the interferometric baseline, generation of a surface deformation image (or a DEM map), estimation of interferometric correlation and rectification of interferometric products. Using a single pair of SAR images as input, a typical InSAR processing chain outputs two SAR intensity images, a deformation map or DEM and an interferometric correlation map.

18.5.1 SAR Intensity Image

Volcanic surfaces do not scatter microwaves uniformly. The strength of the return signal at the SAR is controlled primarily by surface roughness and relative permittivity of the target. Surface roughness refers to the SAR wavelength-scale variation in the surface relief. Surfaces that are rough at the scale of the radar wavelength generally are brighter in radar images than smooth ones, because some of the roughness elements are oriented perpendicular to the incoming signal and reflect energy back towards the source. With smooth surfaces, most of the energy is deflected forward, away from the source, which causes them to appear dark. For this reason, blocky lava flows tend to exhibit stronger backscattering returns than pyroclastic flows, which in turn produce higher backscattering than ash deposits. Therefore, SAR intensity images are useful for distinguishing and mapping volcanic ash deposits, lava flows and pyroclastic flows (Lu et al. 2004; Lu and Dzurisin 2014). In cloud-prone volcanic areas (such as the Aleutian volcanic arc), all-weather SAR intensity imagery can be one of the most useful data sources available to track the course of volcanic eruptions in this way. Relative permittivity is an electric property of material that influences radar return strength and is controlled primarily by moisture content of the imaged surface. The effect of relative permittivity variations on radar images is of secondary importance to surface roughness variations, as most natural, dry rocks and soils have a narrow range of values of relative permittivity. Limited laboratory results have indicated that relative permittivity values of volcanic rocks of similar mineralogy and composition tend to increase with the bulk density but decrease with the porosity of volcanic rocks (Russ et al. 1999). Obviously, mapping volcanic deposits based on relative permittivity can generally be complicated by moisture content, mineralogy, composition and other parameters.

Figure 18.4 shows an example in which time-series SAR intensity images were used to track eruptive activity at Mount Cleveland volcano in the central Aleutian Arc, Alaska. Thermal anomalies at Mount Cleveland were noted in satellite data starting on 19 July 2011, and a small lava dome in the summit crater was first observed on 2 August 2011 (Lu and Dzurisin 2014). Time-series TerraSAR-X images revealed that the new dome grew rapidly until 29 December 2011, when it

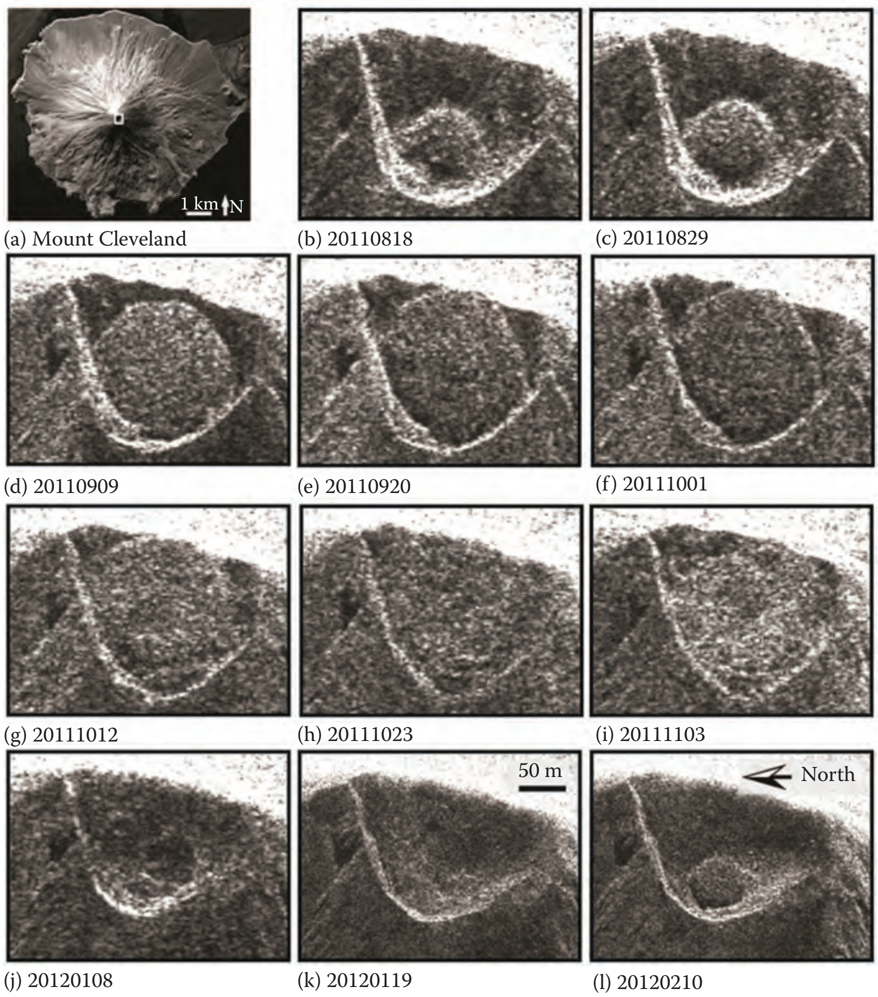

FIGURE 18.4 (a) Airborne L-band SAR intensity image of Mount Cleveland volcano, Alaska, acquired in 2009 by NASA's Uninhabited Aerial Vehicle Synthetic Aperture Radar (UAVSAR). Lava flows of various ages are apparent in the SAR image. The white rectangle in the summit area shows the extent of the SAR intensity images shown in (b–l). (b–l) Time-series X-band TerraSAR-X intensity images of the Mount Cleveland summit crater showing lava dome growth (b–i), destruction (j–k) and regrowth (l) during the period from 18 August 2011 to 10 February 2012. The initial dome was destroyed by an explosive eruption on 29 December 2011, and a second dome was clearly visible in the SAR image acquired on 10 February 2012. Cycles of dome growth and destruction continued into 2013.

was destroyed by an explosion. A new dome was visible in a TerraSAR-X image acquired on 10 February 2012 (Figure 18.4). That dome likely was destroyed by a series of three explosions during 8–13 March 2012. A third dome, which was first seen in satellite imagery on 28 March 2012, was destroyed by an explosive eruption on 4 April 2012. Additional small explosions occurred during April–June 2012, and a fourth dome was observed in the crater on 26 June 2012. Multiple explosions were detected and a small lava flow was extruded in May 2013 (http://avo.alaska.edu/volcanoes/volcact.php?volcname=Cleveland). In this case, morphological changes at the summit of Mount Cleveland that could be discerned in a series of SAR intensity images, but were otherwise obscured from view, played a key role in monitoring activity throughout the course of the eruption (Wang et al. 2015).

18.5.2 InSAR Deformation Image and Source Parameters Derived from Modelling

Unlike a SAR intensity image, an InSAR deformation image is derived from phase components of two overlapping SAR images. SAR is a side-looking sensor, so an InSAR deformation image depicts ground surface displacements in the SAR line-of-sight (LOS) direction, which generally include both vertical and horizontal components. InSAR deformation images have an advantage for modelling purposes over point measurements made with GPS, for example, because InSAR images provide more complete spatial coverage than is possible with even a dense network of CGPS stations. On the other hand, CGPS stations provide better precision and much better temporal resolution than is possible with InSAR images. The temporal resolution of InSAR measurements is constrained by the orbit repeat times of SAR satellites, that is, typically several days to weeks for currently operational satellites. For hazards monitoring, a combination of periodic areal InSAR observations and continuous data streams from networks of in situ deformation sensors (e.g. CGPS, tiltmeters and strainmeters), integrated with seismic, gas emission and other remote sensing information, is highly desirable (Poland et al. 2006b; Dzurisin et al. 2009; Biggs et al. 2010b; Currenti et al. 2011, 2012; Del Negro et al. 2013).

For understanding volcanic processes, numerical models are often employed to estimate physical parameters of the deformation source based on observations. The high spatial resolution of surface deformation data provided by InSAR makes it possible to constrain models with various geometries, such as the spherical point pressure source (Mogi 1958), dislocation source (sill or dyke source) (Okada 1985), ellipsoid source (Davis 1986; Yang et al. 1988) and penny-crack source (Fialko et al. 2001). Among the physical parameters of interest, the location and volume change of the source usually are the most important.

The most widely used source in volcano deformation modelling is the spherical point pressure source (widely referred to as the Mogi source) embedded in an elastic homogeneous half space (Mogi 1958). In a Cartesian coordinate system, the predicted displacement u at the free surface due to a change in volume ΔV or pressure ΔP of an embedded sphere is

$$u_i\left(x_1 - x_1', x_2 - x_2', 0 - x_3'\right) = \Delta P(1-\nu)\frac{r_s^3}{G}\frac{x_i - x_i'}{\left|R^3\right|} = \Delta V\frac{(1-\nu)}{\pi}\frac{x_i - x_i'}{\left|R^3\right|} \qquad (18.12)$$

where x_1', x_2' and x_3' are the horizontal coordinates and depth of the centre of the sphere, R is the distance between the centre of the sphere and the observation point (x_1, x_2 and 0), ΔP and ΔV are the pressure and volume changes in the sphere, ν is Poisson's ratio of the host rock (typical value is 0.25), r_s is the radius of the sphere and G is the shear modulus of the host rock (Johnson 1987; Delaney and McTigue 1994).

A non-linear least-squares inversion approach is often used to optimize the source parameters (Press et al. 2007). Inverting the observed interferogram in Figure 18.2h using a Mogi source results in a best-fit source located at a depth of 6.5 ± 0.2 km. The calculated volume change is

0.043 ± 0.002 km^3. Figure 18.2i shows the modelled interferogram based on the best-fit source parameters, which agrees very well with the observed deformation field shown in Figure 18.1h.

Because many volcanic eruptions are preceded by pronounced ground deformation in response to increasing pressure in a magma reservoir or to upward intrusion of magma, surface deformation patterns can provide important insights into the structure, plumbing and state of restless volcanoes (Dvorak and Dzurisin 1997; Dzurisin 2003, 2007). Numerous studies have shown that in some cases, surface deformation is the first detectable sign of volcanic unrest, preceding seismicity or other precursors to an impending intrusion or eruption (Lu and Dzurisin 2014). Therefore, mapping surface deformation and deriving source characteristics is a primary focus of most InSAR studies of volcanoes (Massonnet et al. 1995; Lu et al. 1997, 2000a,b,c, 2002, 2005, 2007, 2010; Wicks et al. 1998, 2002, 2006, 2011; Dzurisin et al. 1999, 2005; Amelung et al. 2000, 2007; Zebker et al. 2000; Mann et al. 2002; Pritchard and Simons 2002, 2004a,b; Masterlark and Lu 2004; Fukushima et al. 2005; Lundgren and Lu 2006; Poland et al. 2006a; Wright et al. 2006; Yun et al. 2006; Hooper et al. 2007; Calais et al. 2008; Biggs et al. 2009, 2010a,b; Fournier et al. 2010; Lu and Dzurisin 2010; Ji et al. 2013; Lee et al. 2013; Parker et al. 2014).

Figure 18.5 shows several interferograms of Mount Okmok, a dominantly basaltic volcano in the central Aleutian volcanic arc, Alaska; each has a temporal separation of 1 year, and collectively they span from 1997 to 2008. Okmok erupted during February–April 1997 and again during July–August 2008. The inter-eruption deformation interferograms suggest that Okmok began to reinflate soon after its 1997 eruption, but the inflation rate generally decreased with time during 1997–2001: from about 10 cm/year during 1997–1998 to about 8 cm/year during 1998–2000, and further to about 4 cm/year during 2000–2001 (Figure 18.5b–e). The rate increased again during 2001–2003 (Figure 18.5f and g), reaching a maximum of about 20 cm/year during 2002–2003 (Figure 18.5g), before slowing to about 10 cm/year during 2003–2004 (Figure 18.5h). The caldera floor subsided 3–5 cm during 2004–2005 (Figure 18.5i), rose a similar amount during 2005–2006 (Figure 18.5j) and then did not move appreciably during 2006–2007 (Figure 18.5k). About 15 cm of uplift occurred from summer 2007 to 10 July 2008, shortly before the 12 July 2008 eruption (Figure 18.5l). This remarkable series of interferograms was interpreted as indicative of a variable rate of magma supply to a shallow storage zone beneath Okmok during the inter-eruption period of 1997–2008 (Lu et al. 2010; Lu and Dzurisin 2014).

Modelling these interferograms using a Mogi source suggests that a magma storage zone centred about ~3.5 km beneath the centre of the 10 km diameter caldera floor was responsible for the observed deformation at Okmok. The InSAR deformation images can be used to track the accumulation of magma beneath Okmok as a function of time. The total volume of magma added to the shallow storage zone from the end of the 1997 eruption to a few days before the 2008 eruption was 85%–100% of the amount that was extruded during the 1997 eruption (Lu and Dzurisin 2014).

Because InSAR is an imaging technique with good spatial resolution, it is also highly effective for mapping localized deformation associated with volcanic flows. For example, Figure 18.5k shows that the 1997 lava flow at Okmok subsided about 3 cm/year during 2006–2007, nearly a decade after it was emplaced. Lu et al. (2005) constructed two-dimensional finite element models of the localized deformation field and concluded that the subsidence likely was caused by thermoelastic cooling of the 1997 flow. They also reported that a significant amount of subsidence (1–2 cm/year) could be observed with InSAR even 50 years after emplacement of the 1958 lava flows at Okmok. This has implications for positioning geodetic markers and deformation sensors at Okmok and other similar volcanoes, and for interpretation of resulting point measurement data (e.g. GPS, tilt and borehole strain). InSAR images can provide an important spatial context for such endeavours, thus helping to avoid misinterpretations caused by unrecognized deformation sources, such as young flows, localized faulting or hydrothermal activity.

18.5.3 InSAR Coherence Image

An InSAR coherence image is a cross-correlation product derived from two co-registered complex-valued (both intensity and phase components) SAR images (Zebker and Villasenor 1992; Lu and

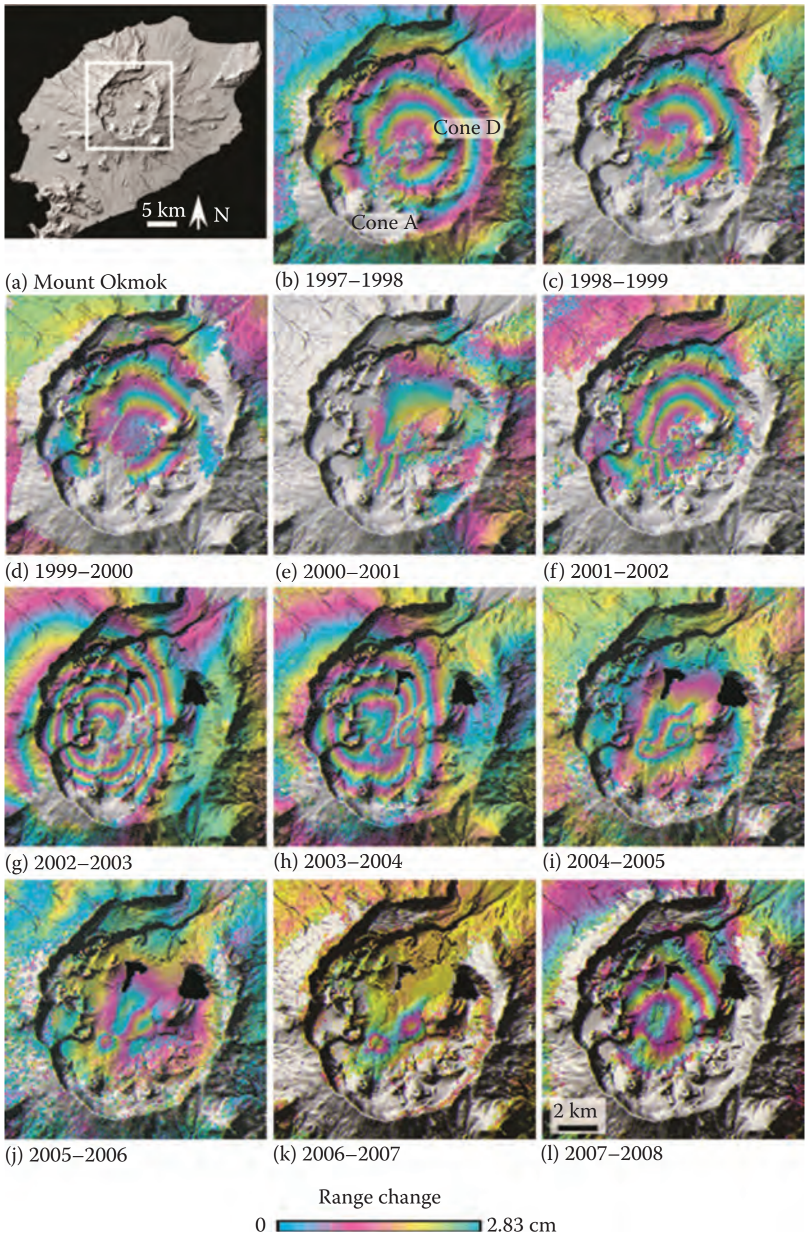

FIGURE 18.5 (a) Shaded relief image of Mount Okmok volcano in the central Aleutian Arc, Alaska. The white square shows the extent of interferograms in (b–l). (b–l) Multitemporal 1-year InSAR images showing the intereruption deformation of Mount Okmok from 1997 (after the end of the 1997 eruption) to 2008 (before the 2008 eruption). InSAR deformation phase values are draped over the corresponding portion of the shaded relief image. Each fringe (full colour cycle) represents 2.83 cm of range change between the ground and satellite along the satellite LOS direction. Areas that lack interferometric coherence are uncoloured.

Freymueller 1998). It depicts changes in backscattering characteristics on the scale of the radar wavelength. Constructing a coherent interferogram requires that SAR images correlate with each other; that is, the backscattering spectrum must be substantially similar over the observation period. Physically, this translates into a requirement that the ground scattering surface be relatively undisturbed at the scale of the radar wavelength during the time between measurements. Loss of InSAR coherence is often referred to as decorrelation. Decorrelation can be caused by the combined effects of (1) thermal decorrelation caused by uncorrelated noise sources in radar instruments, (2) geometric decorrelation resulting from imaging a target from very different look angles, (3) volume decorrelation caused by volume backscattering effects and (4) temporal decorrelation due to surface changes over time (Lu and Kwoun 2008).

InSAR coherence is estimated by cross-correlation of the SAR image pair within a small window of pixels. An InSAR coherence map is generated by computing the cross-correlation in a moving window over the entire image. The reliability of a deformation image or InSAR-derived DEM map can be assessed based on the InSAR coherence map. On the one hand, loss of InSAR coherence renders an InSAR image useless for measuring ground surface deformation. So for this application, the greater the coherence shown by a coherence map, the more reliable is the associated deformation image. Geometric and temporal decorrelation can be mitigated by choosing an image pair with a short baseline and brief temporal separation, respectively, so choosing such a pair is recommended when the goal is to measure surface deformation.

On the other hand, the pattern of decorrelation within a coherence image can provide useful information about surface modifications caused by volcanic activities, such as heavy ash fall or various types of flows. These phenomena modify the surface to a degree that coherence is lost, providing an efficient means to delineate the impacted areas without detailed fieldwork. Even though useful deformation measurements cannot be retrieved over areas of decorrelation, time-sequential InSAR coherence maps can be used to map the extent and progression of eruptive products, such as active lava flows. As an example, Figure 18.6 shows two TerraSAR-X InSAR coherence images along the East Rift Zone and south flank of Kīlauea volcano on the Big Island of Hawaii. The X-band images do not maintain coherence in areas of dense rainforest outside the lava flow field from the 1983 to the present Puʻu ʻŌʻō–Kupaianaha eruption, nor on an active lava flow in the central part of the flow field (dark areas in the images). Elsewhere in the flow field, where young but inactive flows have cooled and stabilized, coherence is generally maintained. As a result of these differences, we can see that (1) flow activity extended all the way to the ocean during 15 September–23 December 2011, and (2) from 25 January to 25 May 2012, the flow expanded laterally but did not reach the ocean. Time-series images such as these can aid in mapping the extent and progress of volcanic flows, and thus also in assessing the inundation threat to nearby areas.

18.5.4 Digital Elevation Model

A precise DEM can be a very important dataset for characterizing and monitoring man-made and natural hazards, including those posed by volcanic activity. For example, a DEM is necessary to simulate potential mudflows (lahars) that are commonly associated with volcanic eruptions, large earthquakes and heavy rainfall in steep terrain. The ideal SAR configuration for DEM production is a single-pass (simultaneous) two-antenna system (e.g. SRTM). However, repeat-pass single-antenna InSAR also can be used to produce useful DEMs. Either technique is advantageous in areas where the traditional photogrammetric approach to DEM generation is hindered by persistent clouds or other factors (Lu et al. 2003; Lu and Dzurisin 2014).

There are many sources of error in DEM construction from repeat-pass SAR images, including inaccurate determination of the InSAR baseline, atmospheric delay anomalies and possible surface deformation due to tectonic, volcanic or other sources during the time interval spanned by the images. To generate a high-quality DEM, these errors must be identified and corrected using a multi-interferogram approach (Lu et al. 2003, 2013; Lu and Dzurisin 2014). A data fusion technique, such as the wavelet method, can be used to combine DEMs from several interferograms with different spatial resolution, coherence and vertical accuracy to generate the final DEM product (Ferretti et al. 1999). One example of the utility of precise InSAR-derived DEMs is illustrated in Figure 18.7, which shows the extent and thickness of a lava flow extruded during the 1997 Okmok eruption. The flow's three-dimensional distribution was derived by differencing two DEMs that represent the

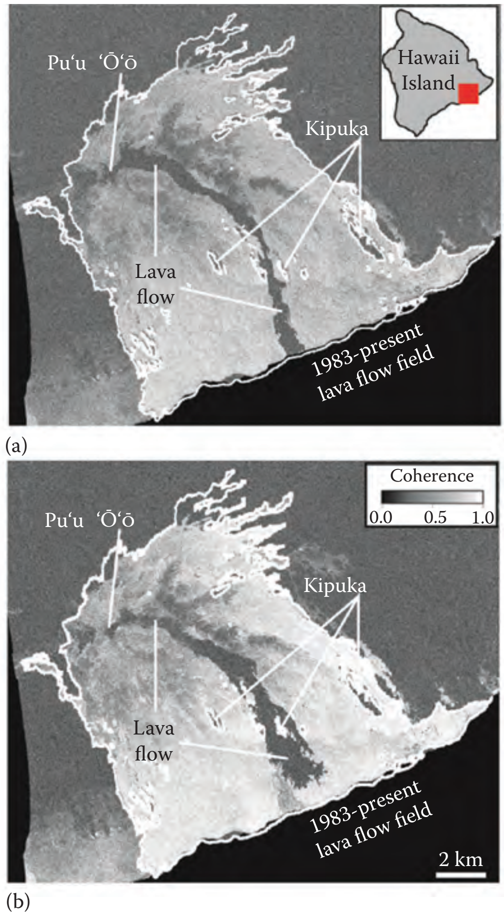

FIGURE 18.6 TerraSAR-X InSAR coherence images showing a portion of the East Rift Zone and south flank of Kīlauea volcano, Hawaii (inset). The images span (a) 15 September–23 December 2011 and (b) 25 January–25 May 2012. The extent of lava flows from the ongoing Pu'u 'Ō'ō–Kupaianaha eruption, which began in 1983, is outlined in white. Areas outside the lava field are covered by dense rain forest, which results in coherence loss (dark areas). The same is true for a flow in the central part of the field that was active while the images were acquired. (Images were processed and provided by Michael Poland, USGS Hawaiian Volcano Observatory.)

surface topography before and after the eruption. Multiple repeat-pass interferograms were used to correct various error sources and generate the two high-quality DEMs (Lu et al. 2003).

The TerraSAR-X tandem mission for DEM measurements (TanDEM-X) was launched by the German Aerospace Center (DLR) in 2010 (http://www.dlr.de/hr/en/desktopdefault.aspx/tabid-2317/). TanDEM-X is a high-resolution InSAR mission that relies on an innovative flight formation of two tandem TerraSAR-X satellites to produce InSAR-derived DEMs on a global scale with accuracy better than that of SRTM (Krieger et al. 2007). X-band SARs on the two satellites record data synchronously with a closely controlled baseline separation of 200–500 m. Precise baseline information and simultaneous data acquisitions result in InSAR images that are nearly immune to the baseline errors, atmospheric contamination and temporal decorrelation that sometimes plague DEMs derived from repeat-pass InSAR. Thus, the TanDEM-X mission enables the production of a global DEM of unprecedented accuracy, coverage and quality: TanDEM-X DEMs have a specified relative vertical accuracy of 2 m and an absolute vertical accuracy of 10 m at a horizontal resolution of 12 m (Krieger et al. 2007).

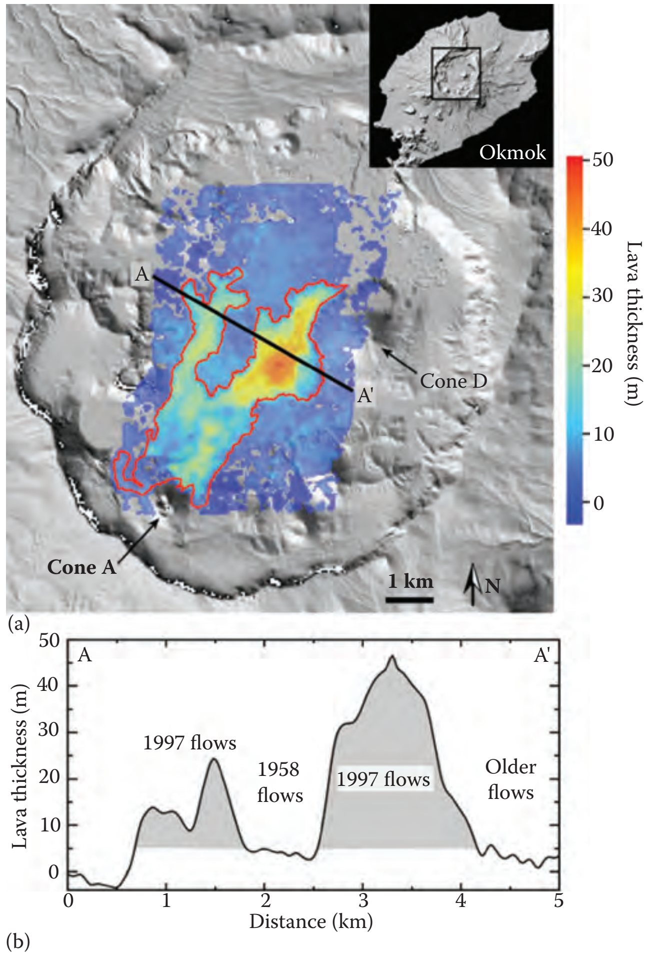

FIGURE 18.7 Thickness of lava flows from the 1997 eruption at Mount Okmok produced by differencing pre- and post-eruption DEMs derived from InSAR. (a) Map view of the 1997 lava flows. The red line represents the flow perimeter based on field mapping in August 2001 (Lu et al. 2003). The inset is a shaded relief image of Okmok; the black rectangle shows the extent of (a). (b) Lava thickness along the profile A-A′ across the 1997 flows and a small portion of the underlying 1958 flows that are not covered by 1997 flows. The locations of A-A′ are shown in (a).

18.6 MULTI-INTERFEROGRAM InSAR

When more than two SAR images are available for a given study area, multi-interferogram InSAR processing can be employed to improve the accuracy of deformation maps (or other InSAR products) (Ferretti et al. 2001, 2007; Berardino et al. 2002; Hooper et al. 2007; Rocca 2007; Zhang et al. 2011, 2012; Lu and Dzurisin 2014; Lu and Zhang 2014). A goal of multi-interferogram InSAR processing is to characterize the spatial and temporal behaviours of the deformation signal plus various artefacts and noise sources (e.g. atmospheric delay anomalies, including radar frequency-dependent ionosphere refraction and non-dispersive troposphere delay of the radar signals; orbit errors; and DEM-induced artefacts) in individual interferograms, and then to remove the artefacts to retrieve time-series deformation measurements at the SAR pixel level.

Among several approaches to multi-interferogram analysis, persistent scatterer InSAR (PSInSAR) is one of the newest and most promising. PSInSAR exploits the distinctive backscattering characteristics of certain ground targets (PS; examples include buildings, houses, bridges, dams, large boulders or rock outcrops) and the unique characteristics of atmospheric delay anomalies to improve the accuracy of conventional InSAR deformation measurements (Ferretti et al. 2001). The SAR backscattering signal of a PS target has a broadband spectrum in the frequency domain, which implies that the radar phase of a PS target correlates over much longer time intervals and over much longer baselines than that of other targets. As a result, if the backscatter signal from a given pixel is dominated by return from one or more PSs, the pixel remains coherent over longer time intervals and longer baselines than it would in the absence of the PS pixels. Therefore, at PS pixels, the limitation imposed by loss of coherence in conventional InSAR analysis can be overcome. Because InSAR coherence is maintained at PS pixels, the atmospheric contribution to the

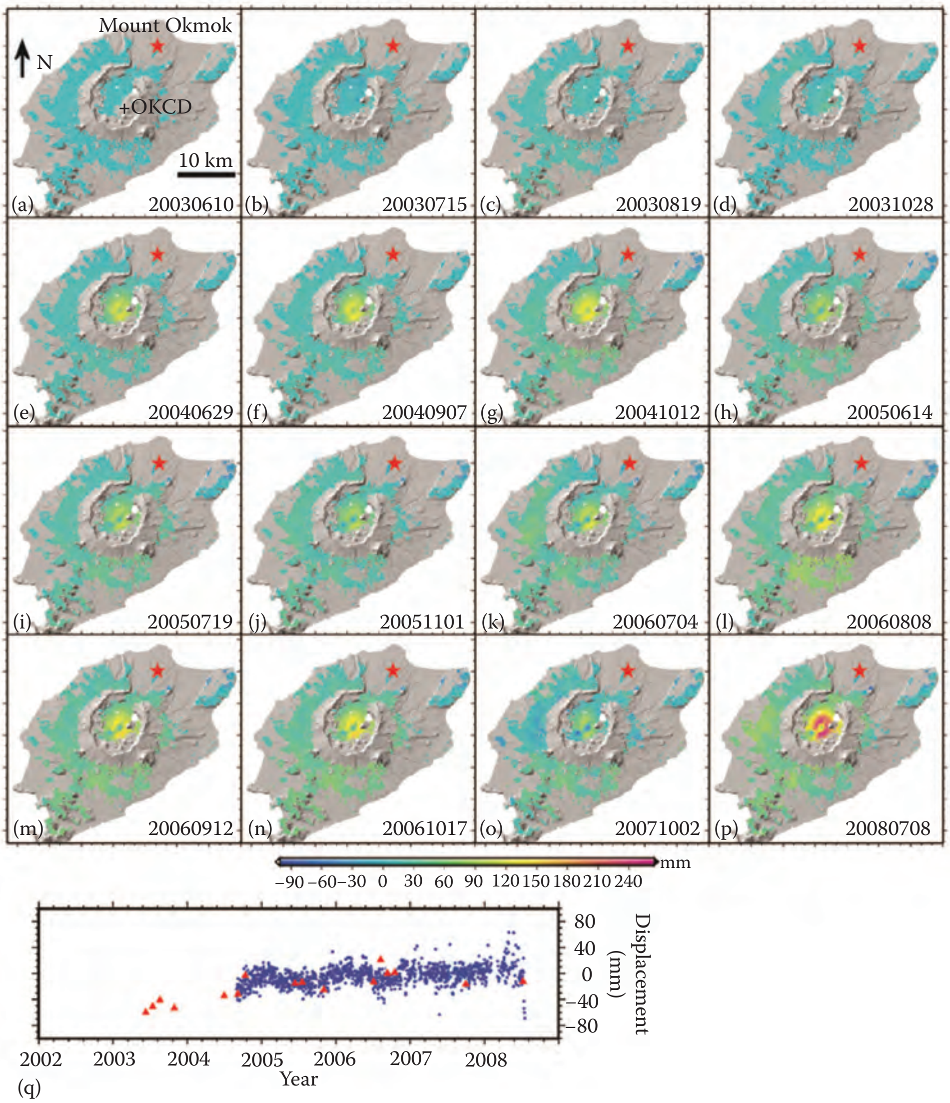

FIGURE 18.8 (a–p) Time-series deformation maps for Mount Okmok based on PSInSAR processing of 19 Envisat SAR images acquired during 2003–2008. The red star in the northeast quadrant represents the pixel used for PSInSAR processing. The location of the CGPS station OKCD is indicated by a black cross (+) in (a). (q) Comparison of time-series PSInSAR measurements (red triangles) with CGPS observations (blue dots) at OKCD. PSInSAR displacements are with respect to the reference pixel; the start time of the PSInSAR time series is 10 June 2003.

backscattered signal, DEM error and orbit error can be identified and removed from the data using a multi-interferogram iterative approach. After these errors are removed, displacement histories at PS pixels can be resolved with millimetre accuracy. If a sufficient number of PS pixels exist in a series of interferograms, relative displacements among them can provide a detailed picture of the surface deformation field.

Figure 18.8a–p shows time-series deformation maps for the period 2003–2008 at Mount Okmok based on PSInSAR processing of a stack of 19 Envisat SAR images. The average inflation rate near the centre of the caldera is slightly less than 50 mm/year. The subsidence of 1997 lava flows on parts of the caldera floor is also discernible in some of the images. The PSInSAR-derived time-series displacements match CGPS measurements at nearby points (Figure 18.8q), demonstrating that PSInSAR can be useful either as a stand-alone tool or in conjunction with other techniques to track volcanic deformation.

18.7 CONCLUSION

Radar in various forms can provide timely observations of volcanic ash clouds, eruptive flows and ground surface deformation before, during and after eruptions. SAR and InSAR products can be used to (1) characterize changing volcanic landscapes that might otherwise be unmonitored or hidden from view, (2) map and measure the deformation of volcanic flows that can persist for decades, (3) estimate physical parameters of subsurface magma reservoirs and conduit systems, (4) monitor changes in reservoir volume and magma migration pathways and (5) contribute to eruption forecasts and volcanic hazard assessments. With more satellite radar platforms either operational or in the planning stages, SAR and InSAR are becoming increasingly important tools for studying volcanoes and associated hazards.

ACKNOWLEDGEMENTS

ERS-1, ERS-2 and Envisat, and TerraSAR-X SAR images are Copyright © 1992–2011 European Space Agency and © 2011–2012 DLR, respectively. ERS-1 and ERS-2 SAR images were provided by Alaska Satellite Facility. We thank Lei Zhang, Michael Poland, and David Schneider and Richard Hoblitt for providing the materials used in Figures 18.8, 18.6 and 18.1, respectively. This work was supported by the National Aeronautics and Space Administration's (NASA) Earth Surface and Interior Program (NNX14AQ95G), the U.S. Geological Survey (USGS) Volcano Hazards Program and the Shuler–Foscue Endowment at Southern Methodist University.

REFERENCES

Amelung, F., Jonsson, S., Zebker, H., and Segall, P. (2000). Widespread uplift and 'trapdoor' faulting on Galapagos volcanoes observed with radar interferometry. *Nature*, 407, 993–996.

Amelung, F., Yun, S. H., Walter, T. R., Segall, P., and Kim, S. W. (2007). Stress control of deep rift intrusion at Mauna Loa volcano, Hawaii. *Science*, 316, 1026–1030.

Bamler, R., and Hart, P. (1998). Synthetic aperture radar interferometry. *Inverse Problems*, 14, R1–R54.

Berardino, P., Fornaro, G., Lanari, R., and Sansosti, E. (2002). A new algorithm for surface deformation monitoring based on small baseline differential SAR interferograms. *IEEE Transactions on Geoscience and Remote Sensing*, 40, 2375–2383.

Biggs, J., Amelung, F., Gourmelen, N., Dixon, T., and Kim, S. W. (2009). InSAR observations of 2007 Tanzania rifting episode reveal mixed fault and dyke extension in an immature continental rift. *Geophysical Journal International*, 179, 549–558.

Biggs, J., Anthony, E. Y., and Ebinger, C. J. (2010a). Multiple inflation and deflation events at Kenyan volcanoes, East African Rift. *Geology*, 37, 979–982.

Biggs, J., Lu, Z., Fournier, T., and Freymueller, J. (2010b). Magma flux at Okmok Volcano, Alaska from a joint inversion of continuous GPS, campaign GPS and InSAR. *Journal of Geophysical Research*, 115, B12401. doi: 10.1029/2010JB007577.

Calais, E., d'Oreye, N., Albaric, J., Deschamps, A., Delvaux, D., Déverchére, J., Ebinger, C. et al. (2008). Aseismic strain accommodation by dyking in a youthful continental rift, East Africa. *Nature*, 456, 783–787. doi: 10.1038/nature07478.

Chen, C., and Zebker, H. (2000). Network approaches to two-dimensional phase unwrapping: Intractability and two new algorithms. *Journal of the Optical Society of America A*, 17, 401–414.

Costantini, M. (1998). A novel phase unwrapping method based on network programming. *IEEE Transactions on Geoscience and Remote Sensing*, 36, 813–818.

Curlander, J. C., and McDonough, R. N. (1991). *Synthetic Aperture Radar: Systems and Signal Processing*. 1st ed., Wiley Series in Remote Sensing and Image Processing. Hoboken, NJ: Wiley-Interscience.

Currenti, G., Napoli, R., and Del Negro, C. (2011). Toward a realistic deformation model of the 2008 magmatic intrusion at Etna from combined DInSAR and GPS observations. *Earth and Planetary Science Letters*, 312, 22–27.

Currenti, G., Solaro, G., Napoli, R., Pepe, A., Bonaccorso, A., Del Negro, C., and Sansosti, E. (2012). Modelling of ALOS and COSMO-SkyMed satellite data at Mt Etna: Implications on relation between seismic activation of the Pernicana fault system and volcanic unrest. *Remote Sensing of Environment*, 125, 64–72.

Davis, P. M. (1986). Surface deformation due to inflation of an arbitrarily oriented triaxial ellipsoidal cavity in an elastic half-space, with reference to Kīlauea Volcano, Hawaii. *Journal of Geophysical Research*, 91, 7429–7438.

Delaney, P. T., and McTigue, D. F. (1994). Volume of magma accumulation or withdrawal estimated from surface uplift or subsidence, with application to the 1960 collapse of Kīlauea volcano. *Bulletin of Volcanology*, 56, 417–424.

Del Negro, C., Currenti, G., Solaro, G., Greco, F., Pepe, A., Napoli, R., Pepe, S., Casu, F., and Sansosti, E. (2013). Capturing the fingerprint of Etna volcano activity in gravity and satellite radar data. *Scientific Reports*, 3, 3089. doi: 10.1038/srep03089.

Dubosclard, G., Cordesses, R., Alard, P., Hervier, C., Coltelli, M., and Kornprobst, J. (1999). First testing of a volcano Doppler radar (Voldorad) at Mt. Etna. *Journal of Geophysical Research*, 26, 3389–3392.

Dvorak, J., and Dzurisin, D. (1997). Volcano geodesy—The search for magma reservoirs and the formation of eruptive vents. *Reviews of Geophysics*, 35, 343–384.

Dzurisin, D. (2003). A comprehensive approach to monitoring volcano deformation as a window on eruption cycle. *Reviews of Geophysics*, 41, 1–29. doi: 10.1029/2001RG000107.

Dzurisin, D. (2007). *Volcano Deformation—Geodetic Monitoring Techniques*. Vol. 7, Springer-Praxis Books in Geophysical Sciences. Berlin: Springer.

Dzurisin, D., Lisowski, M., and Wicks, C. W. (2009). Continuing inflation at Three Sisters volcanic center, central Oregon Cascade Range, USA, from GPS, leveling, and InSAR observations. *Bulletin of Volcanology*, 71, 1091–1110.

Dzurisin, D., Lisowski, M., Wicks, C. W., Poland, M. P., and Endo, E. T. (2005). Geodetic observations and modeling of magmatic inflation at the Three Sisters volcanic center, central Oregon Cascade Range, USA. *Journal of Volcanology and Geothermal Research*, 150, 35–54.

Dzurisin, D., Wicks, C., Jr., and Thatcher, W. (1999). Renewed uplift at the Yellowstone caldera measured by leveling surveys and satellite radar interferometry. *Bulletin of Volcanology*, 61, 349–355.

Farr, T. G., Rosen, P. A., Caro, E., Crippen, R., Duren, R., Hensley, S., Kobrick, M. et al. (2007). The Shuttle Radar Topography Mission. *Reviews of Geophysics*, 45, RG2004. doi: 10.1029/2005RG000183.

Ferretti, A., Prati, C., and Rocca, F. (1999). Multibaseline InSAR DEM reconstruction—The wavelet approach. *IEEE Transactions on Geoscience and Remote Sensing*, 37, 705–715.

Ferretti, A., Prati, C., and Rocca, F. (2001). Permanent scatterers in SAR interferometry. *IEEE Transactions on Geoscience and Remote Sensing*, 39, 8–20.

Ferretti, A., Savio, G., Barzaghi, R., Borghi, A., Musazzi, S., Novali, F., Prati, C., and Rocca, F. (2007). Submillimeter accuracy of InSAR time series: Experimental validation. *IEEE Transactions on Geoscience and Remote Sensing*, 45, 1142–1153.

Fialko, Y., Khazan, Y., and Simons, M. (2001). Deformation due to a pressurized horizontal circular crack in an elastic half-space, with applications to volcano geodesy. *Geophysical Journal International*, 146, 181–190.

Foster, J., Brooks, B., Cherubini, T., Shacat, C., Businger, S., and Werner, C. L. (2006). Mitigating atmospheric noise for InSAR using a high resolution weather model. *Geophysical Research Letters*, 33, L16304. doi: 10.1029/2006GL026781.

Fournier, T. J., Pritchard, M. E., and Riddick, S. N. (2010). Duration, magnitude, and frequency of subaerial volcano deformation events: New results from Latin America using InSAR and a global synthesis. *Geochemistry, Geophysics, Geosystems*, 11, Q01003. doi: 10.1029/2009GC002558.

Fukushima, Y., Cayol, V., and Durand, P. (2005). Finding realistic disk models from interferometric synthetic aperture radar data: The February 2000 eruption at Piton de la Fournaise. *Journal of Geophysical Research*, 110, B03206. doi: 10.1029/2004JG0003268.

Gray, L., and Farris-Manning, P. (1993). Repeat-pass interferometry with airborne synthetic aperture radar. *IEEE Transactions on Geoscience and Remote Sensing*, 31, 180–191.

Goldstein, R., Zebker, H., and Werner, C. (1998). Satellite radar interferometry: Two-dimensional phase unwrapping. *Radio Science*, 23, 713–720.

Goldstein, R. M., and Werner, C. L. (1998). Radar interferogram filtering for geophysical applications. *Geophysical Research Letters*, 25, 4035–4038.

Hanssen, R. (2001). *Radar Interferometry—Data Interpretation and Error Analysis*. Dordrecht, the Netherlands: Kluwer Academic Publishers.

Harris, D. M., and Rose, W. I. (1983). Estimating particle sizes, concentrations and total mass of ash in volcanic clouds using weather radar. *Journal of Geophysical Research*, 88, 10969–10983.

Henderson, F., and Lewis, A. (1998). *Principles and Applications of Imaging Radar: Manual of Remote Sensing*. 3rd ed., vol. 2. Hoboken, NJ: John Wiley & Sons.

Hensley, S., Munjy, R., and Rosen, P. (2001). Interferometric synthetic aperture radar (IFSAR). In *Digital Elevation Model Technologies and Applications—The DEM Users Manual*, ed. D. F. Maune. 2nd ed. Bethesda, MD: American Society for Photogrammetry and Remote Sensing, 142–206.

Hildreth, W., and Fierstein, J. (2012). The Novarupta-Katmai eruption of 1912—Largest eruption of the twentieth century; centennial perspectives. U.S. Geological Survey Professional Paper 1791. http://pubs.usgs.gov/pp/1791/.

Hooper, A., Segall, P., and Zebker, H. (2007). Persistent scatterer interferometric synthetic aperture radar for crustal deformation analysis, with application to Volcán Alcedo, Galápagos. *Journal of Geophysical Research*, 112, B07407. doi: 10.1029/2006JB004763.

Houlié, N., Briole, P., Nercessian, A., and Murakami, M. (2005). Sounding the plume of the 18 August 2000 eruption of Miyakejima volcano (Japan) using GPS. *Geophysical Research Letters*, 32, L05302.

Ji, L. Y., Lu, Z., Dzurisin, D., and Senyukov, S. (2013). Pre-eruption deformation caused by dike intrusion beneath Kizimen volcano, Kamchatka, Russia, observed by InSAR. *Journal of Volcanology and Geothermal Research*, 256, 87–95.

Johnson, D. J. (1987). Elastic and inelastic magma storage at Kīlauea volcano. In *Volcanism in Hawaii*, ed. R. W. Decker, T. L. Wright, and P. H. Stauffer. U.S. Geological Survey Professional Paper 1350. Washington, DC: U.S. Government Printing Office, 1297–1306.

Krieger, G., Moreira, A., Fiedler, H., Hajnsek, I., Werner, M., Younis, M., and Zink, M. (2007). TanDEM-X—A satellite formation for high-resolution SAR interferometry. *IEEE Transactions on Geoscience and Remote Sensing*, 45, 3317–3341.

Lacasse, C., Karlsdóttir, S., Larsen, G., Soosalu, H., Rose, W. I., and Ernst, G. G. J. (2004). Weather radar observations of the Hekla 2000 eruption cloud, Iceland. *Bulletin of Volcanology*, 66, 457–473.

Lee, C. W., Lu, Z., Won, J. S., Jung, H. S., and Dzurisin, D. (2013). Dynamic deformation of Seguam Island, Alaska, 1992–2008, from multi-interferogram InSAR processing. *Journal of Volcanology and Geothermal Research*, 260, 43–51.

Li, Z., Fielding, E., Cross, P., and Muller, J.-P. (2005). InSAR atmospheric correction—GPS topography-dependent turbulence model (GTTM). *Journal of Geophysical Research*, 110, B02404. doi: 10.1029/2005JB003711.

Li, Z., Muller, J.-P., and Cross, P. (2003). Comparison of precipitable water vapor derived from radiosonde, GPS, and moderate-resolution imaging spectroradiometer measurements. *Journal of Geophysical Research*, 108, 4651. doi: 10.1029/2003JD003372.

Lu, Z. (2007). InSAR imaging of volcanic deformation over cloud-prone areas—Aleutian Islands. *Photogrammatric Engineering & Remote Sensing*, 73, 245–257.

Lu, Z., and Dzurisin, D. (2010). Ground surface deformation patterns, magma supply, and magma storage at Okmok volcano, Alaska, inferred from InSAR analysis: II. Co-eruptive deflation, July-August 2008. *Journal of Geophysical Research*, 115, B00B02. doi: 10.1029/2009JB006970.

Lu, Z., and Dzurisin, D. (2014). *InSAR Imaging of Aleutian Volcanoes—Monitoring a Volcanic Arc from Space*. Springer-Praxis Books in Geophysical Sciences. Berlin: Springer.

Lu, Z., Dzurisin, D., Biggs, J., Wicks, C., Jr., and McNutt, S. (2010). Ground surface deformation patterns, magma supply, and magma storage at Okmok volcano, Alaska, from InSAR analysis: I. Inter-eruption deformation, 1997–2008. *Journal of Geophysical Research*, 115, B00B03. doi: 10.1029/2009JB006969.

Lu, Z., Dzurisin, D., Wicks, C., Power, J., Kwoun, O., and Rykhus, R. (2007). Diverse deformation patterns of Aleutian volcanoes from satellite interferometric synthetic aperture radar (InSAR). In *Volcanism and Subduction: The Kamchatka Region*, ed. J. Eichelberger, E. Gordeev, P. Izbekov, M. Kasahara, and J. Lees. American Geophysical Union Geophysical Monograph Series 172. Washington, DC: American Geophysical Union, 249–261.

Lu, Z., Fatland, R., Wyss, M., Li, S., Eichelberger, J., Dean, K., and Freymueller, J. T. (1997). Deformation of volcanic vents detected by ERS 1 SAR interferometry, Katmai National Park, Alaska. *Geophysical Research Letters*, 24, 695–698.

Lu, Z., and Freymueller, J. (1998). Synthetic aperture radar interferometry coherence analysis over Katmai volcano group, Alaska. *Journal of Geophysical Research*, 103, 29887–29894.

Lu, Z., Fielding, E., Patrick, M., and Trautwein, C. (2003). Estimating lava volume by precision combination of multiple baseline spaceborne and airborne interferometric synthetic aperture radar: The 1997 eruption of Okmok volcano, Alaska. *IEEE Transactions on Geoscience and Remote Sensing*, 41, 1428–1436.

Lu, Z., Jung, H. S., Zhang, L., Lee, W. J., Lee, C. W., and Dzurisin, D. (2013). DEM generation from satellite InSAR. In *Advances in Mapping from Aerospace Imagery: Techniques and Applications*, ed. X. Yang and J. Li. Boca Raton, FL: CRC Press, 119–144.

Lu, Z., Mann, D., Freymueller, J., and Meyer, D. (2000c). Synthetic aperture radar interferometry of Okmok volcano, Alaska: Radar observations. *Journal of Geophysical Research*, 105, 10791–10806.

Lu, Z., Masterlark, T., and Dzurisin, D. (2005). Interferometric synthetic aperture radar (InSAR) study of Okmok volcano, Alaska, 1992–2003: Magma supply dynamics and post-emplacement lava flow deformation. *Journal of Geophysical Research*, 110, B02403. doi: 10.1029/2004JB003148.

Lu, Z., and Kwoun, O. (2008). Radarsat-1 and ERS interferometric analysis over southeastern coastal Louisiana: Implication for mapping water-level changes beneath swamp forests. *IEEE Transactions on Geoscience and Remote Sensing*, 46, 2167–2184.

Lu, Z., Power, J., McConnell, V., Wicks, C., and Dzurisin, D. (2002). Pre-eruptive inflation and surface interferometric coherence characteristics revealed by satellite radar interferometry at Makushin volcano, Alaska: 1993–2000. *Journal of Geophysical Research*, 107, 2266. doi: 10.1029/2001JB000970.

Lu, Z., Rykhus, R., Masterlark, T., and Dean, K. (2004). Mapping recent lava flows at Westdahl volcano, Alaska, using radar and optical satellite imagery. *Remote Sensing of Environment*, 91, 345–353.

Lu, Z., Wicks, C., Dzurisin, D., Power, J., Moran, S., and Thatcher, W. (2002). Magmatic inflation at a dormant stratovolcano—1996–98 activity at Mount Peulik volcano, Alaska, revealed by satellite radar interferometry. *Journal of Geophysical Research*, 107, 2134. doi: 10.1029/2001JB000471.

Lu, Z., Wicks, C., Dzurisin, D., Thatcher, W., Freymueller, J., McNutt, S., and Mann, D. (2000b). Aseismic inflation of Westdahl volcano, Alaska, revealed by satellite radar interferometry. *Geophysical Research Letters*, 27, 1567–1570.

Lu, Z., Wicks, C., Power, J., and Dzurisin, D. (2000a). Ground deformation associated with the March 1996 earthquake swarm at Akutan volcano, Alaska, revealed by satellite radar interferometry. *Journal of Geophysical Research*, 105, 21483–21496.

Lu, Z., and Zhang, L. (2014). Frontiers of Radar Remote Sensing. *Photogrammetric Engineering & Remote Sensing*, 80, 5–13.

Lundgren, P., and Lu, Z. (2006). Inflation model of Uzon caldera, Kamchatka, constrained by satellite radar interferometry observations. *Geophysical Research Letters*, 33, L063012. doi: 10.1029/2005GL025181.

Mann, D., Freymueller, J., and Lu, Z. (2002). Deformation associated with the 1997 eruption of Okmok volcano, Alaska. *Journal of Geophysical Research*, 107, 10.1029/2001JB000163.

Marzano, F. S., Barbieri, S., Vulpiani, G., and Rose, W. I. (2006). Volcanic ash cloud retrieval by ground-based microwave weather radar. *IEEE Transactions on Geoscience and Remote Sensing*, 44, 3235–3246.

Massonnet, D., Briole, P., and Arnaud, A. (1995). Deflation of Mount Etna monitored by spaceborne radar interferometry. *Nature*, 375, 567–570.

Massonnet, D., and Feigl, K. (1998). Radar interferometry and its application to changes in the earth's surface. *Reviews of Geophysics*, 36, 441–500.

Massonnet, D., and Souyris, J. S. (2008). *Imaging with Synthetic Aperture Radar.* Lausanne, Switzerland: EPFL Press.

Masterlark, T., and Lu, Z. (2004). Transient volcano deformation sources imaged with InSAR: Application to Seguam island. *Journal of Geophysical Research*, 109, B01401. doi: 10.1029/2003JB002568.

Miller, T. P., and Casadevall, T. J. (2000). Volcanic ash hazards to aviation. In *Encyclopaedia of Volcanolcanology*, ed. H. Sigurdsson. New York: Academic, 915–930.

Mogi, K. (1958). Relations between the eruptions of various volcanoes and the deformation of the ground surfaces around them. *Bulletin of the Earthquake Research Institute, University of Tokyo*, 36, 99–134.

Myers, B., Brantley, S. R., Stauffer, P., and Hendley, J. W., II. (2008). What are volcano hazards? USGS Fact Sheet 002-97. http://pubs.usgs.gov/fs/fs002-97/.

Newhall, C. G., and Punongbayan, R. S. (1996). Eruptive history of Mount Pinatubo. In *Fire and Mud: Eruptions and Lahars of Mount Pinatubo, Philippines*. Seattle: University of Washington Press, 165–195.

Okada, Y. (1985). Surface deformation due to shear and tensile faults in a half-space. *Bulletin of the Seismological Society of America*, 75, 1135–1154.

Parker, A., Biggs, J., and Lu, Z. (2014). Investigating long-term subsidence at Medicine Lake Volcano, CA, using multi-temporal InSAR. *Geophysical Journal International*, 199, 844–859.

Poland, M. P., Bürgmann, R., Dzurisin, D., Lisowski, M., Masterlark, T., Owen, S., and Fink, J. (2006a). Constraints on the mechanism of long-term, steady subsidence at Medicine Lake volcano, northern California, from GPS, leveling, and InSAR. *Journal of Volcanology and Geothermal Research*, 150, 55–78.

Poland, M., Hamburger, M., and Newman, A. (2006b). The changing shapes of active volcanoes: History, evolution, and future changes for volcano geodesy. *Journal of Volcanology and Geothermal Research*, 150, 1–13. doi: 10.1016/j.jvolgeores.2005.11.005.

Press, W. H., Teukolsky, S. A., Vetterling, W. T., and Flannery, B. P. (2007). *Numerical Recipes in C—The Art of Scientific Computing*. 3rd ed. Cambridge: Cambridge University Press.

Pritchard, M. E., and Simons, M. (2002). A satellite geodetic survey of large-scale deformation of volcanic centres in the central Andes. *Nature*, 418, 167–171.

Pritchard, M. E., and Simons, M. (2004a). An InSAR-based survey of volcanic deformation in the central Andes. *Geochemistry, Geophysics, Geosystems*, 5. doi: 10.1029/2003GC000610.

Pritchard, M. E., and Simons, M. (2004b). Surveying volcanic arcs with satellite radar interferometry: The central Andes, Kamchatka, and beyond. *GSA Today*, 14, 4–11.

Robock, A. (2013). The latest on volcanic eruptions and climate. *Eos, Transactions, American Geophysical Union*, 94, 305–312.

Rocca, F. (2007). Modeling interferogram stacks. *IEEE Transactions on Geoscience and Remote Sensing*, 45, 3289–3299.

Rose, W. I. (1977). Scavenging of volcanic aerosol by ash: Atmospheric and volcanological implications. *Geology*, 5, 621–624.

Rose, W. I., Kostinski, A. B., and Kelley, L. (1995). Real time C band radar observations of 1992 eruption clouds from Crater Peak/Spurr volcano, Alaska. *U.S. Geological Survey Bulletin*, 2139, 19–26.

Rosen, P., Hensley, S., Joughin, I. R., Li, F. K, Madsen, S. N., Rodriguez, E., and Goldstein, R. M. (2000). Synthetic aperture radar interferometry. *Proceedings of the IEEE*, 88, 333–380.

Rosen, P., Hensley, S., Zebker, H., Webb, F. H., and Fielding, E. J. (1996). Surface deformation and coherence measurements of Kīlauea volcano, Hawaii, from SIR-C radar interferometry. *Journal of Geophysical Research*, 101, 23109–23125.

Rust, A. C., Russell, J. K., and Knight, R. J. (1999). Dielectric constant as a predictor of porosity in dry volcanic rocks. *Journal of Volcanology and Geothermal Research*, 91, 79–96.

Schneider, D., and Hoblitt, R. (2013). Doppler weather radar observations of the 2009 eruption of Redoubt volcano, Alaska. *Journal of Volcanology and Geothermal Research*, 259, 133–144.

Tupper, A., Oswalt, J. S., and Rosenfield, D. (2005). Satellite and radar analysis of volcanic-cumulonimbi at Mount Pinatubo, Philippines, 1991. *Journal of Geophysical Research*, 110, D9204, http://dx.doi.org/10.1029/2004JD005499.

Wang, T., Poland, M. P., and Lu, Z. (2015). Dome growth at Mount Cleveland, Aleutian Arc, quantified by time series TerraSAR-X imagery. *Geophysical Research Letters*, 42, 1–8. doi: 10.1002/2015GL066784.

Wicks, C., de la Llera, J. C., Lara, L., and Lowenstern, J. (2011). The role of dyking and fault control in the rapid onset of eruption at Chaitén volcano, Chile. *Nature*, 478, 374–377.

Wicks, C., Dzurisin, D., Ingebritsen, S., Thatcher, W., Lu, Z., and Iverson, J. (2002). Magma intrusion beneath the Three Sisters Volcanic Center in the Cascade Range of Oregon, USA, from interferometric radar measurements. *Geophysical Research Letters*, 29. doi: 10.1029/2001GL014205.

Wicks, C., Thatcher, W., and Dzurisin, D. (1998). Migration of fluids beneath Yellowstone caldera inferred from satellite radar interferometry. *Science*, 282, 458–462.

Wicks, C., Thatcher, W., Dzurisin, D., and Svarc, J. (2006). Uplift, thermal unrest and magma intrusion at Yellowstone caldera. *Nature*, 440, 72–75.

Wright, T., Ebinger, C., Biggs, J., Ayele, A., Yirgu, G., Keir, D., and Stork, A. (2006). Magma-maintained rift segmentation at continental rupture in the 2005 Afar dyking episode. *Nature*, 442, 291–294.

Yang, X.-M., Davis, P. M., and Dieterich, J. H. (1988). Deformation from inflation of a dipping finite prolate spheroid in an elastic half-space as a model for volcanic stressing. *Journal of Geophysical Research*, 93, 4249–4257.

Yun, S., Segall, P., and Zebker, H. (2006). Constraints on magma chamber geometry at Sierra Negra Volcano, Galapagos Islands, based on InSAR observations. *Journal of Volcanology and Geothermal Research*, 150, 232–243.

Zebker, H., Amelung, F., and Jonsson, S. (2000). Remote sensing of volcano surface and internal processing using radar interferometry. In *Remote Sensing of Active Volcanism*, ed. P. Mouginis-Mark, J. A. Crisp, and J. H. Fink. AGU Monograph. Washington, DC: American Geophysical Union, 179–205.

Zebker, H. A., Rosen, P. A., Goldstein, R. M., Gabriel, A., and Werner, C. L. (1994). On the derivation of coseismic displacement fields using differential radar interferometry—The Landers earthquake. *Journal of Geophysical Research*, 99, 19617–19634.

Zebker, H., and Villasenor, J. (1992). Decorrelation in interferometric radar echoes. *IEEE Transactions on Geoscience and Remote Sensing*, 30, 950–959.

Zhang, L., Ding, X. L., and Lu, Z. (2011). Modeling PSInSAR time-series without phase unwrapping. *IEEE Transactions on Geoscience and Remote Sensing*, 49, 547–556. doi: 10.1109/TGRS.2010.2052625.

Zhang, L., Lu, Z., Ding, X. L., Jung, H. S., Feng, G. C., and Lee, C. W. (2012). Mapping ground surface deformation using temporarily coherent point SAR interferometry—Application to Los Angeles Basin. *Remote Sensing of Environment*, 117, 429–439.